1 2  9 0

UNIVERSIDADE D
COIMBRA

Ana Isabel Gomes da Mata

Development of a Tumour-targeted Strategy for Photodynamic Therapy

Tese no âmbito do Doutoramento em Química, ramo de Química Médica, orientada pelo Professor Doutor Rui Manuel Pontes Meireles Ferreira de Brito, pela Professora Doutora Teresa Margarida Vasconcelos Dias de Pinho e Melo e pela Doutora Lígia Catarina Gomes-da-Silva e apresentada ao Departamento de Química da Faculdade de Ciências e Tecnologia da Universidade de Coimbra.

Dezembro de 2022

Faculdade de Ciências e Tecnologia
da Universidade de Coimbra

DEVELOPMENT OF A TUMOUR-TARGETED STRATEGY FOR PHOTODYNAMIC THERAPY

Ana Isabel Gomes da Mata

Tese no âmbito do Doutoramento em Química, ramo de Química Médica, orientada pelo Professor Doutor Rui Manuel Pontes Meireles Ferreira de Brito, pela Professora Doutora Teresa Margarida Vasconcelos Dias de Pinho e Melo e pela Doutora Lígia Catarina Gomes-da-Silva e apresentada ao Departamento de Química da Faculdade de Ciências e Tecnologia da Universidade de Coimbra.

Dezembro de 2022

UNIVERSIDADE D
COIMBRA

The research presented in this doctoral thesis was supported by the PhD Fellowship PD/BD/135289/2017 granted by the MedChemTrain PhD programme (PD/00147/2013) in Medicinal Chemistry and the Research Fellowship COVID/BD/152184/2021 as an Exceptional Grant for the Mitigation of the COVID-19 Impact on Research Activities – *Fundação para a Ciência e a Tecnologia*[1] (FCT), *Ministério da Ciência, Tecnologia e Ensino Superior*[2] (MCTES), Portugal. The work performed at *Centro de Química de Coimbra*[3] – Institute of Molecular Sciences (CQC-IMS), University of Coimbra, coordinated by Professor Rui M. M. Brito, PhD, Professor Teresa M. V. D. Pinho e Melo, PhD, and Lígia C. Gomes-da-Silva, PhD, was funded in part by National funds through FCT, I.P., within the project with the reference UIDB/00313/2020 and UIDP/0013/2020 (to CQC-IMS).

[1] Foundation for Science and Technology
[2] Ministry of Science, Technology, and Higher Education
[3] Coimbra Chemistry Centre

Don't be afraid of hard work. Nothing worthwhile comes easily.

Don't let others discourage you or tell you that you can't do it.
In my day I was told women didn't go into chemistry.
I saw no reason why we couldn't.

Gertrude Elion

Dedicated to my favourite sister, Carla, and my nephew, Henrique.

Dedicado à minha irmã preferida, Carla, e ao meu sobrinho, Henrique.

Acknowledgements

It is a truth universally acknowledged, that a scientist in possession of doctoral degree, must be able to autonomously conduct research.[1] While following through with a PhD does strengthen the necessary hard skills to independently plan, execute, and critically analyse one's project, it also allows for the cultivation of soft skills, which are inherently dependent on the network of relationships founded in the process. As such, when reaching the end of one more milestone I feel the need to acknowledge everyone who supported me during this long journey.

É uma verdade universalmente reconhecida que um cientista, na posse de um grau de doutor, necessita de saber conduzir uma investigação de maneira autónoma.[1] Ainda que um doutoramento realmente fortifique as competências necessárias para planear, executar e fazer a análise crítica de um projecto de forma independente, também permite o desenvolvimento de habilidades comportamentais que são inerentemente dependentes dos relacionamentos fundados no processo. Assim, ao atingir mais um patamar, sinto necessidade de agradecer a todos os que me apoiaram durante esta longa jornada.

To my supervisor, Prof. Dr. Rui Brito, I thank the chance to integrate the area of computational chemistry, alongside the contributions from several scientific discussions and advice throughout these years, and the opportunity to broaden my knowledge on the use of such techniques (beyond the ones necessary to complete my project) by including me in different collaborations.

Ao meu supervisor, Prof. Dr. Rui Brito, agradeço a chance de me integrar na área de química computacional, assim como as suas contribuições em discussões científicas e conselhos ao longo destes anos, e a oportunidade de alargar o meu conhecimento com o uso de diferentes técnicas (além das necessárias para o meu projecto) ao me incluir em diferentes colaborações.

[1] Adapted from the original «It is a truth universally acknowledged, that a single man in possession of a good fortune, must be in want of a wife.» found in *Pride and Prejudice*, by Jane Austen.
Adaptado do original «É uma verdade universalmente reconhecida que um homem solteiro, na posse de uma fortuna avultada, necessita de uma esposa.» em *Orgulho e Preconceito*, escrito por Jane Austen.

To my co-supervisor, Prof. Dr. Teresa Pinho e Melo, I am grateful for the guidance and support that made this work possible with efficient troubleshooting at each step. After entering yet another area relatively new to me, I thank her dedication in seeing through my evolution in the lab.

À minha co-orientadora, Prof.ª Dr.ª Teresa Pinho e Melo, estou grata pela orientação e suporte que tornaram este trabalho possível com uma eficiente capacidade de resolução de problemas. Após entrar em mais uma área relativamente nova, agradeço-lhe a dedicação em acompanhar a minha evolução no laboratório.

To Dr. Lígia Gomes-da-Silva, my co-supervisor, who has followed my progress since I began working with photodynamic therapy. I thank all the time and attention devoted towards my scientific growth. She has been an outstanding mentor throughout my academic journey and will always be a role model for me.

À Dr.ª Lígia Gomes-da-Silva, minha co-orientadora, que tem seguido o meu progresso desde que comecei a trabalhar com terapia fotodinâmica. Agradeço-lhe todo o tempo e atenção dedicados ao meu crescimento como cientista. Tem sido uma mentora excepcional na minha jornada académica e será sempre uma inspiração a seguir.

I am thankful to the members of the Protein Biophysical Chemistry group for being a constant support during this time and the shared insights given by continuous discussions on the different themes that each member researched. To Andreia Cunha, Dr. Carlos Simões, Dr. Daniela Vaz, João Luís, Nícia Ferreira, Nuno Alves, Pedro Cruz, and Zaida Almeida, I am also grateful for making the RBritoLab more welcoming and interactive with all the team building experiences. To Pedro Cruz I also thank his collaboration on the nuclear magnetic resonance studies.

Agradeço aos membros do grupo da Química Biofísica de Proteínas por serem um apoio constante durante estes anos e pelas ideias partilhadas durante as contínuas discussões dos temas diferentes, investigados por cada um dos membros. À Andreia Cunha, Dr. Carlos Simões, Dr.ª Daniela Vaz, João Luís, Nícia Ferreira, Nuno Alves, Pedro Cruz e Zaida Almeida agradeço também por terem tornado o RBritoLab mais receptivo e interactivo com as actividades de equipa. Ao Pedro Cruz agradeço ainda a sua colaboração nos estudos de ressonância magnética nuclear.

To the Organic Chemistry group for receiving and sharing their expertise with me, especially Dr. Nelson Pereira and Dr. Ana Lúcia Cardoso, who were my pillars of knowledge, always available to answer any question. To Prof. Dr. Marta Piñero, Dr. Bruno Nascimento, Dr. Susana Lopes, Dr. Isabel Soares, Carla Grosso, Cláudia Alves, Carla Gomes, Américo Alves, and Nélia Tavares, I am grateful for all the help and will always remember the moments spent together. And, of course, I am thankful to Mrs. Lurdes for taking care of the lab and all of us with utmost attention and affection.

Ao grupo de Química Orgânica por me receberem e partilharem a sua experiência comigo, especialmente ao Dr. Nelson Pereira e Dr.ª Ana Lúcia Cardoso, que foram os meus pilares de conhecimento, sempre disponíveis para responder a qualquer questão. À Prof.ª Dr.ª Marta Piñero, Dr. Bruno Nascimento, Dr.ª Susana Lopes, Dr.ª Isabel Soares, Carla Grosso, Cláudia Alves, Carla Gomes, Américo Alves e Nélia Tavares, agradeço toda a ajuda e lembrar-me-ei sempre dos momentos que passámos juntos. E claro, agradeço à Dona Lurdes por tomar conta do laboratório e de todos nós, com a maior atenção e carinho.

I am grateful to the Laboratory for Photomedicine and Reactivity in the Medicinal Chemistry group, where I had the opportunity to start research during my bachelor's degree and I have been fortunate enough to always be a part of it until today. This group has always been a source of companionship, where I could count on to help overcome any obstacles (scientific or not), broadening my views during the process. To Prof. Dr. Luís Arnaut for always being ready to help me reach whatever goal I come forward with; I will always appreciate the support and scientific discussions throughout the years. To Dr. Fábio Schaberle for all the help in the spectroscopic fields and for always encouraging quick thinking and out-of-the-box problem solving, with his endless search for more knowledge. To Ana Catarina Lobo, Maria Inês Mendes, Piotr Gierlich, Claire Donohoe, and Zoi Melissari, I thank all the help and the collaborative discussions that promoted learning more about the applications of photomedicine in your projects and your friendship which "stretched out" farther outside the lab.

Agradeço ao Laboratório para Fotomedicina e Reactividade no grupo de Química Medicinal, onde tive oportunidade de começar a investigar durante a licenciatura e tive a sorte de continuar a ser parte dele até hoje. Este grupo tem sempre sido uma fonte de companheirismo, onde podia contar com ajuda para superar qualquer obstáculo (científico ou não), alargando os meus horizontes durante o processo. Ao Prof. Dr. Luís Arnaut agradeço a sua prontidão em ajudar-me a alcançar qualquer objectivo que lhe tenha apresentado; apreciarei para sempre o apoio e discussões científicas ao longo dos anos. Ao Dr. Fábio Schaberle, pela ajuda no campo da espectroscopia e por sempre encorajar pensamento rápido e resolução de problemas com soluções fora-da-caixa, durante a sua infinita sede de conhecimento. À Ana Catarina Lobo, Maria Inês Mendes, Piotr Gierlich, Claire Donohoe e Zoi Melissari, agradeço todas as discussões colaborativas que ajudaram a aprender mais sobre a aplicação de fotomedicina nos vossos projectos e a vossa amizade que se "expandiu" bem mais longe que o trabalho no laboratório.

To the MedChemTrain PhD programme directors, Prof. Dr. Luís Arnaut and Prof. Dr. Rui Moreira, as well as the remaining executive board, for granting me the opportunity to keep on learning and exploring more areas of Medicinal Chemistry, when selecting me for a scholarship.

Aos directores do programa doutoral MedChemTrain, Prof. Dr. Luís Arnaut e Prof. Dr. Rui Moreira, assim como ao restante conselho executivo, por me darem a oportunidade de continuar a aprender e explorar mais áreas de Química Medicinal, ao me seleccionarem para uma bolsa.

To Senge Group at Trinity College Dublin for providing Foscan®.
Ao *Senge Group* no *Trinity College Dublin* por fornecer Foscan®.

On a more personal note, I also thank Carla Grosso, Pedro Cruz, and Zaida Almeida for inviting me to participate in their photography group, sharing our own vision of the world through a lens and making it a little brighter every week.
Numa nota mais pessoal, agradeço à Carla Grosso, Pedro Cruz e Zaida Almeida por me convidarem a participar no seu grupo de fotografia, partilhando a nossa visão do mundo através da lente e trazendo um pouco mais de luz em cada semana.

And a special "thank you" to my MedChemTrain teammates with whom I worked and shared my PhD experience more closely: João Luís and Nuno Alves, with Andreia Cunha soon joining the fray. To João Luís for his constant back-and-forth in brainstorming ideas and proactive approaches to any project. To Andreia Cunha for all the knowledge and experience in this area, along with the witty personality I got to know better. And last, but definitely not least, to Nuno Alves for his outstanding dedication to research and his unwavering support in both computational and organic chemistry (where I would have been certainly more lost without his help). To all of you I am thankful for your friendship and all the moments of companionship shared.
E um "obrigado" especial aos meus colegas do MedChemTrain com quem trabalhei e partilhei mais da minha experiência de doutoramento: João Luís e Nuno Alves, com a Andreia Cunha a juntar-se logo de seguida. Ao João Luís pela constante troca de ideias e pela sua proactividade nos projectos em que participámos. À Andreia Cunha por todo o conhecimento e experiência nesta área, assim como pela sua personalidade espirituosa que tive o prazer de conhecer. E por último, mas definitivamente não menos importante, ao Nuno Alves pela sua dedicação excepcional à investigação e pelo seu suporte não só na química computacional, mas também em química orgânica (onde de certeza teria estado mais perdida, sem a sua ajuda). A todos eu agradeço a amizade e os momentos de companheirismo partilhados.

To Ana Bárbara, Francisca, and Jéssica I am forever grateful for the emotional support and constant encouragement. I know that I could not always be present, but your understanding and patience have been essential to help me finishing this journey. Thank you for helping me taking a break from the mental load: all the outings and activities shared with you are memories that I will never forget, no matter the distance apart.

À Ana Bárbara, Francisca e Jéssica estarei sempre grata pelo suporte emocional e apoio constante. Sei que nem sempre estive presente, mas a vossa compreensão e paciência têm sido essenciais para me ajudar a terminar esta jornada. Obrigada por me ajudarem a descansar do esforço mental: todas as saídas e actividades que fizemos serão memórias que nunca esquecerei, independentemente da distância que nos separa.

To Carla, still the most important person in my life, I thank all the love and support – no one else has probably listened to my frustrations and worries more than her. Your genuine care in encouraging me and making sure I was alright, always made me feel better and I know that I owe you keeping my sanity during the most difficult times. Without you, finishing this work would have not been possible. Thank you for always being present and believing in me: that's why you'll always be my favourite sister (despite being the only one).
À Carla, ainda a pessoa mais importante da minha vida, agradeço todo o amor e apoio – ninguém terá ouvido mais sobre as minhas frustrações e preocupações do que tu. A tua preocupação genuína em me encorajar e saber se estava bem, sempre me fizeram sentir melhor e sei que te devo manter a sanidade mental durante os momentos mais difíceis. Sem ti, terminar este trabalho não teria sido possível. Obrigada por estares sempre presente e acreditares em mim: por isso é que serás a sempre a minha irmã favorita (mesmo sendo a única).

To the rest of my family, I am grateful for all the support, love, and for giving me the opportunity to carve my own path. To my parents for giving me the space and time to work however I saw fit, supporting me in any way they could. To my grandparents, Joaquim and Maria José, for all their care and dedication, adapting as much as they could to my odd hours. To my aunt Graça, for encouraging me to pursue my goals and her willingness to listen and give advice.
Ao resto da minha família, agradeço o apoio, amor e por me darem a oportunidade de seguir o meu próprio caminho. Aos meus pais por me darem o espaço e tempo para trabalhar como preferisse, apoiando-me como pudessem. Aos meus avós, Joaquim e Maria José, por todo o cuidado e dedicação, adaptando-se tanto quando pudessem aos meus horários. À minha tia Graça, por me incentivar a seguir os meus objectivos e por estar disponível para me ouvir e aconselhar.

Thank you for everything.
Obrigada por tudo.

Resumo

Terapia fotodinâmica (PDT) combina o uso de um fotossensibilizador (PS), irradiação de luz, a um comprimento de onda específico, e oxigénio para matar células através da geração de espécies reactivas de oxigénio (ROS). Está estabelecida como uma terapia contra o cancro, minimamente invasiva, que consegue atacar células cancerígenas com precisão, através da irradiação. Outras vantagens, comparando a terapias anticancerígenas convencionais, incluem não criar resistência, tratamento com cicatrização mínima e imunidade antitumoral (relacionada com o controlo da doença a longo-termo). Ainda assim, o efeito secundário mais comum é pele fotossensível por intervalos de tempo longos, após tratamentos de PDT, causados pela falta de selectividade dos PSs para tecido tumoral, o que leva a razões de concentração em tecidos tumoral/normal que não conseguem prevenir danos ao tecido saudável que se encontra à volta do tumor.

De modo a ultrapassar este problema, diferentes estratégias de direccionamento (*targeting*) têm sido utilizadas em investigação, envolvendo métodos passivos ou activos de *targeting* de receptores específicos que se encontram sobreexpressos em cancros, mas em níveis baixos ou virtualmente nulos em células normais. A conjugação de PSs a diferentes moléculas de *targeting* (e.g., ligandos endógenos, anticorpos ou factores de crescimento) tem sido um dos métodos mais usados, permitindo ao PS conjugado ser reconhecido especificamente por células cancerígenas. Nesta tese pusemos a hipótese de desenvolvimento de uma estratégia para PDT-direccionado, focada em química de "clique" para tornar eficiente o processo de obtenção de conjugados direccionados a tumores a partir de clorinas obtidas através do método de ciclo-adição [8π+2π], desenvolvido previamente no nosso grupo. Com a síntese de novas clorinas, propomos uma estratégia como prova de conceito, seguindo a síntese de PSs que possam participar em reacções de "clique" e a sua conjugação a uma molécula ligando que contenha ácido fólico (FA) para obter um conjugado direccionado selectivamente à isoforma alfa do receptor do folato (FRα), que normalmente está sobreexpressa em vários cancros.

Sintetizámos um conjunto de novas 4,5,6,7-tetra-hidropirazolo[1,5-*a*]piridina-fundida *meso*-tetraquis(3-hidroxifenil)clorinas com diferentes anfifilicidades através de derivatizações subsequentes, com a clorina mais hidrofílica da série mono-funcionalizada ter sido derivatizada de novo para obter um grupo azida, para que pudesse participar em química de "clique" com outra molécula de *targeting* com um grupo alcino. Estas clorinas mostraram actividade fototóxica, a nível

de concentrações nanomolares, contra um modelo altamente agressivo de cancro da mama triplo-negativo, a linha celular humana de adenocarcinoma MDA-MB-231. Especificamente, a clorina mono-funcional mais hidrofílica (semelhante à temoporfina) obteve uma CI_{50} < 100 nM e a variante "clicável" obteve uma CI_{50} ~ 100 nM.

A partir desse derivado "clicável", desenhámos um conjugado para a nossa prova de conceito com base num ligando disponível comercialmente, que continha a parte do FA para *targeting*, um espaçador de polietileno glicol (PEG) com 1 kDa e o fragmento de dibenzociclooctino (DBCO) que contém o alcino para participar na reacção "clique". Com a corroboração obtida da análise *in silico* de uma simulação de docagem molecular da ligação entre o PS conjugado e o FRα, seguimos com a síntese do nosso conjugado. No entanto, a dificuldade em purificar um composto tão grande, dificultou a sua caracterização e avaliação *in vitro*: mesmo sendo possível confirmar indirectamente a presença do conjugado para a nossa prova de conceito, este não mostrou aumento da eficácia da PDT nem na internalização celular, quando comparado com as clorinas anteriores.

Ainda assim, conseguir a síntese do conjugado para PDT-direccionado apoiou a viabilidade do uso desta estratégia. Atingir este marco foi importante, porque apesar de diferentes estratégias para PDT direccionado terrem sido investigadas, ainda nenhuma chegou a ser usada na clínica. A nossa estratégia de conjugação permite uma adaptação fácil a outros alvos e/ou outras clorinas com boa actividade.

Palavras-chave:
terapia fotodinâmica; direccionamento; receptor do folato alfa; clorina; docagem molecular

Abstract

Photodynamic therapy (PDT) combines the use of a photosensitiser (PS), light irradiation at a specific wavelength, and oxygen to kill cells, through the generation of reactive oxygen species (ROS). It has been established as a minimally invasive anticancer therapy that can target tumour cells accurately through irradiation. Other advantages compared to traditional anticancer therapies also include lack of resistance, healing with minimal scarring, and anti-tumour immunity (related to the long-term control of the disease). Nevertheless, the most common side effect is prolonged skin photosensitivity after PDT treatment caused by the lack of selectivity of the PSs for tumour tissue, leading to tumour/normal tissue ratios that are not able to prevent damage to healthy tissue surrounding the tumours.

In order to overcome this issue, different targeting strategies have been used in research involving either passive or active targeting of specific receptors that are overexpressed in cancers but at low or negligent levels in normal cells. The conjugation of PSs to different targeting moieties (e.g., endogenous ligands, antibodies, or growth factors) has been one of the most used methods, allowing for the conjugated-PS to be specifically recognised by cancer cells. In this thesis we hypothesised a strategy for targeted-PDT focused on "click" chemistry to streamline the process of obtaining tumour-targeting conjugates from chlorins obtained using the [8π+2π] cycloaddition method, previously developed within our group. With the synthesis of novel chlorins, we propose a proof-of-concept strategy following the synthesis of a "clickable" PS and further conjugation to a linker containing folic acid (FA) to obtain a targeted-PS selective to the alpha isoform of the folate receptor (FRα), which is usually found overexpressed in cancer cells.

We synthesised a set of novel 4,5,6,7-tetrahydropyrazolo[1,5-*a*]pyridine-fused *meso*-tetrakis(3-hydroxyphenyl)chlorins with varying amphiphilicity through subsequent derivatisations, with the most hydrophilic chlorin from the mono-functionalised series being further derivatised to obtain an azide group, so that it could participate in "click" chemistry with a targeting moiety containing an alkyne group. These chlorins showed phototoxic activity, in the nanomolar range, against the highly aggressive, triple-negative breast cancer model, the MDA-MB-231 human adenocarcinoma cell line. Specifically, the mono-functional, most hydrophilic chlorin (similar to temoporfin) having an IC_{50} < 100 nM and its "clickable" derivative having an IC_{50} ~ 100 nM.

From that “clickable” derivative we designed a conjugate for our proof-of-concept, based on a commercially available linker that contained the FA moiety for targeting, a 1 kDa polyethylene glycol (PEG) spacer, and the alkyne-containing moiety, dibenzocyclooctyne (DBCO) to participate in the “click” reaction. With the corroboration obtained from the *in silico* analysis of a molecular docking simulation of the binding of the conjugated-PS to FRα, we followed through with the synthesis of this conjugate. However, the difficulty in purifying such a large compound, hindered its characterization and *in vitro* evaluation: despite being able to indirectly confirm the presence of the proof-of-concept conjugate, it did not show an improvement in PDT efficacy nor on the cell uptake when compared to the novel chlorins.

Nonetheless, the successful synthesis of the PDT-targeted conjugate supported the viability of this targeting strategies. Reaching this milestone was important, because despite several targeted-PDT strategies have been researched, a targeted-PDT has yet to reach the clinic. Our conjugating strategy allows for an easy adaptation to be used with other targets and/or other chlorins with strong activity.

Keywords:
photodynamic therapy; targeting; folate receptor alpha; chlorin; molecular docking

Contents

List of Figures

Supplementary Figures

List of Schemes

List of Tables

Supplementary Tables

List of Equations

List of Abbreviations

AcOEt	Ethyl acetate
Ac	Acetyl group
ADC	Antibody-drug conjugate
ALA	5-Aminolevulinic acid
aq.	Aqueous
AR	Androgen receptor
Ar	Phenyl derivatives (aromatic)
BR	Biotin receptor
br s	Broad singlet
CADD	Computer-aided drug discovery
$CDCl_3$	Deuterated chloroform
$(CD_3)_2SO$	Deuterated dimethyl sulfoxide
d	Doublet
dd	Doublet of doublets
DBCO	Dibenzocyclooctynes
DCM	Dichloromethane
DLI	Drug-to-light interval
DMAD	Dimethylacetylene dicarboxylate
DMAP	4-Dimethylaminopyridine

DMEM	Dulbecco's Modified Eagle's Medium
DMF	Dimethylformamide
DMSO	Dimethyl sulfoxide
DNA	Deoxyribonucleic acid
e.g.	For example (shortened from the Latin *exempli gratia*)
EGFR	Epidermal growth factor receptor
EMA	European Medicines Agency
EPR	Enhanced permeability and retention
equiv.	Equivalents
ER	Endoplasmic reticulum
EsR	Oestrogen receptor
ESI	Electrospray ionization
FA	Folic acid
FBS	Foetal bovine serum
FDA	Food and Drug Administration
FGFR	Fibroblast growth factor receptor
FR	Folate receptor
FTIR	Fourier-transformed infrared
GA	Golgi apparatus
GFP	Green fluorescent protein
GnRH	Gonadotropin-releasing hormone
HER	Human epidermal receptor

HpD	Haematoporphyrin derivative
HRMS	High-resolution mass spectroscopy
HSQC	Heteronuclear single quantum coherence
IC_{50}	50% Inhibitory concentration
ICB	Immune checkpoint blocker
ICD	Immunogenic cell death
i.e.	That is (shortened from the Latin *id est*)
LD	Light dose
LDL	Low-density lipoproteins
LED	Light-emitting diode
m	Multiplet
mAb	Monoclonal antibody
MCPBA	*m*-Chloroperoxybenzoic acid; 3-Chloroperoxybenzoic acid
Mol2	Tripos molecule structure
mTHPC	*meso*-Tetrakis(3-hydroxyphenyl)chlorin
NAG	*N*-acetyl-*D*-glucosamine
NIR	Near-infrared
NMR	Nuclear magnetic resonance
NP	Nanoparticle
Npe6	Mono-L-aspartyl chlorin e6
PBS	Phosphate buffes saline
PDB	Protein Data Bank

PDBQT	Protein Data Bank, partial charge (Q), & atom type (T)
PDT	Photodynamic therapy
PEG	Polyethylene glycol
PFA	Paraformaldehyde
PgR	Progesterone receptor
PpIX	Protoporphyrin IX
ppm	Part per million
PS	Photosensitiser
RMSD	Root-mean-square deviation
ROS	Reactive oxygen species
RT	Room temperature (T = 25 ºC)
RTK	Receptor tyrosine kinase
s	Singlet
SDF	Structure data file
SEM	Standard error of the mean
SMDC	Small molecule-drug conjugate
SOSG	Singlet oxygen sensor green
SPAAC	Strain-promoted alkyne-azide cycloaddition
t	Triplet
TCB	Trichlorobenzene; 1,2,4-Trichlorobenzene
TEA	Triethylamine
TFAA	Trifluoroacetic anhydride

TfR	Transferrin receptor
THF	Tetrahydrofuran
TLC	Thin-layer chromatography
TMS	Tetramethylsilane
TNBC	Triple-negative breast cancer
UV	Ultraviolet
UV-vis	Ultraviolet-visible
v/v	Volume/volume
VEGF	Vascular endothelial growth factor
VEGFR	Vascular endothelial growth factor receptor
wt%	Weight percent

List of Symbols

A	Absorbance
c	Speed of light ($m.s^{-1}$)
g_{points}	Grid points
g_{size}	Grid size (Å)
$g_{spacing}$	Grid spacing (Å)
h	Planck constant (J.s)
I_{abs}	Intensity of light absorbed by a solution
I_0	Intensity of light before absorption
J	Coupling constant (Hz)
k_B	Boltzmann's constant ($J.K^{-1}$)
K_D	Dissociation constant (M)
l	Length of the light path (cm)
n	Refractive index
N_A	Avogadro constant (mol^{-1})
N_{ph}	Number of photons absorbed
P	Power (W)
r_{gyr}	Radius of gyration (Å)
T	Temperature
V_{irr}	Irradiated volume (mL)

ΔE	Energy difference (J)
Δt	Time interval (s)
Φ	Quantum yield
Φ_{pd}	Photodecomposition quantum yield
Φ_F	Fluorescence quantum yield
Φ_Δ	Singlet oxygen quantum yield
δ	Chemical shift (ppm)
ε	Molar extinction coefficient ($M^{-1}.cm^{-1}$)
λ	Wavelength (nm)
λ_{em}	Emission wavelength (nm)
λ_{ex}	Excitation wavelength (nm)
λ_{max}	Maximum absorption wavelength (nm)
ν	Frequency (Hz or s^{-1})
$\tilde{\nu}$	Wavenumber (cm^{-1})
υ_d	Rate of disappearance of photosensitiser molecules (s^{-1})
υ_p	Rate of absorption of photons (s^{-1})

Amino acid Table Code

Amino acid	Single-letter code	Three-letter code	Property
Alanina	A	Ala	Aliphatic
Arginine	R	Arg	Basic
Asparagine	N	Asn	Amidic
Aspartate	D	Asp	Acidic
Cysteine	C	Cys	Sulfur-containing
Glutamate	E	Glu	Acidic
Glutamine	Q	Gln	Amidic
Glycine	G	Gly	Aliphatic
Histidine	H	His	Basic
Isoleucine	I	Ile	Aliphatic
Leucine	L	Leu	Aliphatic
Lysine	K	Lys	Basic
Methionine	M	Met	Sulfur-containing
Phenylalanine	F	Phe	Aromatic
Proline	P	Pro	Aliphatic
Serine	S	Ser	Hydroxylic
Threonine	T	Thr	Hydroxylic
Tryptophan	W	Trp	Aromatic
Tyrosine	Y	Tyr	Aromatic
Valine	V	Val	Aliphatic

Amino acid chemical structure

Alanine
Ala (A)

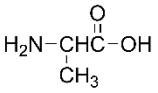

Arginine
Arg (R)

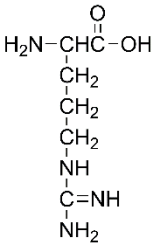

Asparagine
Asn (N)

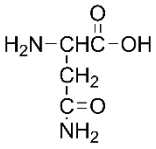

Aspartate
Asp (D)

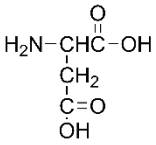

Cysteine
Cys (C)

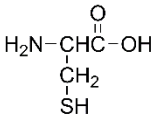

Glutamate
Glu (E)

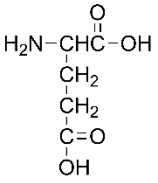

Glutamine
Gln (Q)

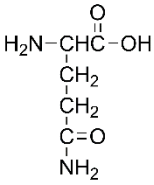

Glycine
Gly (G)

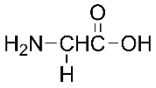

Histidine
His (H)

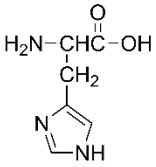

Isoleucine
Ile (I)

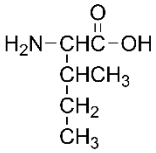

Leucine
Leu (L)

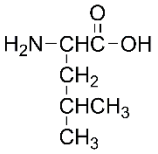

Lysine
Lys (K)

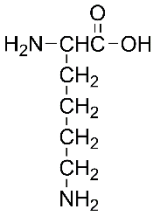

Metionine
Met (M)

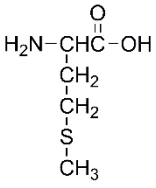

Phenylalanine
Phe (F)

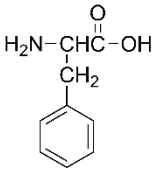

Proline
Pro (P)

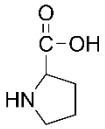

Serine
Ser (S)

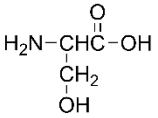

Threonine
Thr (T)

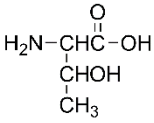

Tryptophan
Trp (W)

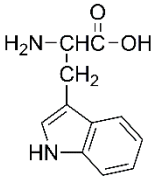

Tyrosine
Tyr (Y)

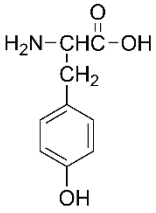

Valine
Val (V)

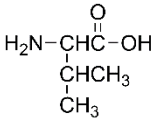

Scientific Production

Publications relevant for the thesis

Gierlich, P.; Mata, A.I.; Donohoe, C.; Brito, R.M.M.; Senge, M.O.; Gomes-da-Silva, L.C. Ligand-Targeted Delivery of Photosensitizers for Cancer Treatment. *Molecules* **2020**, *25*, 5317, doi:10.3390/molecules25225317.

Mata, A.I.; Pereira, N.A.M.; Cardoso, A.L.; Nascimento, B.F.O.; Piñeiro, M.; Rui M. M. Brito; Fábio A. Schaberle; Gomes-da-Silva, L.C.; Pinho e Melo, T.M.V.D. Novel Foscan®-Derived Ring-fused Chlorins for Photodynamic Therapy of Cancer. (*under review*)

Other publications not discussed in this thesis

Luís, J. P.; Mata, A. I.; Simões, C. J. V.; Brito, R. M. M. Conformational Dynamics of the Soluble and Membrane-Bound Forms of Interleukin-1 Receptor Type-1: Insights into Linker Flexibility and Domain Orientation. *Int. J. Mol. Sci.* **2022**, *23*, 2599, doi:10.3390/ijms23052599.

Alves, N. G.; Mata, A. I.; Luís, J. P.; Brito, R. M. M.; Simões, C. J. V. An Innovative Sequence-to-Structure-Based Approach to Drug Resistance Interpretation and Prediction: The Use of Molecular Interaction Fields to Detect HIV-1 Protease Binding-Site Dissimilarities. *Front. Chem.* **2020**, *8*, 1–17, doi:10.3389/fchem.2020.00243.

Conference papers

Luís, J.; Mata, A. I.; Alves, N.; Simões, C.; Pereira-Vaz, J.; Vaz, D. C.; Duque, V.; Brito, R. Influence of codon 35 amino acid insertion in HIV-1 protease: insights from molecular dynamics. *6º Encontro de Jovens Investigadores Biologia Computacional Estrutural (EJIBCE 2018)*, Universidade do Porto, Portugal. **2018**, doi: 10.3390/mol2net-04-06007.

Vaz, D. C.; Brito, R. M. M.; Mata, A. I.; Luís, J. P.; Alves, N. G.; Simões, C. J. V.; Pereira-Vaz, J.; Duque, V. Use of molecular interaction fields to understand drug resistance in HIV-1 protease caused by single point mutations. *10th International Congress on Structural Biology*, Helsinki, Finland. **2018**, doi: 10.4172/0974-276x-c3-119.

Oral communications in national scientific meetings

Mata, A. I.; Alves, N. G.; Luís, J. P.; Simões, C. J. V.; Brito, R. M. M. On the use of molecular interaction fields to predict drug-resistance. *13º Encontro Nacional de Química Orgânica (13ENQO) & 6º Encontro Nacional de Química Terapêutica (6ENQT)*, Universidade de Aveiro, Portugal. **2020**, January 15th.

Poster communications in national scientific meetings

Mata, A. I.; Pereira, N. A. M.; Pinho e Melo, T. M. V. D.; Gomes-da-Silva, L. C.; Simões, C. J. V.; Brito, R. M. M. Novel Targeted-Photodynamic Therapy: New Photosensitisers That "Click". *14º Encontro Nacional de Química Orgânica (14ENQO) & 7º Encontro Nacional de Química Terapêutica (7ENQT)*, Lisboa, Portugal. **2022**, April 20th – 22nd.

Mata, A. I.; Pereira, N. A. M.; Pinho e Melo, T. M. V. D.; Gomes-da-Silva, L. C.; Simões, C. J. V.; Brito, R. M. M. Novel Photosensitisers for Targeted-Photodynamic Therapy. *Coimbra Chemistry Centre Day 2021 (CQC Day 2021)*, Universidade de Coimbra, Portugal. **2021**, December 15th.

Mata, A. I.; Cardoso, A. L.; Pinho e Melo, T. M. V. D.; Gomes-da-Silva, L. C.; Simões, C. J. V.; Brito, R. M. M. Tumour-targeting Photodynamic Therapy: A Strategy to Increase Selectivity. *7º Encontro de Jovens Investigadores Biologia Computacional Estrutural (EJIBCE 2019)*, Universidade de Lisboa, Portugal. **2019**, December 20th.

Luís, J.; Mata, A. I.; Alves, N.; Simões, C.; Pereira-Vaz, J.; Vaz, D. C.; Duque, V.; Brito, R. Influence of codon 35 amino acid insertion in HIV-1 protease: insights from molecular dynamics. *6º Encontro de Jovens Investigadores Biologia Computacional Estrutural (EJIBCE 2018)*, Universidade do Porto, Portugal. **2018**, December 21st.

Mata, A. I.; Alves, N. G.; Luís, J. P.; Simões, C. J. V.; Pereira-Vaz, J.; Vaz, D. C.; Duque, V.; Brito, R. M. M. Análise do impacto da mutação de inserção no codão 35 na protease do VIH-1 com recurso a técnicas computacionais. *V Congresso Nacional de Virologia (5CNV)*, Universidade de Porto, Portugal. **2018**, October 26th – 27th.

Mata, A. I.; Gomes-da-Silva, L. C.; Brito, R. M. M; Arnaut, L.G. Potential Beyond the Use of Conventional Photodynamic Therapy. *12º Encontro Nacional de Química Orgânica (12ENQO) & 5º Encontro Nacional de Química Terapêutica (5ENQT)*, Universidade de Coimbra, Portugal. **2018**, January 17th – 19th.

Chapter I:

General Introduction

Part of the content on this chapter was published on the review article:

[1] Gierlich, P.; Mata, A.I.; Donohoe, C.; Brito, R.M.M.; Senge, M.O.; Gomes-da-Silva, L.C. Ligand-Targeted Delivery of Photosensitizers for Cancer Treatment. *Molecules* **2020**, *25*, 1–54.

If I have seen further than others, it is by standing on the shoulders of giants.

Isaac Newton

1. Cancer and Therapeutics

1.1. Cancer development

Nowadays, cancer is the second-leading cause of death worldwide with a burden expected to grow to 27.5 million new cancer cases and 16.3 million cancer deaths in 2040. This is a consequence mainly of the population aging without taking into account other risk factors [2]. However, the causes that lead to the development of cancer are still not totally understood [2]. To better understand tumourigenesis, cancer research has grown over the years with focus on the dynamic changes in the genome of cancerous cells. This permitted to gain a better insight on the mechanisms underlying cancer that consequently could be targeted with different therapies [3].

With hundreds of cancer types, and considering the diversity of tumour subtypes specific to the organs where they are found in, Hanahan and Weinberg first proposed, in 2000 [4], a simplified set of six hallmarks of cancer which were based on the principle that «virtually all mammalian cells carry a similar molecular machinery». After two decades, they revisited these original hallmarks and broadened their scope to include new emerging hallmarks and enabling characteristics [5,6], as such compiling the 14 acquired capabilities shown in Figure I–1. These acquired traits promote the development of cancer cells by enabling initiation of neoplasia, its progression, and eventual metastasis, along with the influence of the tumour microenvironment [3,5].

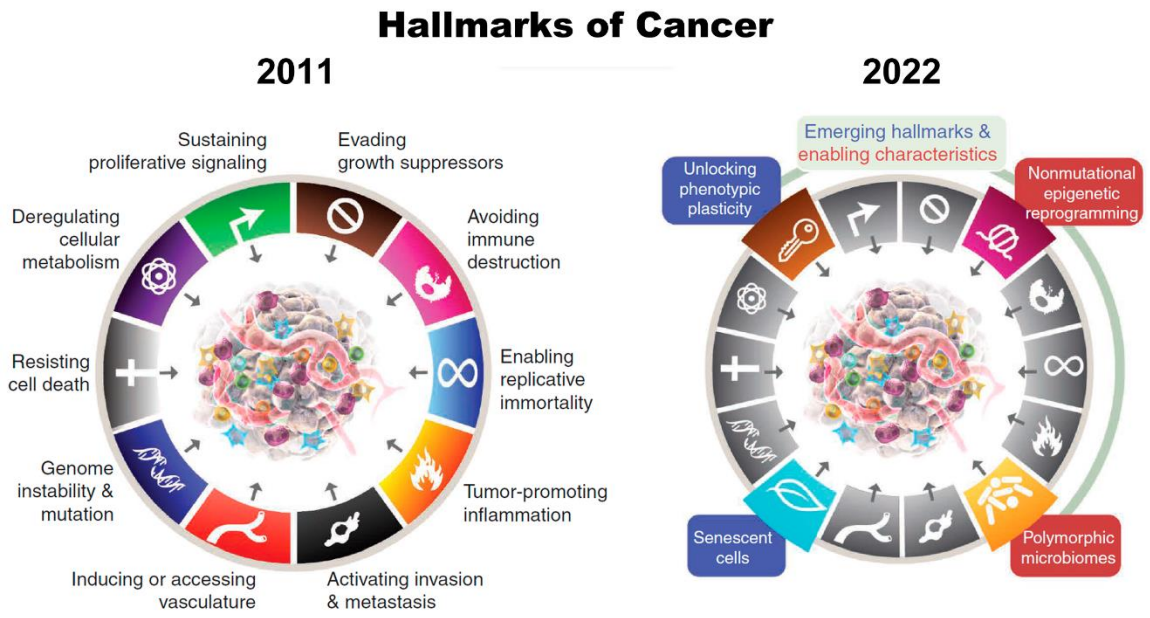

Figure I–1. The revised hallmarks of cancer (adapted from Hanahan [6]**)**

With these drastic biological differences found at various levels between normal and cancer cells, it is easy to understand why such characteristics are attractive targets for therapies. The collaborative interactions between cancer cells, associated stroma cells and the extracellular matrix form the tumour microenvironment are known to be crucial for disease initiation, progression and metastasis formation [7]. An awareness of the complexity of the tumour microenvironment is gaining acceptance as a necessary consideration for the design of novel cancer therapies. Indeed, a successful therapeutic approach should take into consideration the tumour microenvironment dynamics, and potentially, strategies that target different tumour cell populations, like cancer stem cells, endothelial cells, pericytes, cancer-associated fibroblasts and different types of immune infiltrating cells, may enhance therapeutic outcomes [3,7].

1.2. The four pillars of cancer treatment

With cancer dating back to ancient Greek and Egyptian civilizations, the radical surgery available as treatment at the time was often ineffective leading to the death of the patient [8]. Since then, surgery established itself as one of the most conventional treatments for cancer, and one of the preferred options when treating benign and malignant tumours without affecting adjacent healthy tissues [9]. Up to 1960s, it was considered the standard for solid tumour treatment but not an option for metastatic cancers. After that date, radiation started to be used as a way to control local disease and, with time, the adjuvant practice of surgery and radiotherapy showed an increased efficacy in the control of cancer [9,10]. The basis of radiotherapy is the energy transfer to the cells in a way that directly kills them or alters them in a way that will eventually lead to inhibition of cell

proliferation. Radiotherapy is being used to reduce tumour size before surgery or to destruct any remaining cancer cells and decrease the probability of relapse after the surgical removal of tumour lesions [9]. Still, it is a technique which also affects healthy cells surrounding the tumour that, depending on the location and type of the tumour being treated, can lead to several side effects, such as overall fatigue, oral mucositis, dysphagia, hypothyroidism, lung injuries and heart diseases induced by radiation, gastrointestinal toxicity, sexual dysfunction, and fertility concerns [11]. More recently, advances allowed the use of a "radiation-based surgical knife", in which radiation is applied more focused on the region of the tumour mass, reducing the side effects of normal radiotherapy [9].

Chemotherapy was introduced in 1906 by Paul Ehrlich and changed the concept of localised treatment. The first chemotherapeutic drugs were accidentally discovered in 1943 after observing that toxic mustard gases (e.g., alkylating agents), used as weapons during World War II, led to bone marrow aplasia. In 1946, Gilman and Goodman used nitrogen mustard gas as the first chemotherapeutic treatment for lymphomas through the binding of the aziridinium group of the nitrogen mustard to the guanine bases (of the deoxyribonucleic acid, DNA) and subsequent formation of interstrand cross-links. This mechanism prevents the duplication of DNA leading to cytotoxicity [8]. Unlike surgery or radiotherapy, most of the chemotherapeutic drugs (e.g., alkylating agents, antimetabolites, antimitotics, cytotoxic antibiotics, etc.) are administered systemically and inhibit the progression of the tumour by halting their proliferating ability and force cell death. These drugs also affect normal cells, namely cells with high proliferative rates such as gastrointestinal epithelia, bone marrow, and hair follicles [12,13]. For this reason, chemotherapy is associated with several side effects including hair loss, tiredness, feeling sick, anaemia, gastrointestinal disorders, among others [9]. Thus, finding a balance between effective chemotherapy doses and the well-being of the patient is a challenged task. Despite the intrinsic resistance to cell death found in cancer cells, there are currently more than 100 drugs that still translate into a temporary clinical response and a limited survival benefit, which are suggest the development of adaptive drug resistance. [3,9,14] As this number continues to increase, the discoveries on molecular biology helped identify some of the underlying resistance mechanisms and pushed the development of therapies targeting specific molecules involved in the tumourigenic process, enabling the possibility of overcoming the barrier of drug resistance by exploring alternative pathways [3,15,16]. These new drugs included small molecules (e.g. kinases inhibitors) but also monoclonal antibodies (mAB) in the late 1980s [9,10]. Contrary to classic chemotherapy, these cancer-targeted drugs display more specificity and efficacy being associated with better tolerance, as well as less adverse effects [1].

In the last years, immunotherapy has emerged as the fourth pillar of cancer treatment. Immunotherapy is based on the use of components from the immune system to either kill cancer

cells directly or help the patient's body to recognise and destroy the tumour cells [17]. The use of non-specific immunostimulants (e.g., bacteria lysates) has been explored for decades in the scope of cancer treatment [18]. More recently, the use of mAbs targeting immune checkpoints represents a major breakthrough in anti-cancer immunotherapy. Immune checkpoint mechanisms are important to maintain homeostasis avoiding exacerbated immune reactions however, cancer cells have the ability to exploit these mechanisms to evade immune recognition and destruction [17,19,20]. The use of mAbs directed to tumour antigens or to T-cell protein receptors responsible for downregulating the immune responses are known as immune checkpoint blockade (ICB) therapy, with inhibitors for CTLA4 and PD1-PDL1 being the most used so far [8,17,19]. Yet one of the main challenges in immunotherapy is identifying what subsets of biomarkers are predictive of response to ICB as treatment outcomes varied significantly among patients. In fact, while a very small percentage of patients (20-40%) benefit tremendously from ICB inhibitors with significant cancer remission (and even cures), the large majority of patients does not respond to ICB inhibitors [20]. Currently, immunotherapy is often used in combination with other cancer treatments [8,10,17,19–21].

Overall, these traditional options for cancer treatment enable to save millions of lives and their proven efficacy has established their place as pillars of cancer treatment. However, they are not free of disadvantages which are mainly connected to lack of selectivity (and associated toxicity) as well as poor outcomes when aggressive and advanced tumours are aimed to be treated [21]. These limitations keep open the search for other therapies that can overcome the present hurdles as stand-alone or combined, aiming for their place as the fifth pillar.

2. Photodynamic Therapy (PDT)

2.1. The development of PDT

The use of light in therapy goes back 3000 years, when the Greeks first reported the use of sunlight as heliotherapy, and other ancient civilizations such as the Egyptian, Chinese, and Indian, have used it as treatment for psoriasis, vitiligo, ricket, and even skin cancer. Furthermore, the use of photoactivable agents combined with light exposure with therapeutical intent has also been used as far as 1400 BC with the use of psoralens for the repigmentation of vitiliginous skin [22].

However, it was only in the 19th century that phototherapy was developed into a science. In 1903, Niels Finsen was awarded with the Nobel prize in Physiology or Medicine for his discoveries that

ultraviolet (UV) radiation could be used for the treatment of cutaneous tuberculosis, setting the beginning of modern-day phototherapy. That same year, Herman von Tappeiner and Albert Jesionek treated skin tumours using topically applied eosin and, after understanding the necessity of oxygen for the success of the therapy, Von Tappeiner and Albert Jodlbauer published a compilation of these findings in a book where they first coined the term "photodynamic therapy" (PDT) [22]. PDT is nowadays well known to be the results of the activation of molecules, known as photosensitisers (PSs), by light of a certain wavelength. In the presence of oxygen this leads to reactive oxygen species (ROS) generation which are toxic to the cells [1,23].

PDT has improved since then and many more PSs, and more sophisticated sources of light, have been developed. This technique is being used for ophthalmology, cardiovascular, dermatological, and dental diseases [24], but it encountered its main use for the treatment of microbial infections and solid tumours [24–27]. Since Dougherty *et al*. [28] re-discovering haematoporphyrin, the mechanisms of anti-tumour PDT have been extensively studied. In oncology, PSs are typically administered intravenously and after a certain period of time (named drug-to-light interval, DLI), tumour irradiation is performed by means of a laser or light-emitting diode (LED). Damage of the tumour vasculature with ischemic death of the tumour is usually achieved with a short DLI, where the irradiation of the tumour happens when the PS is confined at the bloodstream – vascular-PDT. Alternatively, longer DLI (e.g. DLI > 24h) might be used to achieve higher accumulation of the PS in cellular components – cellular-PDT [1,23].

PDT offers the advantage of being minimally invasive, can be targeted accurately through irradiation, repeated dosage is not an issue (as compared to radiotherapy), does not cause resistance (in contrast to radio and chemotherapy), and healing has little to no scarring [1,23,29,30]. Additionally, PDT can activate the host immune system to recognize and destroy cancer cells regardless of their localization at the body. This anti-tumour immunity was shown to be of the most importance for the long control of the disease and is often capable of abscopal controlled of distant (and not irradiated) metastases [31].

2.2. Mechanism of photodynamic action

PDT is a drug-device combination product that requires the presence of molecular oxygen, light of a specific wavelength, and a PS. Independently, these components do not present toxicity, but when combined they lead to production of ROS which mediate the destruction of the target cells [1,23,29].

There are two known types of photochemical reactions to produce ROS, which are dependent on the oxygen available in the cells [1]. Figure I–2 is a schematic representation of the Jablonski energy

diagram that shows how the activation of the PS – after photon absorption – leads to its excitation from the ground state to an excited state, from where it quickly decays through fluorescence emission (returning to the ground state) or through intersystem crossing, where it reaches a relatively long-lived triplet state. From this triplet state, while it may decay through phosphorescence emission, this is a slow spin-forbidden process, making it more probable to interact with oxygen found in biomolecules via electron transfer or directly with ground-state molecular oxygen via energy transfer. The former is defined as a type I reaction producing the radicals superoxide anion, $O_2^{\bullet -}$, hydroxyl, $HO^{\bullet}$, and hydrogen peroxide, H_2O_2, while the latter is considered to be a type II reaction, producing singlet oxygen, $^1O_2$ [1,23,29].

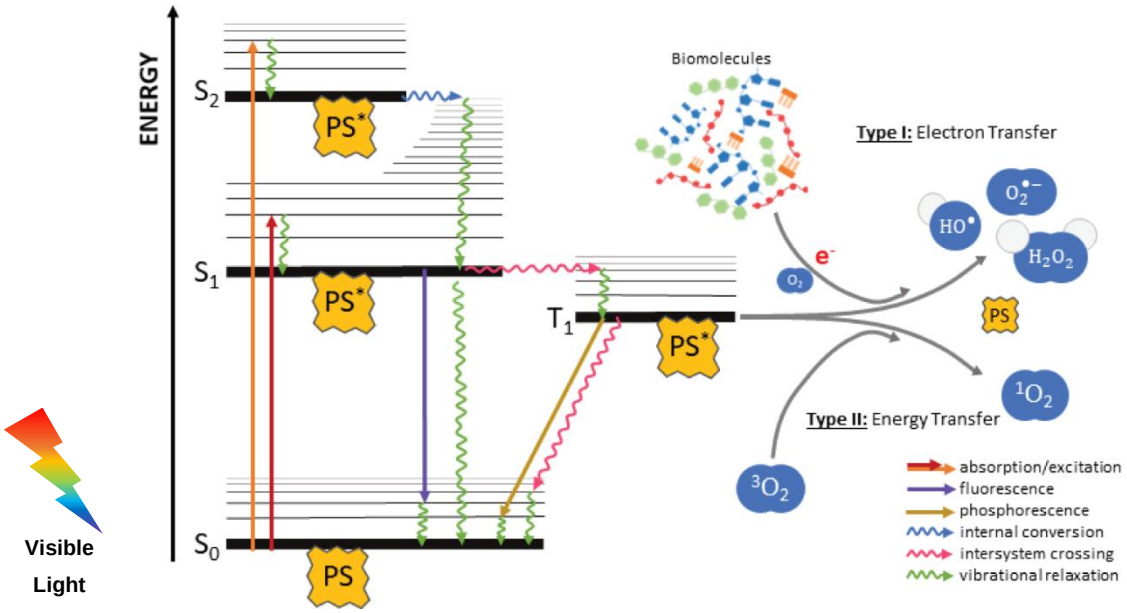

Figure I–2. Jablonski diagram. Adapted from [20].

As type II reactions are much simpler, they are assumed to be the favoured type of mechanism, but the actual ratio depends on the concentration of molecular oxygen available, tissue dielectric constant, pH, and even PS structure [29]. It is also important to notice that, as ROS are relatively short-lived molecules, their radial diffusion will also be limited (e.g.: $HO^{\bullet}$ has a lifetime of 1 ns and can reach distances of up to 1 nm; $^1O_2$ has a lifetime of 2 µs and reaches distances of about 150 nm). This makes PDT an inherently "selective" therapy as the local of treatment is light-targeted and only the PS found in the irradiated spot will be activated [1,23].

The light wavelength used for irradiation needs to be high enough to penetrate deeper into the target tissues, but still, it should have enough energy to induce ROS. Combining these two factors, the phototherapeutic window, is reduced to 650-850 nm (Figure I–3). At this range of wavelengths, tissues are more transparent to light and activation of endogenous chromophores (e.g. melanin) is avoided [1,23,32].

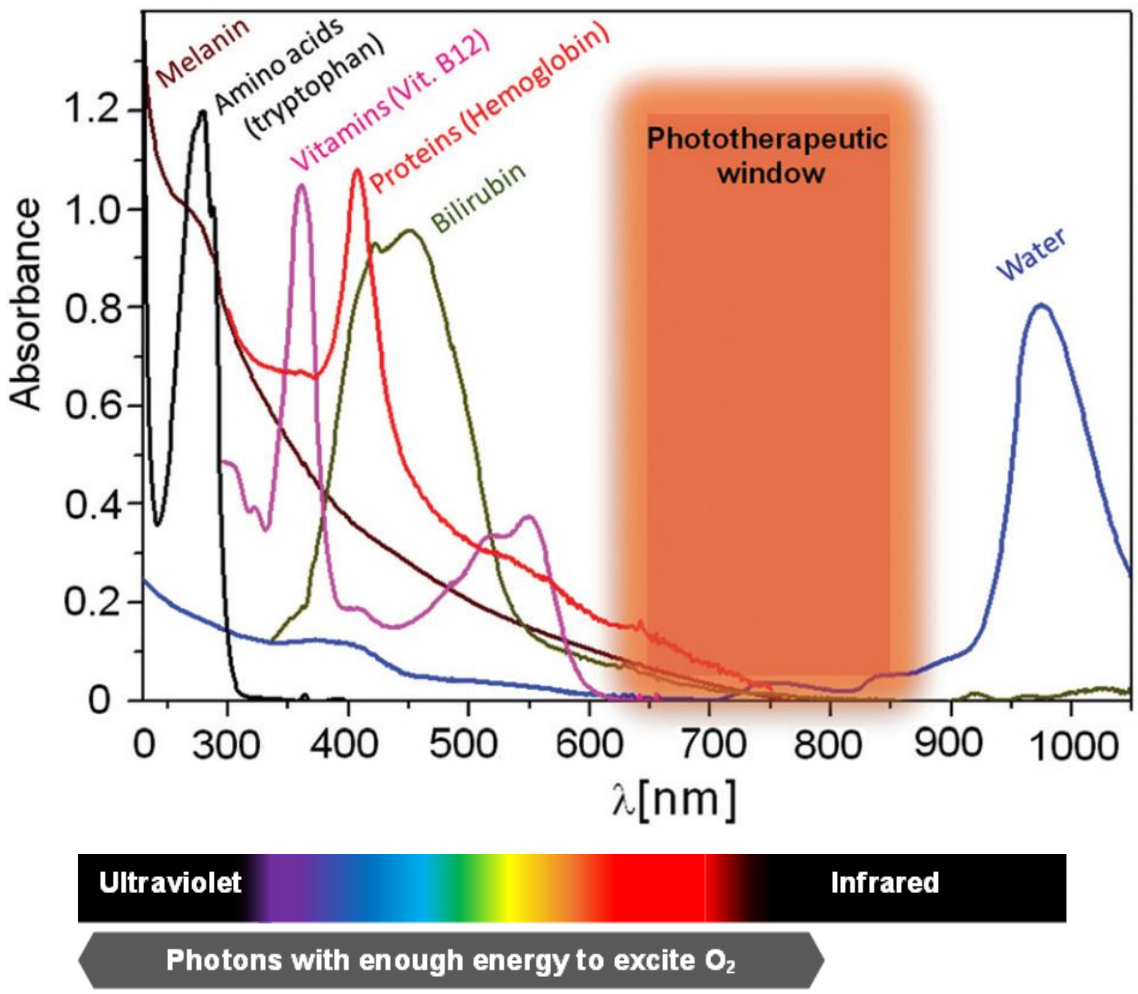

Figure I–3. Phototherapeutic window of PDT. Adapted from [23].

2.3. Photosensitiser classification

Taking into account the requirements needed for a successful PDT protocol, an ideal PS should be characterized by [23,29,32]:

- Simple synthesis with high yields of a pure compound,
- Low manufacturing cost and good stability at room temperature,
- Minimal dark toxicity, becoming cytotoxic only when photoactivated at a specific wavelength,
- High molar absorptivity at 650-850 nm and high quantum yields of ROS production,
- Biocompatible with preferable accumulation at the tumour tissue and rapid clearance to minimise photosensitivity side effects,
- Not mutagenic nor carcinogenic.

In the search for the ideal PS, numerous classes of PSs have been developed for PDT being the porphyrinoid compounds (based on the tetrapyrrole macrocycle) (Figure I–4) the most investigated molecules. This is explained by their extended conjugation and absorption of visible to NIR light [33,34].

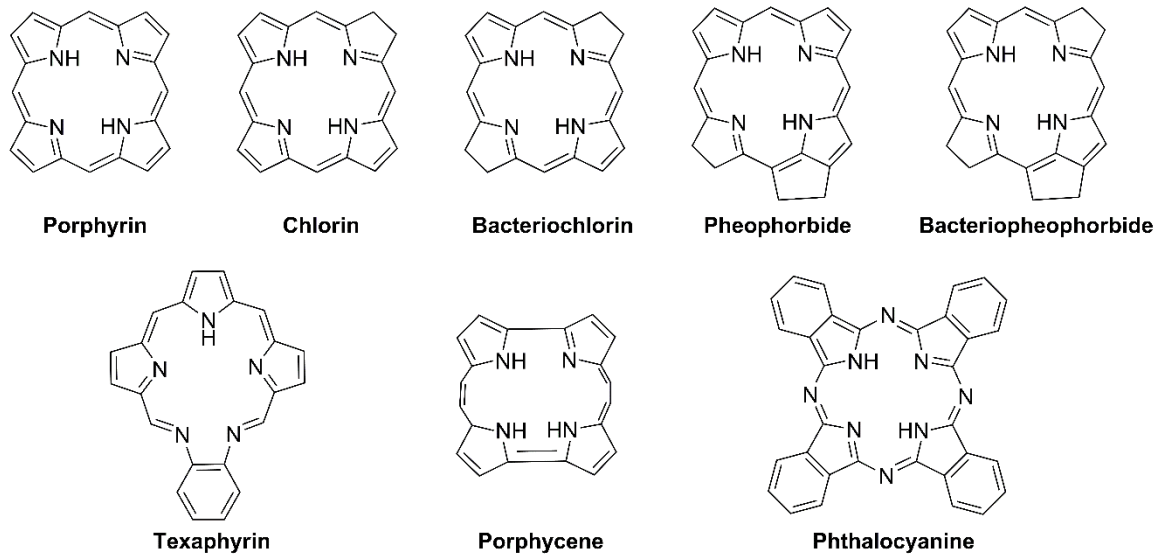

Figure I–4. Backbone structures of tetrapyrrolic macrocycle PS.

However, there are also non-porphyrinoid PSs used in PDT For instance, hypericin is a natural anthraquinone derivative that has been evaluated for the treatment of skin, bladder, and nasopharyngeal cancers; methylene blue and toluidine blue are phenothiazines that have been tested in skin and bladder cancers, as well as Kaposi's sarcoma; rose Bengal is a xanthene that has been tested in breast cancer and metastatic melanoma; the cyanine sensitiser merocyanine 540 showed promising *in vitro* results for leukaemia; and even curcumin has been studied as an oral disinfectant working as an antibacterial agent [33,34]. None of these PSs have received clinical approval.

Porphyrinoid PSs are typically classified as first-, second-, and third-generation. Figure I–5 shows the molecular structures of some PSs employed clinically, or in clinical trials, and their respective irradiation wavelength.

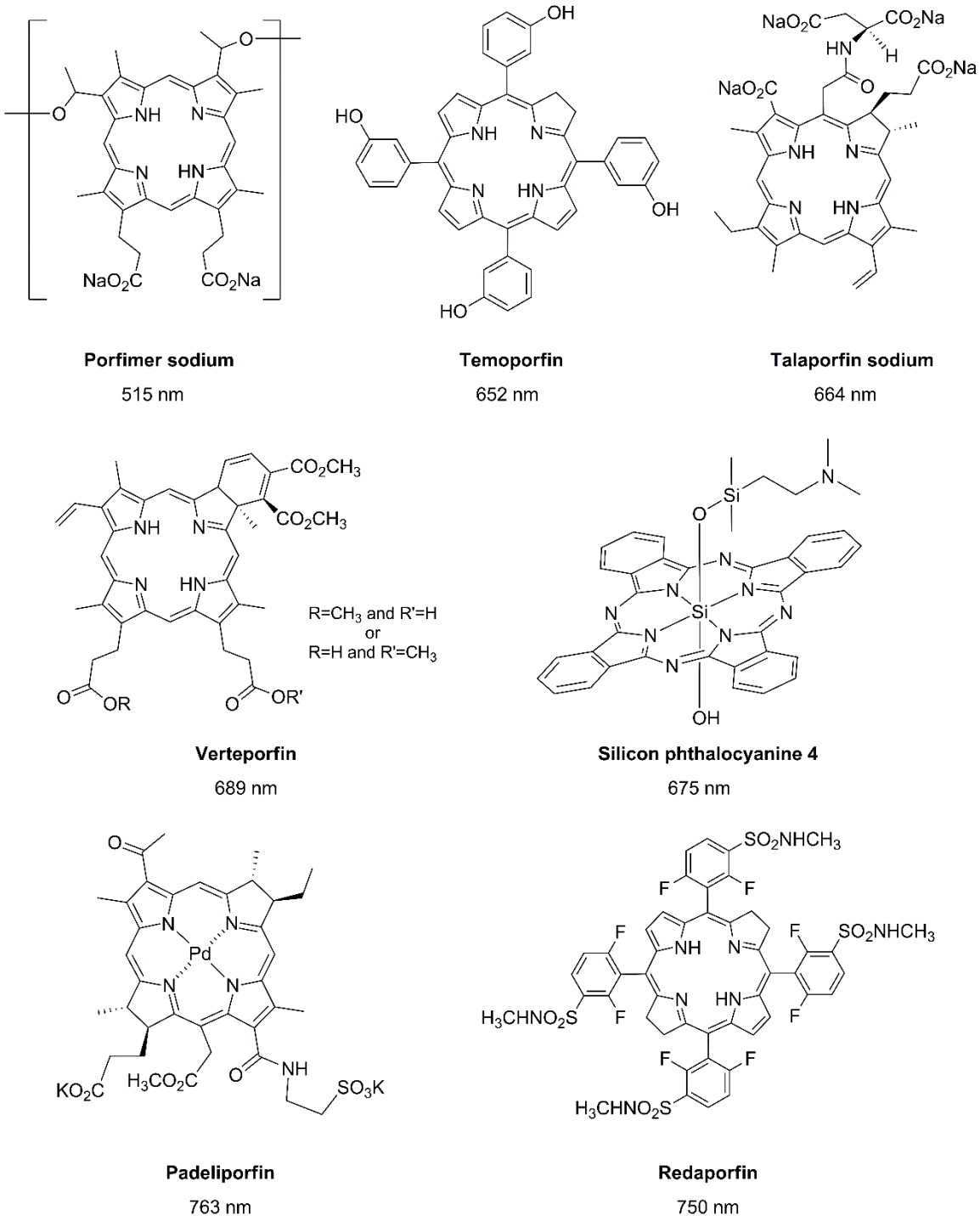

Figure I–5. Examples of clinic or pre-clinic tetrapyrrolic macrocycles.

First-generation PSs mainly included haematoporphyrin and its derivatives (HpD). The use of HpD was first described in 1975 by Dougherty *et al.* [28] which work showed that HpD combined with light with a wavelength superior to 600 nm (i.e. red light) led to long-term cures in different mouse and rat tumours. Subsequent studies with HpD led to the submission of this PS to clinical trials for bladder and skin cancers which were a success. This pushed efforts for the purification of the HpD into porfimer sodium which then received the trade name of Photofrin® The latter became the first

PS to be approved by the United States Food and Drug Administration (FDA) [23,29]. Currently, it is approved for PDT in early- and advanced-stage cancers of the lung, digestive tract, and genitourinary tract in the Netherlands, France, Germany, Japan, Canada and United States [35]. Although, porfimer sodium displays a low molar absorption coefficient at 630 nm that requires high concentrations of PS (e.g., 2 – 5 mg/kg) and 100 – 200 J/cm^2 of light to destroy the tumour. Additionally, its half-life of 452 hours is considerably long leading to a month of skin photosensitivity, which requires patients to stay out of sunlight for that time [23,29,34,35].

These issues led researchers to pursuit with the development of new PSs with higher absorption bands at the phototherapeutic window and shorter blood half-lives. Second-generation PSs appeared as a set of compounds characterised by higher chemical purity and enhanced photophysical properties such as higher ROS quantum yields and maximum absorption bands in the range of 650-800nm. Among several new compounds, only a few of these second-generation PSs actually reached the clinic [29]. The approval of Levulan®, or 5-aminolevulinic acid (5-ALA), by the FDA in 1999 for the topical treatment of actinic keratoses in face and scalp was an important achievement. 5-ALA is a pro-drug as it is the precursor of the endogenous PS, protoporphyrin IX (PpIX). It and its esters can be administered topically, or even orally (Gliolan®). PpIX has a maximum absorption wavelength at 410 nm, along with other smaller bands at 510, 540, 580, and 635 nm. The latter wavelength is used in the clinic [27] to increase the depth of the treatment. irradiation [29,34].

A few chlorines derivatives of second-generation have received clinical approval. Temoporfin [36] is a chlorin that was approved in 2001 by the European Medicines Agency (EMA) for the palliative treatment of head and neck cancer. Temoporfin has an absorption maximum at 652 nm, with a molar extinction coefficient of 3 x 10^4 M^{-1}cm^{-1}, being one of the most active PS to date. This PS requires drug (0.15 mg/kg) and light doses (10 J/cm^2) that are ca. 10 times lower than what is needed for porfimer sodium to obtain a similar response. The high efficacy of temoporfin is however associated with skin photosensitivity due to its half-life of 45-65 hours [29,34,36–38]. Section 2.3.1 will provide a deeper discussion about temoporfin, considering that its molecular structure – namely the presence of *meta*-hydroxyl groups on the phenyl rings, which has been known to improve accumulation in tumour tissue and solubility [32,39–43] – acted as a guide for the main goal of this doctoral thesis which was the synthesis of novel PS that could be adapted for targeted-PDT.

Mono-L-aspartyl chlorin e6 (Npe6) is a derivative of chlorin e6, traded under the name Laserphyrin® (talaporfin sodium), with an absorption maximum at 664 nm that successfully treated breast, skin, lung, and liver cancers in different clinical trials. This chlorin, while consistent with a two-compartment pharmacokinetic model with half-lives of 9 and 143 hours, still shows minimal skin photosensitivity after PDT, being considered to have a rapid clearance from circulation where

PDT efficacy is almost non-existent after 12 hours [34,44–46]. The benzoporhyrin derivative known as verteporfin, is another chlorin (absorption at 689 nm, 3.3 x 10^4 $M^{-1}cm^{-1}$) in clinical use, under the trade name Visudyne®, that was particularly successful in the treatment of age-related macular degeneration. It is also being evaluated in multiple cancers with the advantage that its short half-life (5 – 6 hours) translated to only two days of skin photosensitivity [23,33,45,47].

Phthalocyanines are another class of molecules that have been used in classic PDT or as theranostics agents (i.e., molecules that combine diagnostics and therapeutics by usually taking advantage of fluorescence/phosphorescence for visualization of a tumour and photodynamic activity for its destruction [48,49]). These molecules required a metal complex to be used as PS, since the presence of transition metals is what allows the intersystem crossing that leads to the formation of ROS. The silicon phthalocyanine 4 (Pc4) which is characterized by a strong absorption at 675 nm (2 x 10^5 $M^{-1}cm^{-1}$) and a relative short half-life of 28 hours, has completed clinical trials for actinic keratosis, Bowen's disease, and skin cancer [23,33]. Recently, Pinho e Melo *et al*. [49,50] have described platinum (II) ring-fused chlorins that simultaneously emit fluorescence and phosphorescence in solution at room temperature in the 700-850 nm spectral region. These attractive features in the near-infrared, along with a high thermal and photochemical stability implies that they are true stable theranostics agents.

Further improvements have been recently achieved with bacteriochlorins which are known for longer absorption wavelengths and consequently deeper tissue penetration [23]. Padeliporfin (water-soluble Tookad® or Stakel®) is derived from bacteriochlorophyll α found in benthic bacteria, absorbs at 763 nm (1.1 x 10^5 $M^{-1}cm^{-1}$), and has received approval by the European Medicines Agency, in 2017, for the treatment of localised prostate cancer. Owing to its fast clearance (estimated half-life of 1.19 ± 0.08 hours), PDT with Padeliporfin exhibits minimal skin photosensitivity and requires PDT protocols with short DLIs. Its limited extravasation from vasculature at the irradiation time mediates selective cut off the tumour's blood supply with subsequent cell death by necrosis. Vascular-PDT with padeliporfin resulted in over 80% of patients having a negative prostate biopsy in six months after the treatment [23,33,51]. Redaporfin is a synthetic bacteriochlorin that holds strong absorption at 750 nm (1.2 x 10^5 $M^{-1}cm^{-1}$), high ROS quantum yield and a pharmacokinetic profile (1^{st} compartment half-life of 0.5 h and 2^{nd} compartment half-life of 65 h) that allows for vascular- and cellular-PDT protocols. This bacteriochlorin is on phase I/II clinical trials for advanced head and neck cancer (NCT02070432 [52]), without showing apparent skin photosensitivity [23,53–55].

2.3.1. The case of temoporfin

The synthesis of temoporfin by Bonnett et al. in 1989 [36] followed the necessity of second-generation PSs with emphasis on the improvement of the "high absorption in the red" criterion. Light at the phototherapeutic window (Figure I–3) display reduced scattering and absorption effects which permits to reach deeper tissues. Bonnett *et al*. [36] carried out the reduction of a series of 5,10,15,20-tetrakis(hydroxyphenyl)porphyrin derivatives, that have been previously synthesised [39], into their respective chlorins and bacteriochlorins, and explored different substitution patterns (*ortho*, *meta*, and *para* isomers) in order to obtained PSs with increased absorption in the red. The resulting molecules revealed considerably more potent activity when compared to the original porphyrin series. Highest activity was observed with the *meta* and *para* isomers, where tumour necrosis was achieved with doses that were ineffective using the respective porphyrins. With an absorption maximum red-shifted to 652 nm, the 5,10,15,20-tetrakis(3-hydroxyphenyl)chlorin (mTHPC, known as temoporfin) was obtained as a chemically pure compound that required smaller doses and shorter treatments to achieve optimal PDT response [36,38].

Temoporfin was approved in 2001 by the European Medicines Agency (EMA), under the trade name of Foscan®, as a local therapy for the palliative treatment of patients with advanced head and neck cancer who have failed prior therapies and were unsuitable for radiotherapy, surgery, or systemic chemotherapy [38]. Even as an adjuvant treatment at the time, PDT with temoporfin required lower drug and light doses, compared to the use of porfimer sodium or 5-ALA [38,56,57]. Recently, mTHPC-based PDT has been shown to have equivalent complete response rates to surgery and/or chemo-radiotherapy but with lower morbidity and better cosmetic results [57–60]. Furthermore, a cost-effectiveness analysis in the UK and in Germany revealed that palliative mTHPC-based PDT against advanced head and neck cancers increased the patient´s life quality when compared to traditional palliative surgery/chemotherapy that is associated with several side effects. Additionally, mTHPC-based PDT was more advantageous from the economical perspective [38].

Nonetheless, the use of temoporfin is not absent of adverse effects. One of the greatest disadvantages of using temoporfin is the lasting skin photosensitivity in the following weeks which requires patients to avoid sun exposition. Other side effects include mild to moderate pain in the treatment area. This photosensitivity is due to a slow distribution of temoporfin from the blood into the peripherical tissue, most likely caused by its aggregation in the blood which is followed by the slow monomerization process, after which it binds to lipoproteins [38]. In fact, the poor solubility of temoporfin in aqueous solvents is another issue that brings additional challenges related with to its pharmaceutical development. For instance, Foscan®, contains temoporfin dissolved in mixture

of ethanol anhydrous and propylene glycol, is administered very slowly by infusion to minimize aggregation at the administration site [61]. This has created a shift in development research for the search of alternative pharmaceutical formulations such as Fospeg® and Foslip®, which consist of polyethylene glycol (PEG) derivatives of mTHPC and liposomal formulations, respectively. These delivery vehicles change mTHPC solubility and size, which increases its tumour:tissue distribution and thereof, the treatment specificity [38,62]. Nevertheless, to further improve PDT with temoporfin, efforts have been carried out to upgrade temoporfin as a third-generation PS [62]. Improvement of second-generation PSs has been attempted through their conjugation to targeting motifs that have higher affinity to tumour cells or by taking advantage of a variety of drug delivery strategies. The prime goal of these approaches is to enhance cancer-specific targeting while sparing normal tissues (e.g. skin) [29]. In addition, heightened tumour accumulation and/or cell internalization is expected to improve the efficacy of the PDT treatment as well.

3. Targeted-ligand PDT

3.1. Increasing selectivity

The concept of a "magic bullet" consisting of an entity with the ability to search and bind to a target providing a therapeutic action only in that target, was first coined by Paul Ehrlich in the beginning of the 20th century [63]. Since then, the concept of targeted drug delivery has motivated the development of a variety of approaches that range from simple bioconjugates (targeting ligands attached to pharmaceutical drugs) to the development of sophisticated and complex drug delivery systems with highly controlled properties [64].

Some anti-cancer drugs benefit from the enhanced permeability and retention (EPR) effect which facilitates tumour accumulation. This effect is explained by the deregulated tumour angiogenesis that leads to the formation of leaky blood vessels as well as by the poor lymphatic drainage of tumour tissues [1,51,65]. However, most traditional anti-cancer therapeutics lack tumour specificity which is associated with accumulation in both healthy and tumour tissue indiscriminately. This leads to debilitating side effects and a decreased efficacy of the treatment [1]. As mentioned above, PDT already offers some tumour selectivity, resulting from the photoactivation of PS only at the irradiated region. Additionally, amphiphilic and lipophilic PSs are known to favour interaction with low-density lipoproteins (LDL), which in turn have a preferential accumulation at tumour sites [66]. Still, combining the use of targeting strategies with

PDT will considerably improve therapeutic outcomes namely by reducing side-effects, such as skin photosensitivity and/ or by enhancing cell internalization [1].

An ideal ligand-targeted PS must enable an effective delivery specifically to the cancer cells. As illustrated in Figure I–6, after intravenous administration (Figure I–6, step 1), and by taking advantage of the EPR effect (Figure I–6, step 2), the ligand-targeted PS should accumulate in the tumour tissue where it can be internalised by the cancer cells, which typically occurs through receptor-mediated endocytosis. It might be release into the cytosol and be accumulated in another subcellular compartments or remain entrapped in the endocytic vesicle. After the appropriate DLI, the irradiation of the tumour (Figure I–6, step 3) allows for photons to be absorbed by the PS which leads to the generation of ROS. The generated oxidative stress and associated damage culminates in the activation of different mechanism of cell death and thereof, destruction of the tumour [1].

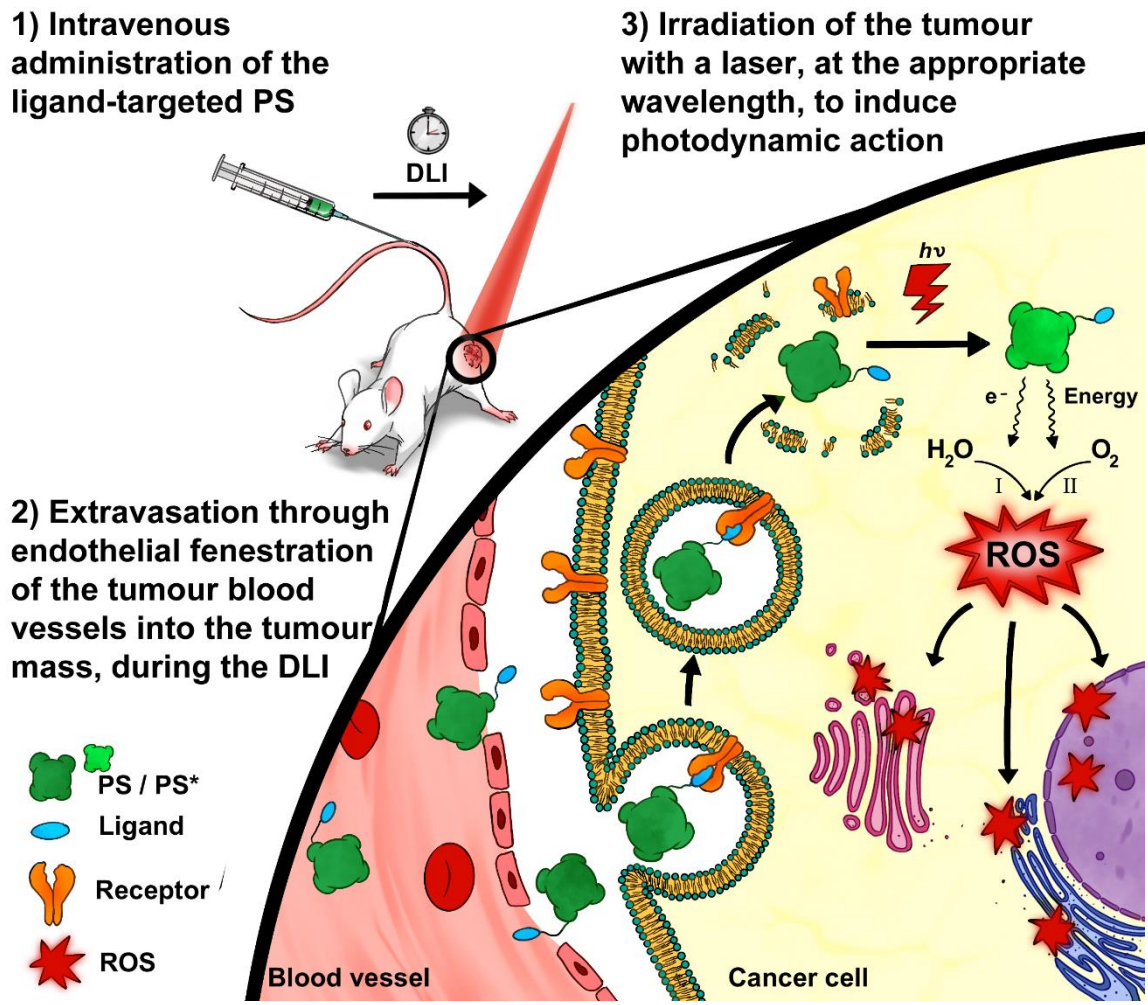

Figure I–6. Graphical representation of a targeted-ligand PS administered intravenously and internalized through receptor-mediated endocytosis. Adapted from Gierlich *et al*. [1].

Besides the targeting of cancer cells, it is important to consider the dynamics of the tumour microenvironment. Benefits might be achieved by targeting other cell populations that support tumour development and aggressiveness [1,3–5], such as: cancer stem cells, the endothelial cells from tumour angiogenic blood vessels, tumour-associated macrophages, and tumour lymphatic endothelial cells [67].

3.2. Targeting receptors overexpressed on cancer cells

Normal cells are dependent on the presence of growth signals (i.e., diffusible growth factors, extracellular matrix components, and cell-to-cell adhesion molecules) to go into a proliferative state. In cancer cells, this exogenous dependency has been overruled by the cancer cell itself, by generating the growth signals it needs by modulating: (1) the extracellular growth signals, (2) their transcellular transducers, or (3) the intracellular translation mechanisms of those signals [4]. This acquired self-sufficiency in growth signals became one of the core hallmarks of cancer, as it provides enough stimulus to enable the rapid proliferation of cancer cells. The enhanced production of growth factor by cancers, leads to the overexpression of transmembrane receptors that are responsible for transducing growth signal stimulus [4,5,65]. In fact, a large number of cell-surface receptor are often overexpressed in cancer cells, and other cells of the tumour microenvironment, to accomplish tumour growth invasion and metastasis. These receptors can be explored as candidates for ligand-targeted cancer therapy.

3.2.1. Receptors tyrosine kinase

Receptors tyrosine kinase (RTK) are membrane receptors activated through their high-affinity for growth factors involved in cell proliferation, such as the fibroblast growth factor receptor (FGFR) and the epidermal growth factor receptor (EGFR). This class of receptors are known to be overexpressed in several types of cancers [65]. The human FGFR consist of a family of four transmembrane receptors from the immunoglobulin superfamily (FGFR1 – FGFR4) that present varied levels of overexpression depending on the localization and type of cancer. For instance, FGFR1 overexpression is usually found in non-small cell lung carcinoma and metastatic breast cancer. In prostate cancer, it is found overexpression of FGFR1, FGFR2, and FGFR4. Papillary thyroid carcinoma presents overexpression of FGFR1 and FGFR3, while overexpression of only FGFR2 is more common in gastric cancers [65,68,69].

As for the human EGFR family (human epidermal receptors 1 – 4; HER1 – HER4), they have been widely used in targeting therapies for the treatment of cancers of different histological origin such as: head and neck, lung, breast, bladder, cervical, and ovarian cancers, where these family of receptors is found overexpressed. Their relevance for cancer progression is confirmed by the

correlation between high levels of expression and malignancy as observed in several types of cancers [1,65,70]. The monoclonal antibody (mAb) cetuximab has received the approval of FDA in 2004 and it is currently used for the treatment of advanced metastatic colorectal and metastatic head and neck squamous cell cancers. [13,70,71]. The HER2 is unique within the EGFR family, because it has no endogenous ligand, but it is the preferred for dimerization with the others EGFR. This makes it an attractive target in therapies for HER2-positive cancers such as breast cancer. For instance, the mAb trastuzumab is clinically approved since 1998 for HER2-positive breast cancer which represent ca. 20-30% of the diagnosed breast cancers [1,16,72–74]. Numerous works have demonstrated that cetuximab, trastuzumab, as well as other antibodies targeting the EGFR family, are targeting moieties with the potential to guide drugs towards cancer cells [1,44,65,70].

3.2.2. Hormone receptors

Another type of receptors commonly found overexpressed in cancer, namely breast and ovarian cancer, are hormone receptors, such as the oestrogen receptor (EsR) and the progesterone receptor (PgR). The EsR can be found in two isoforms that bind the endogenous oestrogens: the αEsR, expressed in breast, ovary, and endometrium tissues, and the βEsR expressed in the kidneys, central nervous system, cardiovascular, prostate, and bone tissues. The overexpression of isoform αEsR in over 70% of breast cancers has led to its study as a therapeutic target and prognostic marker in this type of disease [75]. Similarly, the PgR can be found in two different isoforms (PgR-A and PgR-B) in normal uterus, ovary, and brain tissues. Its low expression in normal breast cells easily contrasts with PgR overexpression in cancerous breast tissue, so the presence of these receptors in breast cancer cells can also be used as an indicator of the prognosis [75].

The androgen receptor (AR) is another hormone receptor found to be overexpressed in certain triple-negative breast cancer (TNBC), such as the luminal AR subtype [75–77], making it an interesting target. The use of antiandrogens such as bicalutamide [78], abiraterone [79], and enzalutamide [80] has been investigated in clinical trials targeting the AR pathway, where the latter showed to be the more potent of the three (29% clinical benefit after six months, compared to the approximately 20% found for the other two) to treat AR-positive TNBC patients, thanks to inhibiting androgen binding, AR translocation to the nucleus, and subsequent transcriptional process [77].

3.2.3. Integrin receptors

Integrins are a family of heterodimeric cell surface transmembrane receptors that mediate interactions between the cell cytoskeleton and the extracellular microenvironment, being essential to the migration, invasion, proliferation, and survival of tumours. They are usually found in

activated endothelial cells and overexpressed in lung, breast, melanoma, prostate, ovarian, and brain tumours – opposed to resting endothelial cells and normal organs – making them potential targets for cancer therapy and imaging [1,65,75,81,82]. Integrins αvβ3 and αvβ5 are the most overexpressed integrins, leading to their frequent use as neoplastic markers. Cyclic or linear derivatives of RGD (Arg-Gly-Asp) oligopeptides have been exhaustively studied as ligands with high affinity to the mentioned integrins [1,75,83]. Another relevant ligand for αv integrins is the mAb abituzumab with the potential to supress metastasis. Although initial preclinical results demonstrating tumour growth blockade [82], later phase clinical trial outcomes were disappointing [81,84].

3.2.4. Transferrin and folate receptors

The increased need for growth factors, such as transferrin and vitamins, by the highly proliferating cancer cells is responsible for overexpressed receptors for these molecules [5,65].

Transferrin receptors (TfR) ensure iron uptake by the cells and can be divided in TfR1 and TfR2 subtypes: TfR1 (or CD71) can be found in most normal tissues at low levels while TfR2 is only found in hepatocytes. When dealing with cancer cells, the expression levels of TfR1 are known to be increased up to 10-fold in breast, ovary, and brain cancers. Its high expression in the blood-brain barrier is also an advantage as a target for drugs that need to enter the nervous system [1,65,85].

As for vitamins, the most investigated receptors are the ones for vitamins B7 and B9, also known as biotin and folate, respectively. The biotin receptor is a sodium-dependent multivitamin transporter that has gained more attention since it was known to be overexpressed in several cancers, such as colon, breast, renal, lung and leukaemia, at very high levels [1,65,75]. For this reason, biotin has been investigated as a ligand for imaging [86] and targeted drugs or theranostic agents [87–90] in cancer cells.

Folate can be internalized by cells through three mechanisms. The most common way is through a transmembrane protein known as reduced folate carrier that is found in normal cells. At low pH levels, such as the one observed at upper the gastrointestinal tract, the proton-coupled folate transporter assumes an optimal activity. However, it is the glycosyl-phosphatidylinositol-anchored receptor, known as folate receptor (FR), the receptor most extensively investigated in cancer. FR have high-affinity for folate (K_D ~ nM) and mediate its internalization *via* endocytosis. FR can be divided in three isoforms: FRα, which is mainly expressed at the apical surface of polarised epithelial cells (except in kidney, lung, and choroid plexus); FRβ, which is limited to the placenta; and FRγ, which is expressed at low levels in haematopoietic tissues [1,65,75,85,91].

FRα is found overexpressed in cancers of different histological origin (like ovary, brain, breast, endometrial, pancreatic, kidney, and lung cancers), but is usually expressed at negligible levels in normal cells. Its increased expression in cancer cells has been used for identification of malignant cells and as a prognostic factor for the expected aggressiveness of the cancer [75,92,93].

Targeting approaches focused on the overexpressed FRα enable a certain degree of cancer selectivity not only by its expression but also its accessibility to blood flow. This selectivity can be further increased by designing conjugates that are not recognized by the facilitative routes of folate internalization used by normal cells – reduced folate carrier and proton-coupled folate transporter [75,85,91,94] – such as the antifolate AGF102 [95,96] which has absolute selectivity towards FR over the other folate transporters by replacing one of the fused rings with a thiophene moiety. With folate being essential in cell proliferation and synthesis of purines and thymine, the dependency of cancer cells on this receptor has been exploited for therapeutic purposes in a wide range of human carcinomas (Figure I–7). Additionally, targeting FRα, namely by means of folate, is one of the targeting approaches most used to improve the selectivity and/or uptake of anti-cancer agents of varied nature[1,65,75,85,93].

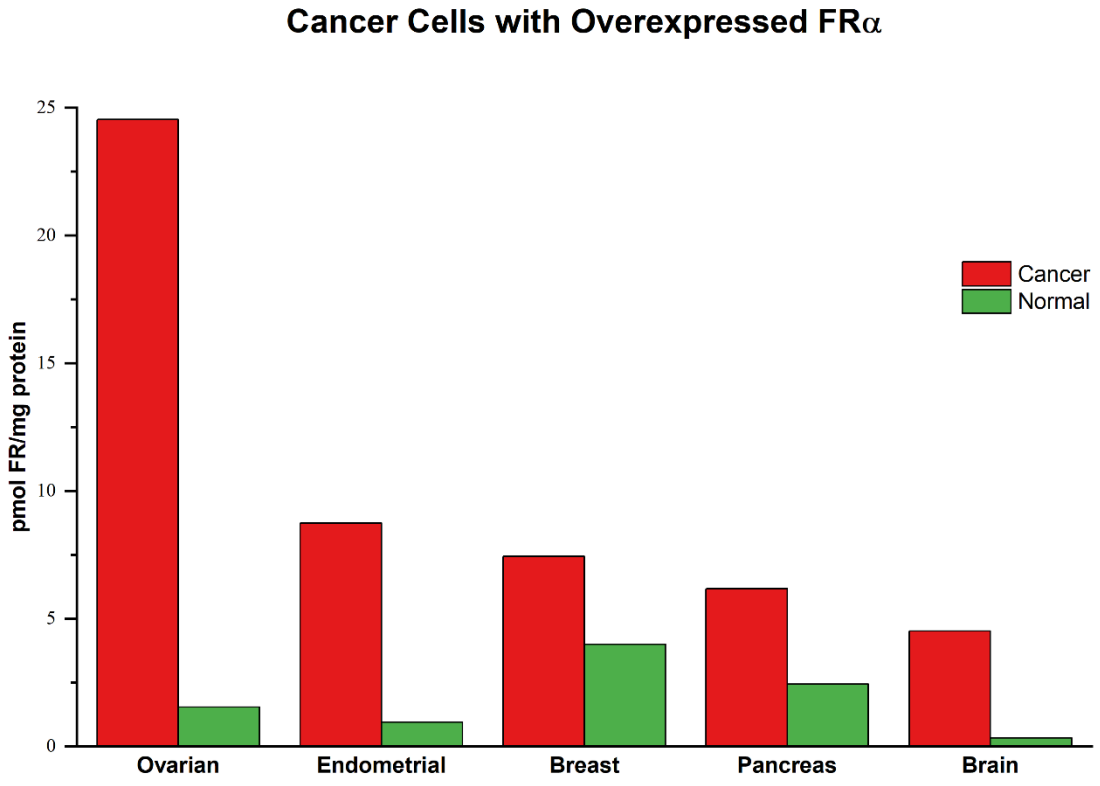

Figure I–7. Overexpression of FR in human cancer tissue compared to their normal levels. Average data adapted from Parker *et al.* [93], includes both α- and β-isoforms of the FR.

3.3. Targeting delivery of PSs

One promising approach to improve PDT efficacy while reducing undesirable side effects relies on the covalent attachment of PSs to ligands that are specifically recognised and, eventually, internalized by cancer cells. Ligands of diverse nature (such as antibodies, proteins, peptides, and small molecules) have been used for a long time. Some of the most promising targeted-PS bioconjugates are then discussed.

3.3.1. Antibody-targeted PSs

Antibodies and their fragments are ones of the most used targeting-ligands with PS due to its popularity with the progression of personalized medicine. With high affinity and specificity for the target, as well as stability *in vivo*, their greatest disadvantages are the potential immunogenicity, high production cost, and their large size [97–100]. Nanobodies and affibodies (peptide mimetics of antibodies) partially solve these problems, while retaining the high specificity for the target, but their small size may lead to a high rate of blood clearance [101–103].

The water-soluble silica phthalocyanine-based PS IRDye700DX (IR700) has been conjugated to different mAbs and could be considered one of the most promising examples of this class of conjugates [1]. Initial studies performed with anti-EGFR mAb (trastuzumab or panitumumab) showed not only preferential *in vitro* accumulation of the PS at the A431 cell membranes, but also necrotic cell death upon illumination at 690 nm. *In vivo* specific A431 (epidermoid) and 3T3/HER2 (breast) tumour accumulation and shrinkage were also reported (300 µg/mouse, DLI = 24 h, LD = 30 J/cm^2) [104]. The same strategy was applied for bladder cancer treatment, either in monotherapy with panitumumab-targeted IR700 [105] or upon combination of the latter with trastuzumab-targeted IR700 [106]. Additional works have demonstrated that this strategy can be effective for tumours of different histological origin by using antibodies against relevant targets: prostate cancer (prostate-specific membrane antigen) [107,108]; oral cancer (CD44); lung cancer (delta-like protein 3) [109,110]; glioblastoma (CD133) [111]; and melanoma (CD146) [112]. In 2020, the cetuximab-targeted IR700 (named as cetuximab saratolacan) was approved by the Japanese government, under the trade name of Akalux®, for the treatment of recurrent and/or advanced head and neck squamous cell cancer, thus becoming the first antibody-photosensitizer conjugate in clinical use [113,114].

IR700 bioconjugates mainly kill cancer cells by accidental necrosis through a mechanism that was recently highlighted by Sato *et al*. [115]. By using trastuzumab, panitumumab, or cetuximab-targeted IR700, the authors showed that the bioconjugates remain at the cell membrane without further cell internalization. After irradiation at 690 nm, a light-induced reaction occurs

leading to the release of the ligand. This affects the physical properties of the conjugate, inducing physical stress. The latter leads to the disruption of the cell membrane, cell swelling, followed by bursting of the membrane. Importantly, this enables the release of the intracellular content (including danger associated molecular patterns), thereby triggering the activation of the host immune system [115]. This systemic response contributes to the long-term control of the disease and further therapeutic improvements can be achieved through combination with ICB inhibitors [1]. For instance, combination of cetuximab-targeted IR700 with blockade of the PD1/PLL1 axis resulted in complete rejection of MC38 tumours and inhibition of distant (and not illuminated) metastasis [1,114,116]. Phase 1/2 clinical trials (NCT04305795) of cetuximab-targeted IR700 combined with the anti-PD1 mAb pembrolizumab are underway in patients with recurrent or metastatic head and neck squamous cell cancer, or advanced cutaneous squamous cell carcinoma [114].

IR700 has also been studied in conjugation with nanobodies [117–119] and affibodies [120] targeting HER2 with promising *in vitro* results [1]. Driel *et al*. [117] demonstrated that a EGFR-targeted nanobody-IR700 conjugate selectively accumulated, as soon as 1 h post-injection, in orthotopic head and neck tumours, leading to ca. 90% tumour necrosis while sparing adjacent healthy tissues [117]. Heukers *et al*. [118] recently published the use of a nanobody to target cancer cells overexpressing the receptor tyrosine kinase c-Met. The nanobody-IR700 conjugate specifically killed gastric MK45N cancer cells in the nanomolar range [118]. De Groof *et al*. [119] reported another nanobody-IR700 conjugate to target cells expressing US28, a viral G protein-coupled receptor that has an oncomodulatory effect in the progression of glioblastoma. PDT with this bioconjugate showed enhanced anti-cancer effects, both in 2D and 3D *in vitro* cultures, by improving cell uptake. Preclinical studies revealed improved tumour penetration and faster clearance, in comparison to an anti-US28 mAb-targeted IR700 conjugate, which highlight the benefits of nanobodies over classical antibodies [119]. On other work, Yamaguchi *et al*. [120] reported the conjugation of IR700 to an affibody targeting HER2, where there was an obvious selectivity of the conjugate for HER2-overexpressing breast cancer cells. This was correlated with a strong phototoxic effect mirrored in the low cell viability measured [120].

3.3.2. Peptide-targeted PSs

The use of peptides, opposed to mAb, have low costs of production, are biocompatible, and easy to conjugate, while still having high specificity and affinity for the target. Although they do have less stability *in vivo*, this might be modulated through chemical modifications [121,122].

The EGFR-targeting peptide GE11 [123] discovered through phage-display has been significantly studied in conjugation with different PSs [1]. Yu *et al.* [124] reported enhanced *in vitro*

accumulation and phototoxicity in EGFR-positive cancer cells (A431 cell line) treated with a GE11-phthalocyanine (i.e., 1,4-bis(triethylene glycol)-substituted carboxyl ZnPc) conjugate. This bioconjugate also preferentially accumulated in EGFR-positive A431 tumours *in vivo*, although, PDT studies were not performed being difficult assess the real therapeutic value of the proposed strategy. The same peptide conjugated to chlorin e4 (named as RedoxT) showed specific accumulation, both *in vitro* (HCC70 cells) [125] and *in vivo* (TNBC cell lines MDA-MB-213 and MDA-MB-468 cells) [126]. Another promising strategy can be found in the work of Xu *et al*. [127] with the conjugation of a phthalocyanine (mono-substituted β-carboxyl ZnPc) to gonadotropin-releasing hormone (GnRH) peptide analogues (the native peptide, conjugate 1, and a $_{D}$-Lysine anchoring point that substituted the original sixth residue glycine, conjugate 2). The analogue bioconjugate with *D*-Lys6 showed higher selectivity and phototoxicity, both *in vitro* and *in vivo* towards breast cancer, than the free phthalocyanine. It is also of note that the optimised *D*-Lys6 analogue inhibited the blood-brain barrier crossing that is typically observed with other ligands targeting the GnRH receptor. Less skin accumulation was also observed. Thus, the latter conjugate constitutes a valuable targeting approach for breast cancer [127].

More recently, Zhang *et al*. [128] developed an approach with the intent of targeting the cell membrane of cancer cells without promoting cellular internalisation. For this, PpIX was conjugate to a K-Ras-derived peptide (PCPK) which has the ability to target the plasma membrane. The photoactivated bioconjugate was able to destroy the cellular membrane of 4T1 cells at low concentrations, allowing a fast release of damage-associated molecular pattern and immunogenic cell death. Both *in vitro* (4T1 cell line) and *in vivo* (4T1 tumour-bearing mice) assays showed increased anti-tumour effects of the conjugate when compared with its non-targeted counterpart. The triggered anti-tumour immunity permit to inhibit the growth of contralateral, non-illuminated, tumours and was potentiated upon combination with PD-1 blockade [1,128].

3.3.3. Small molecule-targeted PSs

With small molecules, the high affinity and specificity for the target continues to be secured, with the advantages of low production costs, longer shelf-life, and minimal immunogenicity. Disadvantages include off-target toxicity when dealing with high doses, or competitive binding when dealing with endogenous ligands [1,85,129,130]. Endogenous ligands have been used to enhance cell internalization and specificity of PSs to cancer cells. Examples include biotin [131–133], testosterone [134] or carbohydrates [135,136]. Yet, transferrin and folate are likely the most used endogenous ligands, included in PDT. Although more frequently explored in nanocarriers for the targeted delivery of PSs, a few works have reported the synthesis of bioconjugates, with transferrin or folate, with improved selectivity for cancer cells [64].In 1994, Hamblin and Newman [137] were the first to report the conjugation of transferrin to haematoporphyrin. Their studies

revealed that there was an improvement in the internalization of transferrin-targeted haematoporphyrin by HT29 cancer cells and normal fibroblasts (3T3), which increased the phototoxicity of hematoporphyrin. However, the improved uptake was only observed in an iron-deficient environment (that leads to upregulated transferrin receptors) and in a medium supplemented with polycations (to increase binding to cell membranes). With this knowledge, it was anticipated that the *in vivo* translation of this targeting approach would be challenged by competition with the native form of transferrin. Cavanaugh [138] renewed the attention on TfR1 as a PDT target and developed a method for the conjugation of chlorin e6 to transferrin, involving the preliminary binding of the protein to quaternary amino ethyl-sephadex. The transferrin-targeted chlorin e6 had the ability to kill *in vitro* breast cancer cells at concentrations 10- to 40-fold lower than the ones used with the free chlorin e6. More recently, Kaspler *et al*. [139] reported the conjugation of a ruthenium (II)-based PS (known as TLD1433) with transferrin. The TLD1433 conjugate showed enhanced uptake and phototoxicity in rat bladder cancer cells when compared with the non-targeted control. *In vivo* studies with mice bearing the highly immunogenic CT26.CL25 tumours revealed approximately 70% of overall survival with the transferrin-targeted conjugate (50 mg/kg, 600 J/cm^2 at 808 nm), whereas only ca. 30% was attained with the ruthenium complex alone [1,140–142].

Transferrin enables efficient uptake while FR is best known for the enhanced tumour-specificity. By using folate, it is possible to target FR overexpressed in cancer cells while avoiding normal tissue where FR are found in negligible levels [65].

Folate is an inexpensive, non-immunogenic small molecule of 441.40 Da. It is considerably stable in different temperatures and pH values and is still able to bind to FR after conjugation through the γ-carboxylate groups. This is possible as the γ-carboxylate domain is found outside the binding pocket [65,75]. These characteristics make folate an attractive ligand for targeting, [64] and a few folate-targeted PSs have been described [1]. The γ-carboxylate groups in folate facilitates its conjugation through condensation with amino groups as shown by Stallivieri *et al*. [143] and Suvorov *et al*. [144]. In their synthetic work, this methodology was used to conjugate different PSs ((e.g., 5,10,15,20-tetraphenylporphyrin (TPP), PpIX, 5,10,15,20-tetraphenylchlorin, chlorin e6, pheophorbide *a* and zinc(II) phthalocyanines)) to folate. The same strategy can be applied to a linker/spacer, as shown by Yang *et al.* [145] in their work by conjugating folate to a platinum (II) porphyrin complex through an ethylenediamine linker. In this case, the activation of the carboxylic acids from both folate and the PS allowed the formation of amide bonds with the linker (first the folate, followed by the PS), yielding a new folate-targeted PS selective for FRα-positive cell lines (HeLa cells). *In vitro* studies confirmed the endocytosis of the conjugate by HeLa cells, as opposed to the FRα-negative cell line (A549 cells). This was correlated with higher phototoxicity, with a decrease of 78% of the viability of the FRα-positive cell line whereas only 25% of cell death was

attained in the FRα-negative cell line. Similarly, another folate-PS conjugate involving a π-extended diketopyrrolopyrrole-porphyrin was also shown to be selective for FRα-positive HeLa cells [146].

In addition to these *in vitro* examples, Liu *et al*. [147] recently reported an *in vivo* validation of the benefits of using folate-targeting conjugates. In their work, conjugation of pyropheophorbide to folate was achieved by means of a 1 kDa PEG spacer. Studies in a mouse model of nasopharyngeal epidermoid carcinoma showed that the folate-targeted bioconjugate exhibit higher tumour accumulation and photodynamic activity, when compared with the free PS or the non-targeted controls. Inferior results were reported with folate-targeted PS without the PEG spacer that highlights the importance of PEG to increase blood circulation times, which are needed to take advantage of the EPR effect. The PEGylated folate-targeted PS was able to eradicate subcutaneous KB tumours in BALB/c nude mice, at a considerably reduced dose (60 nmol/mouse, DLI = 4 h, DL = 180 J/cm^2 at 670 nm) and no recurrence occurred in the 90 days following treatment, unlike PDT with the non-targeted PS or with the non-PEGylated targeted PS [1,147].

Gravier *et al*. [148] also reported the synthesis of a folate-targeted PS conjugate using a temoporfin-like chlorin. Selective accumulation (tumour:tissue ratio 5:1) of the conjugate was observed in nude mice xenografted with KB tumours (FRα-positive model) when compared to the HT29 tumours (FRα-negative model), 4 hours after intravenous injection (2.2 x 10^{-6} mol/kg). In contrast, similar tumour accumulation was found for free temoporfin on both tumour mouse models. Although this work provided evidence for increased selectivity of the folate-targeted conjugate, phototoxicity was not evaluated *in vivo* [148].

3.4. Developing a new tumour-targeted strategy for PDT

Although there have been several improvements regarding cell internalization, as observed *in vitro* in different cancer cells, ligand-targeting approaches still display little success *in vivo* with tumour-bearing mice. Some studies even show similar tumour accumulation for targeted- and non-targeted drugs upon systemic administration [149]. This highlights the importance of the pharmacokinetics of the targeted drug and of the tumour pathophysiology, rather than solely the presence of a ligand, for effective tumour accumulation. For instance, only up to 0.01% of a targeted radiotherapy with a high binding antibody was shown to achieve tumour accumulation [150–152].

Still, it is important to emphasise that, at the tumour level, the presence of the targeting-ligand might enhance cellular internalization which is expected to improve therapeutic outcomes when compared with free drugs [1]. In addition, it is important to mention that despite the knowledge and

advances on conjugate systems, there is still the need for suitable and general synthetic methods for the "linker" chemistry when preparing conjugates [62].

The literature review herein presented serves its purpose as a general introduction to this doctoral thesis, which aimed at obtaining a new strategy for targeted-PDT with mTHPC, or its derivatives. To achieve this goal, novel chlorins related to mTHPC were synthesized following the [8π+2π] cycloaddition method previously developed within our group by Pinho e Melo *et al*. [153–157]. This permits to easily functionalise them with a targeting moiety to obtain conjugates that could act as third-generation PSs. For proof-of-concept of the developed methodology, folate was used as the targeting moiety. After synthesis and *in silico* evaluation of the obtained folate-targeted conjugate, the latter was submitted to photophysical characterisation. This was followed by *in vitro* studies that aimed to assess their cellular internalization and phototoxicity, both in cancer and non-cancer cells. In all the *in vitro* studies, the clinically-approved temoporfin was included as control.

Overall, this thesis provides a synthetic pathway to obtain a mTHPC derivative that can be easily conjugated, by “click” chemistry, to different targeting moieties, namely the development of folate-targeted bioconjugates. Currently, new biotin conjugates are under investigation.

Chapter II:

Outline

Science is fun. Science is curiosity. We all have natural curiosity. Science is a process of investigating. It's posing questions and coming up with a method. It's delving in.

Sally Ride

The work presented herein aims to contribute with a new strategy for targeted-photodynamic therapy (targeted-PDT), focusing on "clickable" chlorin derivatives of *meso*-tetrakis(3-hydroxyphenyl)chlorin (mTHPC). The goal of the project was to develop a proof-of-concept to increase the specificity of PDT, since the lack thereof in most photosensitisers (PSs) – as mentioned in the previous chapter – is one of the few disadvantages of this technique. With the development of an efficient synthetic strategy to obtain targeted-PSs, the scope of third-generation PSs could be expanded and with simple variations of the warhead used target different receptors. The research developed on this subject was reported in the present thesis, divided in five parts, from Chapter III to Chapter VII. Chapters I and II present an introductory review of the theme of this thesis, concluding with the general outline of the work developed.

In **Chapter III**, the full synthetic pathway for novel chlorins is described. From the synthesis of the precursors to the choice of derivatisation to allow the study of the effects of amphiphilicity of the chlorins, afterwards. Furthermore, within this study we were able to expand the scope of the [8π+2π] cycloaddition method for the synthesis of chlorins, previously developed by Pinho e Melo *et al*. [153–157], developing novel chlorins focused on mono-functionalisation. The production of a novel chlorin with a chemical function to be used in "click chemistry" workflows was a critical milestone of the present work.

Chapter IV focuses on the *in silico* analysis of the interaction of a chlorin conjugate with its biological target (i.e., folate receptor; FR) and the synthesis of the conjugate, which combines a folic acid (FA) "warhead", a polyethylene glycol (PEG) spacer, and the synthesised "clickable" chlorin. The analysis involved an in-depth investigation of the three-dimensional structure of the biological target and the putative molecular interactions with the FA moiety of the conjugate. This was followed by a molecular docking study to assess the feasibility of binding of the conjugate to FR. With the predicted ligand poses evaluated, the synthesis of the designed conjugate was performed.

The photophysical and photochemical characterisation of the new chlorins and the synthesized conjugate is reported in **Chapter V**. Using mTHPC as a positive control for comparison, the newly synthesised compounds were thoroughly characterised to ensure their viability as PSs.

In **Chapter VI,** *in vitro* studies with normal (negative for the target receptor) and/or cancer (positive for the target receptor) cell lines were performed to evaluate compound toxicity in the dark, phototoxicity, and cellular uptake. Furthermore, subcellular localisation of the compounds is also described in this chapter.

Lastly, **Chapter VII** contains the general conclusions obtained from the work reported in this dissertation, as well as a brief discussion of the future perspectives.

Disclaimer: The original research content reported in the present doctoral thesis (except when referenced otherwise) has not been submitted to obtain any degree, in any other educational institution.

Chapter III:

Synthesis of new photosensitisers

A scientist in his laboratory is not a mere technician:
he is also a child confronting natural phenomena that impress him as though they were fairy tales.

Marie Skłodowska-Curie

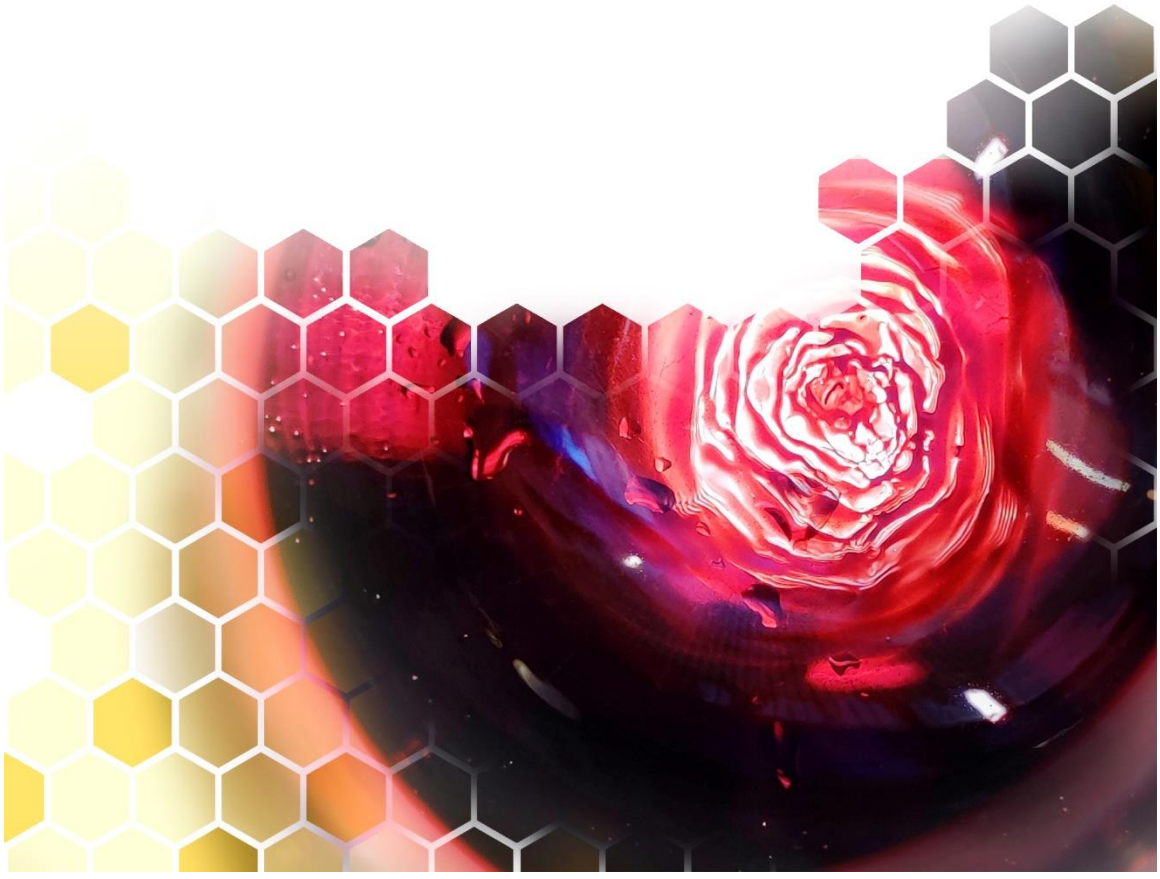

1. Introduction

As mentioned in Chapter I, tetrapyrrolic macrocycle structures are among the most used photosensitisers (PS), since their physicochemical properties encompass most characteristics of interest to a PS, namely the strong light absorption within the phototherapeutic window (600-850 nm) and the ability to generate a significant amount of reactive oxygen species (ROS) when irradiated [23,29,32,48,158]. Chlorins present the advantages of being irradiated at wavelengths that allow deeper tissue penetration than porphyrins and being overall more photostable than bacteriochlorins [23,158–160], which is why this class was chosen for the development of the novel PS described in this chapter.

Chlorins can be fully synthesised using methods like the "2+2" condensation from two dipyrrolic compounds (that also have to be previously prepared) as described by Jacobi *et al*. [161], Lindsey [162], and Montforts *et al*. [163,164], and, similarly, the "3+1" approach proposed by Burns *et al*. [165], or cyclisation starting from bilatrienes as reported by Battersby *et al*. [166]. While these approaches remain to be of interest for obtaining multi-substituted chlorins [167], the simpler way to synthesise chlorins is by derivatisation of the porphyrinic core. Some examples of chlorins synthetised by this synthetic strategy include a few of the most relevant clinical chlorins, such as temoporfin (Foscan®; mTHPC; 5,10,15,20-tetrakis(3-hydroxyphenyl)chlorin) [36,42,43], verteporfin [168,169], and talaporfin (chlorin e6) [167,170–172].

Temoporfin (chlorin **III.2** in Scheme III-1) is still considered one of the most active PS, having been synthesised in 1989, by Bonnett et al. [36]. Temoporfin was obtained through diimide reduction of its respective porphyrin (Scheme III-1), a method first developed by Whitlock *et al*. [173] that has since then been adapted to obtain *meso*-tetraarylchlorins in improved yields. Another method to obtain chlorins from porphyrins is through oxidation with OsO_4, first described by Fischer *et al*. [174], but only reported later by Dolphin and Brückner [175] on the oxidation of *meso*-tetraphenylporphyrin and its zinc complex leading to their respective 2,3-*vic*-dihydroxy-*meso*-tetraphenylchlorins. Furthermore, they also confirmed the success of OsO_4 oxidation for derivatives with different substituents at the *meso*-phenyl group (2,5-dichlorophenyl, 4-sulfonatophenyl, 3,4,5-trimethoxyphenyl, 4-nitrophenyl, 3-hydroxyphenyl, 4-carbomethoxyphenyl), with different metal complexes (Zn(II), Fe(III)Cl, Cu(II)), as well as with *meso*-tetrapyridylporphyrin and 5,15-diphenylporphyrin. These results led Dolphin and Brückner to consider this oxidation methodology general for *meso*-arylporphyrins and their metal complexes [175].

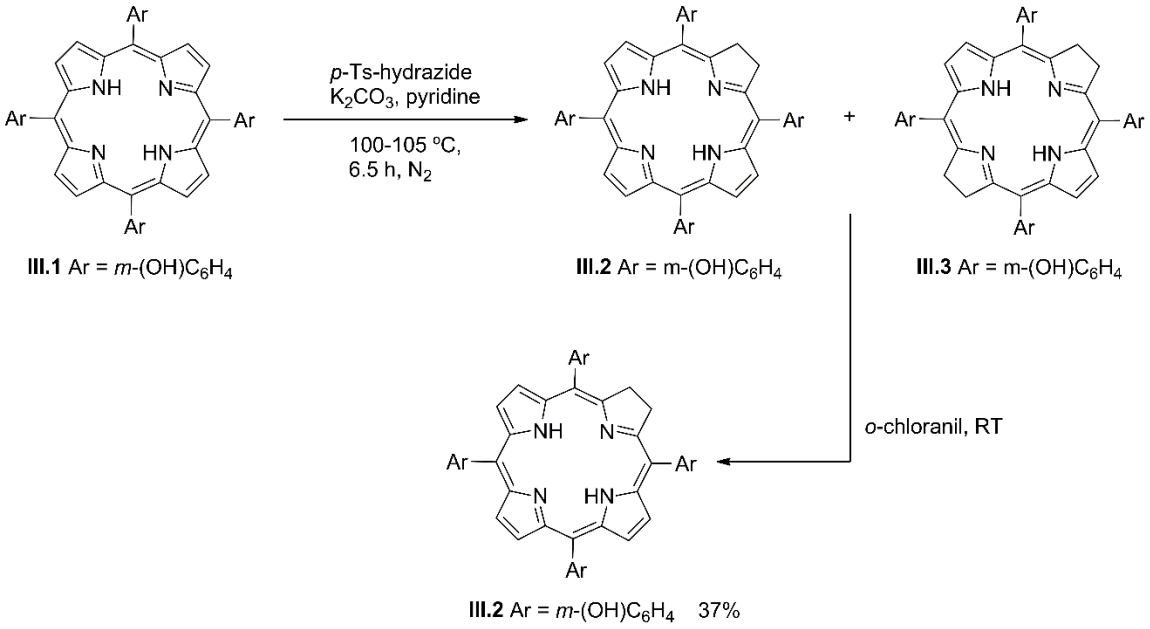

Scheme III-1. Bonnett *et al.* [36] **synthesis of temoporfin III.2, through Whitlock's method** [173]**.**

However, the interest in alternatives to the synthesis of chlorins through reduction or oxidation kept pushing researchers to the development of other approaches, namely cycloaddition strategies by exploring the beta positions of the pyrrole units. Johnson *et al*. were the first [176] to describe the participation of protoporhyrin IX as a diene in Diels-Alder reaction with dimethylacetylene dicarboxylate (DMAD) obtaining a mixture of products including an isobacterioclorin and the isomeric chlorins (later identified by Dolphin *et al*. [177]).

In 1997, Cavaleiro *et al*. [178] published their research on the first use of porphyrins as dienophiles in the Diels-Alder reaction (Scheme III-2). The porphyrins **III.4** reacted with *o*-benzoquinonedimethane (formed after the extrusion of SO_2 from the sulfone), successfully obtaining the chlorins **III.5**, as well as the oxidated porphyrin **III.6** and naphthoporphyrin **III.7** (the yields for the different substituents were similar to the ones reported for the derivatives of **III.4a**) [178].

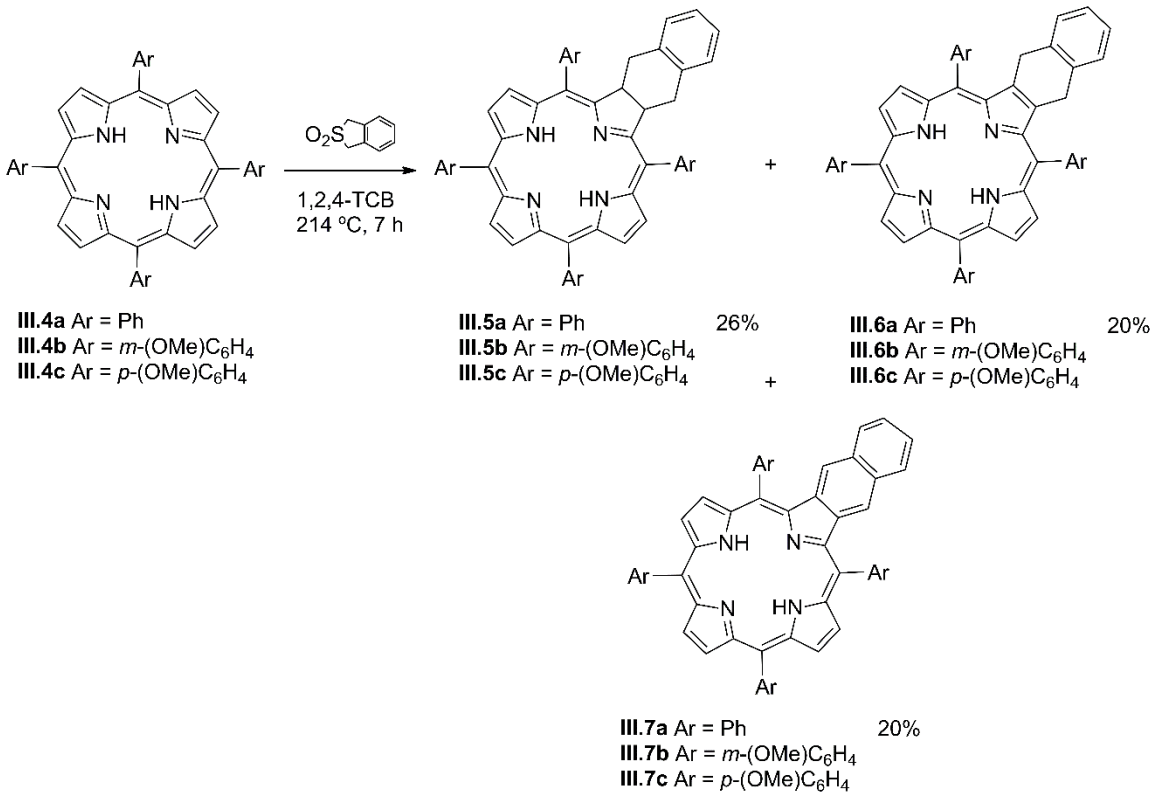

Scheme III-2. Chlorins and derivatives obtained by a Diels-Alder approach, as described by Cavaleiro *et al*. [178]**.**

The same group reported the use of *meso*-tetraarylporphyrins in 1,3-dipolar cycloadditions (Scheme III-3) [179,180] by using porphyrins **III.8a** and **III.8b**, with electron-withdrawing substituents at the *meso*-aryl groups, acting as dipolarophiles in the reaction with azomethine ylides obtaining chlorins **III.9** together with the formation of isobacteriochlorins **III.10**. The azomethine ylides were generated *in situ* from the reaction of *N*-methylglycine with *p*-formaldehyde. Using less reactive porphyrins (e.g., **III.4a** and **III.4c**), the corresponding chlorins were obtained in low yields as the only isolated macrocyles. Using an excess of azomethine ylides percursors led to the production of a mixture of bis- and trisadducts [180].

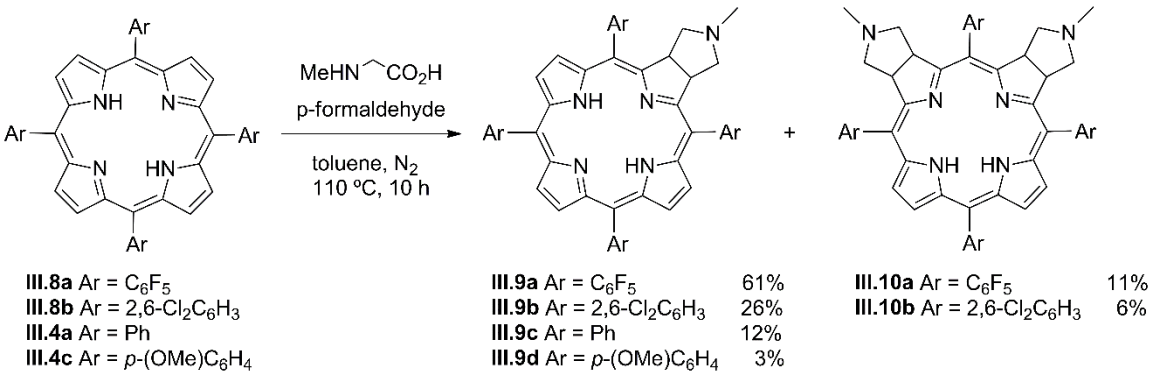

Scheme III-3. Chlorins and isobacteriochlorins obtained by 1,3-dipolar cycloaddition, as described by Cavaleiro *et al.* [180]**.**

These cycloaddition protocols, where porphyrins act as dieno- or dipolarophiles, produce chlorins with higher stability than the ones obtained through diimide reduction. This was one of the reasons that led Pinho e Melo *et al*. [153,154] to research 1,7-dipolar reactions with diazafulvenium methide anions, 1,7-dipoles with eight π-electrons. By exploring the reactivity of this intermediate the group reported a novel [8π+2π] cycloaddition approach to chlorins by the reaction of in situ generated diazafulvenium methide **III.12** with porphyrins. It was also demonstrated that the novel chlorins participate in [8π+2π] cycloaddition reactions with diazafulvenium methide **III.12** to give a new type of bacteriochlorin (Scheme III-4) [153,154].

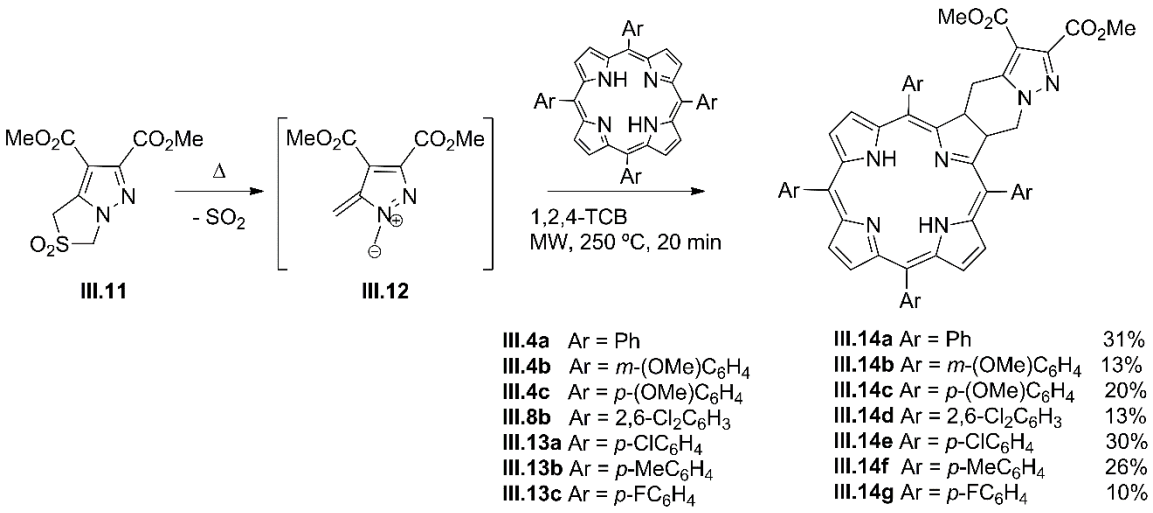

Scheme III-4. Chlorins obtained by [8π+2 π] cycloaddition, as described by Pinho e Melo *et al.* [153,154]**.**

As a matter of fact, in 2010 Pinho e Melo *et al*. [154] successfully reported the synthesis of new and stable 4,5,6,7-tetrahydropyrazolo[1,5-*a*]pyridine-fused chlorins **III.14** derived from *meso*-tetraarylporphyrins (**III.4a-c**, **III.8**, and **III.13a-c**) via microwave-induced [8π+2π] cycloaddition reactions. Furthermore, chlorins **III.14** can undergo another [8π+2π] cycloaddition to obtain the respective 4,5,6,7-tetrahydropyrazolo[1,5-*a*]pyridine-fused bacteriochlorin, with the

second ring in *cis* configuration. Since then, the group has reported further developments on the scope of this route, describing novel chlorins (e.g., derivates with different functionalities at the 4,5,6,7-tetrahydropyrazolo[1,5-*a*]pyridine moiety [155,157] and 5,10,15,20-tetrakis(pentafluorophenyl) chlorin derivatives [156]) with promising photodynamic activity against melanoma [155], bladder [157], and oesophagus [155–157] cancer cells. They have also broadened their synthetic scope through the incorporation of platinum (II) into the structure of 4,5,6,7-tetrahydropyrazolo[1,5-*a*]pyridine-fused chlorins, reporting *in vitro* (human A375 melanocytic melanoma cells) and *in vivo* (Balb-c mouse model inoculated with A375 subcutaneous tumour) efficacy of these Pt(II)-4,5,6,7-tetrahydropyrazolo[1,5-*a*]pyridine-fused chlorins as potential theranostic agents for melanoma [49,50].

The interesting features of this novel type of 4,5,6,7-tetrahydropyrazolo[1,5-*a*]pyridine-fused chlorins with intense absorption bands ca. 650 nm led us to select the [8π+2π] cycloaddition approach as the strategy to develop our targeted-PSs for photodynamic therapy (PDT).

2. Porphyrin synthesis

The presence of hydroxyl groups at the *meta* positions of the aryl groups of *meso*-tetraarylporphyrins has been known to improve PS accumulation in tumour tissue and solubility [39–41], and these properties seem to translate to *meso*-tetraarylchlorins, which might be the reason why temoporfin **III.2** is still one of the most active PS to date [32,42,43]. As such, we chose to use [8π+2π] cycloaddition of diazafulvenium methides to porphyrins to obtain new chlorins with this desired 5,10,15,20-tetrakis(3-hydroxyphenyl) core, as well as other derivatives with different degrees of hydrophilicity for comparison of phototoxic activity.

The first step was the synthesis of the *meso*-tetraarylporphyrin **III.17**, using the Adler-Longo's method [181,182], as shown in Scheme III-5. We started with the protection of the hydroxyl groups of the benzaldehyde **III.15** with acetic anhydride, obtaining **III.16** in very good yield (98%).

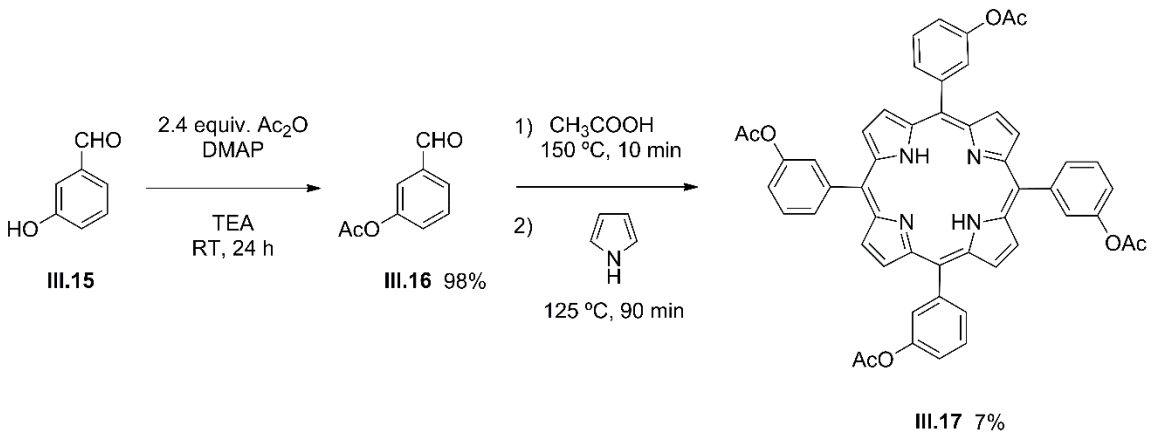

Scheme III-5. Synthesis of 5,10,15,20-tetrakis(3-acetoxyphenyl)porphyrin (III.17).

For the porphyrin synthesis, we allowed the Adler-Longo's reaction to occur in the presence of oxygen and undergo conventional heating. A solution of *m*-acetoxybenzaldehyde **III.16** in glacial acetic acid was brought to reflux for 10 minutes followed by the slow addition of 1 equiv. of pyrrole. After further heating, the product was purified and recrystallised from methanol, giving porphyrin **III.17** in 7% yield. Ormond *et al*. [183] reported a 17% yield using a different isolation procedure; this difference might be due to the use of a different solvent (propionic acid instead of acetic acid), leading to a contamination of chlorin.

3. [8π+2π] Cycloaddition reaction approach to chlorins

Following the method described by Pinho e Melo *et al*. [153–157] to obtain the *meso*-tetraarylchlorins, first we synthesised the diazafulvenium methide precursors **III.11** and **III.24**, as shown in Scheme III-6.

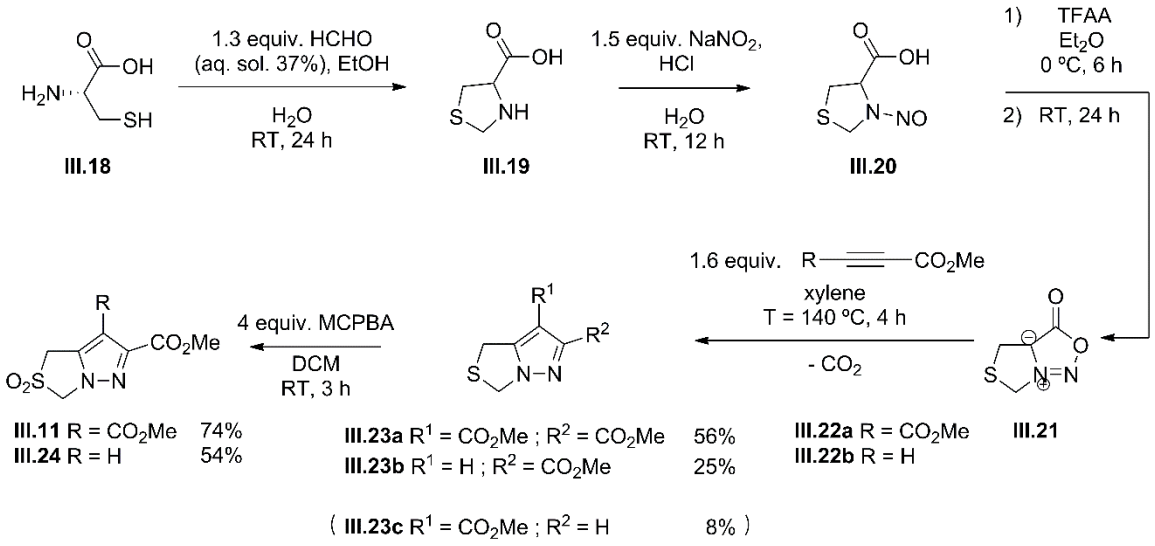

Scheme III-6. Synthesis of the sulfones III.11 and III.24 [184]**.**

As previously described [154,184,185], we started by reacting *L*-cysteine **III.18** with formaldehyde to obtain the thiazolidine **III.19**, which then underwent *N*-nitrosation to yield compound **III.20**. By reacting the latter with trifluoroacetic anhydride (TFAA), the mesoionic 4*H*,6*H*-thiazolo[3,4-*c*][1,2,3]oxadiazole-7-io-3-olate **III.21** was obtained.

Our focus was on the synthesis of a monoester sulfone that would work as the single "anchor" for functionalising the novel chlorins for targeting – avoiding obtaining a mixture of products expected from the functionalisation of diester derivatives, while we were still at a proof-of-concept level. However, the diester derivative was also synthetised for comparison purposes with the pyrazole monofunctionalised chlorins. As such, the masked azomethine ylide **III.21** was made to react with either of the dipolarophiles **III.22a,b** to yield the 1*H*,3*H*-pyrazolo[1,5-*c*][1,3]thiazoles **III.23a-c**, through 1,3-cycloaddition reaction and *in situ* extrusion of carbon dioxide. DMAD (**III.22a**) yielded the dimethyl 1*H*,3*H*-pyrazolo[1,5-*c*][1,3]thiazole-6,7-dicarboxylate **III.23a** in relatively moderate yield (56%). As expected, the efficiency of this synthesis was higher than the synthesis of the monoester derivatives 1*H*,3*H*-pyrazolo[1,5-*c*][1,3]thiazoles **III.23b** (25%) and **III.23c** (8%), obtained from the reaction with the less activated dipolarophile methyl propiolate (**III.22b**), The two regioisomers **III.23b** and **III.23c** were separated by column chromatography. The oxidation of 1*H*,3*H*-pyrazolo[1,5-*c*][1,3]thiazoles **III.23a** and **III.23b** was carried out with 3-chloroperoxybenzoic acid (MCPBA), affording 2,2-dioxo-1*H*,3*H*-pyrazolo[1,5-*c*]thiazoles **III.11** (74%) and **III.24** (53%), respectively. Compound **III.23c** was obtained as a minor product, so we did not follow through with it for the diazafulvenium precursor synthesis.

Compounds **III.11** and **III.24** were used as 1,7-dipole precursors to participate in the [8π+2π] cycloaddition reaction with porphyrin **III.17**, under conventional heating conditions [154], as shown in Scheme III-7.

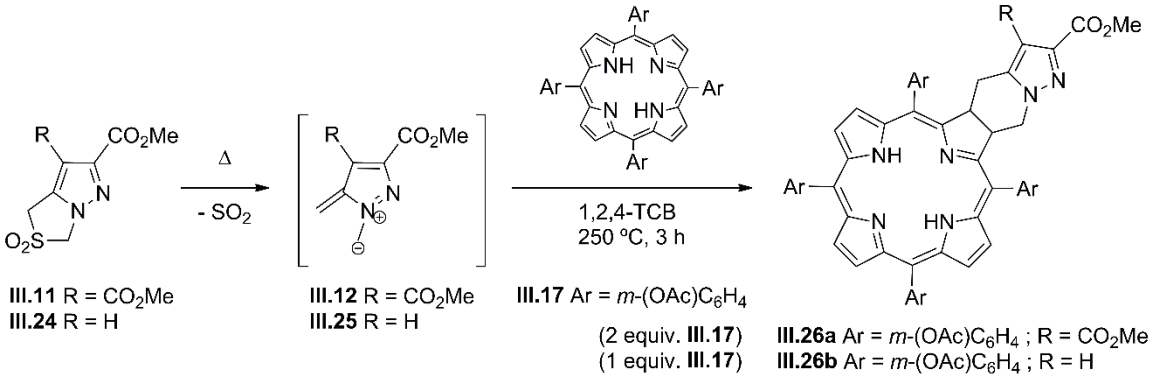

	Chlorin	Porphyrin recovered
III.26a	15%	58%
III.26b	9%	35%

Scheme III-7. Synthesis of chlorins III.26a and III.26b.

The *in situ* SO_2 extrusion of sulfone **III.11** or **III.24** happens when refluxing in 1,2,4-trichlorobenzene (TCB), in the presence of porphyrin **III.17**. The *meso*-tetraarylchlorins **III.26a** and **III.26b** were obtained (UV-visible absorption spectrum confirmed the profile and presence of a peak ca. 650 nm, for which chlorins are known). While the strategy to obtain chlorin **III.26a** involved the use of 2 equiv. of porphyrin **III.17** in the reaction – to avoid the formation of bacteriochlorin, – the decreased reactivity of 2,2-dioxo-1*H*,3*H*-pyrazolo[1,5-*c*]thiazole **III.24** allowed the use of just 1 equiv. of porphyrin **III.17** to obtain chlorin **III.26b**. This *meso*-tetraarylchlorin will be the most hydrophobic of its series, acting as a starting point to obtain derivatives with different degrees of hydrophilicity.

The structure assignment of **III.26b** was confirmed based on the information obtained from the ^{1}H NMR (Figure III–1) and ^{13}C NMR spectra (Figure III–2), as well as the heteronuclear single quantum coherence (HSQC) bidimensional spectrum (Figure III–3). A comparison of these results with the ones obtained from structures with a similar core synthesised by Pinho e Melo *et al.* [154], supports our conclusions which then guided the signal assignment of the other synthesised chlorins obtained.

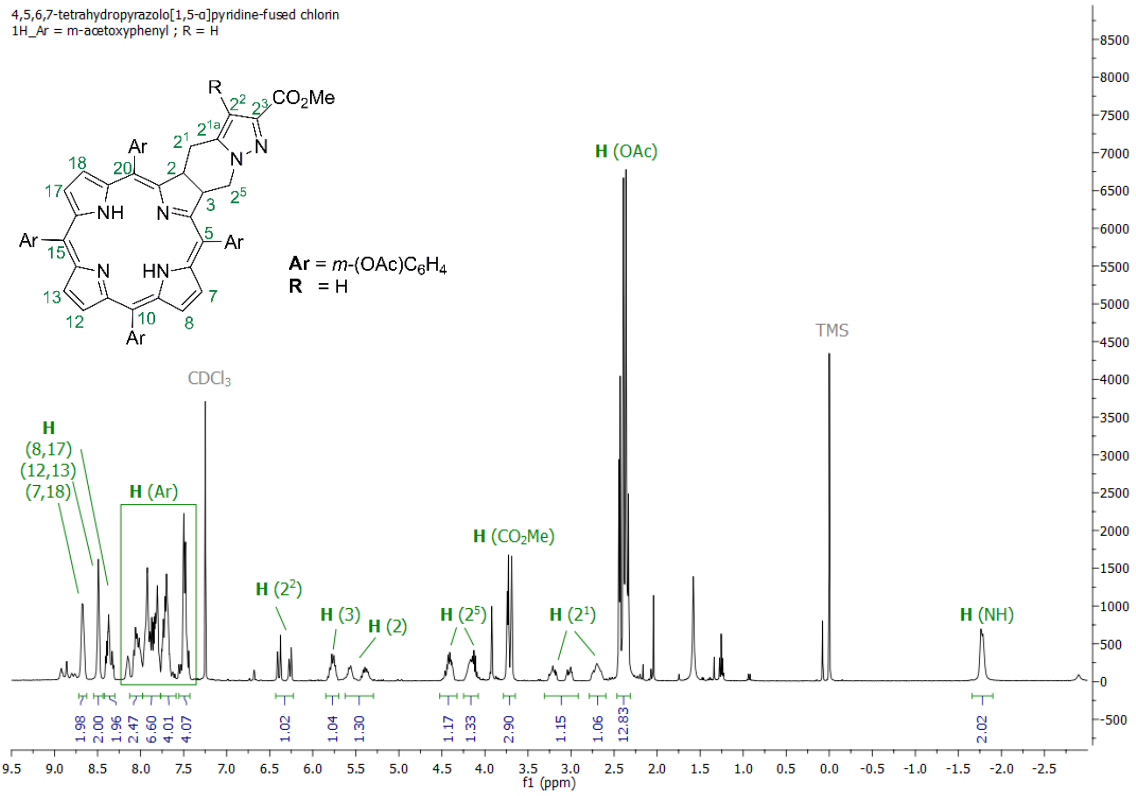

Figure III–1. ^{1}H NMR (400 MHz) spectrum of chlorin III.26b ($CDCl_3$).

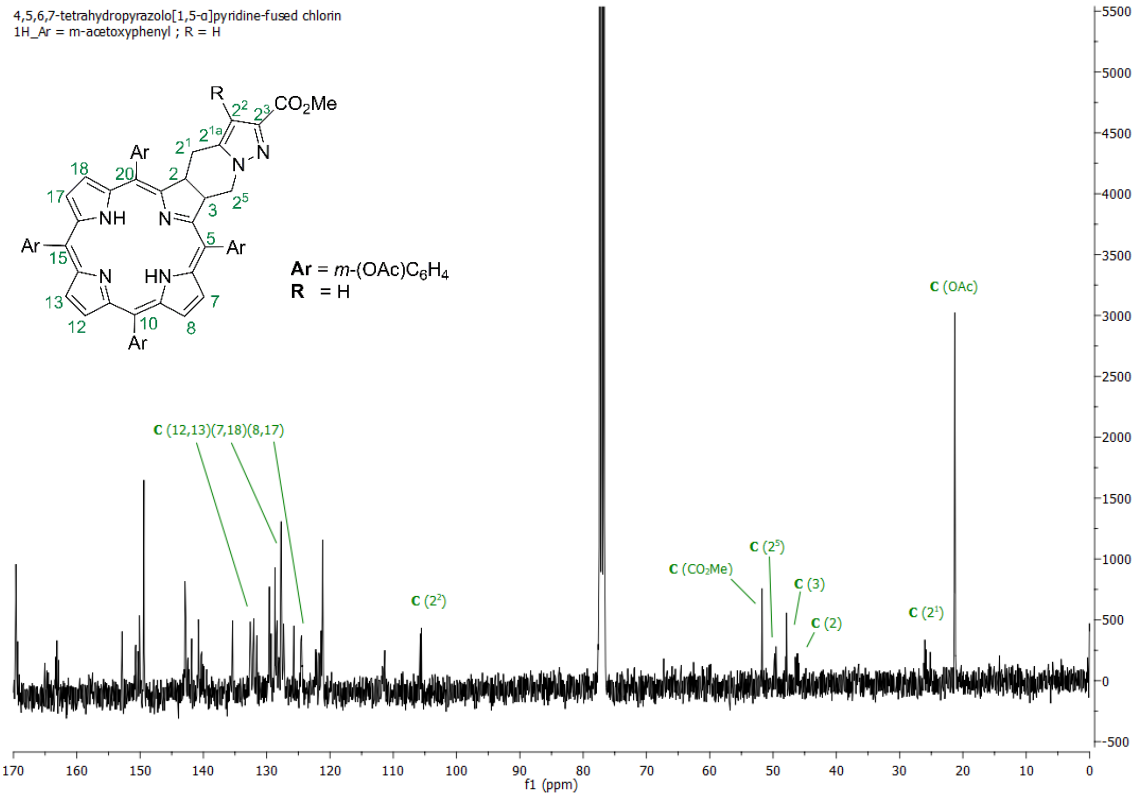

Figure III–2. ^{13}C NMR (100 MHz) spectrum of chlorin III.26b ($CDCl_3$).

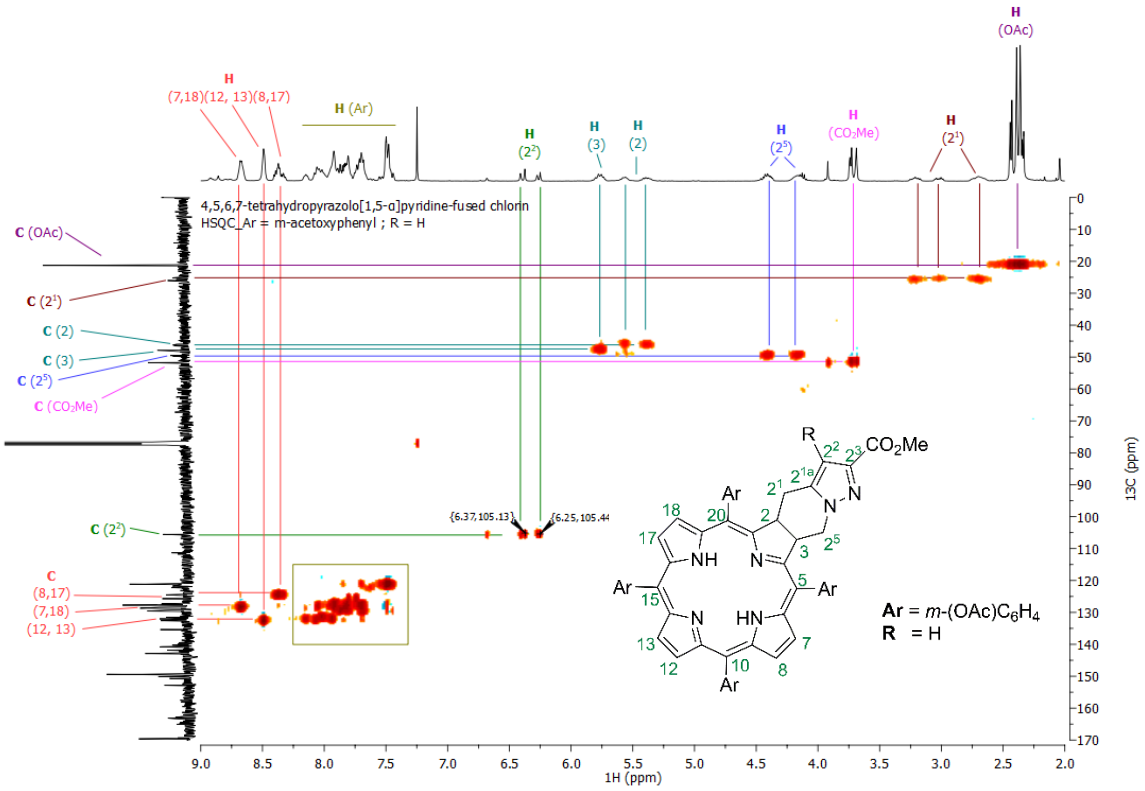

Figure III–3. HSQC bidimensional spectrum of chlorin III.26b ($CDCl_3$).

4. Derivatization of chlorins for "click" chemistry

We proceeded as described in Scheme III-8 to obtain the desired chlorins with different hydrophilicity levels for phototoxic evaluation, starting from chlorin **III.26b**.

In the first approach, the deprotection of the hydroxyl groups was achieved by reacting chlorin **III.26b** with sodium methoxide. Thus, chlorin **III.26b** was dissolved in dry methanol, to which sodium was added and left to react. Under these conditions, chlorin **III.27** was obtained in 46% yield. For the other route, a significant excess of lithium aluminium hydride was used to ensure the complete reduction of the ester groups to alcohols. Starting with a suspension of $LiAlH_4$ in dry tetrahydrofuran (THF), under N_2, the chlorin was added to the reaction mixture, either of the chlorins **III.26a** or **III.26b**, brought to reflux and left to react for a day. After purification and isolation, the hydroxymethylchlorins **III.28a** and **III.28b** were obtained in 62% and 19% yield, respectively.

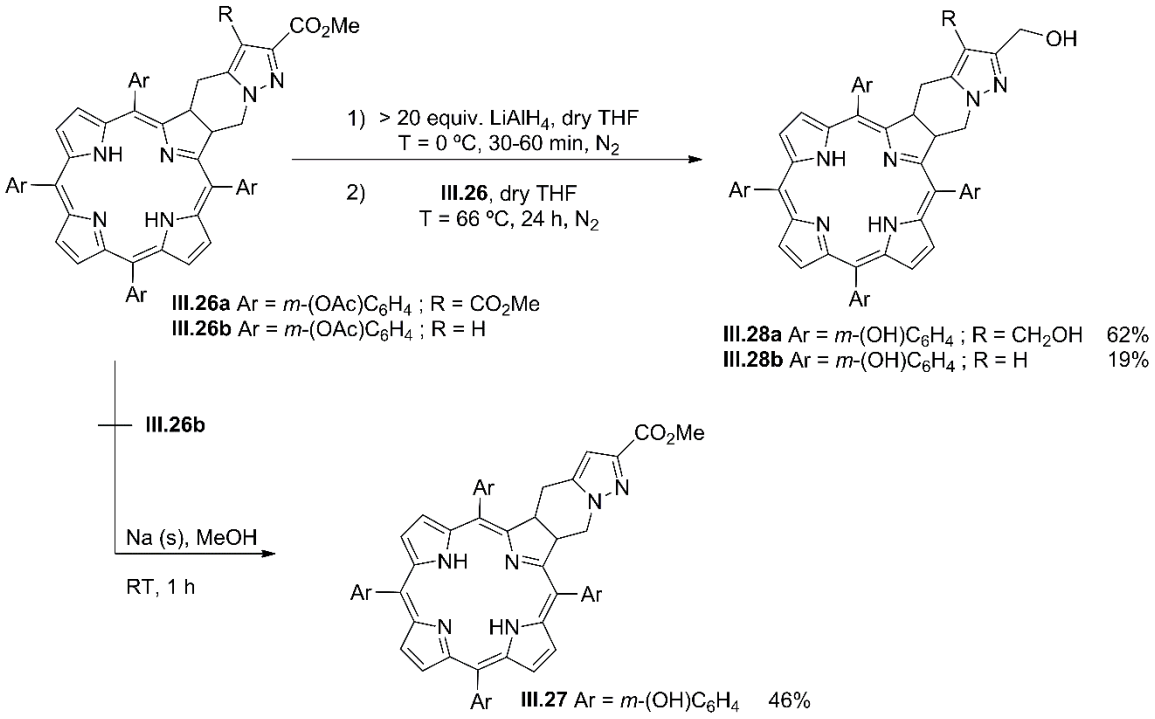

Scheme III-8. Derivatization of chlorins III.26 to obtain chlorins III.27, III.28a, and III.28b.

After these derivatization routes, besides the novel chlorin **III.26b**, we also attained compounds:

- **III.27**, which is a more hydrophilic chlorin with the same phenol groups found in the *meso* positions of temoporfin (**III.2**), while still maintaining the methyl ester group in the 4,5,6,7-tetrahydropyrazolo[1,5-*a*]pyridine-fused ring (^{1}H NMR spectrum in Figure III–4);
- **III.28a** and **III.28b** (^{1}H NMR spectra in Figure III–5 and Figure III–6, respectively), that present even more hydrophilic groups after the reduction of, not only the ones derived from the acetyl groups from the aromatic *meso*-substituents, but also the hydroxymethyl group derived from the methyl ester group.
    - The comparison of these two chlorins will allow for deeper insight into the influence of the disubstituted pyrazolo moiety vs. monosubstituted pyrazolo moiety in photodynamic activity (i.e., effects of amphiphilicity and size).

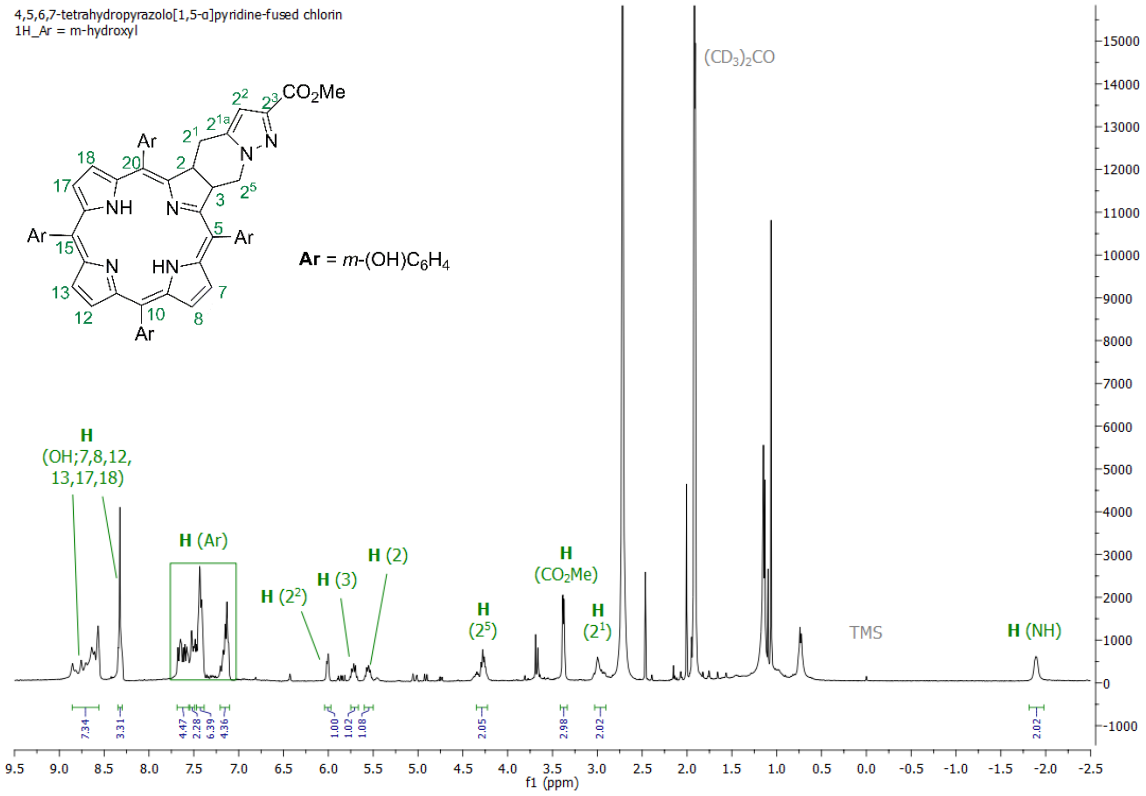

Figure III–4. ^{1}H NMR (400 MHz) spectrum of chlorin III.27 ($(CD_3)_2CO$).

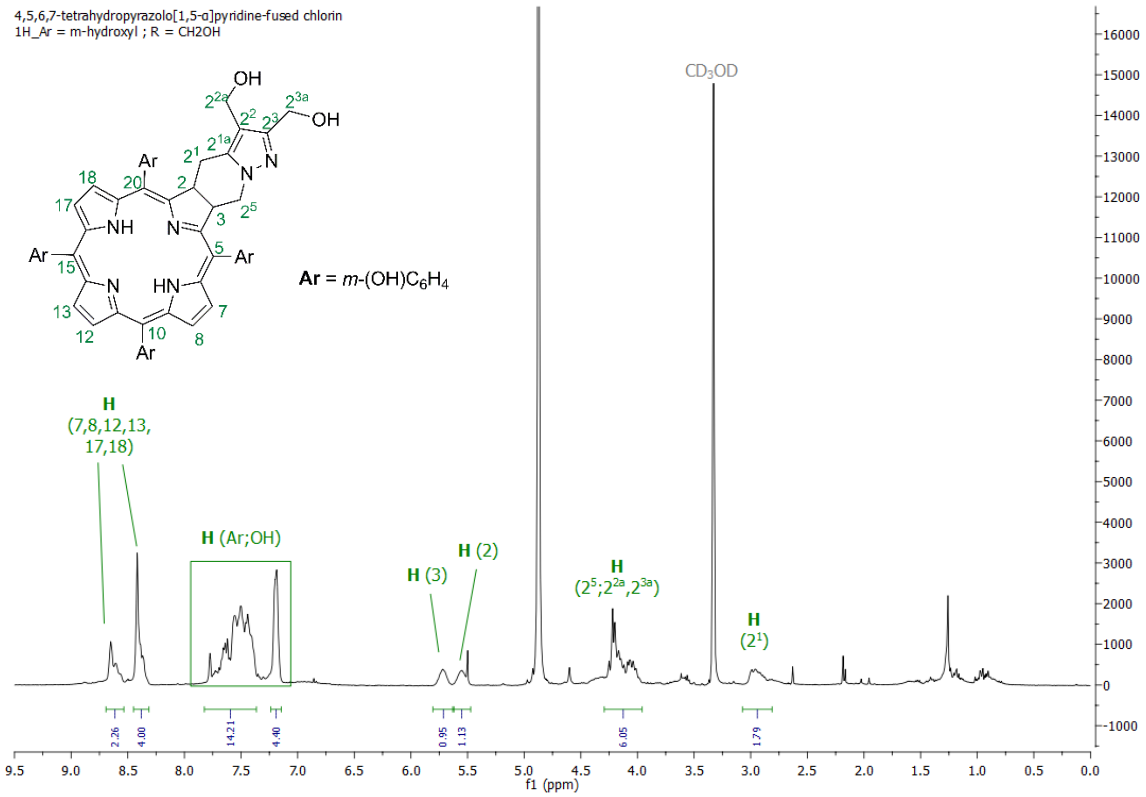

Figure III–5. ^{1}H NMR (400 MHz) spectrum of chlorin III.28a (CD_3OD).

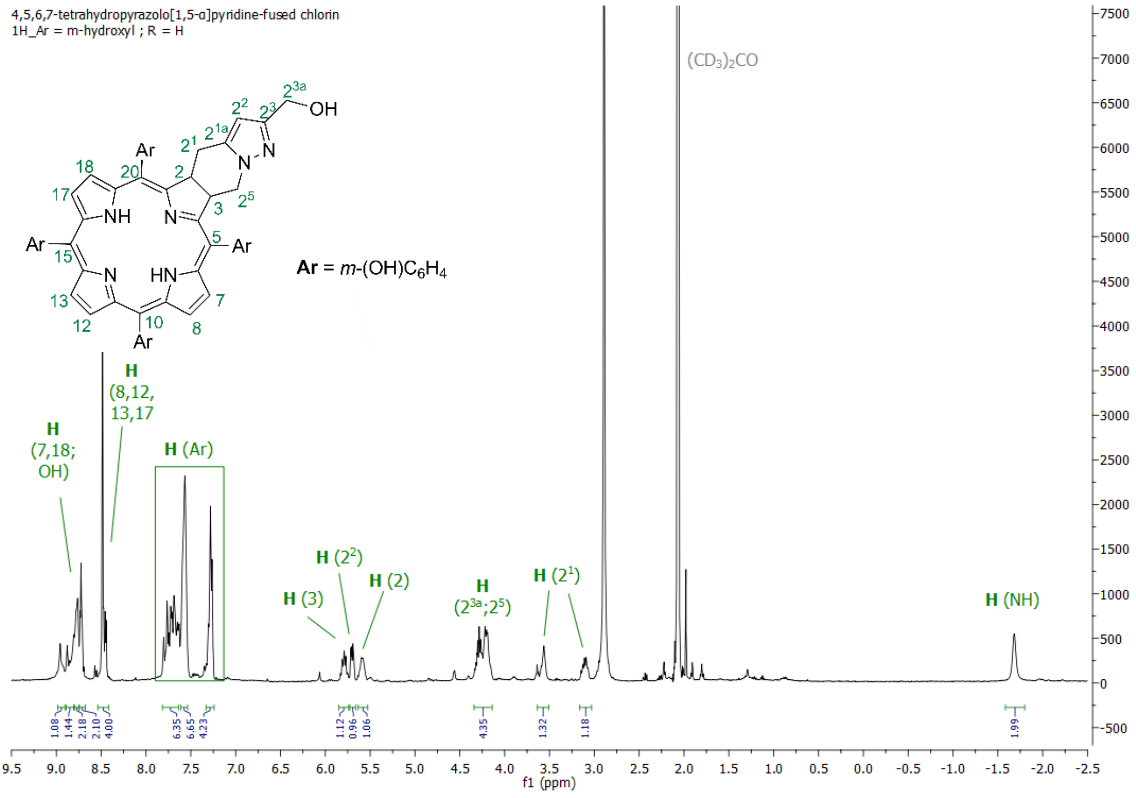

Figure III–6. ^{1}H NMR (400 MHz) spectrum of chlorin III.28b($(CD_3)_2CO$).

From this series of compounds, our goal was to obtain a new chlorin derived from the most hydrophilic monoester chlorin **III.28b** that could allow for a quick and efficient targeting strategy.

The term "click" chemistry was first mentioned by Kolb *et al.* [186] in 2001, describing a natural, spring-loaded approach to generate substances through heteroatom links using a set of modular "blocks". Among the most useful "click" reactions, his group regarded cycloaddition reactions as one of the most powerful in reflecting their ideals for "click" chemistry and even going as far as «(…) to regard the Huisgen dipolar cycloaddition of azides and alkynes as the "cream of the crop".» [186,187]. Accordingly, research on these types of cycloadditions has been one of the focal points of "click" chemistry [188,189].

By replacing the terminal alcohol group in the pyrazolo ring of chlorin **III.28b** with an azide group, obtaining a "clickable" PS, we could aim the development of targeting strategies for third-generation PS. Scheme III-9 illustrates the protocol used to attain the "clickable" azide derivative. Chlorin **III.28b** was submitted to an Appel reaction [190] with excess PPh_3 and CBr_4 as the halide source, in DMF, and left to react. This produces an alkyl halide (and PPh_3 oxide) that could then undergo a substitution reaction with excess NaN_3.

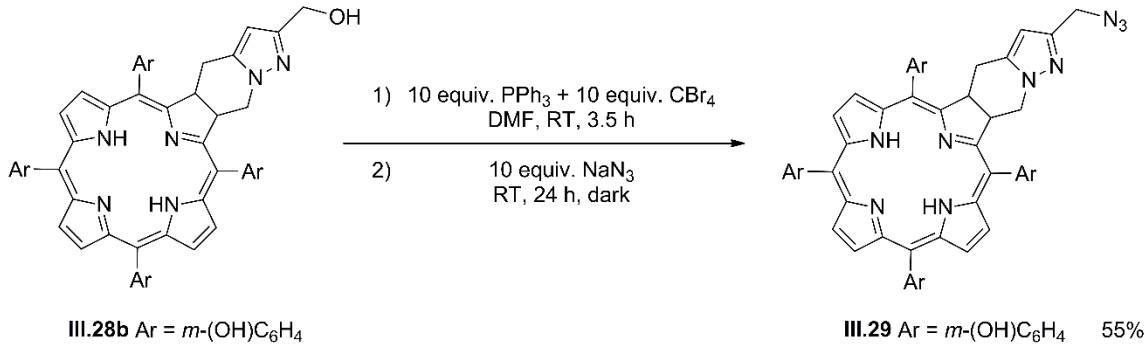

Scheme III-9. Synthesis of chlorin III.29.

After isolating chlorin **III.29** in a moderate yield of 55%, the presence of the azide group was confirmed through Fourier-transformed infrared (FTIR) spectroscopy – by the presence of a strong band ca. 2100 nm^{-1}, as seen in Figure III–7 – and supported by the ^{1}H NMR spectrum (Figure III–8).

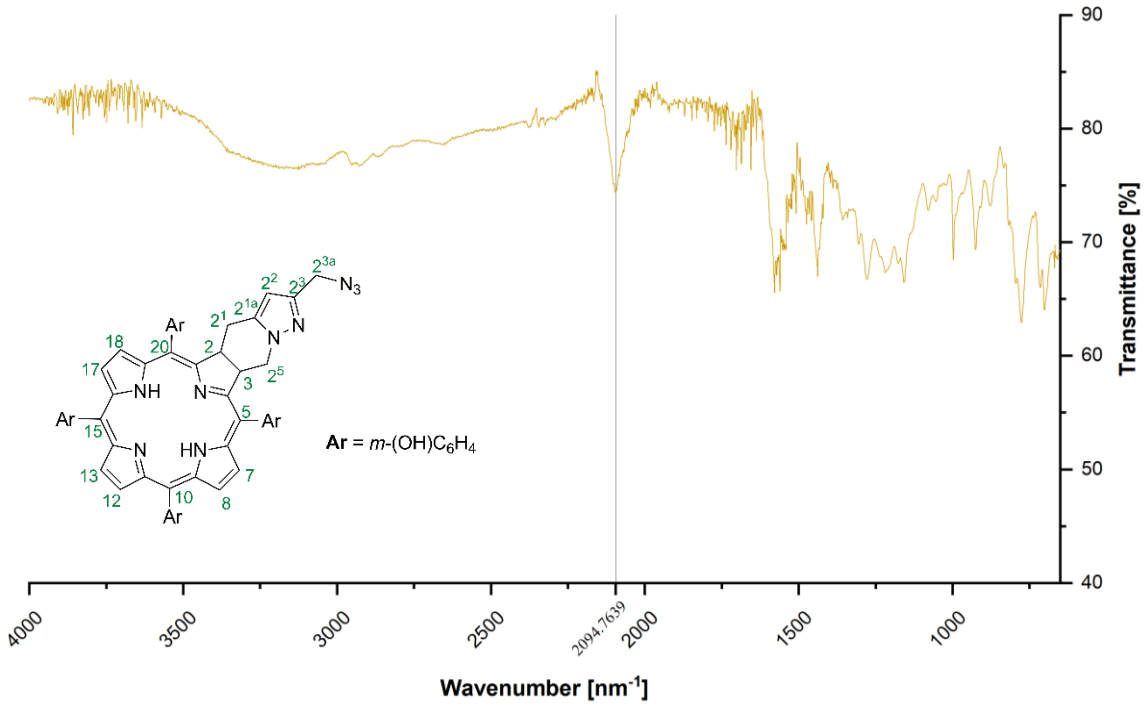

Figure III–7. Expansion of FTIR analysis for chlorin III.29.

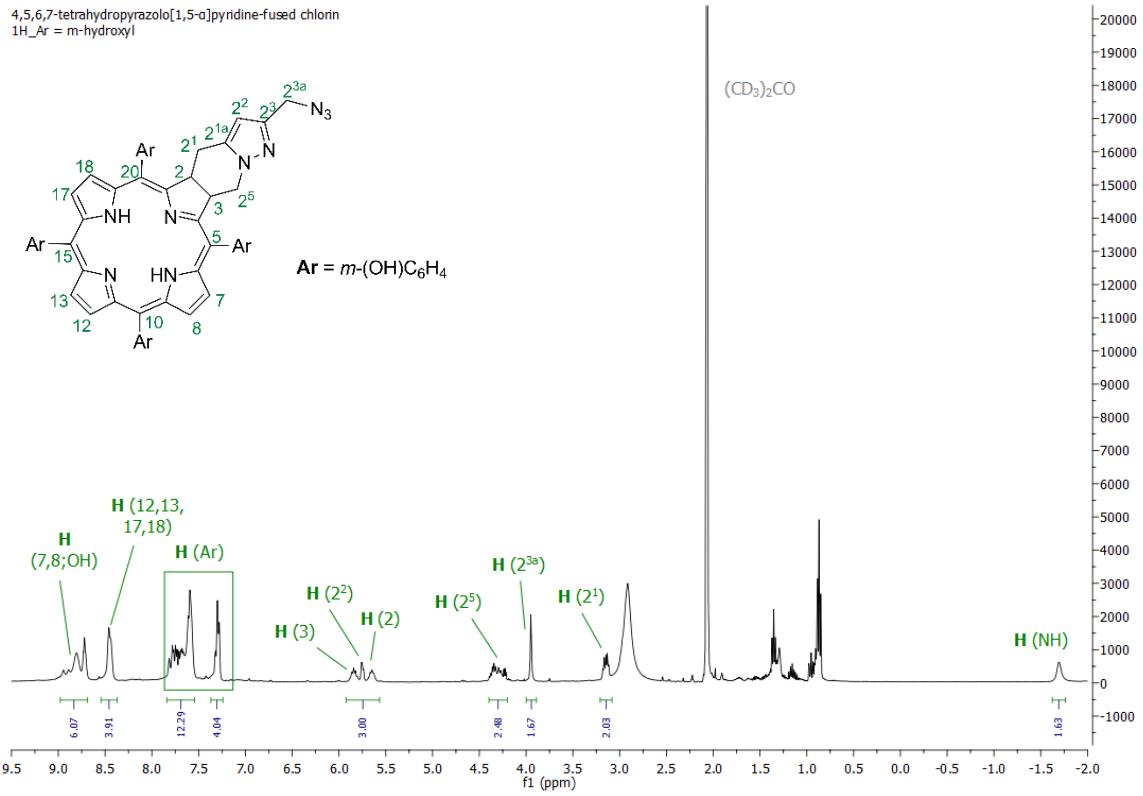

Figure III–8. ^{1}H NMR (400 MHz) spectrum of chlorin III.29 ($(CD_3)_2CO$).

An UV-visible absorption spectrum was run after each chlorin derivatization to confirm the presence of chlorin (local maximum ca. 650 nm) and possible impurities.

5. Discussion

Using [8π+2π] cycloaddition reaction of diazafulvenium methides, a method developed by Pinho e Melo *et al*. [153–157] to obtain 4,5,6,7-tetrahydropyrazolo[1,5-*a*]pyridine-fused chlorins from *meso*-tetraaryl porphyrins, we successfully obtained novel PS for further research. We aimed to use monosubstituted 2,2-dioxo-1*H*,3*H*-pyrazolo[1,5-*c*][1,3]thiazoles as precursors of the 1,7-dipoles to avoid competitive reactions in further derivatization of the novel chlorins, exploring a different scope of the chlorins described previously [49,50,153–157] which focused on disubstituted thiazoles.

Consequently, we synthetised the methyl 2,2-dioxo-1*H*,3*H*-pirazolo[1,5-*c*]thiazole-7-carboxylate (**III.24**) [185], for the development of chlorins mono-functionalised at the pyrazole moiety, and dimethyl 2,2-dioxo-1*H*,3*H*-pirazolo[1,5-*c*]thiazole-6,7-dicarboxylate **III.11** [185] to obtain the

corresponding difunctionalised for comparison of their phototoxicity. The lower yield with which the **III.24** precursor (**III.23b**) was obtained, compared to the **III.11** precursor (**III.23a**), was likely to happen if we analyse the structure of the dipolarophiles used, in particular the presence of just one electron-withdrawing group, instead of two (that increased the reactivity of the dipolarophile). The difference in yields of the regioisomers 1*H*,3*H*-pyrazolo[1,5-*c*][1,3]thiazoles **III.23b** (25%) and **III.23c** (8%) can be explained by the frontier molecular orbital theory and how the more efficient orbital overlap is the one in which the atoms with orbital higher coefficients of the dipole and dipolarophiles interact with each other.

With the 2,2-dioxo-1*H*,3*H*-pyrazolo[1,5-*c*][1,3]thiazoles ready, the next step was the synthesis of the novel chlorins, which were obtained in low yields. This was the cost of the choice to develop the synthetic approach relying on conventional heating – since diazafulvenium methide works in both conventional heat and microwave approaches [153] – in favour of being able to scale-up the synthetic process easily since several derivatizations were planned to obtaining the target chlorins. Another adaptation of the protocols described by Pinho e Melo *et al.* [154] when performing the [8π+2π] cycloaddition reaction with monoester 1*H*,3*H*-pyrazolo[1,5-*c*][1,3]thiazoles **III.24** was the use of 1:1 stoichiometric ratio (thiazole/porphyrin), instead of the 1:2 used when involving diester 1*H*,3*H*-pyrazolo[1,5-*c*][1,3]thiazoles **III.11**, as **III.25** is a less reactive dipole and does not pose the same risk of further reacting to produce bacteriochlorins.

As such, from the new chlorins synthetised, five were chosen (Figure III–9) for further studies and evaluation of their activities as PS.

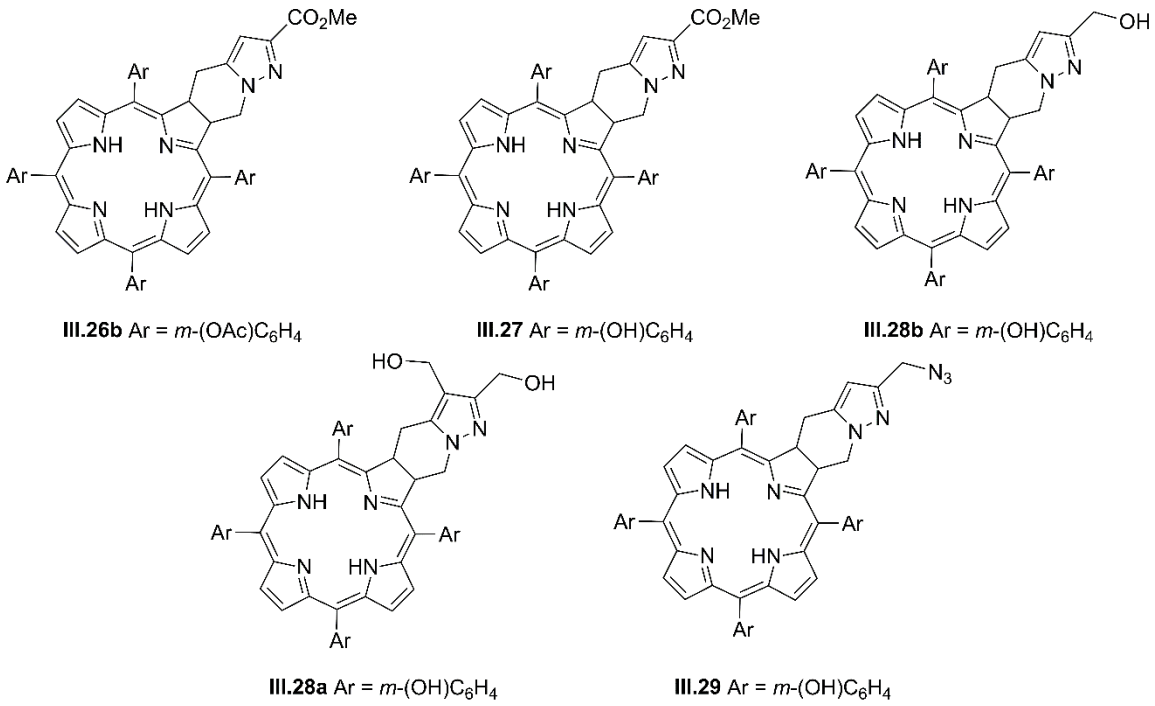

Figure III–9. Novel chlorins for phototoxicity studies.

Chlorins **III.26b**, **III.27**, and **III.28b** have different levels of hydrophilicity due to the presence of the hydroxyl groups, to which we expect observe a correlation between their hydrophilicity and an increased activity (as seen by the activity of temoporfin **III.2** [32,42,43]). The dihydroxymethyl chlorin **III.28a** and its monosubstituted derivative **III.28b** will be evaluated to ascertain if there is any advantage in synthesise disubstituted derivatives with this core. The methylazide chlorin **III.29**, which was one of our main goals of the synthetic component of this doctoral thesis: obtaining a strategy for "clickable" PS that can be used for development of third-generation PS.

6. Experimental

6.1. Instrumentation

6.1.1. Nuclear Magnetic Resonance

^{1}H and ^{13}C nuclear magnetic resonance (NMR) spectra were recorded on Bruker Avance III spectrometer operating at 400 MHz and 100 MHz, respectively.

Deuterated solvents were used as acquired and mentioned for each situation. The values of the chemical shifts are presented in ppm, respectively to the internal standard tetramethylsilane (TMS) or solvent residual peak, and the values of the coupling constants (*J*) are presented in Hz.

6.1.2. Infrared Spectroscopy

Infrared spectra were obtained from Agilent Technologies Cary 630 FTIR spectrometer, using the attenuated total reflectance (ATR) method.

6.1.3. Mass Spectroscopy

The mass spectrums were obtained from a mass spectrophotometer Bruker FTMS APEXIII with electrospray ionization (ESI).

6.1.4. UV-visible Spectrophotometer

Absorption spectra were recorded in a UV-visible Recording Spectrophotometer (Shimadzu UV-2100). The samples were dissolved in the indicated solvent and measured in quartz cuvettes with an optical path of 1 cm.

6.2. Materials

6.2.1. Reagents

All reagents were purchased from Sigma-Aldrich, Merck, or Fluka, and used directly without further purification procedures.

6.2.2. Solvents

All the solvents used (except for 1,2,4-TCB, which was used directly, as acquired) were purified and, when needed, dried according to the methods described in the literature [191].

6.2.3. Others

TLC analyses were performed on Merck Silica gel 60 F254 plates. Column chromatography was performed with silica gel 60 (0.040-0.063 mm) as the stationary phase.

6.3. Methods

6.3.1. *m*-Acetoxybenzaldehyde III.16 [192]

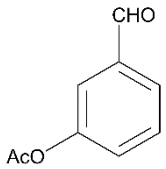

Acetic anhydride (2.4 equiv.; 11.1 mL, 117.52 mmol) was added dropwise with stirring, at room temperature, to a solution of *m*-hydroxylbenzaldehyde (**III.15**; 6.01 g, 49.20 mmol) and a catalytic amount of DMAP (20 mg; 0.164 mmol) in TEA (7.5 mL), and the reaction mixture was left for 24 hours. Then, ethyl acetate (200 mL) was added, and the solution washed with water (100 mL) followed by a saturated aqueous solution of $NaHCO_3$ (4 x 100 mL). The organic layer was retrieved, dried over anhydrous Na_2SO_4 and the solvent removed by evaporation under reduced pressure. The product *m*-acetoxybenzaldehyde (**III.16**) was obtained as an orange oil in 98% yield (7.91 g; 48.22 mmol).

^{1}H NMR (400 MHz, $CDCl_3$): δ = 9.99 (s, 1H, CHO), 7.77-7.71 (m, 1H, Ar), 7.64-7.59 (m, 1H, Ar), 7.54-7.36 (m, 2H, Ar), 2.32 (s, 3H, CH_3) ppm.

6.3.2. 5,10,15,20-Tetrakis(*m*-acetoxyphenyl)porphyrin III.17 [33]

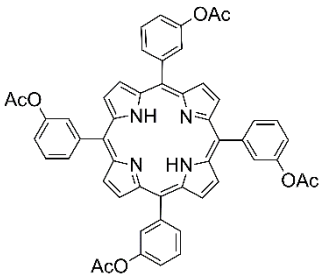

The synthesis of the *meso*-tetraarylporphyrin **III.17** was performed based on the Adler-Longo's method for the porphyrin synthesis [181,182]. A solution of *m*-acetoxybenzaldehyde (**III.16**; 50.40 mmol) in glacial acetic acid (120 mL) was brought to reflux and after 10 minutes stirring, pyrrole (1 equiv.; 3.5 mL, 50.40 mmol) was slowly added. The reaction mixture was kept stirring for 90 minutes, afterwards was left to cool at room temperature. The acetic acid was evaporated under reduced pressure, and the product purified by silica gel flash chromatography, using the mixture [DCM/AcOEt (9:1 v/v)] as eluent. The porphyrin **III.17** was obtained as a purple solid, after recrystallization from methanol, in 7% yield (747 mg, 0.88 mmol).

^{1}H NMR (400 MHz, $CDCl_3$): δ = 8.93 (s, 8H, pyrrolic β-H), 8.08 (d, *J* = 7.0 Hz, 4H, Ar), 7.96 (s, 4H, Ar), 7.75 (t, *J* = 8.0 Hz, 4H, Ar), 7.54 (dd, *J* = 8.0, 1.5 Hz, 4H, Ar), 2.39 (s, 12H, CH_3), -2.87 (s, 2H, NH) ppm.

6.3.3. 1,3-Thiazolidine-4-carboxylic acid III.19 [193]

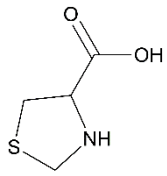

Compound **III.19** was prepared according to a procedure described in the literature [193]. A solution of formaldehyde (12.00 mL, 156.0 mmol; 37 wt% in water) in ethanol (90 mL) was added to a solution of *L*-cysteine **III.18** (14.78 g, 122.0 mmol) in 120 mL of water. The reaction mixture was left stirring for 24 h at room temperature. The precipitated white solid was filtered off, washed with cold diethyl ether, and dried under vacuum. The product was obtained in 84% yield (13.65 g, 102.50 mmol).

^{1}H NMR (400 MHz, $(CD_3)_2SO$): δ = 4.21 (d, *J* = 8.9 Hz, 1H, CH_2), 4.02 (d, *J* = 8.9, 1H, CH_2), 3.83 (t, *J* = 6.7 Hz, 1H, CH), 3.07 (dd,1 H *J* = 10.0, 6.7 Hz, CH_2), 2.81 (dd, *J* = 10.0, 6.7 Hz, 1H, CH_2) ppm.

6.3.4. *N*-Nitroso-thiazolidine-4-carboxylic acid III.20 [184]

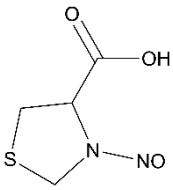

Compound **III.20** was prepared according to a procedure described in the literature [184]. To a suspension of 1,3-thiazolidine-4-carboxylic acid (**III.19**; 13.28 g, 99.72 mmol) in water (60 mL) was slowly added concentrated hydrochloric acid until achieving a complete dissolution. An aqueous solution of $NaNO_2$ (10.45 g, 149.60 mmol; 1.5 equiv.) was added dropwise and the reaction mixture stirred for 12 h at room temperature. A few more drops of concentrated HCl were added to ensure the acidic medium, and then the reaction mixture extracted with AcOEt (3 x 100 mL). The combined organic extracts were dried over anhydrous Na_2SO_4, and the solvent removed under reduced pressure. A yellow solid was obtained in 78% yield (12.61 g, 77.78 mmol). A mixture of two rotamers was observed in the ^{1} H NMR (ratio ≈ 60/40).

^{1}H NMR (400 MHz, $(CD_3)_2SO$): (major isomer) δ = 5.95 (d, *J* = 6.0 Hz, 1H), 4.73 (d, *J* = 12.2 Hz, 1H), 4.48 (d, *J* = 12.2 Hz, 1H), 3.56-3.47 (m, 1H), 3.41-3.38 (m, 1H) ppm. (minor isomer) δ = 5.70 (d, *J* = 10.5 Hz, 1H), 5.27 (d, *J* = 10.5 Hz, 1H), 4.82 (t, *J* = 7.0 Hz, 1H), 3.56-3.47 (m, 1H), 3.25-3.20 (m, 1H) ppm.

6.3.5. 4*H*,6*H*-Thiazolo[3,4-*c*][1,2,3]oxadiazole-7-io-3-olate III.21 [184]

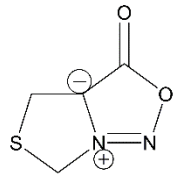

Compound **III.21** was prepared according to a procedure described in the literature [184]. TFAA (10.8 mL, 77.78 mmol; 1 equiv.) was added dropwise to a suspension of *N*-nitroso-thiazolidine-4-carboxylic acid (**III.20**; 12.61 g, 77.78 mmol) in diethyl ether (750 mL), cooled in an ice bath, and the reaction mixture stirred for 6 h. The ice bath was removed, and the mixture stirred for more 24 h at room temperature. It was then extracted with AcOEt (3 x 100 mL) and washed with a saturated aqueous solution of $NaHCO_3$ (2 x 100 mL). The organic layer was dried over anhydrous Na_2SO_4 and the solvent evaporated under reduced pressure. The product was obtained as a yellow solid in 76% yield (8.52 g, 59.11 mmol).

^{1}H NMR (400 MHz, $(CD_3)_2SO$): δ = 5.41 (s, 2H, CH_2), 4.03 (s, 2H, CH_2) ppm.

6.3.6. General procedure for the synthesis of 1*H*,3*H*-pyrazolo[1,5-*c*][1,3]thiazoles III.23

The thiazoles **III.23a-c** were prepared adapting procedures described in the literature [184,185]. A mixture of 4*H*,6*H*-Thiazolo[3,4-*c*][1,2,3]oxadiazole-7-io-3-olate (**III.21**) and the appropriate dipolarophile (1.6 equiv.) in xylene (20 mL) was refluxed, under N_2, for 4 h. After cooling to room temperature, solvent was removed under reduced pressure and the products purified by silica gel flash chromatography using the mixture [AcOEt/hexane (1:2 v/v)] as eluent.

6.3.6.1. Dimethyl 1*H*,3*H*-pirazolo[1,5-*c*]thiazole-6,7-dicarboxylate III.23a [184]

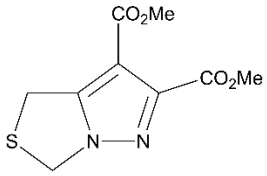

Compound **III.23a** was obtained as a white solid in 56% yield (1.89 g, 7.81 mmol) following the general procedure, from **III.21** (2.01 g, 13.94 mmol) and DMAD (2.9 mL, 22.30 mmol).

^{1}H NMR (400 MHz, $(CD_3)_2SO$): δ = 5.24 (s, 2H, CH_2), 4.30 (s, 2H, CH_2), 3.95 (s, 3H, Me), 3.85 (s, 3H, Me) ppm.

6.3.6.2. 1*H*,3*H*-Pirazolo[1,5-*c*]thiazole-7-methyl carboxylate III.23b and 1*H*,3*H*-Pirazolo[1,5-*c*]thiazole-6-methyl carboxylate III.23c [185]

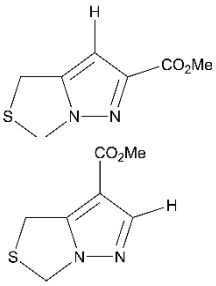

Compounds **III.23b** and **III.23c** were obtained as white solids in 25% (642 mg, 3.48 mmol) and 8% yield (205 mg, 1.11 mmol), respectively, following the general procedure from **III.21** (2.01 g, 13.94 mmol) and methyl propiolate (2.0 mL, 22.30 mmol).

III.23b

^{1}H NMR (400 MHz, $CDCl_3$): δ = 3.81 (s, 3H, Me), 4.26 (br s, 2H, CH_2), 5.19 (br s, 2H, CH_2), 7.95 (s, 1H, CH) ppm [185].

III.23c

^{1}H NMR (400 MHz, $CDCl_3$): δ = 3.89 (s, 3H, Me), 4.09 (br s, 2H, CH_2), 5.20 (br s, 2H, CH_2), 6.57 (br s, 1H, CH) ppm [185].

6.3.7. General procedure for the synthesis of 2,2-dioxo-1*H*,3*H*-pyrazolo[1,5-*c*][1,3]thiazoles III.11 and III.24

The 2,2-dioxo-1*H*,3*H*-pyrazolo[1,5-*c*][1,3]thiazoles **III.11** and **III.24** were prepared adapting procedures described in the literature [184,185]. To a solution of the appropriate 1*H*,3*H*-pyrazolo[1,5-*c*]thiazole **III.23** in DCM (70 mL) at 0 °C, MPCBA (77%; 4 equiv.) was added portion wise with stirring over a period of 1 h. Then, the reaction mixture was left warm to room temperature and stirred for 3 h. The mixture was washed with $NaHSO_3$ (10%; 1 x 100 mL) and a saturated aqueous solution of $NaHCO_3$ (3 x 100 mL). The organic layer was dried over anhydrous Na_2SO_4 and the solvent evaporated under reduced pressure. The products were purified by silica gel flash chromatography.

6.3.7.1. Dimethyl 2,2-dioxo-1*H*,3*H*-pirazolo[1,5-*c*]thiazole-6,7-dicarboxylate III.11 [184]

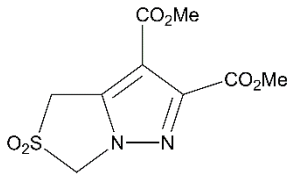

Compound **III.11** was obtained in 74% yield (1.10 g, 4.00 mmol), after chromatography using the mixture [AcOEt/hexane (1:1 v/v)] as eluent, following the general procedure from **III.23a** (1.31 g, 5.40 mmol).

^{1}H NMR (400 MHz, $CDCl_3$): δ = 5.24 (s, 2H, CH_2), 4.70 (s, 2H, CH_2), 3.99 (s, 3H, Me), 3.89 (s, 3H, Me) ppm.

6.3.7.2. Methyl 2,2-dioxo-1*H*,3*H*-pirazolo[1,5-*c*]thiazole-7-carboxylate III.24 [185]

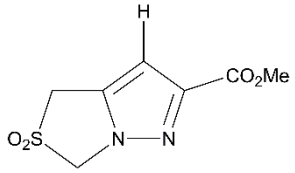

Compound **III.24** was obtained in 54% yield (630 mg, 2.91 mmol), after chromatography using the mixture [AcOEt/hexane (1:2 v/v)] as eluent, following the general procedure from **III.23b** (996 mg, 5.40 mmol).

^{1}H NMR (400 MHz, $CDCl_3$): δ = 6.87 (s, 1H, CH), 5.26 (s, 2H, CH_2), 4.52 (d, *J* = 0.8 Hz, 2H, CH_2), 3.96 (s, 3H, Me) ppm.

6.3.8. General procedure for the synthesis of 4,5,6,7-tetrahydropyrazolo[1,5-*a*]pyridine-fused chlorins III.26

Chlorins **III.26** were prepared adapting procedures described in the literature for other derivatives [153–155,157]. A solution of 5,10,15,20-tetrakis(3-acetoxyphenyl)porphyrin (**III.17**; 600 mg, 0.71 mmol) and the appropriate 2,2-dioxo-1*H*,3*H*-pyrazolo[1,5-*c*][1,3]thiazole **III.11** or **III.24** (1 equiv.) in 1,2,4-trichlorobenzene (12 mL) was refluxed (T = 250 °C) for 3 h, under inert atmosphere of N_2. After cooling to room temperature, few drops of triethylamine were added, and crude product purified by silica gel flash chromatography [gradient elution with AcOEt (0-15%) in DCM].

6.3.8.1. Chlorin III.26a

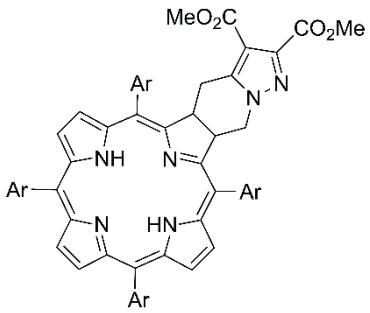

Following the general procedure, chlorin **III.26a** was obtained as a purple solid in a 15% yield (71.8 mg, recrystallised from hexane), using 2,2-dioxo-1*H*,3*H*-pyrazolo[1,5-*c*][1,3]thiazole **III.11** (1 equiv.; 124.2 mg, 0.453 mmol), and 58% of the starting porphyrin was recovered.

A set of NMR peaks (e.g.: m, 3H, CO_2Me) reveal the presence of a mixture of chlorin rotamers.

^{1}H NMR (400 MHz, $CDCl_3$): δ = 8.75-8.71 (m, 2H, β-H pyrrole), 8.53 (s, 2H, β-H pyrrole), 8.47 (d, *J* = 4.7 Hz, 1H, β-H pyrrole), 8.44 (d, *J* = 4.7 Hz, 1H, β-H pyrrole), 8.41-8.39 (m, 1H, β-H pyrrole), 8.17-8.13 (m, 1H, Ar), 8.098.03 (m, 2H, Ar), 7.97-7.83 (m, 5H, Ar), 7.78-7.70 (m, 4H, Ar), 7.53-7.51 (m, 1H, Ar), 5.86-5.76 (m, 1H, reduced β-H pyrrole), 5.61-5.48 (m, 1H, reduced β-H pyrrole), 4.50-4.37 (m, 1H, CH_2 ring), 4.17-4.07 (m, 1H, CH_2 ring), 3.85-3.74 (m, 6H, CO_2Me), 3.81-3.47 (m, 1H, reduced β-H pyrrole), 2.96-2.79 (m, 1H, reduced β-H pyrrole), 2.46-2.36 (m, 12H, OAc), -1.72 (s, 2H, NH) ppm.

^{13}C NMR (100 MHz, CDCl3): δ = 169.5, 169.4, 169.3, 164.8, 164.6, 164.3, 162.5, 162.50, 162.3, 162.3, 162.2, 161.9, 153.1, 153.0, 152.9, 152.8, 150.7, 150.3, 150.1, 149.3, 143.5, 143.4, 143.3, 143.2, 142.9, 142.8, 142.7, 142.6, 142.5, 142.3, 142.2, 142.1, 140.9, 140.9, 140.8, 140.6, 135.5, 135.3, 132.6, 132.0, 131.5, 129.7, 129.6, 129.5, 129.3, 129.2, 128.5, 128.4, 128.3, 128.2, 128.1, 127.7, 127.6, 127.3, 127.1, 125.7, 125.7, 124.6, 124.5, 122.4, 122.3, 122.2, 122.1, 122.0, 121.7, 121.5, 121.4, 121.2, 121.1, 121.0, 111.6, 111.5, 111.4, 110.8, 110.7, 52.4, 52.3, 51.5, 51.4, 49.3, 49.1, 47.9, 47.8, 47.7, 45.5, 45.3, 45.2, 45.0, 26.0, 25.9, 25.9, 25.8, 21.3, 21.2 ppm.

HRMS (ESI): m/z = 1057.3388, [$C_{61}H_{49}N_6O_{12}$ $(M+H)^+$, 1057.3403].

6.3.8.2. Chlorin III.26b

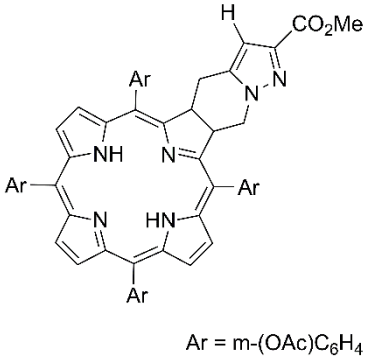

Following the general procedure, chlorin **III.26b** was obtained as a purple solid in a 9% yield (63.7 mg; 0.064 mmol; recrystallised from hexane), using 2,2-dioxo-1*H*,3*H*-pyrazolo[1,5-*c*][1,3]thiazole **III.24** (1 equiv.; 153.2 mg, 0.709 mmol), and 35% of the starting porphyrin (210 mg, 0.248 mmol) was recovered.

A set of NMR peaks (e.g.: m, 3H, CO_2Me) reveal the presence of a mixture of chlorin rotamers.

^1H NMR (400 MHz, $CDCl_3$): δ = 8.68-8.67 (m, 2H, β-H pyrrole), 8.49 (s, 2H, β-H pyrrole), 8.41-8.30 (m, 2H, β-H pyrrole), 8.13-7.98 (m, 2H, Ar), 7.98-7.77 (m, 6H, Ar), 7.77-7.59 (m, 4H, Ar), 7.55-7.43 (m, 4H, Ar), 6.41-6.25 (m, 1H, CH pyrazolo), 5.81-5.72 (m, 1H, reduced β-H pyrrole), 5.61-5.34 (m, 1H, reduced β-H pyrrole), 4.49-4.36 (m, 1H, CH_2 ring), 4.22-4.09 (m, 1H, CH_2 ring), 3.76-3.67 (m, 3H, CO_2Me), 3.27-2.98 (m, 1H, CH_2 ring), 2.74-2.65 (m, 1H, CH_2 ring), 2.45-2.32 (m, 12H, OAc), -1.77 (s, 2H, NH) ppm.

^{13}C NMR (100 MHz, $CDCl_3$) δ = 169.7, 169.6, 169.5, 169.3, 165.0, 164.7, 164.4, 163.3, 163.1, 162.9, 162.8, 150.7, 150.6, 150.3, 150.1, 149.3, 142.9, 142.7, 142.5, 142.4, 141.9, 141.8, 140.7, 140.6, 140.3, 140.2, 140.0, 139.9, 135.4 (β-H pyrrole), 135.3 (β-H pyrrole), 132.6, 132.4, 132.0 (Ar), 131.6 (Ar), 131.5, 129.6 (Ar), 129.5 (Ar), 129.2 (Ar), 128.6 (Ar), 128.4 (Ar), 128.3, 127.7 (β-H pyrrole), 127.6 (β-H pyrrole), 127.3 (Ar), 125.7 (Ar), 124.6, 124.5 (β-H pyrrole), 124.4 (β-H pyrrole), 122.3 (Ar), 122.2 (Ar), 122.1 (Ar), 121.7 (Ar), 121.6 (Ar), 121.5 (Ar), 121.4, 121.1 (Ar), 121.0, 111.4, 111.3 (CCO_2Me pyrazolo), 105.7, 105.5 (CH pyrazolo), 51.7 (CO_2Me), 49.7, 49.5, 47.9 (CH_2 ring), 47.8, 46.4 (reduced β-H pyrrole), 46.2 (reduced β-H pyrrole), 46.1, 26.1 (CH_2 ring), 26.0, 25.8, 25.1, 21.2 (OAc) ppm.

UV/Vis (DMSO): λ_{max} = 421, 518, 546, 596, 651 nm.

HRMS (ESI): m/z = 999.3309, [$C_{59}H_{47}N_6O_{10}$ $(M+H)^+$, 999.3348].

6.3.9. Chlorin III.27

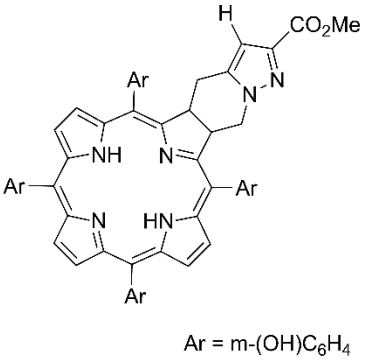

To a stirred solution of chlorin **III.26b** (28.7 mg, 0.03 mmol) in dry methanol (2 mL) was added, portion wise, a catalytic amount of sodium. The reaction mixture was kept stirring at room temperature for 1 h. Afterwards, the pH of the solution was adjusted to ≈ 5-6 by the carefully addition of glacial acetic acid. The solvent was then evaporated under reduced pressure and the crude product was purified by silica gel flash chromatography, using the mixture [DCM/AcOEt (85:15 v/v)] as eluent. Product was obtained in 46% yield as a crimson solid.

A set of NMR peaks (e.g.: m, 3H, CO_2Me) reveal the presence of a mixture of chlorin rotamers.

^{1}H NMR (400 MHz, $(CD_3)_2CO$): δ = 8.85-8.57 (m, 6H, overlapping β-H pyrrole and OH), 8.32-8.31 (m, 4H, β-H pyrrole), 7.68-7.41 (m, 12H, Ar), 7.20-7.11 (m, 4H, Ar), 6.02-6.00 (m, 1H, CH pyrazolo), 5.74-5.68 (m, 1H, reduced β-H pyrrole), 5.57-5.53 (m, 1H, reduced β-H pyrrole), 4.34-4.26 (m, 2H, CH_2 ring), 3.38-3.37 (m, 3H, CO_2Me), 3.0-2.93 (m, 2H, CH_2 ring), -1.89 (s, 2H, NH) ppm.

UV/Vis (DMSO): λ_{max} = 421, 519, 548, 596, 651 nm.

HRMS (ESI): m/z = 829.2752, [$C_{51}H_{37}N_6O_6$ $(M-H)^+$, 829.2769].

6.3.10. General procedure for the synthesis of hydroxymethyl chlorins III.28

The synthesis was adapted from a procedure from literature [155]. A solution of the appropriate chlorin **III.26** (0.03-0.10 mmol) in dry THF (3-5 mL) was added dropwise to a suspension of $LiAlH_4$ (24-30 equiv.) in dry THF (2-5 mL) at 0 ˚C. The reaction mixture was stirred for 60 min, under N_2, at this temperature and then 24 h at 66 ˚C. The reaction mixture was cooled with an ice bath and the excess of $LiAlH_4$ was quenched with AcOEt (2 mL), water (2 mL), and aqueous solution of HCl (0.1 M, 0.5 mL), left stirring for 20 min. Solvents were removed under reduced pressure, then the residue was dissolved with a mixture of [AcOET:MeOH (1:1 v/v)], and filtered through celite. The filtrate was dried with anhydrous Na_2SO_4 and the solvent evaporated off. The crude product was purified by silica gel flash chromatography.

6.3.10.1. Chlorin III.28a

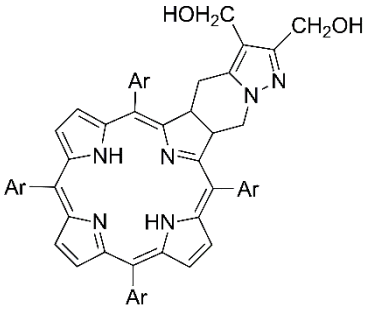

Obtained as green solid in 61% yield, after elution with [AcOEt/MeOH (9:1 v/v)], from chlorin **III.26a** (31.7 mg; 0.03 mmol) and $LiAlH_4$ (27.3 mg; 0.72 mmol; 24 equiv.), following the general procedure.

^{1}H NMR (400 MHz, CD_3OD): δ = 8.65-8.56 (m, 2H, β-H pyrrole), 8.42-8.37 (m, 4H, β-H pyrrole), 7.77-7.41 (m, 12H, Ar), 7.20-7.19 (m, 4H, Ar), 5.80-5.65 (m, 1H, reduced β-H pyrrole), 5.61-5.50 (m, 1H, reduced β-H pyrrole), 4.25-3.99 (m, 6H, overlapping CH_2 ring and CH_2OH), 2.99-2.89 (m, 2H, CH_2 ring) ppm.

^{13}C NMR (100 MHz, CD_3OD): δ = 165.2, 165.1, 158.9, 158.8, 158.2, 158.0, 157.1, 154.1, 154.0, 150.3, 144.3, 144.0, 142.0, 141.9, 141.8, 140.4, 136.4, 136.4, 136.3, 133.1, 130.8, 130.1, 129.7, 128.9, 128.8, 128.2, 127.9, 127.2, 127.1, 126.9, 125.4, 125.3, 125.2, 124.8, 124.1, 123.9, 123.8, 123.5, 122.7, 122.5, 120.6, 120.5, 116.2, 116.1, 115.9, 114.0, 113.9, 113.8, 57.1, 53.9, 47.2, 25.4 ppm.

UV/Vis (DMSO): λ_{max} = 423, 519, 548, 597, 651 nm.

HRMS (ESI): m/z = 833.3067, [$C_{51}H_{41}N_6O_6$ $(M+H)^+$, 833.3082].

6.3.10.2. Chlorin III.28b

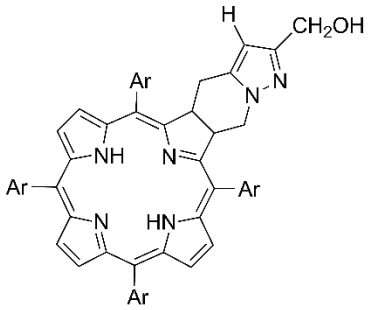

Ar = m-(OH)C_6H_4

Obtained as green solid in 19% yield, after elution with AcOEt, from chlorin **III.26b** (100.0 mg; 0.1 mmol) and $LiAlH_4$ (113.9 mg; 3.0 mmol; 30 equiv.), following the general procedure.

^{1}H NMR (400 MHz, $(CD_3)_2CO$): δ = 8.96-8.71 (m, 6H, overlapping β-H pyrrole and OH), 8.49 – 8.44 (m, 4H, β-H pyrrole), 7.80-7.57 (m, 12H, Ar), 7.30-7.26 (m, 4H, Ar), 5.81-5.77 (m, 1H, reduced β-H pyrrole), 5.70 (dd, *J* = 8.9, 3.8 Hz, 1H, CH pyrazolo), 5.63-5.52 (s, 1H, reduced β-H pyrrole), 4.32-4.20 (m, 4H, overlapping CH_2 ring and CH_2OH), 3.64-3.56 (m, 1H, CH_2 ring), 3.15-3.09 (m, 1H, CH_2 ring), -1.68 (s, 2H, NH_2) ppm.

^{13}C NMR (100 MHz, $(CD_3)_2CO$): δ = 156.9, 153.6, 153.5, 143.9, 143.8, 140.1, 132.9, 130.5, 128.7, 126.7, 126.5, 125.1, 123.5, 123.3, 122.3, 121.1, 120.4 115.8, 101.2, 58.9, 49.6, 49.1, 47.5, 26.8 ppm.

UV/Vis (DMSO): λ_{max} = 422, 517, 548, 596, 651 nm.

HRMS (ESI): m/z = 803.2964 [$C_{50}H_{39}N_6O_5$ $(M+H)^+$, 803.2976]

6.3.11. Chlorin III.29

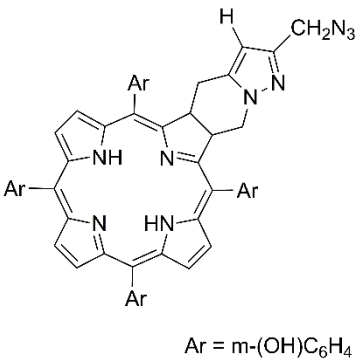

To a solution of chlorin **III.28b** (48.9 mg, 60.91 µmol) in DMF (2 mL) was carefully added PPh_3 (159.8 mg; 0.609 mmol; 10 equiv.;) and CBr_4 (202.0 mg; 0.609 mmol; 10 equiv.) (portion wise to prevent overheating), and the reaction mixture was stirred for 3.5 h. Then, NaN_3 (39.6 mg, 0.609 mmol; 10 equiv.) was added and the mixture kept stirring at room temperature for 24 h in the dark. The product was then extracted with AcOEt (50 mL), washed with brine (50 mL) and water (50 mL). The organic layer was then dried with anhydrous Na_2SO_4 and the solvent removed under reduced pressure. The crude product was purified by silica gel flash chromatography [AcOEt as eluent]. Product was obtained as a dark purple solid in 55% yield (27.7 mg, 33.50 µmol).

^{1}H NMR (400 MHz, $(CD_3)_2CO$): δ = 8.94-8.72 (m, 6H, overlapping β-H pyrrole and OH), 8.46 (s, 4H, β-H pyrrole), 7.82-7.59 (m, 12H, Ar), 7.32-7.28 (m, 4H, Ar), 5.86-5.82 (m, 1H, reduced β-H pyrrole), 5.76-5.74 (s, 1H, CH pyrazolo), 5.67-5.65 (m, 1H, reduced β-H pyrrole), 4.36-4.23 (m, 2H, CH_2 ring), 3.95 (s, 2H, CH_2N_3), 3.16-3.13 (m, 1H, CH_2 ring), -1.70 (s, 2H, NH_2) ppm.

^{13}C NMR (100 MHz, $(CD_3)_2CO$): δ = 158.5, 157.7, 157.0, 145.8, 143.7, 141.9, 140.8, 136.2, 130.6, 130.4, 129.8, 129.6, 129.5, 128.7, 127.7, 126.8, 125.3, 125.2, 124.5, 123.3, 122.4, 120.4, 116.3, 116.2, 116.0, 115.9, 102.3, 68.3, 49.5, 48.3, 47.3, 46.5, 26.7 ppm.

HRMS (ESI): m/z = 828.3026 [$C_{50}H_{38}N_9O_4$ $(M+H)^+$, 828.3041].

UV/Visible (DMSO): λ_{max} = 421, 517, 548, 597, 651 nm.

FTIR (ATR): $\tilde{\nu}$ = 3126, 2931, 2659, 2506, 2378, 2095, 1774, 1702, 1655, 1579, 1439, 1357, 1278, 1220, 1157, 1079, 997, 925, 776, 702 cm^{-1}.

Chapter IV:

Development of a novel conjugate for targeting: *in silico* analysis and synthesis

Prediction is very difficult, especially about the future.

Niels Bohr

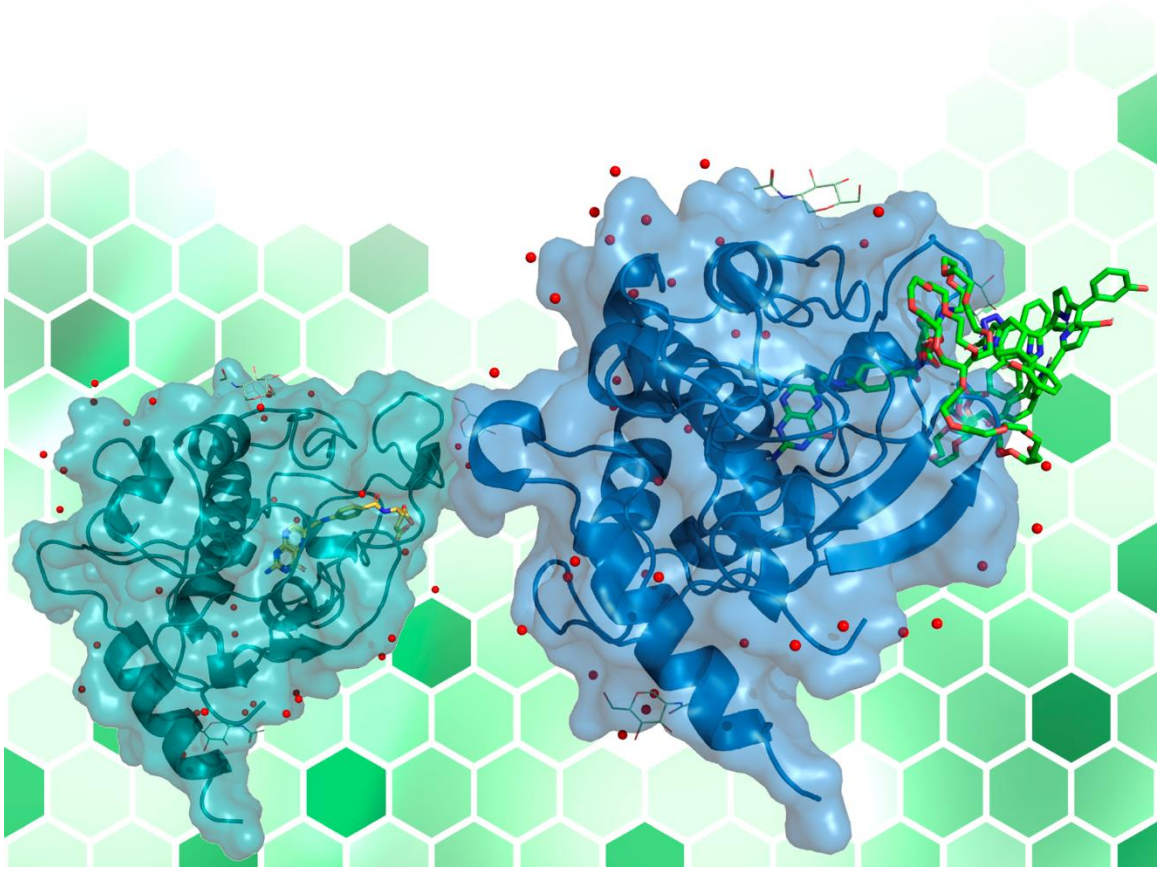

1. Introduction

As mentioned in Chapter I, the folate receptor (FR) is one of the most studied receptors for targeted therapy approaches by improving selectivity and/or uptake of anti-cancer therapeutics. In particular, the isoform FRα, with high affinity for folic acid (FA), is overexpressed in several cancer cells, while existing in negligible levels in normal cells. In fact, there is correlation between FRα expression levels and the expected aggressiveness of the cancer [1,75,92,93,194].

The chemical structure of FA, represented in Figure IV–1, is composed by three main blocks: pterin, *p*-aminobenzoic acid, and glutamic acid [75,144]. The pterin head of this vitamin is the main block ensuring FA binding specificity, by forming several molecular interactions, deep in the FRα binding site. In fact, the lack of the exocyclic oxygen of the pterin ring in folate derivates, like methotrexate and aminopterin, leads to reduce affinity for FRα [75,194,195]. When complexed with the receptor, both carboxylates of the glutamic acid fragment extend from the positively-charged entrance of the binding site, which is why these groups can be used for conjugation approaches. It is important to highlight that the α-carboxylate participates in four out of the six hydrogen bonds [194,195] that mediate the FA-receptor interactions, justifying the rational for choosing the γ-carboxylate in most functionalisation strategies, with the least impact on affinity for FRα [75,194,195].

As a highly-selective, non-immunogenic small molecule that is easily cleared from FRα-negative tissues [75], FA is an attractive moiety to use in targeted therapy. Despite contradictory reports on its water solubility [75,196] [144], more in depth studies have shown the influence of pH and temperature in FA solubility and stability [197,198]. FA instability to light, high temperatures, or solution conditions [198,199] is a known issue and should be taken into account, to prevent degradation of the molecule which can lead to loss of activity.

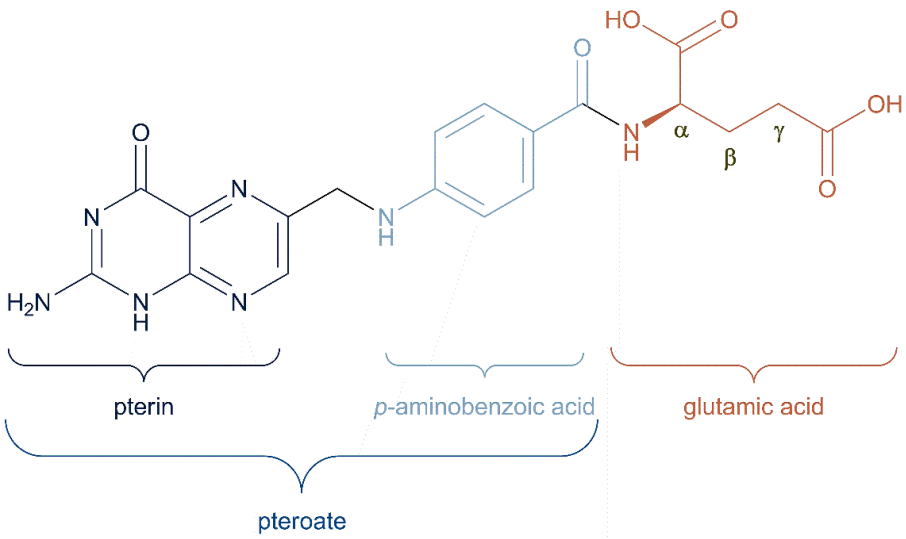

Figure IV–1. Chemical structure of FA and its main structural blocks.

Nonetheless, cell internalisation of FA through endocytosis of FA through endocytosis of the FRα is not extended to the full conjugate if the cargo is too hydrophobic to be internalised [65,75,86,200–202]. As such, an hydrophilic linker (usually polyethylene glycol, PEG) is usually used as spacer between the FA moiety and the compound to be internalised, but aliphatic chains, polysaccharides, and peptides are also used [75,144].

In photodynamic therapy (PDT), the lack of specificity of the photosensitiser (PS) for the target tissue is one of the main problems, leading to the most limiting side effect of this therapeutic approach: skin photosensitivity. The development of new targeted-PDT strategies, more than focusing on modulating the solubility of the PS, seek to increase the PS specificity for overexpressed receptors in the tumour tissue, through conjugation with moieties that will act as vectors to bind to those receptors [1].

The use of computer-aided drug discovery (CADD) methods allows for the simulation and/or prediction of binding of a ligand to a biological target by structure- or ligand-based strategies [1,203]. If the structure of a certain cancer target is readily available, structure-based techniques can predict potential molecular interactions between the target and a desired ligand and binding information from known ligands of the target may be explored to design new ligands. On the other hand, if there is no available information on the structure of the cancer target/receptor, new ligands can be designed using common substructures/physicochemical features from available ligands for that target. For instance, Hidayat *et al*. [204] used a structure-based approach to design a new ligand targeting the integrin $\alpha_v\beta_3$ receptor by: (1) creating pharmacophores from the known complexes of integrin $\alpha_v\beta_3$ receptor-peptidomimetic (RGD) to guide the design of the new ligand; (2) performing molecular docking to confirm the interactions of the new ligand with the integrin $\alpha_v\beta_3$ receptor; and (3) runing molecular dynamics simulations to predict the stability of the complex between the new

ligand and the integrin $\alpha_v\beta_3$ receptor. Although these studies indicated potentially good activity, this ligand was never validated with *in vitro* or *in vivo* studies [1,204]. Even so, it is an example that showcases the use of different CADD approaches to design and evaluate novel compounds as therapeutic drugs.

As our work focused on targeting the well documented FRα, data mining of the literature and the Protein Data Bank (PDB) repository [205,206] returned several three-dimensional structures, as expected. This meant that it was possible to use a structure-based strategy for an *in silico* evaluation of the FRα, and thus to derive knowledge on the pose prediction of the conjugate. Among the most popular and successful structure-based methods, molecular docking helps predicting the molecular interactions between a ligand and a target protein by exploring possible binding poses and then evaluating these poses through a scoring function (which can be physics-based, empirical, knowledge-based, or machine-learning-based) [207–209].

2. *In silico* evaluation of the three-dimensional structures of folate receptor

The first step to follow through with a structure-based strategy is to choose a structure that has the best quality, as inaccuracies in atomic coordinates will have a negative effect on the prediction of intermolecular contacts [210].

The full amino acid sequence of human FRα was found available at the UniProt knowledgebase [211,212] entry P15328, with additional information on the three-dimensional structures deposited in PDB [205,206] matching the sequence. From the PDB [205,206] repository, all entries of interest were downloaded (4KM6, 4KM7, 4KMX, 4LRH, and 5IZQ) and, using the software UCSF Chimera 1.14 [213,214], separated into single protein files (each chain of the PDB entry representing the monomeric FRα protein). Each of these structures was submitted to PROCHECK [215] obtaining the results shown in Table IV-1. For each PDB entry (from best to worst resolution), the protein structures were ordered by percentage of residues with favoured geometries (core regions of the Ramachandran plot [216]). The other columns allowed for a general evaluation of: (1) the "normality" of the structure (higher G-factors), (2) overall structural quality classification (classes 1 to 4, from best to worst) according to Morris *et al*. [217] for Φ-Ψ favoured regions, χ_1 dihedral angle standard deviation, and standard deviation of main-chain H-bond energy; and (3) the number of bad contacts (any pair of non-bonded atoms within a distance $\leq$ 2.6 Å).

Table IV-1. PROCHECK summary report for FRα structures (PDB).

PDB_ch.	Res (Å)	RAMACHANDRAN PLOT (%)				G-factor	MORRIS *ET AL.*				Bad contacts
		Core	Allowed	Generously allowed	Disallowed		φ-ψ	χ_1-sd	H_{bond}-sd	N	
4KM6	1.55	87.8	11.6	0.6	0.0	0.12	1	1	2	4	20
4KM7_a	1.80	88.8	11.2	0.0	0.0	0.11	1	1	2	4	37
4KM7_b	1.80	88.0	11.4	0.6	0.0	0.10	1	2	2	5	31
4KMX	2.20	87.4	12.1	0.6	0.0	0.17	1	1	2	4	12
4LRH_a	2.80	84.2	15.3	0.5	0.0	0.22	1	2	2	5	7
4LRH_h	2.80	82.9	16.0	1.1	0.0	0.21	1	2	2	5	7
4LRH_b	2.80	82.3	17.1	0.6	0.0	0.22	1	2	2	5	10
4LRH_c	2.80	82.2	17.8	0.0	0.0	0.23	1	1	2	4	6
4LRH_e	2.80	80.3	19.7	0.0	0.0	0.21	1	1	2	4	5
4LRH_d	2.80	79.7	19.8	0.5	0.0	0.21	1	2	2	5	7
4LRH_f	2.80	77.7	21.7	0.5	0.0	0.24	1	2	2	5	6
4LRH_g	2.80	77.5	22.0	0.5	0.0	0.24	1	2	2	5	7
5IZQ_h	3.60	86.1	13.9	0.0	0.0	0.03	1	2	2	5	0
5IZQ_c	3.60	84.8	15.2	0.0	0.0	0.09	1	2	2	5	0
5IZQ_b	3.60	84.4	15.0	0.6	0.0	0.04	1	2	2	5	2
5IZQ_a	3.60	82.5	17.5	0.0	0.0	0.05	1	2	2	5	0
5IZQ_d	3.60	82.3	17.2	0.5	0.0	0.09	1	2	2	5	0
5IZQ_e	3.60	82.0	18.0	0.0	0.0	0.06	1	2	3	6	2
5IZQ_g	3.60	80.2	19.8	0.0	0.0	0.08	1	2	2	5	1
5IZQ_f	3.60	79.9	19.6	0.5	0.0	0.11	1	2	2	5	0

Individual FRα structures available on PDB, ordered by resolution and percentage of residues in the core region of the Ramachandran Plot.

PDB_ch. identifies the PDB code and the chain on the respective PDB file.

N is the sum of "Morris *et al*." classes; for each class, classification varies between 1 (best) and 4 (worst), N varies between 3 and 12.

For each of the best chains, their respective homologous chains were downloaded from the repository of re-refined models PDB-REDO [210,218]. As the previous chains, these structures were submitted to PROCHECK obtaining the results summarised in Table IV-2. The same parameters were evaluated, in addition to the R-free value – which represents an unbiased measure of the quality of the model obtained from the crystallographic data (the lower the value, the best is the fit). Most structures showed an improved R-free value after the re-refinement obtained from PDB-REDO [210,218]. However, other parameters from PROCHECK seemed to "deteriorate", especially the G-factor, with the exception of chain A from entry 4LRH, where the PDB-REDO entry had a better evaluation of the structural quality throughout the table (i.e., improved R-free, higher percentage of residues in the core region of the Ramachandran plot, and improved Morris *et al*. classification), all other entries were kept as obtained from the original PDB entry.

The next step was analysing the original articles for each entry from the chosen repository. This text mining allowed the prompt exclusion of PDB structures 4KM6, 4KM7, and 4KMX deposited by Wibowo *et al*. [219], as they were *apo*-FRα structures, but they also represented trafficking states present in the endosome (acidic pH) after endocytosis. As for 4LRH [194] and 5IZQ [91], they were both *holo*-FRα structures complexed with FA and an antifolate, respectively. As our work uses a FA conjugate and the chain A from 4LRH had the best quality parameters out of both structures, we chose this structure for the *in silico* studies (Figure IV–2 and Supplementary Figure IV-1).

Figure IV–2.B shows the FA (yellow ligand) bound to FRα (teal protein) with the pteroate fragment of FA buried deep in the binding site and the glutamic acid fragment readily accessible to the solvent, justifying the conjugation strategy from the carboxylic groups of the glutamic acid fragment.

Table IV-2. PROCHECK summary report for FRα structures (PDB and PDB-REDO).

PDB_ch.	Res (Å)	DB	R-free	RAMACHANDRAN PLOT (%)				G-factor	MORRIS *ET AL.*				Bad contacts	Chosen DB
				Core	Allowed	Gen. allowed	Disall.		φ-ψ	χ_1-sd	H_{bond}-sd	N		
4KM6	1.55	PDB	0.200	87.8	11.6	0.6	0.0	0.12	1	1	2	4	20	✓
	*1.55**	REDO	0.187	87.8	11.6	0.6	0.0	-0.00	1	1	2	4	24	-
4KM7_a	1.80	PDB	0.269	88.8	11.2	0.0	0.0	0.11	1	1	2	4	37	✓
	*1.80**	REDO	0.282	88.8	10.7	0.6	0.0	-0.03	1	1	2	4	24	-
4KMX	2.20	PDB	0.206	87.4	12.1	0.6	0.0	0.17	1	1	2	4	12	✓
	*2.20**	REDO	0.201	87.4	12.1	0.6	0.0	0.03	1	1	2	4	21	-
4LRH_a	2.80	PDB	0.267	84.2	15.3	0.5	0.0	0.22	1	2	2	5	7	-
	*2.77**	REDO	0.222	87.4	11.5	0.5	0.5	0.05	1	1	2	4	8	✓
5IZQ_h	3.60	PDB	0.257	86.1	13.9	0.0	0.0	0.03	1	2	2	5	0	✓
	*3.56**	REDO	0.238	82.8	17.2	0.0	0.0	-0.19	1	2	2	5	3	-

PDB_ch. identifies the chain on the respective PDB entry. "DB" identifies the database of origin ("REDO" was shortened from "PDB-REDO" for simplicity).

Improved or worsened parameters in the refined structure (PDB-REDO) are coloured in green and red, respectively.

* Resolution of the PDB structure according to the evaluation done by PDB-REDO.

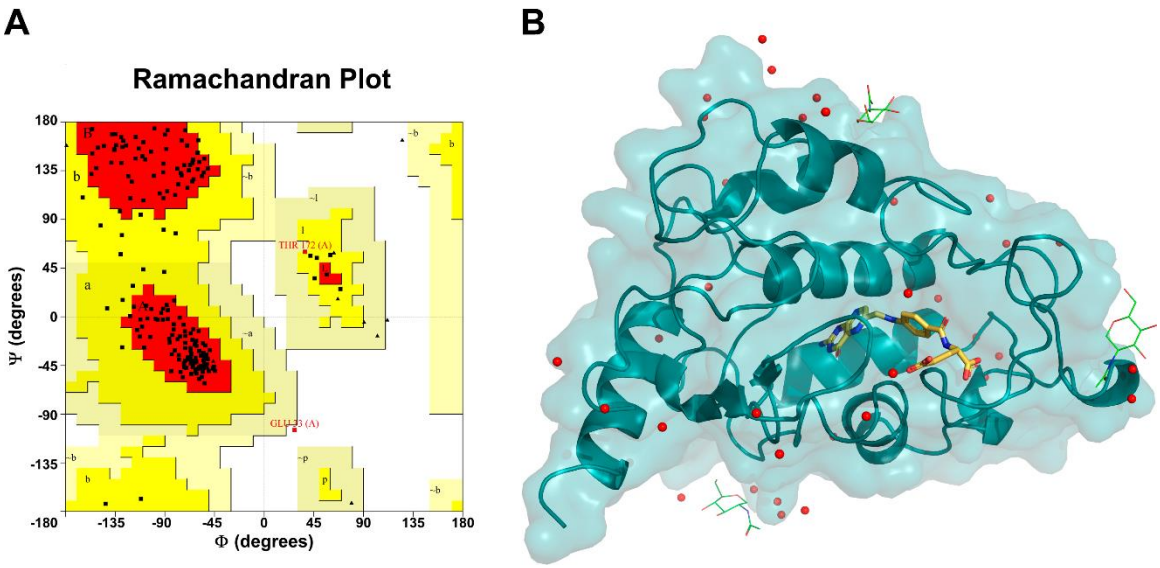

Figure IV–2. Three-dimensional structure of FRα used in docking studies (4LRH, chain A, from PDB-REDO). (A) Ramachandran plot: each black square represents a residue found in the core (red area) and allowed (bright yellow) areas; residues found in generously allowed (pale yellow) and disallowed (white) areas are flagged as red squares and labelled, e.g., Thr172 and Glu33, respectively. (B) Crystallographic *holo*-structure: the secondary structure and surface of FRα are coloured in teal, the complexed FA is coloured yellow, the water molecules are represented as red spheres, and the *N*-acetyl-*D*-glucosamine (NAG) molecules are represented as green wires.

Comparison of UniProt entry P15328 to the sequence of amino acids of the chosen 3D structure shows that the 4LRH entry only contains the sequence of residues in the range of 23-235, instead of the full sequence of 257 amino acids.

To ascertain the need for modelling the missing residues, the UniProt [211] P15328 entry was inspected and showed the first 24 amino acids act as a signal sequence and are not part of the mature FRα. Similarly, the propeptide sequence 235-257 is removed in the mature form of the protein [220], which indicates the full mature sequence of FRα encompasses residues 25-234. The three-dimensional structure 4LRH_chainA includes amino acid residues in the range 29-236. As the missing residues found at the edges of the sequence and are not involved in FA binding to the target, there was no need to rebuild the full sequence through homology modelling.

3. Molecular Docking

As mentioned before, molecular docking is a structure-based approach with the goal of predicting non-covalent binding poses and relative binding affinity of small molecules to a macromolecule [209,221]. Depending on the conformational freedom allowed to macromolecule or ligand, molecular docking algorithms may be classified as: (1) rigid-body, where both macromolecule and ligand are considered rigid-bodies without conformational variability; (2) semi-flexible, the most common type of molecular docking, where the macromolecule is rigid, but the ligand is allowed to adopt different conformations; and (3) flexible, where both ligand and the macromolecule are allowed conformational flexibility [209].

As the folate receptor α (FRα) has high affinity for its endogenous ligand and different three-dimensional structures of *apo*- and *holo*- forms of the receptor are known [91,194,219], our work with a FA-conjugate did not foresee the need to explore flexible docking approaches and their consequent higher computational cost. By compromising with a semi-flexible molecular docking approach, any necessary "extra" computational effort could be put in exploring the conformational space of the larger conjugate. With the open-source software suite MGLTools 1.5.6 [222,223], the AutoDockTools package [222,224] can be used to prepare molecules for running semi-flexible simulations on AutoDock 4.2.6 [225–227] or AutoDock Vina [228]. Both molecular docking software packages are considered stochastic algorithms (i.e., they cause random changes in the values of the degrees of freedom of a system) based on the Monte Carlo method. This method introduces an evolution criterion of acceptance where – after a random change in the ligand – if the energy score is improved, the change is accepted; otherwise, the acceptance depends on the probability of Equation IV-1:

$$Probability \sim exp\left[-\frac{\Delta E}{k_B T}\right] \tag{IV-1}$$

where ΔE is the difference in energy, k_B is Boltzmann's constant, and T is a user defined temperature (high temperatures will accept almost all steps, while lower temperature lead to more selective conformations) [209,221,226]. After obtaining different conformations, they are ranked according to the empirical scoring functions [229], specific to each software. In AutoDock 4.2.6, the scoring function is based on the AMBER force-field [221] that estimates the free energy of binding [225], while in AutoDock Vina the function is described as «(…) more of "machine-learning" than directly physics-based in its nature.» [228] as it extracts empirical information from conformational preferences of complexes and experimental affinity measurements.

3.1. Preparation of the files

The preparation of the FRα PDB file for docking, using UCSF Chimera 1.14, involved the removal of all water molecules (except those mediating ligand/target interactions) and other ligands (normally used to stabilise the crystallographic structure), and the confirmation that the structure did not have multiple conformations, i.e., alternate locations for the same set of atoms. The crystallographic FA was removed from the FRα structure with a simple text line command, without compromising the original file:

```
grep ^HETATM 4lrhA.pdb > FA.pdb
grep -v ^HETATM 4lrhA.pdb > FRalpha.pdb
```

The receptor file was then edited with AutoDockTools, which added and merged all non-polar hydrogens, and computed Gasteiger charges, saving the output as a PDB, partial charge, and atom type (PDBQT) file.

The radius of gyration, r_{gyr}, of the crystallographic FA was measured (using VMD 1.9.3 [230]) to be approximately 5.68 Å, which allowed to calculate the size of the docking box in grid points (g_{points}, for AutoDock 4.2.6) or Å (g_{size}, for AutoDock Vina) according to Equation IV-2. By multiplying r_{gyr} by a 2.9 factor [231], it returned a grid size of 16.48 Å – which is equivalent to 43.95 grid points (g_{size} divided by the default $g_{spacing}$ = 0.375 Å resolution in AutoGrid 4.2.6) – per dimension of a cubic box.

$$g_{points} = \frac{2.9 \times r_{gyr}}{g_{spacing}} = \frac{g_{size}}{g_{spacing}} \qquad \text{(IV-2)}$$

To develop the conjugate for proof-of-concept we propose the use of the commercially available compound **IV.1** (Figure IV–3) with a folic acid (FA) warhead, to conjugate with the novel chlorin **III.29** *via* "click" chemistry. The conjugate **IV.2** with a polyethylene glycol (PEG) spacer of 1 kDa, results in a considerable large molecule. The cycloaddition reaction between the azide group in chlorin **III.29** and the dibenzocyclooctynes (DBCO) group of the linker, was predicted to give two regioisomers (shown in Figure IV–3) – **IV.2a** and **IV.2b** – that are usually not separable [232,233].

For the *in silico* studies described in this chapter, we considered a linker with 23 units of ethylene glycol in isomer **IV.2a** (Figure IV–4.A), as the differences between both isomers or a slightly shorter PEG chain, were not expected to significantly affect binding. Open Babel 2.3.2 [234,235] with its *Gen3D* functionality was used to generate a three-dimensional structure of the conjugate, by performing geometry optimization and a conformational search, to obtain the structure closest to a global energy minimum (Figure IV–4.B,C). As was done for crystallographic FA, the radius

of gyration of the conjugate was measured (r_{gyr} = 22.54 Å) obtaining the values of g_{size} = 65.37 Å (or g_{points} = 174.31), through Equation IV-2.

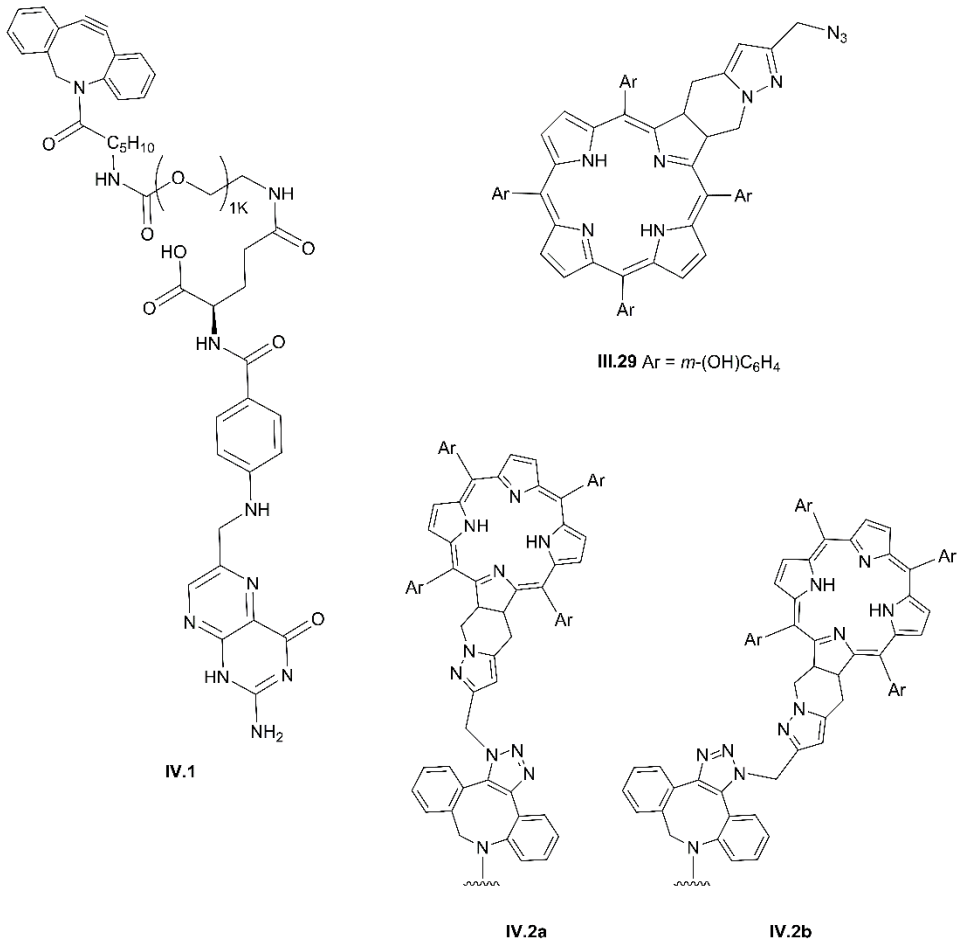

Figure IV–3. Structures of the FA-PEG$_{1k}$-DBCO linker (IV.1) and the expected conjugates IV.2, after "click" chemistry with chlorin III.29.

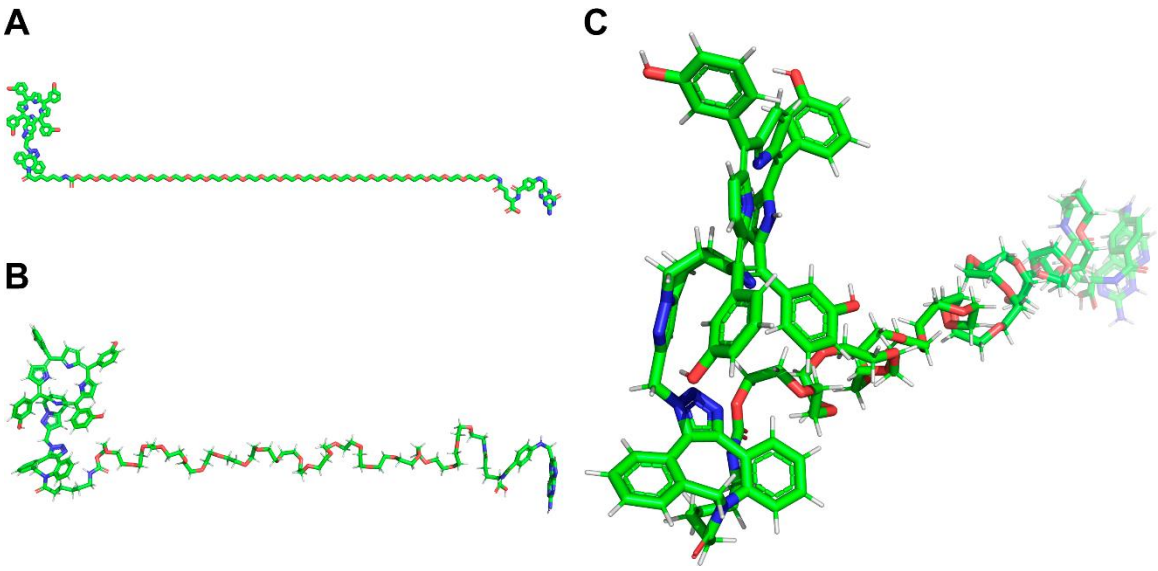

Figure IV–4. Three-dimensional structure of the conjugate IV.2. (A) Two-dimensional structure in SDF. (B) Final three-dimensional structure in Mol2. (C) Side view of the three-dimensional structure.

AutoDockTools identifies 97 rotatable bonds in the conjugate **IV.2**. Because AutoDock 4.2.6 can only handle a maximum of 32 rotatable bonds, we chose to use AutoDock Vina for the molecular docking simulations.

3.2. Redocking of crystallographic of folic acid (FA)

As mentioned in the previous section, AutoDockTools automatically processed crystallographic FA by adding hydrogens, Gasteiger charges, and identifying nine rotatable bonds. After detecting the root of the torsion tree, we reviewed the default torsions parameter by considering amide bonds as non-rotatable and saved the output as a PDBQT file.

With both the ligand and macromolecule PDBQT files ready in AutoDockTools, FA was chosen as the ligand for the grid box which was then centred on it.

In AutoDock Vina we created a configuration file for docking (described in the Experimental section), using the information previously obtained for the centre of the grid box and size of 16.48 Å for each side, using the defaults for other parameters, except the number of poses to be calculated (defined as 10). After running the molecular docking simulation, the binding poses were visually evaluated and the root-mean-square deviation (RMSD) of each pose from the crystallographic FA was measured in Chimera 1.14. However, the binding pose with higher score from AutoDock Vina was not in accordance with the crystallographic pose, having a “flipped” orientation relative to the crystallographic pose where the pteroate fragment is buried deep in the binding pocket (Supplementary Figure IV-2). Running tests with increased exhaustiveness or higher number of conformers (results not shown) did not change the orientation of the best ranking pose. As an

attempt to overcome this issue, we took a step back and decided to use entry 4LRH, chain A, from the PDB repository (Supplementary Figure IV-3) that had been discarded in favour of the re-refined model from PDB-REDO, to see if the docking algorithm was able to predict correct simulation runs.

The process of preparing the files and defining the grid box for molecular docking was repeated and a new configuration file for redocking (described with greater detail in the Experimental section; example shown in Supplementary Figure IV-4.A) was executed in AutoDock Vina. The predicted binding poses can be seen in Figure IV–5.

While there were a few binding poses that had the "flipped" orientation, with this receptor file the best ranked pose had a very strong overlap with the crystallographic FA pose (RMSD < 1 Å). When comparing the interactions between the crystallographic FA (Figure IV–6.A) and the redocked pose (Figure IV–6.B), using LigPlot^{+} 2.2.5 [236,237] it is possible to see that most interactions remained after redocking FA.

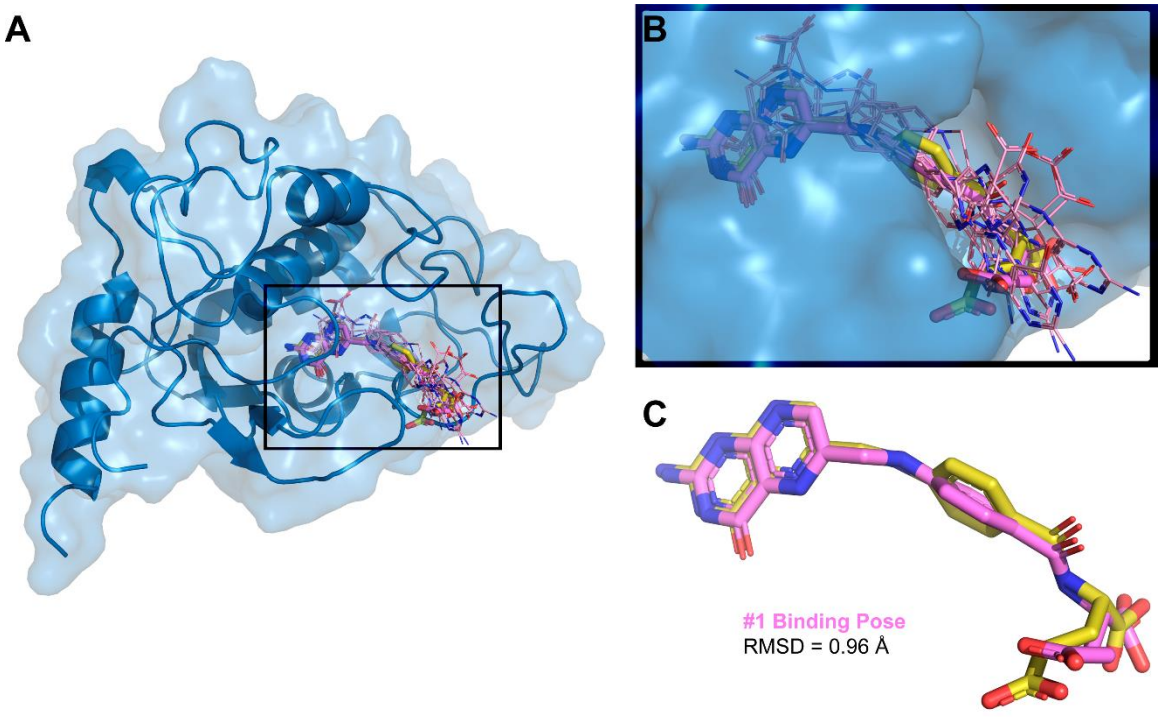

Figure IV–5. Redocking simulation of crystallographic FA (yellow) to FRα (blue) (PDB entry 4LRH, chain A; blue receptor). (A) FRα structure with all ligand docking poses overlapped. (B) Close-up of the ligand docking poses (pink) overlapped with FA in the binding pocket. (C) Best predicted pose (pink) and crystallographic FA (yellow).

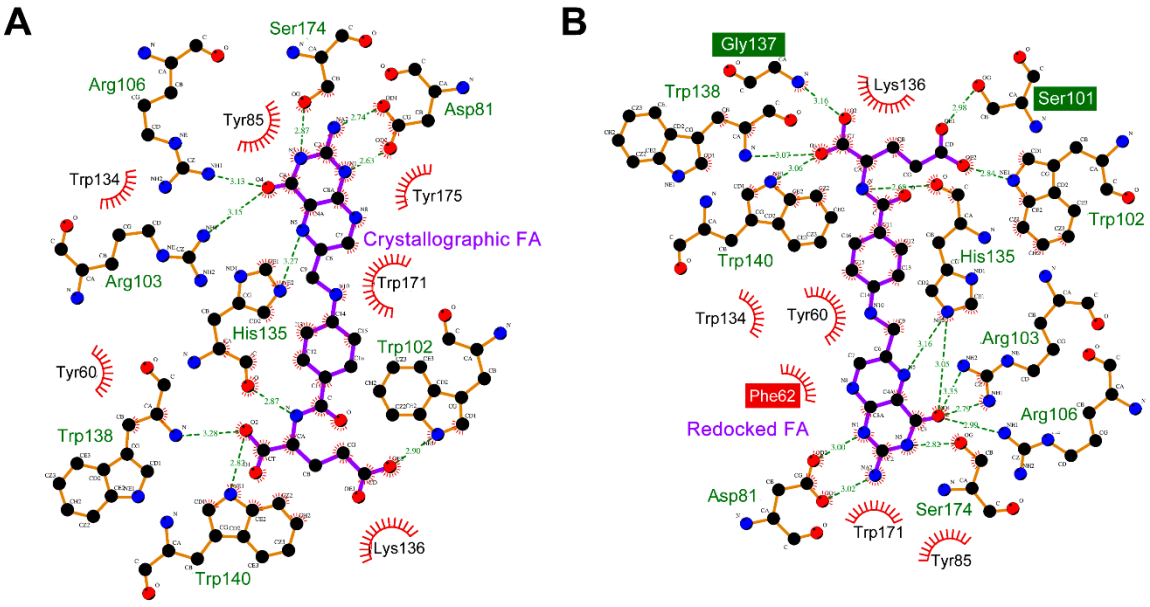

Figure IV–6. Ligand-protein interaction diagram (LigPlot$^+$ 2.2.5) for (A) crystallographic PDB entry 4LRH and (B) redocked FA into the receptor structure of PDB entry 4LRH.
H-bonds are coloured green and hydrophobic interactions are coloured red. FRα residues that interact with FA are labelled and coloured with orange bonds when explicitly represented. FA is coloured with purple bonds.

The missing interactions after redocking are the close contact with Tyr185 and the H-bond with Lys136 (but the interaction remained as a close contact). Additionally, new interactions appeared as the close contact with Phe62 and the H-bonds with Ser101 and Trp138.

The RMSD values and predicted affinity from the scoring function from both redockings with the PDB and PDB-REDO entries 4LRH, chain A, are summarised in Table IV-3.

Table IV-3. Redocking results in AutoDock Vina for the FRα.

Rank	PDB-REDO		PDB	
	Binding Affinity (kcal/mol)	RMSD (Å)	Binding Affinity (kcal/mol)	RMSD (Å)
1	-10.6	10.88	-10.5	0.96
2	-10.4	11.20	-10.4	2.70
3	-10.2	3.14	-10.4	11.01
4	-9.9	1.07	-9.8	2.93
5	-9.7	10.96	-9.7	10.64
6	-9.4	2.89	-9.3	10.89
7	-9.3	3.51	-9.3	2.51
8	-9.1	11.64	-9.2	11.50
9	-8.8	3.40	-9.0	11.24
10	-8.6	2.41	-8.8	3.72
	Exhaustiveness: 8	**6.11 ± 4.41**	**Exhaustiveness: 8**	**6.81 ± 4.53**

Results from poorly predicted poses are coloured red.

3.2.1. Redocking results with AutoDock 4.2.6

Despite not being able to run the docking protocols for the conjugate with AutoDock 4.2.6, we still ran a standard redocking protocol (see Experimental section, 6.3.2.2) to assess the viability of the experiment with another scoring function. Using the default values for a Lamarckian Genetic Algorithm (GA-LS) as our search function, we simulated 10 runs for the FRα structures from each database and used the respective grid centres and grid points calculated in Equation IV-2.

The RMSD values and predicted affinity from the scoring function from both redockings with the PDB and PDB-REDO entries 4LRH, chain A, are summarised in Table IV-4.

Table IV-4. Redocking results in AutoDock 4.2.6 for the FR*α*.

Rank	PDB-REDO		PDB	
	Binding Affinity (kcal/mol)	RMSD (Å)	Binding Affinity (kcal/mol)	RMSD (Å)
1	-11.66	1.53	-10.95	1.65
2	-11.51	1.87	-10.59	1.71
3	-11.37	2.27	-10.30	1.79
4	-11.27	1.64	-10.05	2.06
5	-11.21	1.50	-9.71	2.19
6	-11.20	1.70	-9.63	2.37
7	-11.02	1.20	-9.53	2.02
8	-10.87	1.28	-9.05	2.22
9	-11.25	4.17	-10.23	2.52
10	-10.55	0.93	-9.60	2.57
	GA-LS	**1.81 ± 0.91**	**GA-LS**	**2.11 ± 0.32**

With AutoDock 4.2.6, the scoring function had no issues in consistently predicting the correct ligand binding pose within the FRα structure obtained from either database.

Particularly, in the three-dimensional structure from PDB-REDO, there was a lower average RMSD value across the 10 runs compared to the structure from PDB. When visually analysing the ligand docked poses (not shown in this document, as this was just to test the structures against another scoring function), this difference was explained by AutoDock 4.2.6 having preferred to dock FA less buried in the structure from PDB, than the one from PDB-REDO.

3.3. Blind docking of the chlorin-PEG_{1K}-FA conjugate

As mentioned above, the conjugate **IV.2a** was loaded to AutoDockTools and set as input for the ligand to prepare the molecule for docking. With a molecule this large, there were extra

precautionary steps taken to prepare the conjugate for molecular docking, such as manually setting the same root found for the FA molecule and establish an adequate grid box.

Previously, when calculating the size of the grid box, the value obtained from Equation IV-2 should have been g_{size} = 65.37 Å per side of the cubic box, but the maximum value allowed in AutoDockTools is g_{points} = 126, or g_{size} = 47.25 Å, so it was the value used for the grid box.

As molecular docking aims to predict the optimal binding pose – by sampling different conformations searching the potential energy landscape to find a global energy minimum, while the scoring function assesses the steric and chemical complementarity between ligand and macromolecule [209,238], – the algorithm will try to maximise the number of favourable interactions between just receptor and ligand (without solvents) in a static way. So, when establishing the centre of the grid box, the large size of the molecule had to be considered.

3.3.1. Blind docking with the PDB structure of FRα

By centring the box on the ligand or on the macromolecule, the box would envelope most of the FRα, but would not leave enough space for the conjugate to adopt some conformations to fully explore the binding pocket in the receptor. Thus, we decided to centre the box on the ligand and offset it in the direction of the known binding pocket, so that the faces of both boxes met (i.e., the centre of the box was offset on the x-axis as shown in Figure IV–7). This way the box for docking of the conjugate would still wrap around a great part of the surface of the receptor and allow "negative" space for more prominent torsions of the ligand.

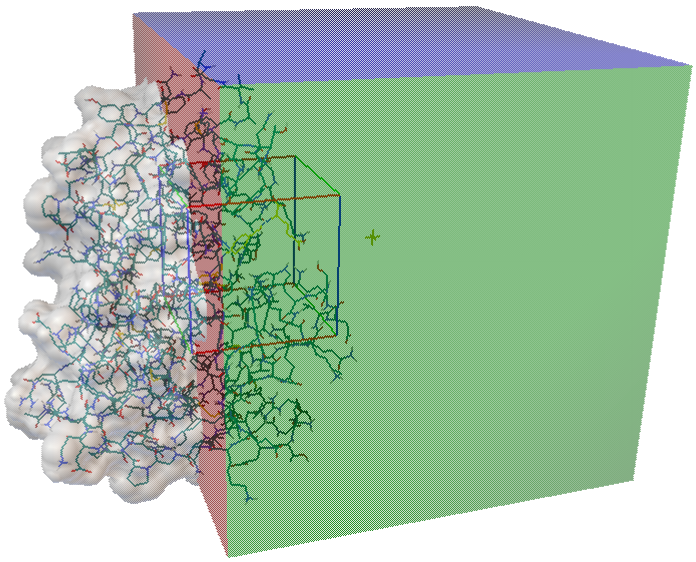

Figure IV–7. Defining the centre of the grid box for blind docking, as observed in AutoDockTools. The box represented by lines was the one used for redocking of FA; the larger mesh box was used for blind docking of the conjugate.

Therefore, after processing and saving the conjugate in PDBQT format with AutoDockTools, the configuration file to be used in AutoDock Vina was updated with the following: i) the centre of the box moved to the coordinates (22.873, 3.553, -6.055); ii) the size of the box increased; iii) the exhaustiveness increased up to 32; iv) the search increased to 20 conformers (maximum value), and v) a higher energy difference between conformers was also accepted (Supplementary Figure IV-4.B).

The results of the docking of the conjugate **IV.2a** (Figure IV–8 and Supplementary Figure IV-5.A and B; binding affinity output is detailed in Supplementary Table IV-1) showed that the binding pose with the highest score was able to fit the FA in the FRα binding pocket. This was also observed for the first five ranked poses out of 20 conformers. Of the remaining predicted poses, excluding the 11th ranked conformer, the FA fragment was found either at the outer edge of the pocket (Supplementary Figure IV-5.B) or not even inside the pocket, favouring interactions with the surface of FRα.

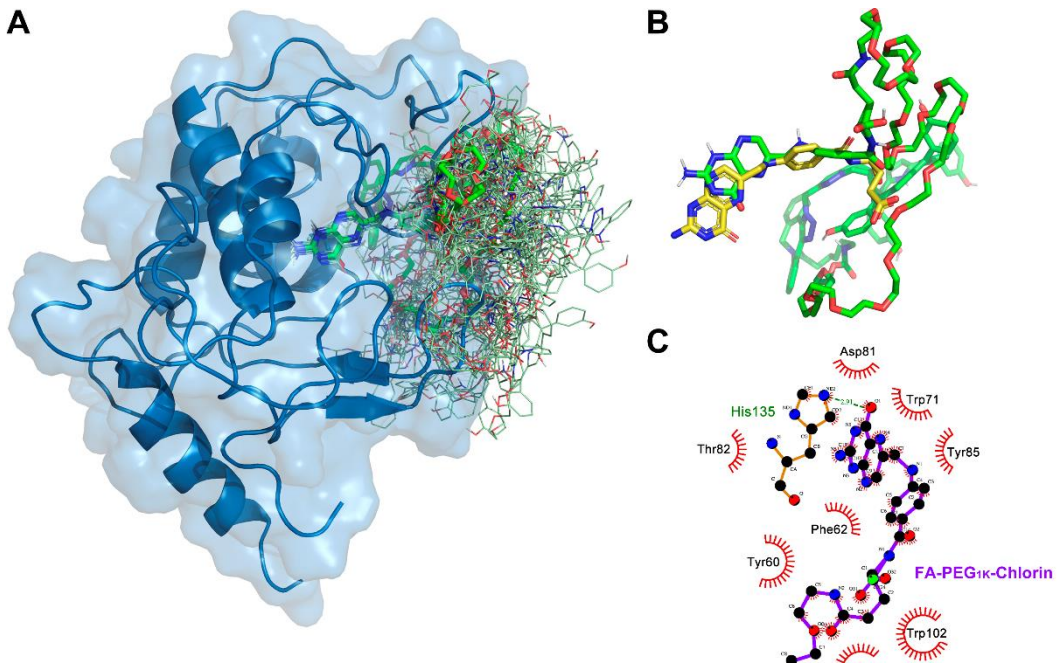

Figure IV–8. Molecular docking simulation of conjugate IV.2a (green) with FRα (PDB entry 4LRH, chain A; blue).
(A) Receptor complexed with all 20 ligand conformers overlapped. (B) Overlap of the best ranked binding pose (green) with crystallographic FA (yellow). (C) Ligand-protein interaction diagram (LigPlot$^+$ 2.2.5) for the FA fragment of the conjugate IV.2a in the FRα binding pocket.

Figure IV–8.B shows that, even though the best pose of the conjugate **IV.2a** found the binding pocket, the FA fragment of the conjugate is not buried as deep as the crystallographic FA (coloured yellow). And this was further evidenced by the analysis in Figure IV–8.C, where only one H-bond interaction with the binding residues was maintained (His135); other H-bond interactions, such as Asp81 and Trp102, became classified as close contacts.

This *in silico* analysis suggested a validation of the expectation set for a FA-conjugate in finding the binding pocket of FRα, despite the large size of our designed conjugate **IV.2a**.

3.3.2. Blind docking with the PDB-REDO structure of FRα

Although the redocking simulation of the crystallographic FA with the re-refined model from PDB-REDO (4LRH entry, chain A) did not result in favourable predictions of the binding pose, we decided to test the performance of molecular docking of the conjugate IV.2a with this FRα structural model, using the same protocols as in the previous section (extensively described in the Experimental section, 6.3.2.3) for defining the grid box – centred on (22.360, 20.809, 3.022) with 47.25 Å per side – and docking.

These molecular docking results with the conjugate **IV.2a** are shown in Figure IV–9 (Supplementary Figure IV-5.C, D, and E; binding affinity output is detailed in Supplementary Table

IV-1). The analysis of the results showed that the predicted binding poses were consistently located inside of the binding pocket, except in two cases: the 7th ranked pose placed at the edge of the pocket (represented in Supplementary Figure IV-5.E); and the 13th ranked pose found outside the binding pocket. The best ranked pose (Figure IV–9.B,C) showed that the FA fragment kept the H-bond interactions with Asp81 and Arg103, but made a H-bond with His134 instead of His135; as for the close contacts, some were kept (Tyr60, Phe62, Trp171) or became close contacts instead of H-bonds (Trp102 and Trp140).

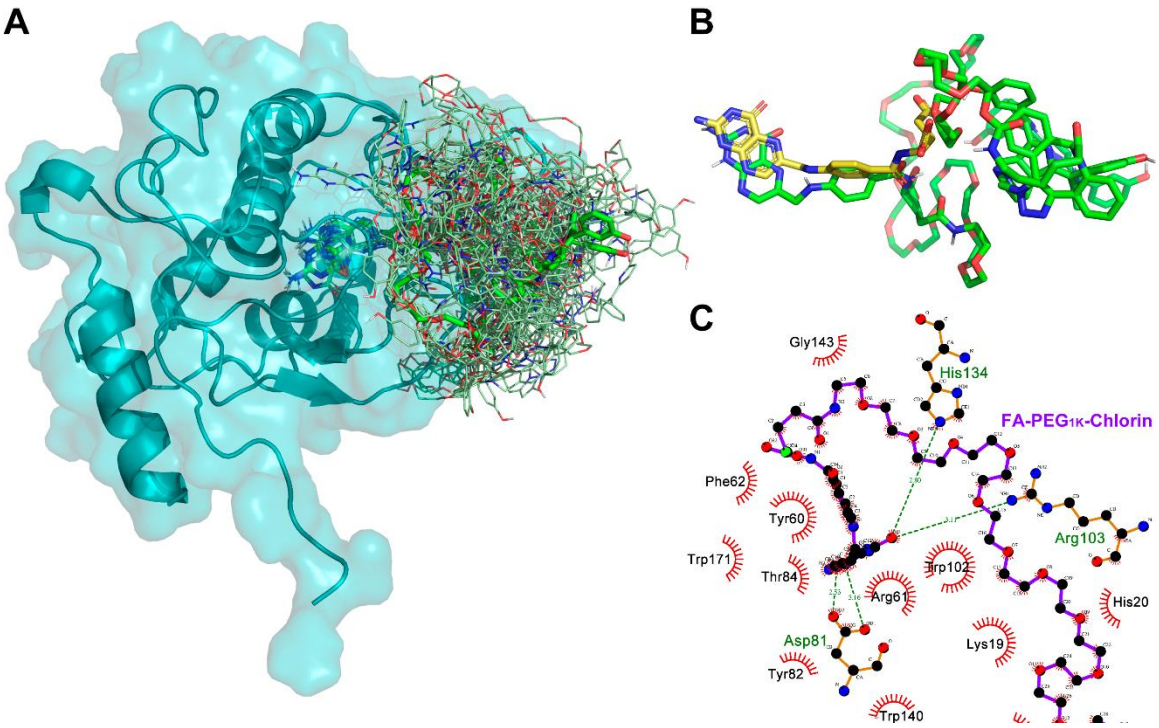

Figure IV–9. Molecular docking simulation of conjugate IV.2a (green) with FRα (PDB-REDO entry 4LRH, chain A; teal).

(A) Receptor complexed with all 20 ligand conformers overlapped. (B) Overlap of the best ranked binding pose (green) with crystallographic FA (yellow). (C) Ligand-protein interaction diagram (LigPlot+ 2.2.5) for the FA fragment of the conjugate IV.2a in the FRα binding pocket.

Even though the redocking experiment of FA with the PDB-REDO structure of FRα, using AutoDock Vina, did not yield a reasonable best predicted pose, the docking experiment with the same receptor model and the conjugate **IV.2a** produced a model with the pterin moiety of the conjugate placed deep in the binding site and in a pose similar to that assumed by FA (Supplementary Figure IV-5).

4. Synthesis of the conjugated-PS

The use of this strain-promoted alkyne-azide cycloaddition (SPAAC) was first explored by Bertozzi *et al*. [239–242] with the advantage reacting under physiological conditions in the absence of copper catalysts and/or microwave heating [187,189]. Later developments by Van Delft *et al.* [243,244], led to the synthesis of stable DBCO reagents that were easily functionalised (such as PEGylation [243]) for bioconjugation and specifically reactive towards azides.

Adapting the work from Trindade *et al*. [195] with FA-PEG conjugates, we proposed the reaction mechanism represented in Scheme IV-1 to obtain the conjugate **IV.2**. An excess of chlorin **III.29** was mixed with the linker **IV.1** in DMSO, to push the "click" reaction towards completion and avoid as much free linker as possible at the end of the 24-hour reaction. Any attempts to follow the consumption of the reagent with thin-layer chromatography (TLC) using AcOEt as the eluent was unsuccessful, with the presence of DMSO from the mixture preventing a clear visualization of individual spots. Nevertheless, when no changes were observed by TLC, the stirring was stopped at the 24-hour timepoint, and the reaction mixture was poured into stirring cold diethyl ether/acetone (8:2 v/v) mixture.

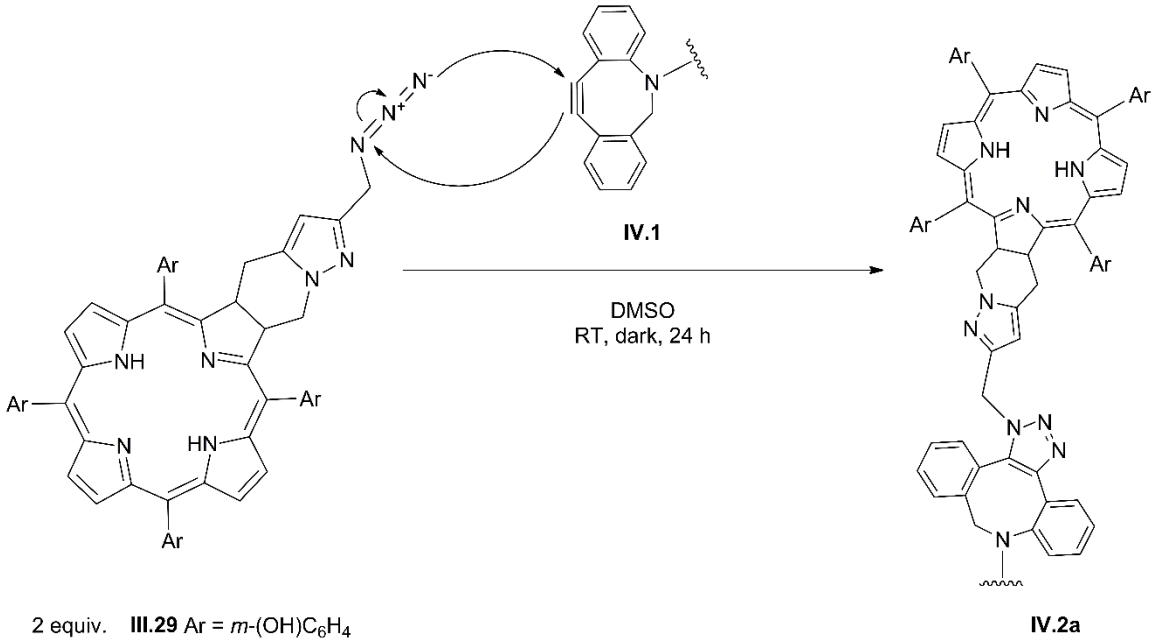

Scheme IV-1. SPAAC to obtain chlorin III.29 conjugated with linker IV.1 (example shown for IV.2a).

After filtering and washing the resulting solid with the same solution and acetone to remove any excess chlorin, we observed that the product was only soluble in polar solvents such as DMSO and dimethylformamide (DMF). After a stock solution of the compound was prepared in DMSO, the ultraviolet (UV) and visible absorption spectrum of product **IV.2** was measured and compared to

the absorption spectrum of the precursor chlorin **III.29** (diluted to a similar absorbance at the Soret band) and, as seen in Figure IV–10, the same peak was found at λ = 651 nm, which confirms the presence of chlorin in the sample of **IV.2**. Furthermore, the FTIR spectrum (Figure IV–11) of the conjugate **IV.2** sample was also evaluated and overlapped with the spectrum from **III.29**: the visible decrease in the characteristic azide signal ca. 2100 nm^{-1}, supports that most free chlorin **III.29** either reacted or was washed from the precipitate.

From both these observations – the presence of chlorin (Figure IV–10) with the diminished signal at $\tilde{\nu}$ = 2095 cm^{-1} (Figure IV–11), – it suggests that the chlorin **III.29** reacted with the DBCO and successfully formed the expected conjugate **IV.2**.

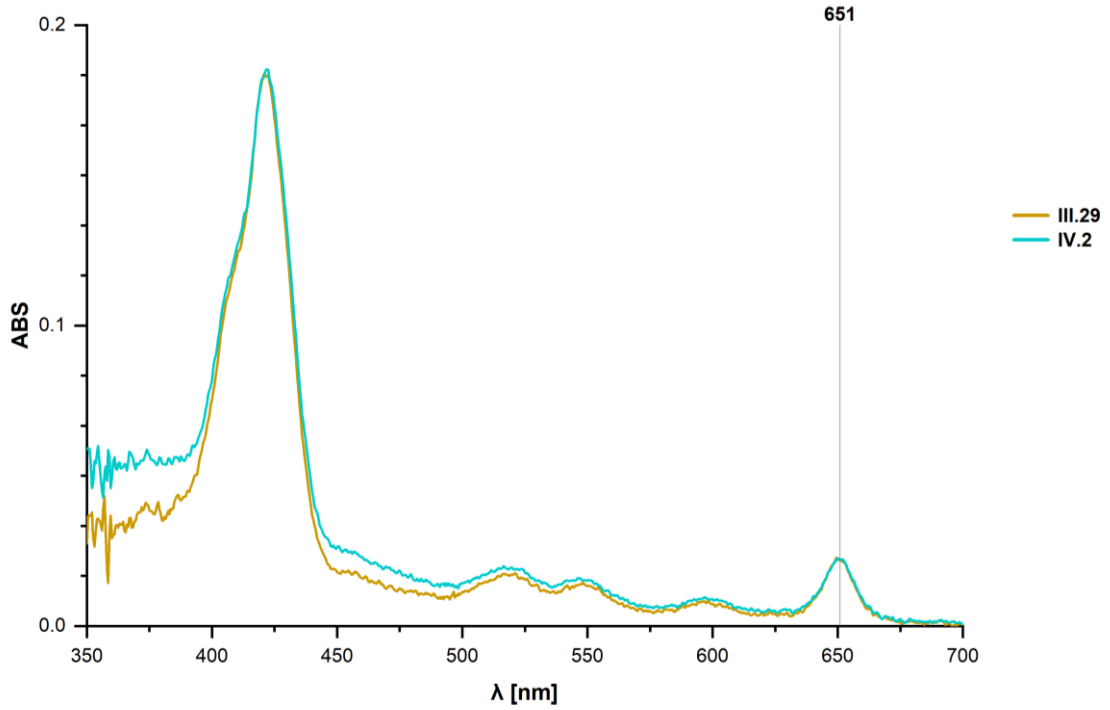

Figure IV–10. UV-visible absorption spectra (DMSO) of chlorin III.29 and conjugate IV.2.

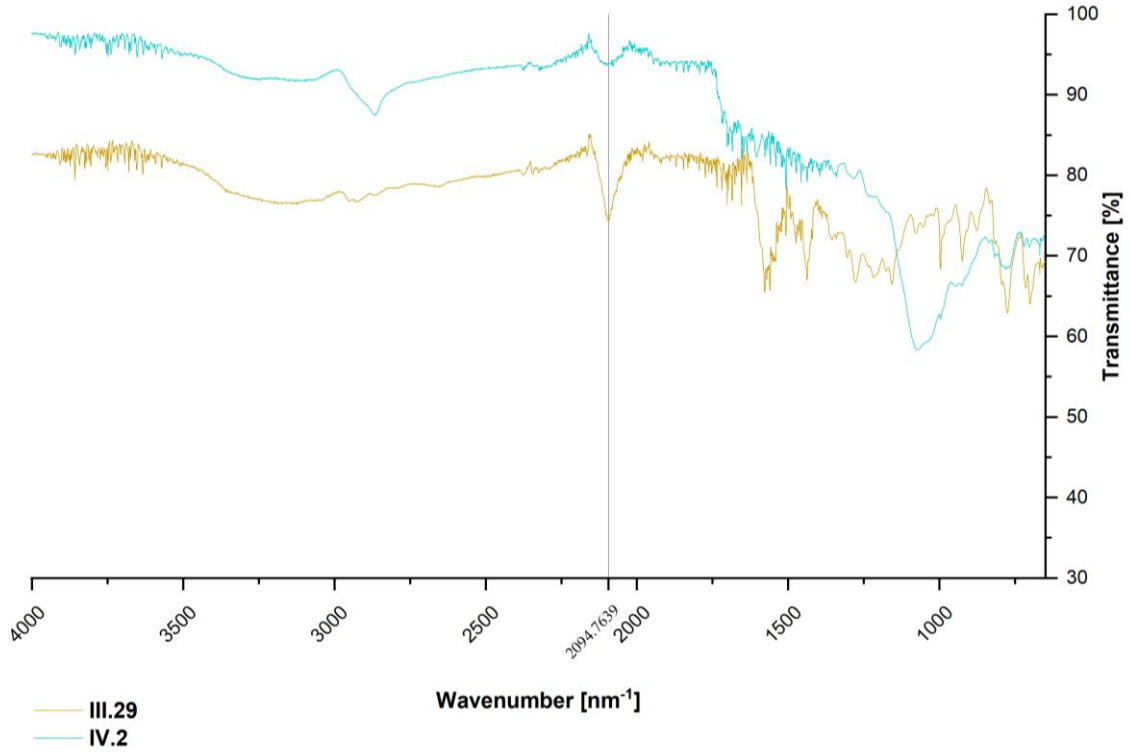

Figure IV–11. Expansion of FTIR analysis for chlorin III.29 and conjugate IV.2.

5. Discussion

As the *in silico* modelling of the interaction of the proof-of-concept conjugate **IV.2a** with the folate receptor FRα followed a structure-based approach, the first step carried out was the analysis of the quality of the available three-dimensional structures of the receptor. Data mining from PDB [205,206] returned a total of 20 individual experimental structures (from five independent entries), which after being submitted to PROCHECK [215] and evaluated, were ranked (Table IV-1) by resolution, percentage of residues in core regions of the Ramachandran plot [216], G-factor, Morris *et al*. [217] classifications, and number of bad contacts. For the best ranked structure of each PDB entry, we also submitted the equivalent structure from the database of re-refined structures, PDB-REDO [210,218], to PROCHECK [215] and compared the structures statistics. From this ranking (Table IV-2), *apo*-receptors were eliminated, as we had interest in the interactions formed in the binding site and there were *holo*-receptor structures available. The resulting best ranked FRα structure was chain A from PDB-REDO entry 4LRH, which has an improved R-free value (which represents a less biased assessment of the model's quality in representing the experimental data not used in refinement [245,246]), higher percentage of residues found in the core region of the

Ramachandran plot [216], and higher classification according to Morris *et al*. [217]. However, besides one extra bad contact, the worst parameter in the PDB-REDO entry was the G-factor – which, according to the PROCHECK manual [247], is a value that defines the "normality" of the structure.

While initially our intention was to compare docking results from AutoDock 4.2.6 [225–227] and AutoDock Vina [228], technical limitations of the former – relative to the maximum acceptable number of rotatable bonds, – did not allow to run docking simulations of the conjugate with AutoDock 4.2.6. As such, we began by evaluating AutoDock Vina for the docking protocols.

Starting with redocking simulations of the crystallographic natural ligand (FA) to ensure the adequacy of the software and docking protocol, the results from PDB-REDO (Table IV-3 and Supplementary Figure IV-2) immediately showed issues with the scoring function in discriminating *best poses*. Giving lower predicted binding affinity to ligand poses that are "flipped" and not expected to interact with the binding pocket, followed by ligands with the expected binding pose with very similar predicted binding affinities. On the other hand, using the structure from PDB (Figure IV–5 and Table IV-3), even though some of the binding poses had a "flipped" orientation, the best scored pose was very similar to the experimental pose of crystallographic FA (RMSD < 1 Å).

When comparing with a standard redock protocol using the GA-LS algorithm from AutoDock 4.2.6, the redocking had no issues in predicting the expected FA binding pose and did it consistently across the 10 runs (Table IV-4), for the three-dimensional structures of both databases (though PDB-REDO yielded lower average RMSD values). As this consistent behaviour between structures from PDB-REDO and PDB was not seen for AutoDock Vina, it reinforces that the issue with "flipped" ligand binding poses stems from its scoring function and not the re-refinement done on structures from PDB-REDO. Yet, we followed through with AutoDock Vina as part of the open-source MGLTools, but more aware about the possibility of issues in the predicted ligand binding poses when docking the conjugate **IV.2a**, since the Glu fragment of FA would not be available for interaction and the only free ends would be either the pteroate fragment or the chlorin (much too large for the binding pocket).

As such, the next step was performing molecular docking of the conjugate **IV.2a**. In Figure IV–4.C it is possible to better visualise how the structure of the conjugate was optimised in three-dimensional space. While the "folding" of FA between the pterin and *p*-aminobenzoic acid fragments (seen on the right of Figure IV–4.B) was not expected, it is important to highlight that Open Babel 2.3.2 [234,235] was able to correctly determine the coil-like shape of the PEG linker [248], as well as an approximate "wave" stereochemistry, observed in porphyrinoid compounds

[249,250]. The greatest obstacle for the docking protocol was the size of the conjugate molecule, with a radius of gyration to which the size of the docking box could not be accommodated. However, AutoDock Vina has been known to predict binding poses of large ligands due to strong computing capabilities [251,252]. As most docking programs are successful in performing binding of small molecules with only five or six rotatable bonds [253], and the designed conjugate had 97 rotatable bonds, there was an unsuccessful attempt to run a test with the structure of the commercially available linker (**IV.1**) in the webserver DINC 2.0 [254–256]. This webserver reports that increasing the exhaustiveness to increase the conformational search space in AutoDock Vina is rarely beneficial [253], while presenting itself as an incremental meta-docking tool for large ligands, but it never processed the uploaded file, claiming the structure was too large. Consequently, we resorted to increase the exhaustiveness in AutoDock Vina running locally, minding the warning that the ligand exceeded 32 rotatable bonds.

Unlike the redocking protocol of FA, the docking simulations of the conjugate did not start inside the binding pocket (Supplementary Figure IV-6 for the PDB structure and Supplementary Figure IV-7 for the PDB-REDO structure), which removed bias from the protocol. With the FRα from PDB (Figure IV–8), AutoDock Vina was able to predict a best binding pose inside the pocket, with a total of 6 out of 20 poses inside the pocket (Supplementary Figure IV-5.A). As the conjugate is "built" upon the glutamic acid fragment from the FA "warhead", we run the same protocol with the FRα from PDB-REDO (Figure IV–9), with the expectation that the software's scoring function overcame the preference for "flipped" docking poses, as now only the pteroate (from FA) and the chlorin fragments were available to interact with the binding site. Unlike what was observed for redocking, the re-refined structure was actually able to return better predictions in quality and number: the best ranked prediction found more buried in the binding pocket, as were other six poses (Supplementary Figure IV-5.C), with a total of 18/20 poses predicted to be inside the binding pocket.

These docking results highlighted the ability of the designed conjugate, with a FA warhead, to bind to the folate receptor´s binding site, so we moved forward with the synthesis of conjugate **IV.2**. We run into difficulties with the purification of the product obtained after the proposed SPAAC reaction. While the size of the linker **IV.1** is considerably large, it is not unusual in PEGylated conjugates and it is not even the largest linker used successfully in the synthesis of PS conjugates [257]. Although DBCO's asymmetry raises the issue of producing a mixture of usually inseparable regioisomers [232,233] (**IV.2a** and **IV.2b** detailed in Figure IV–3), we maintained the choice of using this linker since it is readily available and adequate for a proof-of-concept project. The resulting conjugate **IV.2** was analysed by UV-visible absorption spectroscopy (Figure IV–10) and FTIR spectroscopy (Figure IV–11), which supported the success of the "click" chemistry. However, it was not possible to confirm its structure by mass spectrometry due to chemical

instability under the experimental conditions used. Yet, as there was evidence of the success of the "click" reaction and the presence of the chlorin core, it was decided to move forward with the photochemical characterization and *in vitro* activity of the synthesized conjugate. As such, from the new chlorins synthetised and reported in Chapter III:, five were chosen along with the conjugate **IV.2** (Figure IV–12) for further studies and evaluation of their activities as PS.

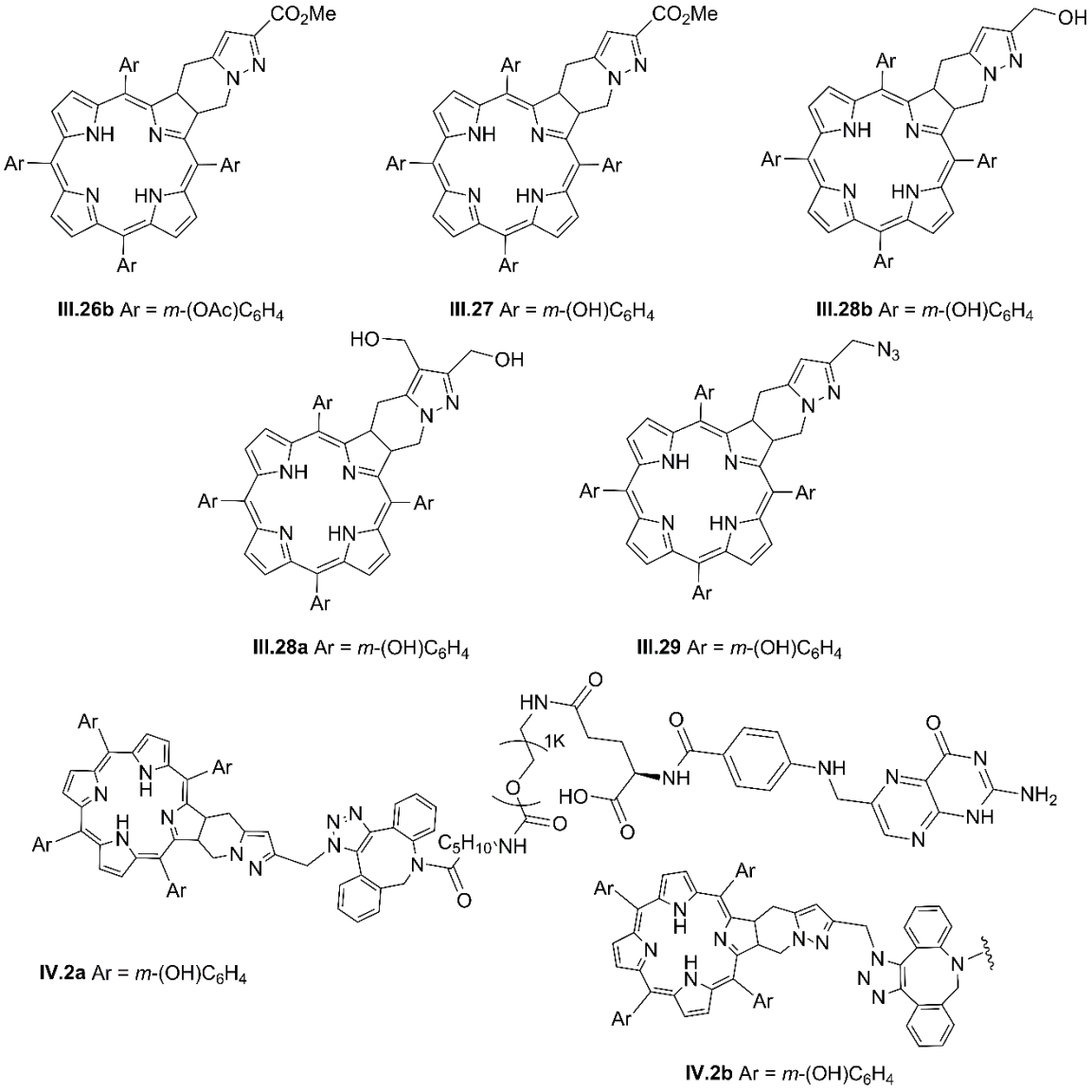

Figure IV–12. Set of the novel chlorins and designed targeted-conjugate chosen for further *in vitro* evaluation.

As mentioned before in Chapter III:, chlorins **III.26b**, **III.27**, and **III.28b** will allow to observe a correlation between hydrophilicity and photodynamic activity [32,42,43], while chlorin **III.28a** will also stand for a direct comparison in activity with the monosubstituted derivative **III.28b**. Chlorin **III.29** as one of the main synthetic goals, will be evaluated as PS by itself with the potential of being used in the development of third-generation PS, as a "clickable" PS. And finally, the

conjugate **IV.2** will be our proof-of-concept molecule of the targeted-PDT strategy derived from the novel "clickable" chlorin **III.29**.

6. Experimental

6.1. Instrumentation

6.1.1. *In silico* experiments

6.1.1.1. Hardware

Molecular docking protocols were run on a 64-bit CentOS 6 Linux server with an Intel Xeon CPU (E5620) at 2.40 GHz (Supplementary Table IV-2).

6.1.1.2. Software and repositories

The full sequence of residues for FRα was retrieved from UniProt Knowledgebase [211,212]. Three-dimensional structures of FRα were retrieved from databases PDB [205,206] and PDB-REDO [210,218]. PROCHECK [215,247] was used to perform structural analysis of all structures. The three-dimensional structure of the conjugate **IV.2** was generated with Open Babel 2.3.2 [234,235].

Visualisation and simple editing of the three-dimensional structure files was performed with UCSF Chimera 1.14 [213], VMD 1.9.3 [230], or PyMOL 2.0 [258]. Molecular docking protocols used MGLTools 1.5.6 [222,223] and AutoDock Vina [228]. Protein-ligand interactions of interest were further analysed using LigPlot^{+} 2.2.5 [236,237].

Images of two- and three-dimensional structures were generated with ChemDraw Ultra 12.0 [259] and PyMOL 2.0 [258], respectively. Figures with multiple images were assembled in the Photo Editor utility from Adobe® Photoshop® Elements 11 [260].

6.1.2. Nuclear Magnetic Resonance

^{1}H and ^{13}C nuclear magnetic resonance (NMR) spectra were recorded on Bruker Avance III spectrometer operating at 400 MHz and 100 MHz, respectively.

Deuterated solvents were used as acquired and mentioned for each situation. The values of the chemical shifts are presented in ppm, respectively to the internal standard tetramethylsilane (TMS) or solvent residual peak, and the values of the coupling constants (*J*) are presented in Hz.

6.1.3. Infrared Spectroscopy

Infrared spectra were obtained from Agilent Technologies Cary 630 FTIR spectrometer, using the attenuated total reflectance (ATR) method, where the solid samples were measured directly

6.1.4. UV-visible Spectrophotometer

Absorption spectra were recorded in a UV-visible Recording Spectrophotometer (Shimadzu UV-2100). The samples were dissolved in the indicated solvent and measured in quartz cuvettes with an optical path of 1 cm.

6.2. Materials

6.2.1. Reagents

All reagents were purchased from Sigma-Aldrich, Merck, or Fluka, and used directly without further purification procedures. The FA-PEG_{1k}-DBCO linker (**IV.1**) was purchased from Biopharma PEG Scientific Inc. (catalogue no. HE048057-1K).

6.2.2. Solvents

All the solvents used (except for 1,2,4-TCB, which was used directly, as acquired) were purified according to the methods described in the literature [191].

6.2.3. Others

TLC analyses were performed on Merck Silica gel 60 F254 plates. Column chromatography was performed with silica gel 60 (0.040-0.063 mm) as the stationary phase.

6.3. Methods

6.3.1. Three-dimensional structure of chlorin-PEG_{1K}-FA conjugate (IV.2)

The covalent structure of conjugate **IV.2a** with 23 PEG units in the linker was initially drawn using ChemDraw Ultra 12.0 [259]. The two-dimensional structure was saved in Structure Data File (SDF) format. From this SDF file, using the *Gen3D* functionality from Open Babel 2.3.2 [234,235], a three-dimensional structure of the conjugate **IV.2a** was generated, followed by geometry optimization: (1) 250 steps of steepest descent with MMFF94s force-field, (2) 200 iterations of weighted rotor conformational search, and (3) 250 steps of conjugate gradient geometry optimization. This ensures that the structure obtained is close to a global minimum energy conformer, which was submitted to an additional conformer search with weighed rotor using the same MMFF94s force-field. An example of the command used is presented below:

```
obabel -isdf conjugate.sdf -omol2 -O conjugate.mol2
--gen3d best --conformers --nconf 50 --ff mmff94s --weighted
---errorlevel 4 &> conjugate.log
```

As the previous command focuses on the generation of the three-dimensional structure based on rules and common fragments, even with the minimization steps, there might be some clashes/strains in the structure. Further energy minimisation was performed under similar conditions applied by the *Gen3D* functionality but using 5000 steps of steepest descent with MMFF94s force-field. The command used is presented below:

```
obabel -imol2 conjugate.mol2 -omol2 -O conjugate-min.mol2
--minimize --sd --ff mmff94s --steps 5000 --log ---errorlevel
4 &> conjugate-min.log
```

This final three-dimensional structure was saved in Tripos molecule structure (Mol2) file format.

6.3.2. Docking protocols

6.3.2.1. Pre-processing of the molecules

The crystallographic structures of FRα (entry 4LRH, from databases PDB and PDB-REDO) as well as the three-dimensional structures of the ligands (crystallographic FA and conjugate **IV.2**) were separated and "cleaned" of waters and other molecules present in the crystallographic unit using UCSF Chimera 1.14 [213,214]. Afterwards, they were prepared using the AutoDockTools package [222] from the software suite MGLTools 1.5.6 [222,223]. They were converted to PDBQT format, with automatic addition and merging of non-polar hydrogens, and computation of Gasteiger charges. Moreover, for FA, the root of the ligand was detected automatically, obtaining nine rotatable bonds (making sure to select amide bonds as non-rotatable). As for the conjugate, we took the extra step of manually setting the same root found for the FA molecule (as this was the expected fragment that would bind to the receptor), taking note of the warning of the existence of 97 rotatable bonds.

6.3.2.2. Redocking of crystallographic FA

The AutoGrid 4.2.6 utility was used to define the grid box containing the target binding site where the ligand is docked. Using Equation IV-1, the length of each side of the cubic box – 16.48 Å – was calculated using the radius of gyration of the FA molecule. AutoGrid allowed to centre the box on the ligand and obtain the coordinates (6.976, 20.809, 3.022) for the PDB-REDO structure and (7.489, 3.553, -6.055) for the PDB structure. These values were inserted in a configuration file of parameters necessary to run AutoDock Vina (e.g., Supplementary Figure IV-4.A). In this file, the number of ligand poses to predict was specified to be 10, along with the default values for exhaustiveness of the global search and the allowed energy difference between the best and worst binding poses (kcal/mol).

AutoDock 4.2.6 used the GA-LS hybrid search function [225] with the respective default settings for 10 runs: 150 individual in population, maximum of 2,500,000 energy evaluations, maximum of 27,000 generations, and elitism of only one individual surviving to the next generation, with a 0.02 gene mutation rate and 0.80 crossover rate.

As AutoDock Vina only presents RMSD values compared to the best docking pose, UCSF Chimera 1.14 was used to calculate the RMSD between FA of each docking pose and the original crystallographic pose (Table IV-3).

6.3.2.3. Blind docking of chlorin-PEG$_{1K}$-FA conjugate (IV.2a)

For the blind docking of the conjugate, AutoGrid 4.2.6 was also used to define the docking grid box. Using Equation IV-2, the length of each side of the cubic box – 65.37 Å – was calculated using the radius of gyration of the conjugate **IV.2a.** However, the maximum length of the cubic box allowed by the software is 47.25 Å. AutoGrid 4.2.6 allowed to centre the box on the ligand and offset it along the x-axis (as seen in Figure IV–7) and obtain the coordinates (22.873, 3.553, -6.055) for the PDB structure. The same process was repeated for the PDB-REDO structure to obtain the coordinates (22.360, 20.809, 3.022). These values were added to the configuration file of parameters necessary to run AutoDock Vina (e.g., Supplementary Figure IV-4.B). To increase the chances of the conjugate to find the binding pocket, the number of predicted poses was altered to the maximum allowed of 20, exhaustiveness of the global search was increased up to 32, and the allowed energy difference between the best and worst binding poses (kcal/mol) was also increased.

6.3.3. Synthesis of chlorin-PEG$_{1K}$-FA conjugate IV.2

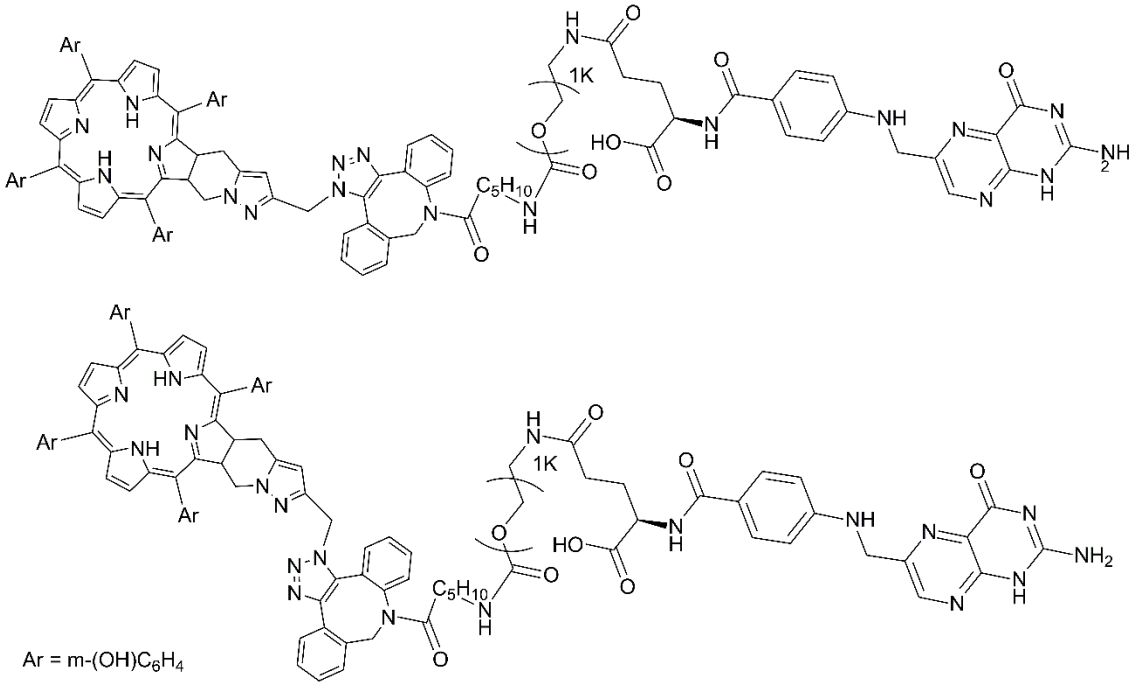

The conjugation was adapted from a procedure described in the literature [195]. DBCO-PEG$_{1k}$-FA **IV.1** (8.9 mg, 0.005 mmol) in DMSO (500 μL) was sonicated until complete dissolution. Then, the solution was added to a solution of 2 equiv. of chlorin **III.29** (8.3 mg, 0.010 mmol) in DMSO (1 mL). The reaction mixture was left stirring for 24 h at RT, in the dark. The product was precipitated from the dropwise addition of the reaction mixture to a stirred cold solution of diethyl ether and acetone (30 mL; 8:2 v/v). The precipitate was filtered, washed with acetone followed by a mixture

of [diethyl ether/acetone (8:2 v/v)], originating a dark orange solid after being dried under vacuum (7.7 mg).

Comparison of the FTIR spectra of free chlorin **III.29** and conjugate **IV.2** (Figure IV–11) showed that the peak at $\tilde{\nu}$ = 2095 cm^{-1}, assigned to the azide group from chlorin **III.29**, disappeared after its reaction with linker **IV.1**, yielding chlorin-PEG_{1K}-FA conjugate **IV.2**. This indicates that the azide group was modified after undergoing "click" chemistry. Accordingly, as the UV-visible absorption peak that characterises chlorin **III.29** (e.g., λ_{max} = 651 nm) is still observed in the conjugate's spectrum, we assumed the success of the conjugation due to the high efficiency of "click" chemistry [261–263].

UV/Visible (DMSO): λ_{max} = 422, 517, 547, 597, 651 nm.

FTIR (ATR): $\tilde{\nu}$ = 2866, 1654, 1605, 1508, 1458, 1396, 1341, 1075, 781 cm^{-1}.

7. Supplementary information

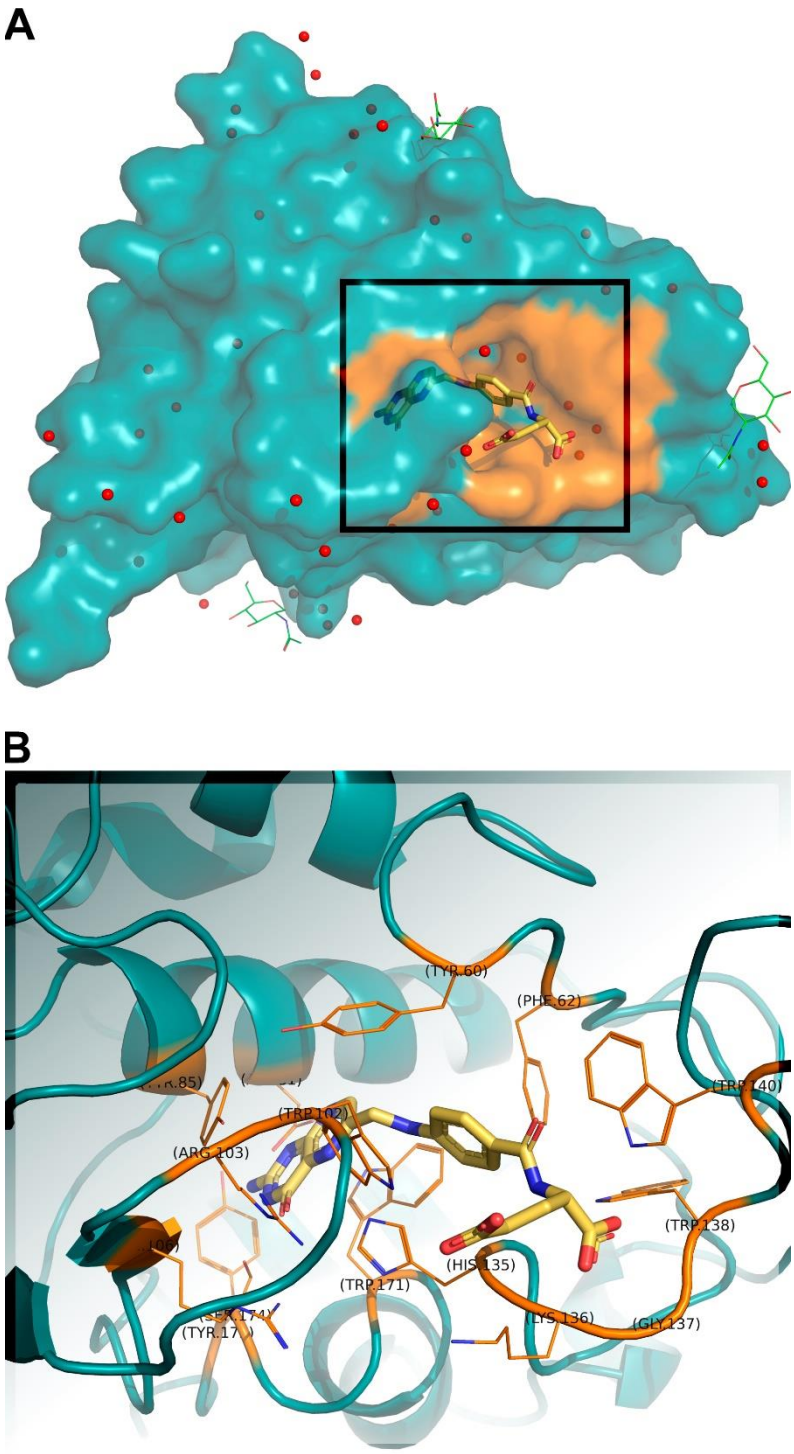

Supplementary Figure IV-1. Binding pocket of the FA/FRα complex (Supplementary Table IV-3) [194]. **A) Full *holo*-FRα structure (FRα structure is represented by its surface in teal with the binding pocket in orange, FA in yellow stick presentation, water in red dots, and NAG in green wire presentation). B) Zoom in of the binding pocket, with the explicit side-chains of the residues (with the same colour code, FRα structure is represented in cartoon by the secondary structure with the binding pocket residues labelled and FA in stick presentation).**

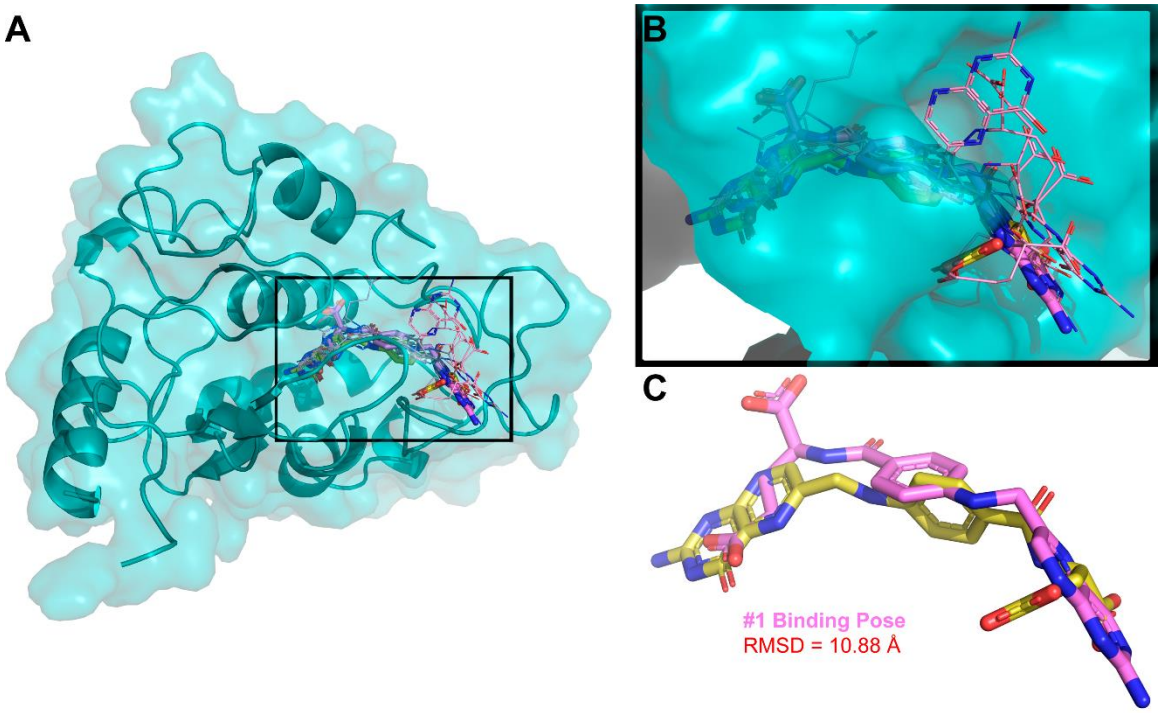

Supplementary Figure IV-2. Redocking of crystallographic FA (yellow) results from AutoDock Vina for FRα structure from PDB-REDO (entry 4LRH, chain A; teal). (A) Receptor complexed with all ligands overlapped. (B) Close-up of the predicted binding poses (pink) overlapped with FA inside the binding pocket. (C) Best predicted pose (pink) and crystallographic FA (yellow).

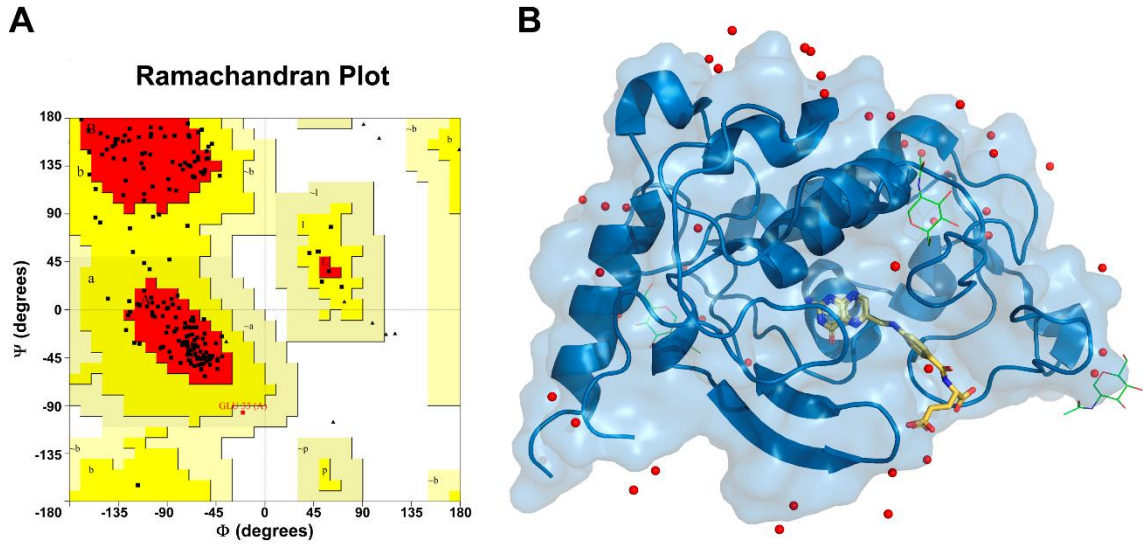

Supplementary Figure IV-3. Structure of FRα chosen for docking from PDB (entry 4LRH, chain A).
(A) Ramachandran plot: each black square represents a residue found in the core (red area) and allowed (bright yellow) areas; residues found in generously allowed (pale yellow) and disallowed (white) areas are flagged as red squares and labelled, e.g., Glu33.
(B) Crystallographic *holo*-structure: the secondary structure and surface of FRα are coloured in blue, the complexed FA is coloured yellow, the water molecules are represented as red spheres, and the NAG molecules are represented as green wires.

A

```
receptor = FRalpha.pdbqt
ligand = FA.pdbqt

center_x = 7.489
center_y = 3.553
center_z = -6.055

size_x = 16.4795
size_y = 16.4795
size_z = 16.4795

out = redock.pdbqt
log = redock.log

exhaustiveness = 8
num_modes = 10
energy_range = 3
```

B

```
receptor = FRalpha.pdbqt
ligand = conjugate.pdbqt

center_x = 22.873    # offset by +15.384
center_y = 3.553
center_z = -6.055

size_x = 47.250      # maximum
size_y = 47.250      # maximum
size_z = 47.250      # maximum

out = dock.pdbqt
log = dock.log

exhaustiveness = 32
num_modes = 20
energy_range = 4
```

Supplementary Figure IV-4. Examples of configuration files for executing AutoDock Vina: (A) redocking parameters for crystallographic FA; (B) blind docking parameters for chlorin-PEG$_{1K}$-FA conjugate (IV.2).

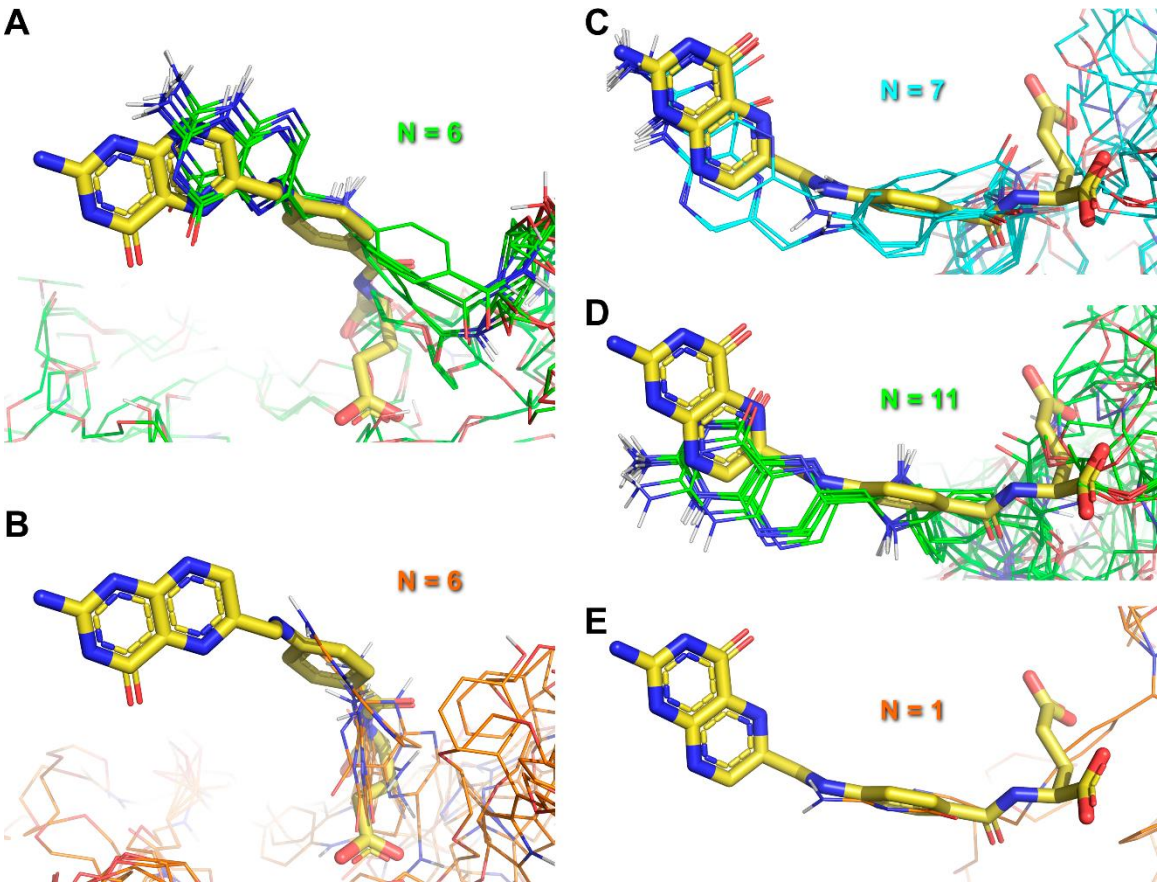

Supplementary Figure IV-5. Quality of the predicted docked poses on the FRα structure from PDB (A and B) and PDB-REDO (C, D, and E) compared to FA (yellow).

Distance between the nitrogen atom from the amine substituent of the pterin fragment and Asp81 from FRα was used to define buriedness of the pose inside the binding pocket (from more to less): cyan-coloured poses as < 4 Å, green-coloured poses as ≥ 4 Å, and orange-coloured poses as ≥ 8 Å.

N equals the number of conformers found in each category.

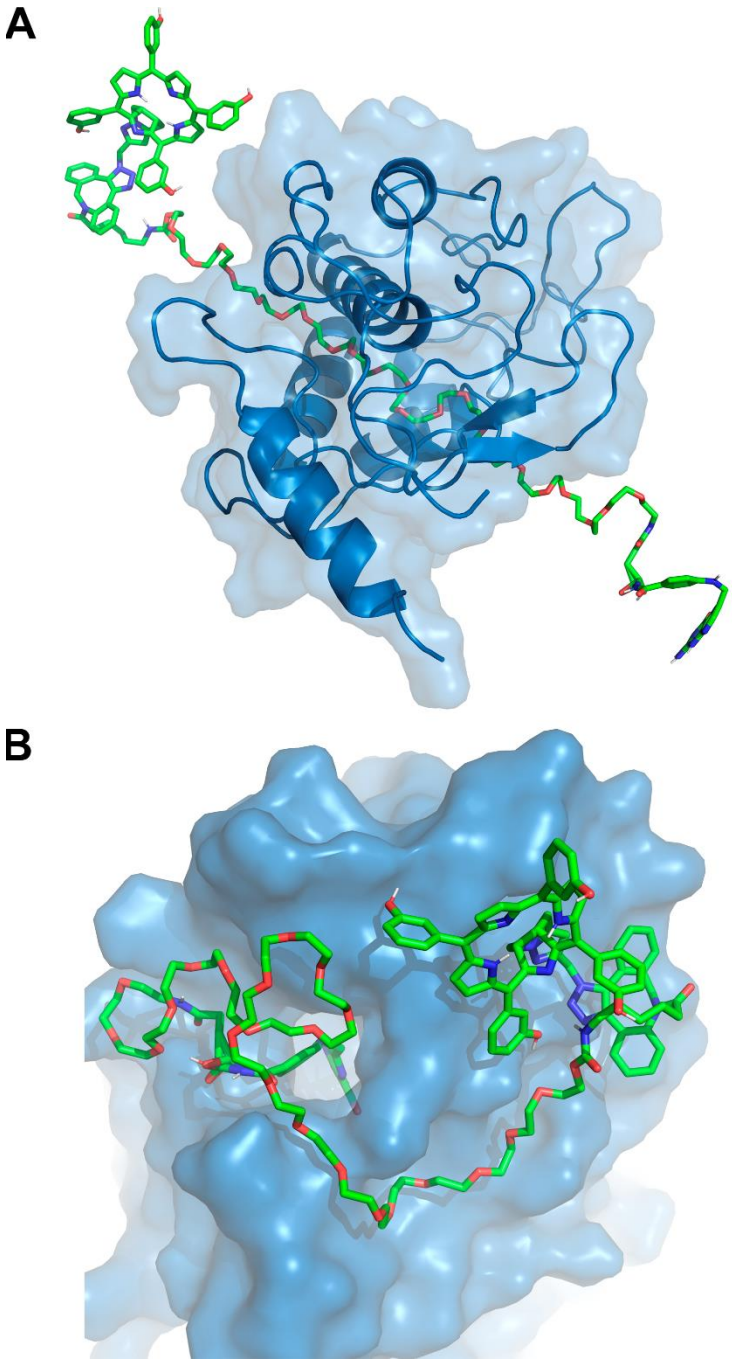

Supplementary Figure IV-6. (A) Starting configuration of the molecules during blind docking of conjugate IV.2a in FRα (PDB entry 4LRH, chain A). (B) Conformation adopted by the best docked pose of the conjugate, outside the binding pocket.

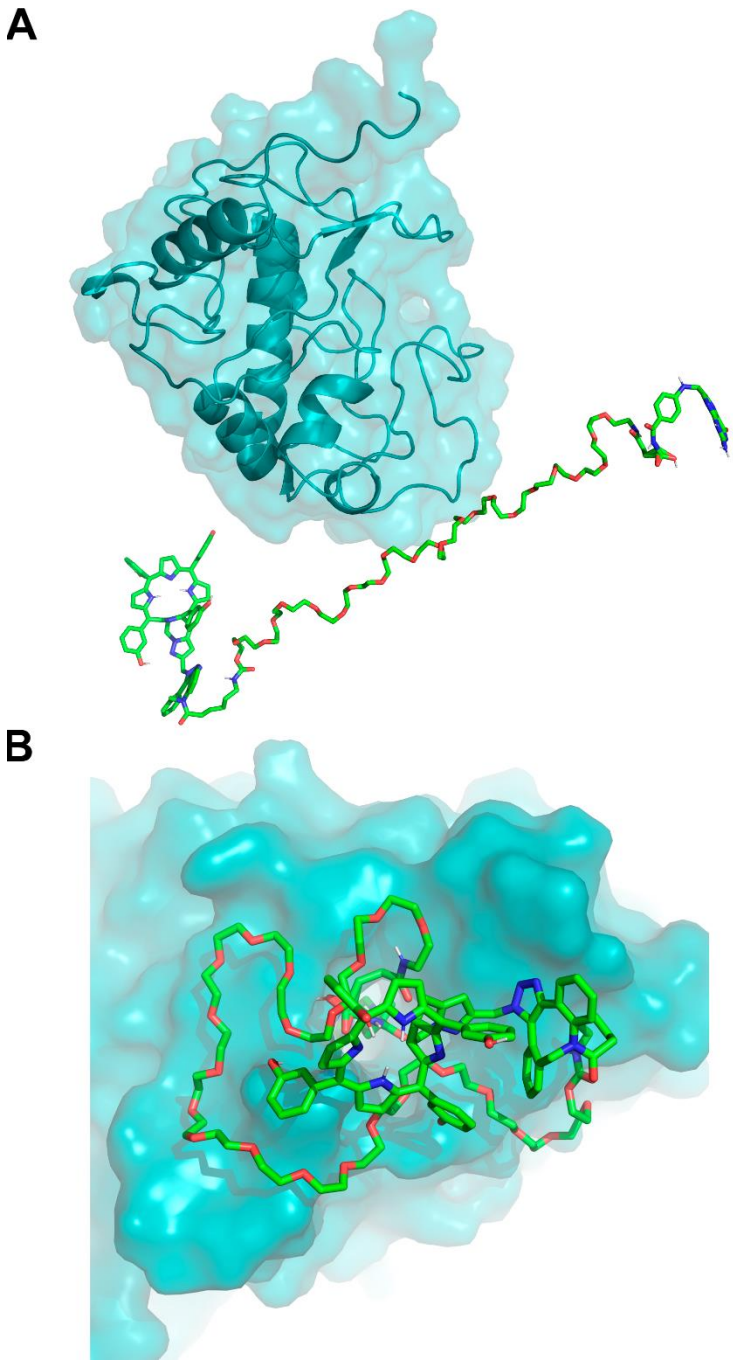

Supplementary Figure IV-7. (A) Starting configuration of the molecules during blind docking of conjugate IV.2a in FRα (PDB-REDO entry 4LRH, chain A). (B) Conformation adopted by the best docked pose of the conjugate, outside the binding pocket.

Supplementary Table IV-1. Blind docking results in AutoDock Vina for the FRα.

Rank	PDB Binding Affinity (kcal/mol)	PDB-REDO Binding Affinity (kcal/mol)
1	-6.1	-5.7
2	-5.7	-5.7
3	-5.5	-5.6
4	-5.5	-5.5
5	-5.5	-5.5
6	*-5.4*	-5.4
7	-5.4	*-5.4*
8	-5.2	-5.3
9	-5.2	-5.3
10	*-5.2*	-5.3
11	-5.2	-5.3
12	-5.2	-5.3
13	*-5.1*	-5.3
14	*-5.1*	-5.2
15	*-5.1*	-5.2
16	-5.0	-5.2
17	*-5.0*	-5.2
18	-5.0	-5.2
19	-5.0	-5.2
20	-5.0	-5.1

Results from predicted poses with FA fragment outside the binding pocket are coloured red. Predicted poses with FA fragment at the edge of the binding pocket are in italic.

Supplementary Table IV-2. Hardware information for the CentOS Linux server.

Architecture	x86_64
CPU op-mode(s)	32-bit, 64-bit
Byte Order	Little Endian
CPU(s)	8
Thread(s) per core	1
Core(s) per socket	4
Socket(s)	2
Vendor ID	GenuineIntel
Model name	Intel(R) Xeon(R) CPU E5620 @ 2.40GHz
Stepping	2
CPU MHz	2393.995

Supplementary Table IV-3. Binding pocket residue interactions with the FA fragments [194]**.**

	Pterin	*p*-Aminobenzoic acid	Glutamic acid
Tyr60			
Phe62			
Asp81			
Tyr85			
Trp102			
Arg103			
Arg106			
Trp134 †			
His135			
Lys136			
Gly137			
Trp138			
Trp140			
Trp171			
Ser174			
Tyr175			

† Was not indicated as a FA-binding residue by Chen *et al*. in their Supplementary Figure 4 [194,202], but was described in the paper. Residues with described interactions are shown with solid backgrounds, while the others lining the pocket have a dashed background.

Green represents hydrogen bond interactions and orange represents hydrophobic interactions.

Chapter V: Photophysical and photochemical characterization

Science is spectral analysis. Art is light synthesis.

Karl Kraus

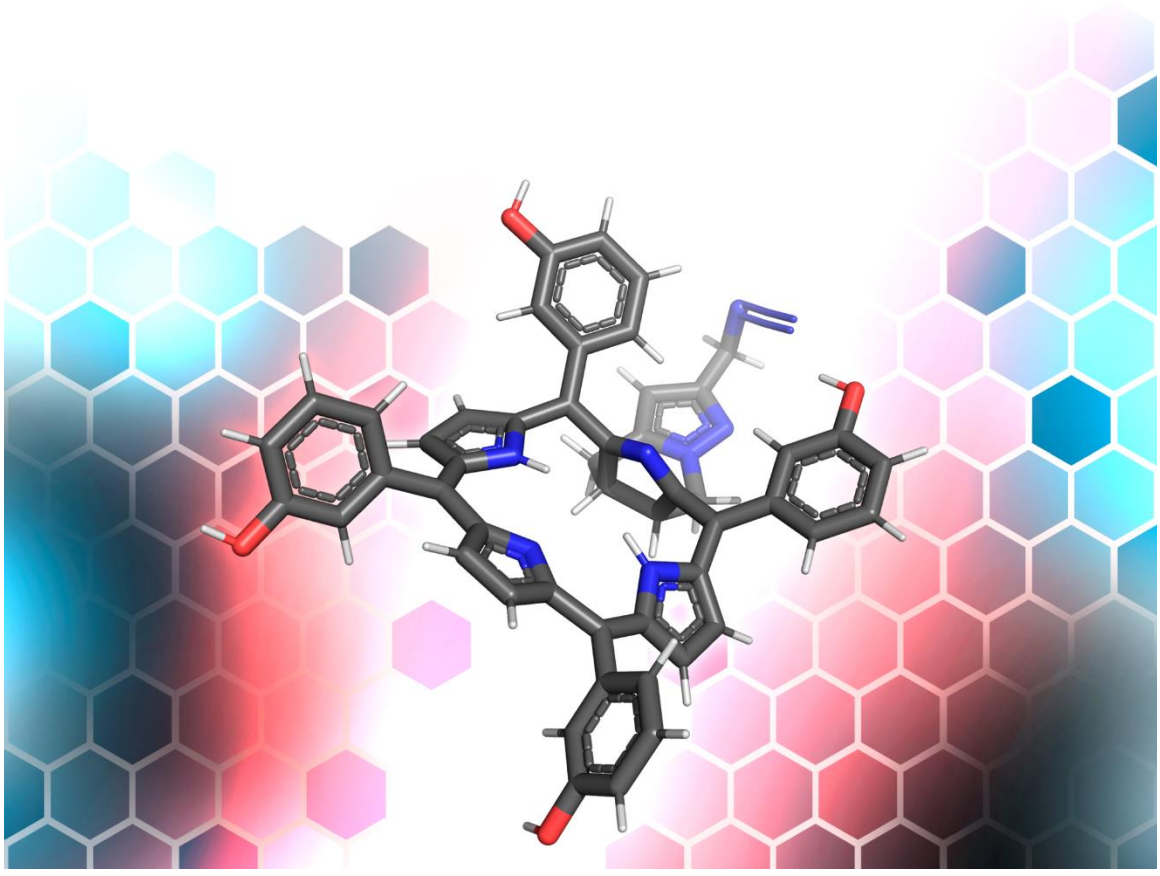

1. Introduction

The understanding of the properties of photosensitisers (PSs) and how to apply them in clinical conditions is key to the success of photodynamic therapy (PDT). As mentioned in Chapter I, the development of new PSs has evolved to get closer to the desired characteristics of an ideal PS, such as high absorption inside the phototherapeutic window (600-800 nm), minimal dark toxicity, photostability, high photochemical reactivity, and high selectivity [23,29].

The first first-generation PSs to be approved, porfimer sodium or Photofrin®, presented several disadvantages as a PS, and yet is still commonly used [28,35,48]. From low chemical purity (as it was first a mixture of monomeric and aggregated porphyrins), to a low tissue penetration, and lasting skin photosensitivity after PDT, a lot could be improved, which became the focus on later generations of PSs. The characteristics sought in these new PSs were the red-shift in absorption to allow for deeper tissue penetration, higher yields of singlet oxygen that increased the phototoxicity of the compound, and higher selectivity to tumour tissues leading to less side effects [29,32,48].

The ultraviolet-visible (UV-vis) absorption spectra for porphyrin-type photosensitisers are known for the typical strong Soret band (~400 nm) followed by four less intense Q-bands (500-700 nm). These peaks have been interpreted and extensively discussed based on the four-state model defined by Gouterman [264,265]. The reduction of porphyrins to chlorins leads to a decrease in symmetry that consequently red-shifts the longest wavelength Q-band to ~650 nm [154,266]. One of the most active 2nd generation PSs, the chlorin Foscan® (temoporfin **III.2**) [36,39], presents this absorption profile (Figure V–1.A), to which our chlorins (**III.26b**, **III.27**, **III.28a**, **III.28b**, and **III.29**) and conjugate **IV.2** have a very similar spectra (Figure V–1.A; structures found in Figure V–1.B).

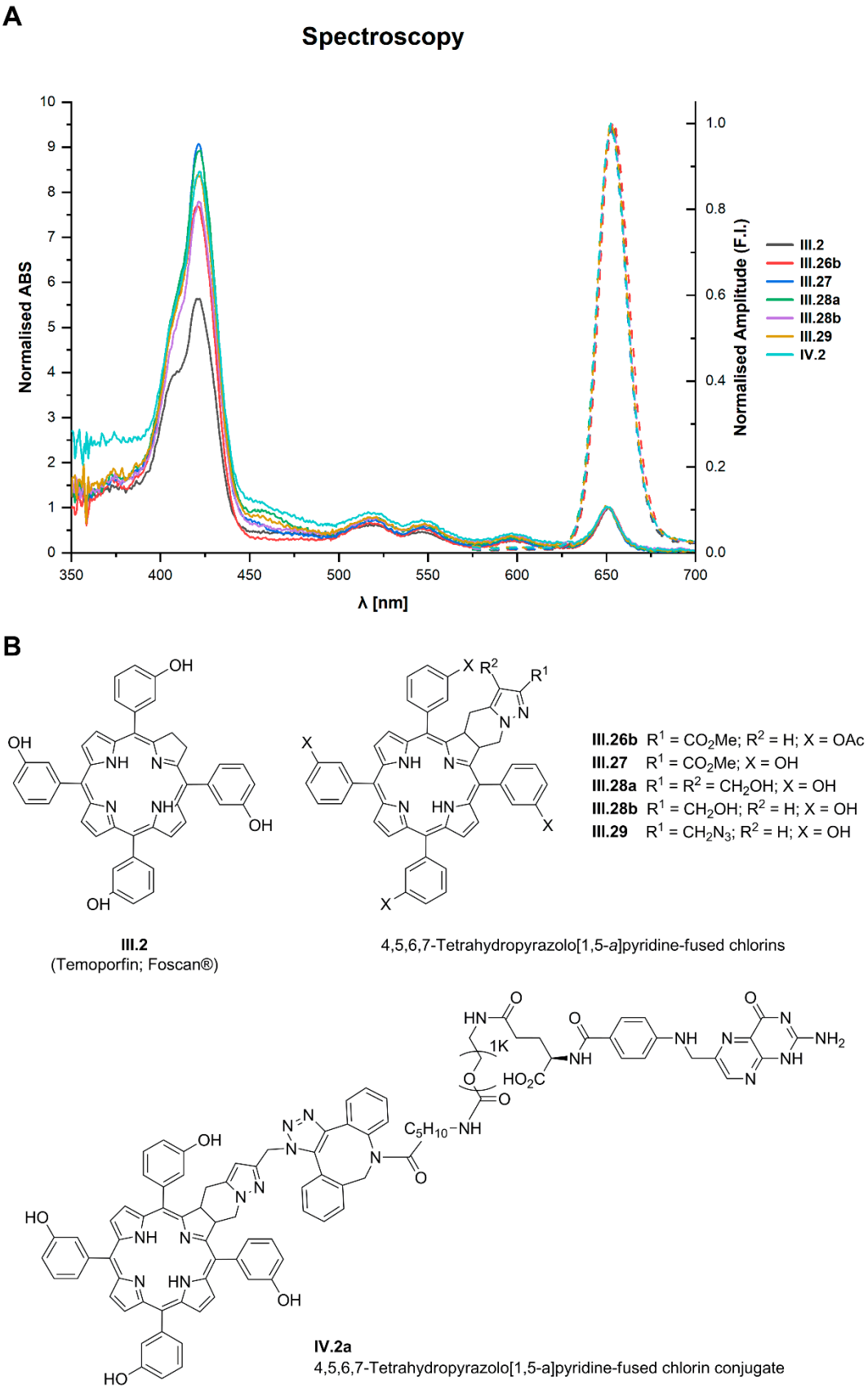

Figure V–1. (A) Normalised spectra, in DMSO, for UV-vis absorption (left axis and solid line) and fluorescence intensity, λ_{ex} = 548 nm (right axis and dashed line) of temoporfin and synthesised chlorins. (B) Structures of the novel PSs evaluated in this thesis.

Accounting for the structural likeness of our PSs to temoporfin **III.2**, we expected not only similar spectra, but also similar photophysical and photochemical features that make temoporfin **III.2** one of the most potent PSs and observe the effects of the substituents on our novel chlorins. Nevertheless, modulation of these properties due to the presence of the 4,5,6,7-tetrahydropyrazolo[1,5-*a*]pyridine ring-system fused to the macrocycle as well as the effect of the chlorins' substituents would also be anticipated.

In this chapter, we started by assessing the light dose correction (LDC) factor which would ensure that an equal number of photons are absorbed by the PS and allow for a correct comparison between PSs in later studies (e.g.: photodegradation, phototoxicity). As for the characterisation of the PSs, we also evaluated fluorescent, photodegradation, and singlet oxygen quantum yields, to have a better insight on the phototoxicity of the studied PSs.

2. Light dose correction

Schaberle [267] reported a method to calculate the LDC factor to ensure that the cells were irradiated with the intended light dose (LD), in photoactivation experiments. This is particularly relevant for the study of PSs as the light source used was a light-emitting diode (LED) lamp (HIGROW LED, model GL36A) with an emission maximum at 660 nm, while the chlorins' absorption peak is at 651 nm (Figure V–1), leading to the shift shown in Figure V–2.A.

Deriving from the Beer-Lambert law, we can obtain Equation V-1, where the intensity of light absorbed by a solution, I_{abs}, can be calculated from the initial light intensity, I_0, and the optical absorption, A, from a photon's frequency ν.

$$I_{abs}(\nu) = I_0(\nu)(1 - 10^{-A(\nu)}) \quad \text{(V-1)}$$

Schaberle [267] described the number of photons absorbed, N_{ph}, by re-writing Equation V-1 as follows,

$$N_{ph} = \Delta t \sum \frac{P(\nu)}{h\nu}(1 - 10^{-A(\nu)}) \quad \text{(V-2)}$$

where Δt is the time of irradiation, P is the output power of the light source, *h* is the Planck constant, and ∑ represents the sum over all the frequencies.

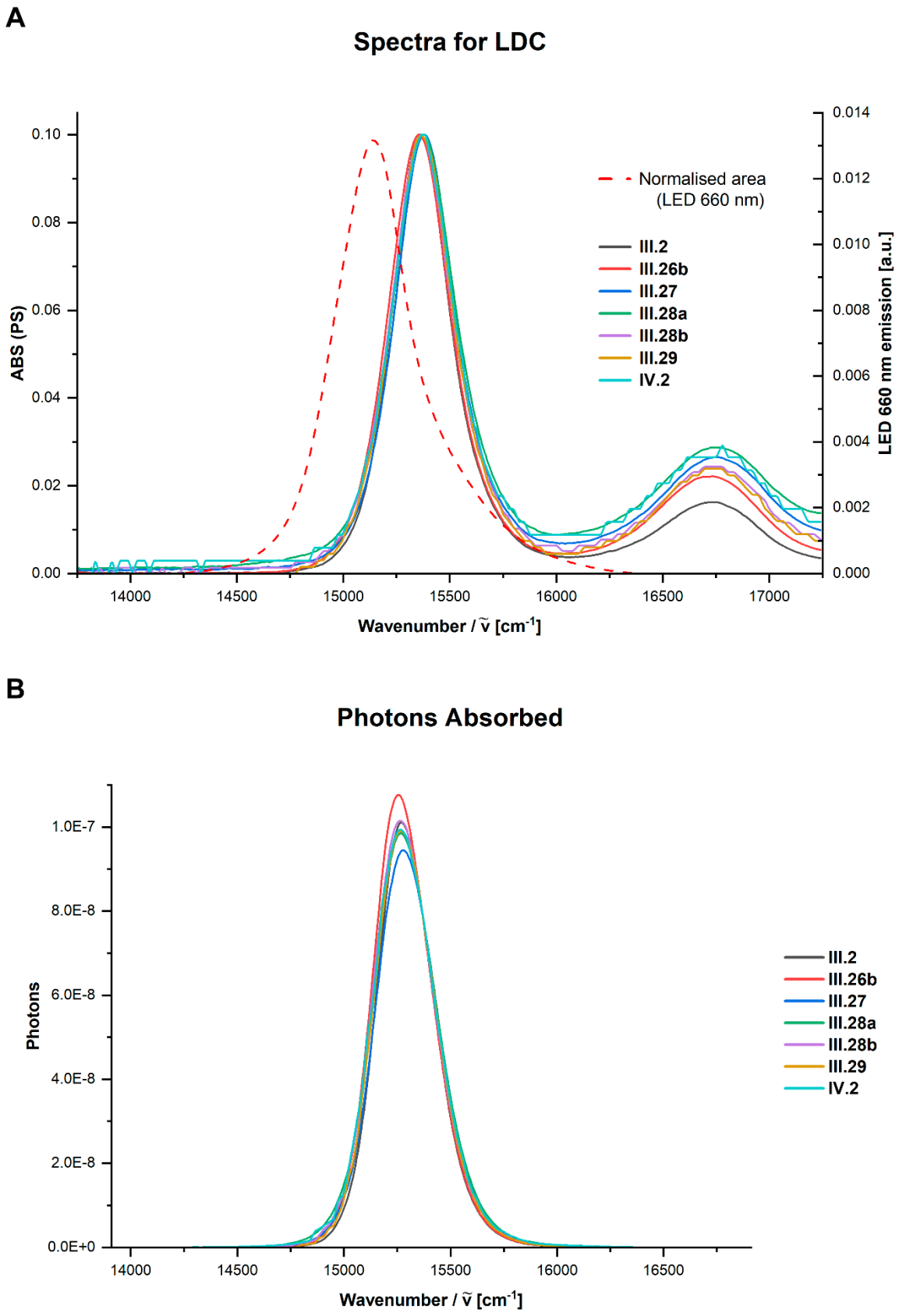

Figure V–2. (A) PS absorption spectrum, in DMSO, and LED emission spectrum (normalised area). (B) Number of photons absorbed calculated with Equation V-2.

Following the same process for an ideal light source, where all light power emitted, P_r, is emitted at the same wavenumber, $\tilde{\nu}$, of maximum absorption of the PS, A_r, to obtain the maximum number of photons that could be absorbed, N_{ph}^{r}, LDC factor can be calculated from Equation V-3.

$$LDC = \frac{N_{ph}}{N_{ph}^{r}} = \frac{\sum \frac{P(\tilde{\nu})}{\tilde{\nu}}(1-10^{-A(\tilde{\nu})})}{\frac{P_r}{\tilde{\nu}_r}(1-10^{-A_r})} \quad \text{(V-3)}$$

The optical absorption in the peak must be equal or lower than 0.1, in order that the absorption intensity is in a linear range. As previously described [267], by normalising the area of the emission spectrum of the light source, $P_r = 1$, and using the data from the PSs optical absorption as well as the light source emission, Equation V-3 can be re-written into Equation V-4 that includes the values for temoporfin **III.2**, as an example.

$$LDC\ (\mathbf{III.2}) = \frac{\sum \frac{P(\tilde{\nu})}{\tilde{\nu}}(1-10^{-A(\tilde{\nu})})}{\frac{1}{\tilde{\nu}_r}(1-10^{-A_r})} = \frac{4.92596E-6}{\frac{1}{15360.9831}(1-10^{-0.1})} = 0.38 \quad \text{(V-4)}$$

Samples of each PS were prepared through dilution in dimethyl sulfoxide (DMSO), to obtain the same optical absorption at 651 nm. An absorption of approximately 0.1 was aimed at and then all the spectra were adjusted to that exact value. As seen in Figure V–2.A, despite having similar structures and a common absorption maximum, all chlorins present slight differences in their spectra that affect the N_{ph} (Figure V–2.B). Consequently, the values calculated for the LDC factor were slightly different, as shown on Table V-1, but given the similarity between the chlorins' spectra, an average of the LDC was calculated for the PSs studied.

Table V-1. LDC factor and adjusted LD (LD_a).

PS	LDC FACTOR	MEAN	LD (J/cm^2)	LD/LDC = LD_a (J/cm^2)
III.2	0.37	0.4 or 40%	1.0	2.5
III.26b	0.40			
III.27	0.38			
III.28a	0.40			
III.28b	0.40			
III.29	0.38			
IV.2	0.40			

3. Fluorescence quantum yield

In Photochemistry, quantum yield (Φ) can be defined as a number of events occurring per photon absorbed by the system and can be applied to photophysical processes or photochemical reactions [268]. In the case of fluorescence quantum yield, it is applied to the ability of converting the absorbed photons into emitted photons in a particular environment [269,270].

While a high fluorescence quantum yield limits the photodynamic activity of PSs, a moderate emission in the phototherapeutic window can be advantageous for its use in imaging. This has led to the development of assays to quantify internalised PSs, as well as take advantage of *in vivo* fluorescence to measure PS distribution and/or pharmacokinetics [25].

To calculate the fluorescence quantum yield (Φ_F) relative to the standard oxazine-170 in ethanol, Equation V-5 [270] was used, with the value of $\Phi_{F_{ref}}$ = 0.579, taking into account the absorbances at the excitation wavelength used, A(λ_{ex}), the integral fluorescence across the spectrum, F(λ_{em}), and the refractive indexes of the solvents used, *n*.

$$\Phi_F = \Phi_{F_{ref}} \frac{1-10^{-A_{ref}(\lambda ex)}}{1-10^{-A(\lambda ex)}} \frac{\int_{\lambda em} F(\lambda_{em})}{\int_{\lambda em} F_{ref}(\lambda_{em})} \frac{n^2}{n_{ref}^2} = 0.579 \frac{0.01689}{1-10^{-A(548\ nm)}} \frac{\int_{\lambda em} F(\lambda_{em})}{-1.4538E6} \frac{1.479^2}{1.360^2} \qquad \text{(V-5)}$$

We started by measuring the absorption spectra of each PS and oxazine-170 – a quantum yield standard that absorbs in a similar wavelength region – and adjusting their absorbance to 0.1 at 651 and 629 nm, respectively. As the solutions should be sufficiently diluted to ensure that there is an homogeneous irradiation without reabsorption effects (which is usually achieved by adjusting the absorbance to ≤ 0.08 at the maximum) [270], the samples were then diluted by a factor of four, the absorbance was recorded again (inset plot of Figure V–3), followed by the measure of the emission spectra with a λ_{ex} = 548 nm represented in Figure V–3.

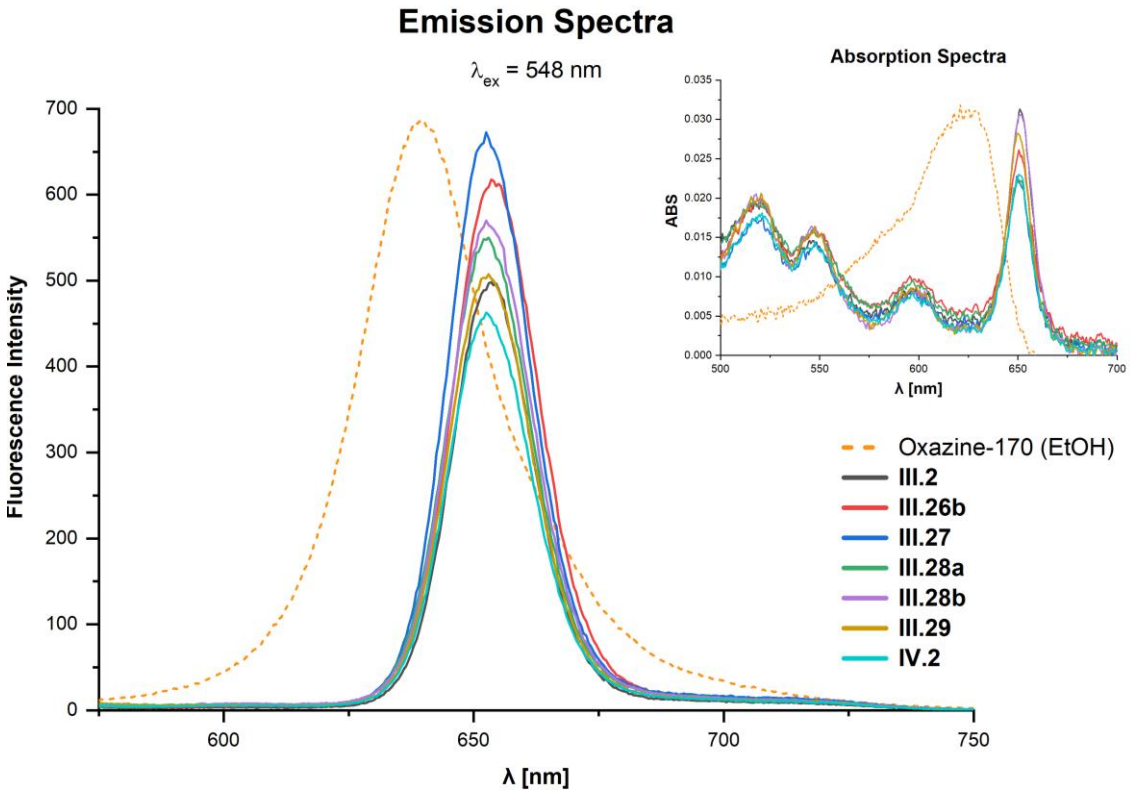

Figure V–3. Emission spectra (λ_{ex} = 548 nm) of our samples in DMSO (solid lines) and oxazine-170 in ethanol (dashed line), with their respective absorption spectra (inset plot).

With the information retrieved from both the absorption and emission spectra measured, the fluorescence quantum yield values for our samples were determined (Equation V-5) and reported in Table V-2.

Table V-2. Fluorescence quantum yields (Φ_F) for the PS (N = 1).

PS	Φ_F (DMSO)[†]
III.2	0.11
III.26b	0.11
III.27	0.11
III.28a	0.10
III.28b	0.11
III.29	0.12
IV.2	0.094
Oxazine-170	0.23

[†] Calculated using Equation V-5.

For the studied PS, there is not a considerable difference between the synthesised chlorins as shown on Table V-2. The chlorins in DMSO (temoporfin **III.2** included) have similar Φ_F values, with the conjugate **IV.2** having the lowest quantum yield and its azide precursor **III.29** having the highest

fluorescence quantum yield. However, they are still very similar to the other chlorins and within the expected reference value of a moderate to high fluorescence, $\Phi_F \geq 0.1$ [270].

4. Photodecomposition

It is known that the photodecomposition of temoporfin **III.2** does not limit its use in the clinic [271]. Nevertheless, photostability is still an important characteristic of a suitable PS. To ascertain how photostable our chlorins were, we used Equation V-6 [53], which calculates the photodecomposition quantum yield (Φ_{pd}) through the ratio between the rate of disappearance of PS molecules, v_d, and the rate of absorption of photons, v_p. The terms from Equation V-6 are expanded into Equations V-7 and V-8, presented below.

$$\Phi_{pd} = \frac{v_d}{v_p} \tag{V-6}$$

To compare our PSs, the bleaching of the molecules, v_d, was simplified by using samples with the same irradiated volume, V_{irr}, and – considering the structural similarity of the chlorins – assuming that the molar extinction coefficient, ε, at 651 nm was equivalent to temoporfin's. The value present in Equation V-7 is the $\varepsilon_{651\,nm}$ for temoporfin in methanol [53,272], since the value in DMSO was not available, which led to an approximate estimation (with a systematic error associated to the calculations in different solvents) of the rate of the PS disappearance. With these constant values known, the expression for v_d becomes dependent on the ratio of variation of absorbance, dA, between the last and first timepoints, dt.

$$v_d = \frac{V_{irr}\, N_A}{\varepsilon l}\,\frac{dA}{dt} \approx \frac{3.00E{-}3\ .\ 6.022E23}{2.96E4\ .\ 1.00}\,\frac{dA}{dt} \tag{V-7}$$

As for the rate of photon absorption, v_p, the expression from Arnaut *et al.* [53] was slightly altered by accounting the average LDC factor for the PS (Table V-1, column "Mean") and using the absorbance, A, values at 660 nm which is the emission maximum of the LED, λ. As such, with an output power, P, of 13 mW from the LED, Equation V-8, was used as follows:

$$v_p = \frac{\lambda P}{hc}(1 - 10^{-A}) = LDC\ \frac{\lambda P}{hc}(1 - 10^{-A}) = 0.40\ \frac{660E{-}9\ .\ 13.0E{-}3}{6.626E34\ .\ 3.00E8}(1 - 10^{-A}) \tag{V-8}$$

The samples were continuously irradiated with the LED and their absorption spectra were recorded at different timepoints, as described in the Photodecomposition protocol. Figure V–4 shows the variation of absorbance at λ = 651 nm, at those timepoints.

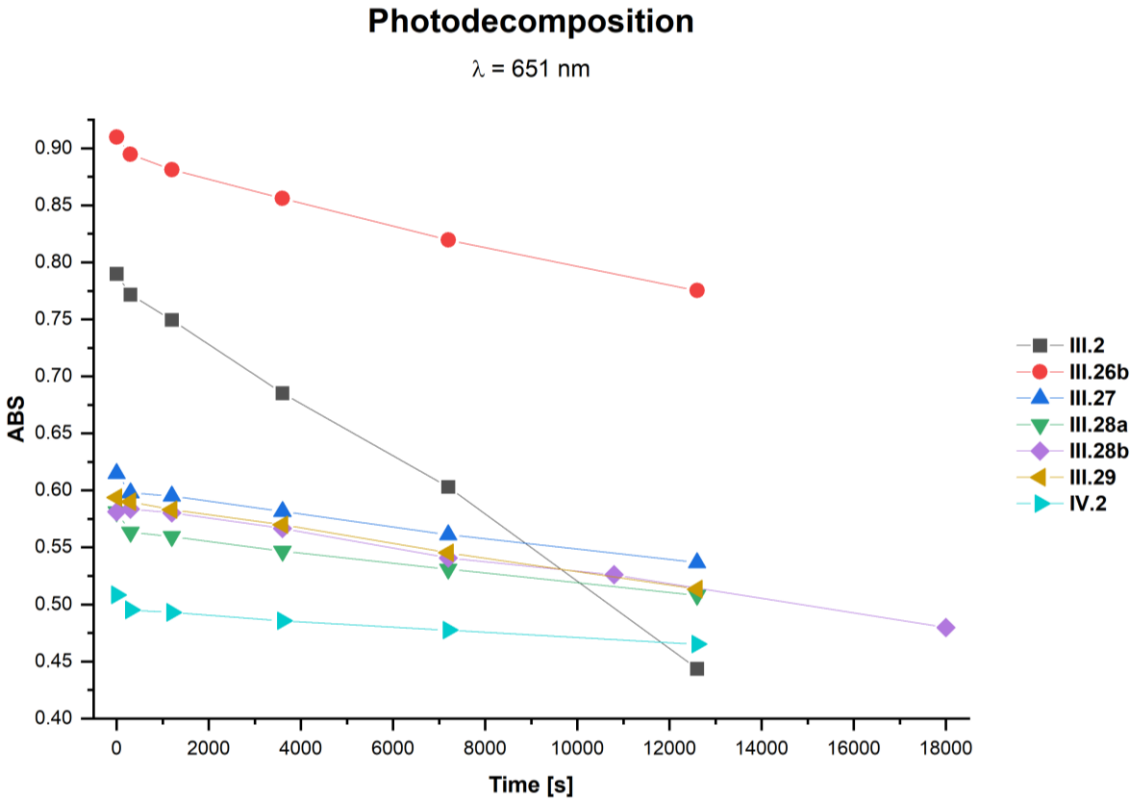

Figure V–4. PS sample absorbance variation after continuous irradiation time, in DMSO (N = 1).

The variation in absorbance already indicates how temoporfin **III.2** should be less photostable compared to the synthesised chlorins. Nonetheless, to define their photostability, we used the values taken from the differences in the absorption spectra after an extended time interval of irradiation to estimate their photodecomposition quantum yield (reported in Table V-3), by using Equation V-6.

Table V-3. Calculated photodecomposition quantum yields (Φ_{pd}) for the PS, in DMSO (N = 1).

PS	Φ_{pd} x 10^{-6} (DMSO)†
III.2	220
III.26b	66.9
III.27	60.8
III.28a	54.8
III.28b	52.7
III.29	60.8
IV.2	36.3

† Estimated values, based on $\varepsilon_{651\ nm}$(temoporfin, methanol) = 2.96E4 $M^{-1}.cm^{-1}$ [53,272].

As shown in Table V-3, temoporfin **III.2** had the highest photodecomposition quantum yield of the studied PS. As for the synthesised chlorins, they were all more photostable as concluded from Figure V–4 with chlorin **III.26b** being the least photostable, followed by chlorins **III.29**, **III.27**, **III.28a**, and **III.28b**, which had very similar values, and the conjugate **IV.2** being the most photostable.

5. Singlet oxygen quantum yield

Among the reactive oxygen species (ROS), the longer intracellular lifetime of singlet oxygen ($^1O_2$) and its consequent larger range of oxidative damage draws the focus on type II reactions [23,32]. As a simpler mechanism, it is believed that most PS undergo this type of photosensitization reaction instead of type I, and temoporfin **III.2** is known to undergo both [23,38]. Given the structural similarity between temoporfin **III.2** and the novel chlorins, it is expected that the photoactivation of these PS also produces singlet oxygen. An ideal PS should have a high singlet oxygen quantum yield, which should translate to higher photooxidative stress caused by this major ROS, leading to cancer cell death. Therefore, it was important to calculate this parameter for the characterisation of the synthesised PS.

The singlet oxygen quantum yield, Φ_Δ, can be estimated through a relative method from Equation V-9 [37,273] using the emission intensity of the sample and a standard, I and I_{ref} respectively, as well as their absorbance, A and A_{ref}, and the known $\Phi_{\Delta ref}$ of the standard compound.

$$\Phi_\Delta = \frac{I}{1-10^{-A}} \times \frac{1-10^{-A_{ref}}}{I_{ref}} \Phi_{\Delta_{ref}} \quad \text{(V-9)}$$

Different techniques can be used for the determination of this quantum yield, using either direct or indirect methods [274]. The most common direct approach is through near-infrared luminescence since it is possible to directly monitor the presence of singlet oxygen with the measurement of phosphorescence at 1270 nm [274,275].

Herein, singlet oxygen sensor green (SOSG) reagent was used to detect the presence of this ROS as a chemical indirect method, since this probe is highly selective for singlet oxygen and emits a green fluorescence when in its presence. Considering that all PS have a similar LDC factor (Table V-1), by diluting all samples to the same absorbance of the standard, the previous Equation V-9 could be simplified to Equation V-10, where the experimental data of the fluorescence intensity in function of the light dose maintained its linearity (m is the first order reaction rate constant).

$$\Phi_{\Delta} = \frac{m}{m_{ref}} \Phi_{\Delta_{ref}} \quad \text{(V-10)}$$

Since the SOSG reagent kit advised to not use DMSO, this was the only experiment that was run in another solvent. As our standard, temoporfin **III.2** in ethanol has a $\Phi_{\Delta\ ref} = 0.63$ [276], this value was used for the calculation of the different singlet oxygen quantum yields in ethanol (due to the PS stocks being prepared in DMSO, the value never exceeded 0.05% DMSO in ethanol).

As noted in Methods, the SOSG protocol was run in three different sets of concentrations. This was a failsafe to ensure the most data points without saturation of the probe. Figure V–5.A and Figure V–5.B showed an obvious divergence from the linear regression at the last data point (15 J/cm^2), which indicates that the probe was starting to saturate. However, the linearity of all data points in Figure V–5.C (seen in the high adjusted R^2 values reported in Table V-4) allowed for the calculation of their singlet oxygen quantum yields, reported in Table V-4.

Table V-4. Singlet oxygen quantum yield for the different PS, in ethanol (N = 1).

PS	*m* (A)	R^2	*m* (B)	R^2	*m* (C)	R^2	Φ_{Δ} (EtOH)†
III.2	906.64	0.961	625.33	0.983	365.97	0.992	**0.63**
III.26b	757.48	0.980	466.73	0.990	259.74	0.995	0.45
III.27	909.65	0.955	554.78	0.984	307.40	0.991	0.53
III.28a	819.72	0.967	490.97	0.989	282.37	0.994	0.49
III.28b	1033.24	0.971	572.89	0.988	288.67	0.994	0.50
III.29	825.82	0.975	466.12	0.992	271.30	0.996	0.47
IV.2	657.50	0.978	387.43	0.993	211.69	0.995	0.36

† Calculated with Equation V-10, based on the experimental data from Figure V–5.C.

The higher SOSG fluorescence from the photoactivation of temoporfin **III.2** produces the most singlet oxygen, followed by a moderate production of singlet oxygen (approximately 0.5) from chlorins **III.27**, **III.28b**, **III.28a**, **III.29**, and **III.26b**, and a lower production of singlet oxygen from the conjugate **IV.2** (Figure V–5.C).

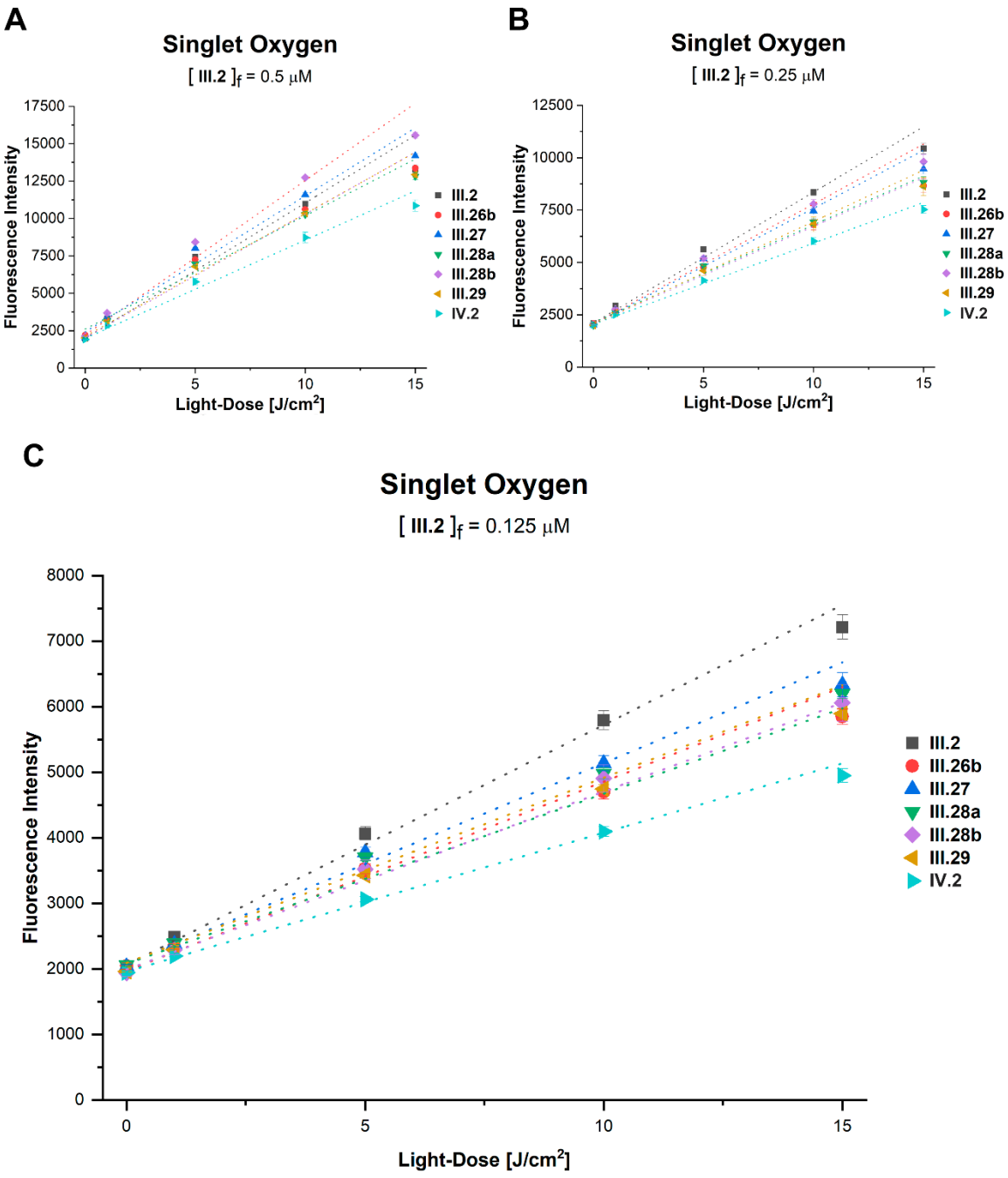

Figure V–5. Generation of $^1O_2$ in ethanol (DMSO did not exceed 0.05%) assessed by the fluorescence of SOSG reagent. Experimental data of triplicate wells shown as mean ± SEM (N = 1).
Linear fit represented as a dotted line.
Different concentrations of the standard: temoporfin III.2 in (A) 0.5 μM; (B) 0.25 μM; (C) 0.175 μM.

6. Discussion

We started by performing a preliminary study to define the LDC factors for the different PSs (Table V-1) to correct the number of photons absorbed by the compounds when irradiated by a LED lamp, as this would be the light source to be used in phototoxicity studies.

As for the photophysical studies, it is important to highlight that most of them were performed in DMSO, as this was the only solvent in which all PSs were soluble. Initially, evaluation of the fluorescence quantum yield was done (Table V-2), to ascertain the similarity of the 4,5,6,7-tetrahydropyrazolo[1,5-*a*]pyridine-fused chlorins to temoporfin **III.2** and whether the structural differences between them would lead to different photophysical features. However, it was observed that the synthesised PSs were almost equivalent amongst themselves and to the positive control used for comparison, temoporfin **III.2**, allowing for further characterisation without the need to consider correction factors when comparing these PSs.

The photodecomposition quantum yields in DMSO (Table V-3) of the synthesised chlorins were considerably lower than for temoporfin **III.2** – which is known to have high photodecomposition [271], – followed by **III.26b**, **III.29**, **III.27**, **III.28a**, and **III.28b** in a similar range, and with the conjugate **IV.2** being the more photostable. This reinforces previous observations indicating that the photostability of chlorins can be greatly enhanced with the simple introduction of the 4,5,6,7-tetrahydropyrazolo[1,5-a]pyridine-fused ring system present in the new chlorin derivatives [153,154,157]. Nevertheless, it is also important to highlight – even if dealing with a different solvent – that the singlet oxygen quantum yields (Table V-4) of the synthesised chlorins were lower (with **IV.2** having the lowest value) than the one of temoporfin **III.2**, and it is known that singlet oxygen contributes to photodecomposition [23]. However, since the differences between the singlet oxygen quantum yield of all PSs are not very disparate, compared to the obvious decrease of photodecomposition quantum yield going from temoporfin **III.2** to the synthesised chlorins, the difference cannot be attributed only to bleaching effects from singlet oxygen generation.

For instance, the ratio of the singlet oxygen quantum yields of temoporfin **III.2** (0.63) and 4,5,6,7-tetrahydropyrazolo[1,5-a]pyridine-fused chlorin **III.28b** (0.50) is not proportional to the ratio of the observed photodecomposition quantum yields for the same chlorins (1.26 vs. 4.29). As such, it demonstrates that the fused ring added to the general substructure of temoporfin **III.2** yielded "locked" chlorins [153,155,157] – geminal dialkylated β-substituted chlorins that minimise the problems of photodegradation and stability known to chlorins [277,278] – and that none of them surpassed the recommended value of 10^{-5} [53,279]. As for the synthesised chlorins, except **IV.2**, it seems that the presence of hydroxyl groups decreases the photodegradation.

For the singlet oxygen quantum yields, as mentioned above, temoporfin **III.2** had the highest value compared to the synthesised chlorins and the conjugate **III.2** had the lowest. Among the other synthesised chlorins, the values were within the same range, but it appears to be no direct relationship between the photodecomposition quantum yields and the ability to generate singlet oxygen. Chlorins **III.26b** and **III.29** were the least photostable and yet produce the least singlet oxygen, while **III.28a** and **III.28b** that were the more photostable, have a higher singlet oxygen quantum yield. However, chlorin **III.27** that was expected to rank somewhere between chlorins **III.26b** and **III.28**, as its structure is in an intermediate level of alcohol deprotection (Figure V–1.B: same ester as **III.26b**; same Ar group as **III.28**), was actually the synthesised chlorin with the highest singlet oxygen quantum yield. The low singlet oxygen quantum yield found in the conjugate **IV.2** might be due to poor solubility in an aqueous solvent.

Overall, it was expected that the photophysical properties of the PSs would not change after coupling with FA [143], and this seemed to be the case for the fluorescence quantum yield evaluation among all the PSs. Still, while not drastically different, the conjugate **IV.2** had relatively lower values for the photodecomposition and singlet oxygen quantum yields, in comparison to the free PS **III.29**. Without disregarding the effect that lower single oxygen generation will consequently lead to more photostability, it is also important to not discard the possibility of purity issues concerning the conjugate **IV.2** (as the SOSG test deals in concentrations of the PSs).

7. Experimental

7.1. Instrumentation

Absorption spectra were measured in UV-visible Recording Spectrophotometer (Shimadzu UV-2100), while emission spectra were recorded on Fluorescence Spectrometer (Perkin Elmer LS45). The samples were diluted in the desired solvent and measured at room temperature using either standard or fluorescence quartz cuvettes, as appropriate, with an optical path of 1 cm.

The light source used for photodecomposition evaluation and to detect the singlet oxygen quantum yield was a LED lamp from HIGROW LED (model GL36A), emission maximum at 660 nm with HWL = 26.4 nm. The fluence of the LED was verified with a Coherent LaserCheck power meter, choosing a wavelength of 651 nm.

For the singlet oxygen detection protocol, fluorescence emission of the SOSG reagent (λ_{ex} = 504 nm; λ_{em} = 525 nm) was measured using a Synergy HT Multi-Mode Microplate Reader (BioTek) with the filters of λ_{ex} = 485/20 nm and λ_{em} = 530/20 nm.

Graphical representations and linear regression calculations were created and processed with OriginPro© 2018 (64-bit) software (OriginLab Corporation, Northampton, MA, USA).

7.2. Materials

7.2.1. Reagents and solvents

Ethanol, oxazine-170, DMSO and DMSO Hybri-Max™ were purchased from Sigma-Aldrich. Invitrogen™ SOSG reagent (S36002) was purchased from Thermo Fisher Scientific.

7.2.2. Photosensitisers

Chlorins **III.26b**, **III.27**, **III.28a**, **III.28b**, and **III.29** were synthesised as described in Chapter III. The conjugate **IV.2** was synthesised as described in Chapter IV. Temoporfin **III.2** was kindly provided by Senge Group at Trinity College Dublin. All structures represented in Figure V–1.B.

Stock solutions were prepared in DMSO Hybri-Max™ in the mM range and stored at -20 ºC. The analysed samples were prepared by diluting from the stock solution with the intended solvent.

7.3. Methods

7.3.1. Fluorescence quantum yield protocol

The fluorescence spectra of all PS and oxazine-170 samples were measured with λ_{ex} = 548 nm. The PS samples were prepared in DMSO with an initial absorbance of 0.1 at 651 nm and then diluting three times. For the reference, oxazine-170 in ethanol (Φ_F = 0.579 [270]) was used. The values reported in Table V-2 were calculated with Equation V-5.

7.3.2. Photodecomposition protocol

All samples were prepared for a final volume of 3 mL in a quartz cuvette and placed in a setup with a magnetic stirrer to ensure a homogeneous irradiation of the sample, with the LED at 13 mW of output power (fluence rate of 49 mW/cm^2). The absorption spectrum of each sample was recorded after each timepoint of irradiation, at 651 nm. Using the changes in the optical absorption, the

respective variables were replaced in Equations V-7 and V-8 to calculate the photodecomposition quantum yield (Equation V-6).

7.3.3. Singlet oxygen detection protocol

The SOSG reagent was used as a fluorescent probe for singlet oxygen. Temoporfin **III.2** in ethanol was used as the standard in three different final concentrations (0.5, 0.25, and 0.175 μM), to ensure the best fit of the linear regression without saturating the probe.

The general procedure is hereby described for the data used to estimate the singlet oxygen quantum yield (Figure V–5.C), i.e., a final concentration of the standard **III.2** of 0.175 μM/well in ethanol, after adding the SOSG reagent. After preparing and measuring the absorbance of the standard, the samples of the synthesised chlorins were diluted from their stocks in ethanol to have the same absorbance as temoporfin **III.2**. Next, all the samples were transferred to triplicate wells in a 96-well plate. The fluorescent SOSG probe was then added at the final concentration of 5 μM/well and the fluorescence emission was measured, using the microplate reader, before (LD = 0 J/cm^2) and after each consecutive 5 J/cm^2 irradiation with the LED lamp (up to a total LD = 15 J/cm^2). The singlet oxygen quantum yield for each synthesised PS was then estimated using Equation V-10.

Chapter VI:

In vitro evaluation

There is no such thing as a special category of science called applied science; there is science and its applications (…).

Louis Pasteur

1. Introduction

According to the Global Cancer Observatory [280], breast cancer has the highest incidence across all ages and both sexes, worldwide, reaching over 2.3 M cases (Figure VI–1). It is the leading cause of cancer death in females [2,281].

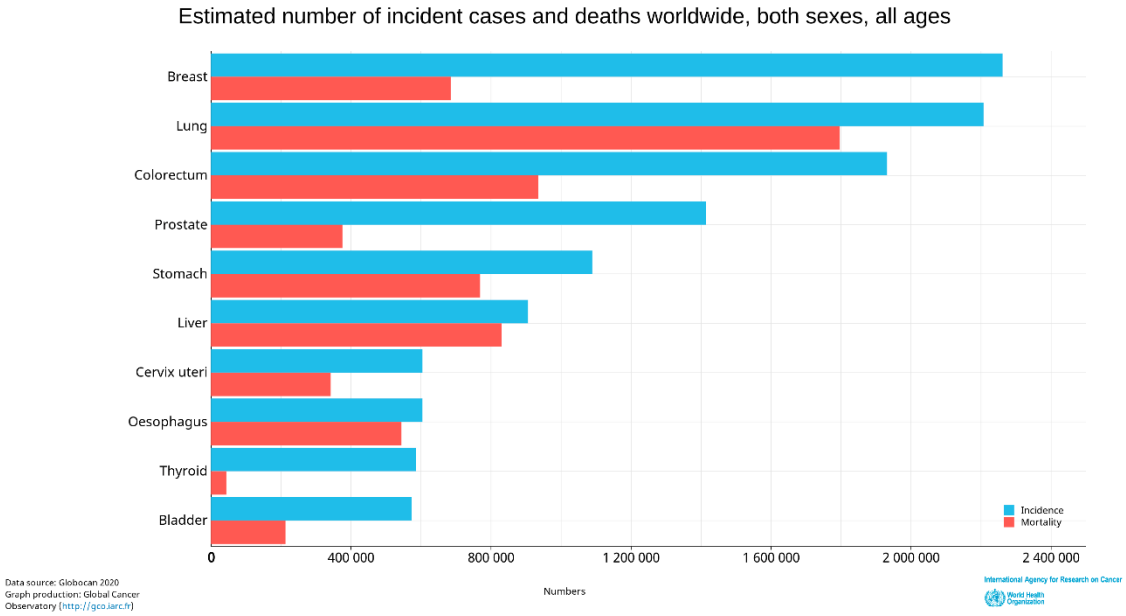

Figure VI–1. Estimated incidence and mortality of the most prevalent cancers worldwide; adapted from Globocan 2020 [280]**.**

As a highly heterogeneous disease, breast cancer can be defined through different molecular subtypes, according to the presence, or absence, of specific receptors. Breast cancer subtypes include luminal A, luminal B, human epidermal growth factor receptor-2 (HER-2) positive B2, HER-2 overexpression, and basal-like triple-negative breast cancer (TNBC), as characterised in Table VI-1 [76,282]. The TNBC accounts for 10-15% of the diagnosed breast cancer [77] and it is known to be highly invasive and metastatic, prone to relapse, and with a poor prognosis, due to the negative expression of oestrogen receptor (EsR), progesterone receptor (PgR), and HER-2. This molecular phenotype makes it unable to take advantage of hormone- and molecular-targeted therapies (e.g., HER-2 antibodies). Therapeutic options include surgery, chemotherapy and radiotherapy, which often lead to an insufficient outcome – the median overall survival for a metastatic patient is ca. 18 months [77], compared to the two-thirds of women worldwide [2] making up the five-year net survival for breast cancer [76,77]. These numbers attest for the need of more effective targeted therapies for the TNBC subtype.

Table VI-1. Breast cancer molecular subtypes.

SUBTYPE	DESCRIPTION
Luminal A	EsR^+ and/or PgR^+, HER-2^-, $Ki67^+ < 20\%$ Luminal A cancers are sensitive to hormone treatments, tend to grow slowly, and have a good prognosis.
Luminal B	EsR^+ and/or PgR^+, HER-2^-, $Ki67^+ \geq 20\%$ Luminal B cancers are less sensitive to hormone treatments and tendo to grow slightly faster than luminal A cancers, with a worse prognosis.
HER-2^+ B2	EsR^+ and/or PgR^+, HER-2 overexpression HER-2 enriched cancers usually grow faster than luminal subtypes and are associated with a worse prognosis but are often successfully treated with targeted therapies aimed at the HER-2 protein.
HER-2 overexpression	EsR^- and PgR^-, HER-2 overexpression Like the HER-2^+ B2 subtype, it is usually treated by targeting HER-2.
TNBC	EsR^-, PgR^-, and HER-2^- TNBC cancers are more aggressive and highly invasive, with the worst prognosis, as it is not sensitive to hormone treatments.

Ki67 is a protein that serves as an indicator of how fast cancer cells grow, with the percentage indicating the immunohistochemical staining results for patient samples [76].

As mentioned in Chapter I, photodynamic therapy (PDT) presents an effective, light-delivered, less invasive treatment instead of/adjuvant to traditional therapies, with the possibility of increasing selectivity through targeting [1]. Higher selectivity means preferential accumulation in tumour tissue and, consequently, a reduction of unwanted side effects (e.g., prolonged skin photosensitivity in temoporfin, **III.2**, due to a half-life of up to 65 hours [29,34,36–38]).

In 2006, El-Akra *et al.* reported an example of targeted-PDT against breast cancer [283]. The purpose of their work was developing an oestradiol-linked PS that targeted the EsR which is involved not only in cell growth, but also in angiogenesis, and with this method El-Akra *et al.* would selectively tackle the destruction of the tumour via cell death and by inducing damage of the blood vessels that supply the tumour with the necessary nutrients for its development. As represented in Scheme VI-1, the PS chosen was pheophorbide *a* (**VI.1**), a derivative of chlorophyll *a* with a high singlet oxygen yield, which was conjugated to the oestradiol via amide bonds to linkers with different sizes (**VI.2a** and **VI.2b**), yielding two conjugates. The assays were conducted in the EsR-positive breast cancer cell line, MCF-7, and the EsR-negative SKBR3 cell line, with conjugate **VI.3b** showing an uptake 2.5-fold higher after five hours of incubation, as well as seven times more phototoxicity ($\lambda > 400$ nm, 8.2 J/cm^2; ED_{50} = 1.3 E-8 M) than the free pheophorbide *a* (ED_{50} = 8.5 E-8 M). The other conjugate **VI.3a** was deemed to have a linker too small to allow for recognition of the oestradiol by the EsR). Besides these results they also successfully selectively inhibited the EA.hy 926 vascular endothelial cells [283].

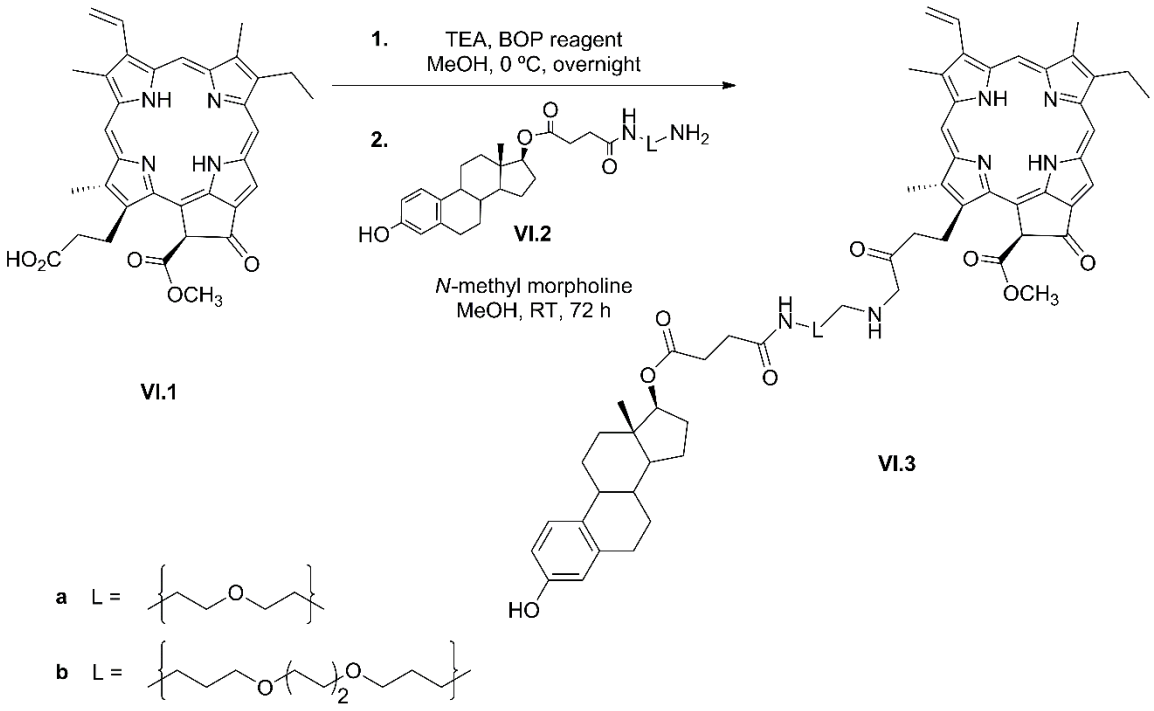

Scheme VI-1. Conjugation of phephorbide *a* with different linkers, as reported by El-Akra *et al.* [283].

Regarding TNBC in which targeting the EsR is not viable, Hu *et al.* [284] conjugated factor VII, a highly selective, endogenous ligand for tissue factor receptor, with the PS verteporfin. The resulting conjugate decreased the effective concentration needed to kill 50% of the cells (EC_{50}) by at least three-fold (EC_{50} = 0.25 µM, compared to the non-targeted protocol EC_{50} = 1.11 µM) with the irradiation of a 689 nm laser for a light dose (LD) of 60 J/cm^2. They further reported that their conjugate was also more effective *in vivo* by inhibiting tumour growth in mice [284].

More recently, Kim *et al.* [126] took advantage of the overexpression of the epidermal growth factor receptor (EGFR) found in TNBC and developed a theranostic compound, RedoxT, by conjugating chlorin e_4 with peptide GE11 (specific to EGFR) [126]. Kim *et al.* showed an increase in the uptake with the increase of the level of EGFR expression and reported an improved phototoxicity when comparing RedoxT with the free chlorin-e_4: RedoxT had an IC_{50} (20 J/cm^2) of 0,66 µM for MDA-MB-468 (high EGFR expression) and 1.80 µM for MDA-MB-231 (moderate EGFR expression), while chlorin-e_4 had IC_{50} of 2.22 µM and 2.98 µM, respectively [126].

In this chapter, the evaluation of our novel chlorins **III.26b**, **III.27**, **III.28a, III.28b**, and **III.29**, as well as the synthesised conjugate **IV.2** targeting folic acid (FA) as PDT agents is described (all structures shown in Figure VI–2). A better understanding of the photobiology results for the free chlorins will be decisive in the use of these molecules as PS, especially the azide derivative **III.29**, which was synthesised with the goal of being the precursor of future third-generation PS. By undergoing "click" chemistry, this chlorin could be personalised and used in targeted-PDT specific

to the molecular needs of any cancer patient. Regarding TNBC, the MDA-MB-231 cell line is compatible with our interest in evaluating the free chlorins as PS against aggressive breast cancer cells, as well as observing how the conjugate **IV.2** – synthesised as proof-of-concept of a targeted-PS for folate receptor-α (FRα) using **III.29** – is internalised, in terms of uptake and cellular localisation by a TNBC that overexpresses this receptor [76,201,285].

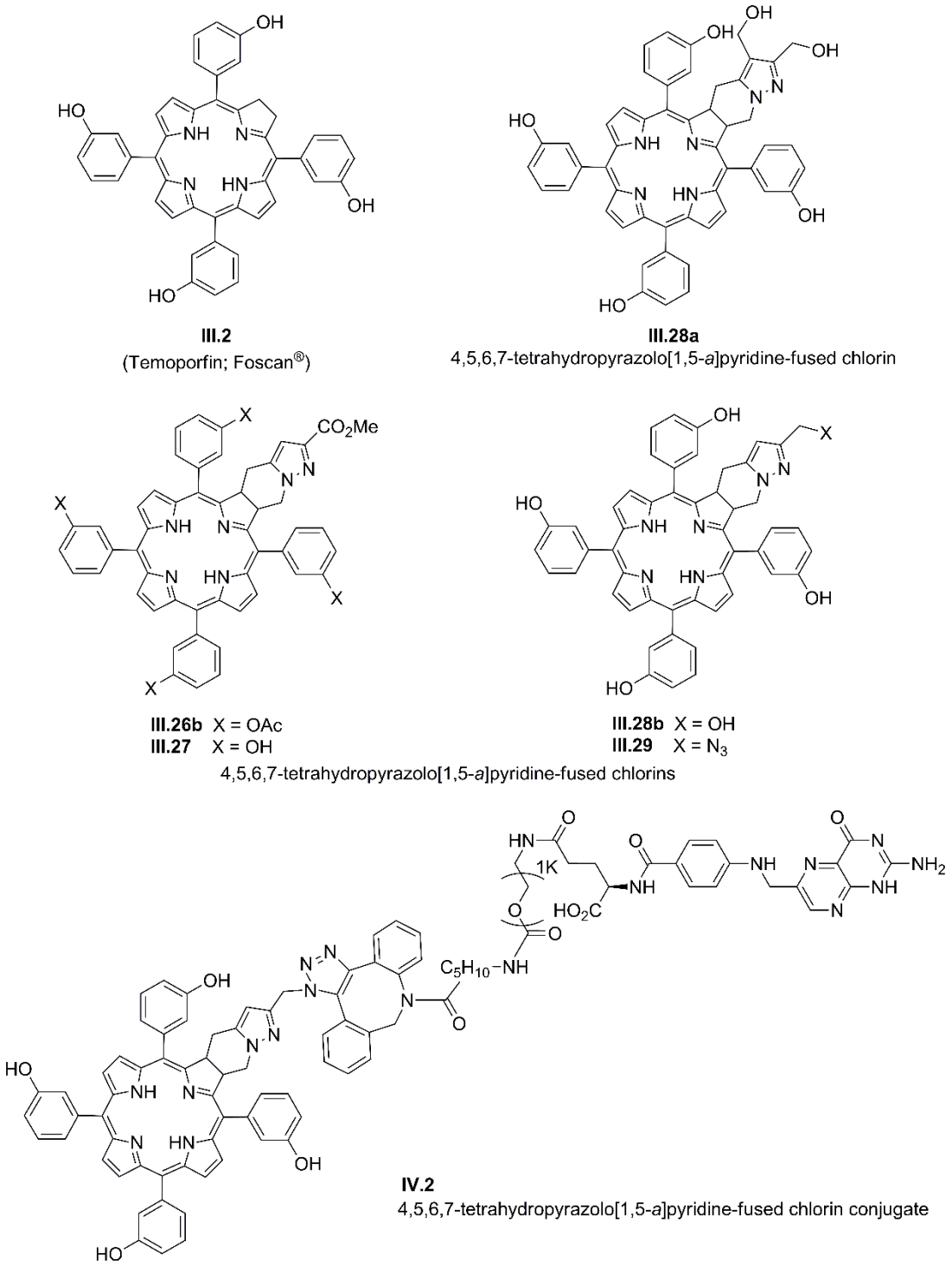

Figure VI–2. Structures of temoporfin (III.2) and the novel chlorins III.26b, III.27, III.28a, III.28b, III.29, and IV.2 (as a mixture of regioisomers).

2. Dark toxicity

An ideal photosensitizer should not exhibit toxicity in the absence of light. To ascertain optimal sub-lethal doses without photoactivation, solutions of each PS in Dulbecco's Modified Eagle's Medium (DMEM) in concentrations ranging from 0.3125 µM to 10 µM were added to the plated MDA-MB-231 cells/well in 96-well plates and left to incubate in the dark. After 24-hour, cell viability was assessed by measuring the fluorescence intensity of metabolised resazurin of the treated cells relatively to the negative controls. The results and respective half-maximal inhibitory concentrations (IC_{50}) are represented in Figure VI–3.

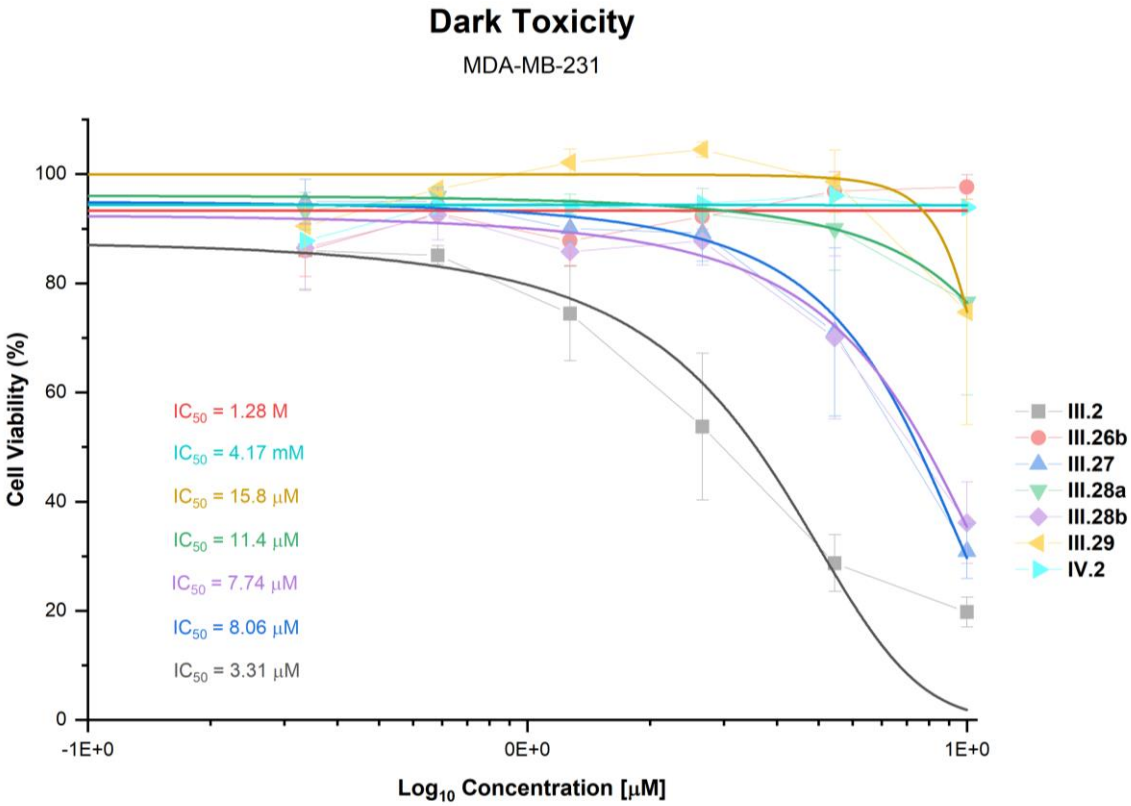

Figure VI–3. Dark toxicity in MDA-MB-231 cells. Data is presented as mean ± SEM (N=3), with the respective dose-response fitted curve used for IC_{50} calculation.

As PSs, it is important for these compounds to show negligible toxicity in the dark, and yet, our positive control – temoporfin **III.2** – showed the lowest IC_{50} (3.31 µM) making it the most cytotoxic from the evaluated compounds.

Chlorins **III.27** and **III.28b**, which have *meso*-tetra(3-hydroxyphenyl) substituents as in temoporfin but with different exocyclic-ring substituents (methyl ester vs. hydroxymethyl group), were the next two more cytotoxic compounds. Chlorins **III.26b, III.28a**, **III.29**, and **IV.2** were the safest PS in the dark, with an estimated IC_{50} > 10 µM. The low dark toxicity was especially visible for chlorin

III.26b – making up a group of the chlorins that were bulkier and/or had less hydroxyl substituents – and the conjugate **IV.2**.

The fact that PSs with similar sizes can be grouped from lowest to highest IC_{50}, according to changes in the substituents that lead to decrease in amphiphilicity or a disturbance of the molecule's geometry, supports the hypothesis that cellular uptake might be the factor which weighs more in differences found between the six chlorins regarding photodynamic activity.

3. Phototoxicity

Considering the results from dark cytotoxicity, PS concentrations for phototoxicity assays were adjusted as required. Cells were incubated with the selected concentrations of each PS during 24 h followed by irradiation with a light-emitting diode (LED) lamp.

In Chapter V, a LD correction (LDC) factor was calculated according to the method described by Schaberle [267], through defining the number of photons absorbed, it was possible to accurately report the LD used. LED lamp (λ_{em} = 660 nm) used has a shift from the chlorins' absorption peak at 651 nm, as seen in Figure V–2, and we found that, on average, the PS would absorb only 40% of the intended LD. Therefore, to evaluate the phototoxicity of the PS at a LD = 1.0 J/cm^2, the LD delivered to cells had to be 2.5 times higher (LD_a = 2.5 J/cm^2) (see Table V-1).

By using a power meter to measure the fluence rate, F_R, of the LED lamp, the time interval (Δt) of irradiation was calculated as follows (Equation VI-1):

$$\Delta t\ (s) = \frac{LD_a\ (J/cm^2)}{F_R\ (W/cm^2)} \qquad \text{(VI-1)}$$

One day after the irradiation, cell viability was assessed through the resazurin reduction assay described for dark toxicity. The fitted dose-response curve adjusted to the data and the IC_{50} for each PS are shown in Figure VI–4 and Figure VI–5, for MDA-MB-231 and NIH/3T3, respectively.

In the breast cancer cells, almost all the photoactivated PSs exhibited IC_{50} in the nM range, except for **III.26b** which had an IC_{50} = 1.30 μM. The evaluated PSs could be ranked from the most to the least phototoxic as follows: **III.2** > **III.28b** > **III.29** > **III.27** > **III.28a** > **IV.2** >> **III.26b**.

The phototoxicity of the different chlorins in NIH/3T3 followed a similar trend as the one observed in the breast cancer cells: **III.2** > **III.28b** ~ **III.29** ~ **III.27** > **III.28a** > **IV.2** > **III.26b**.

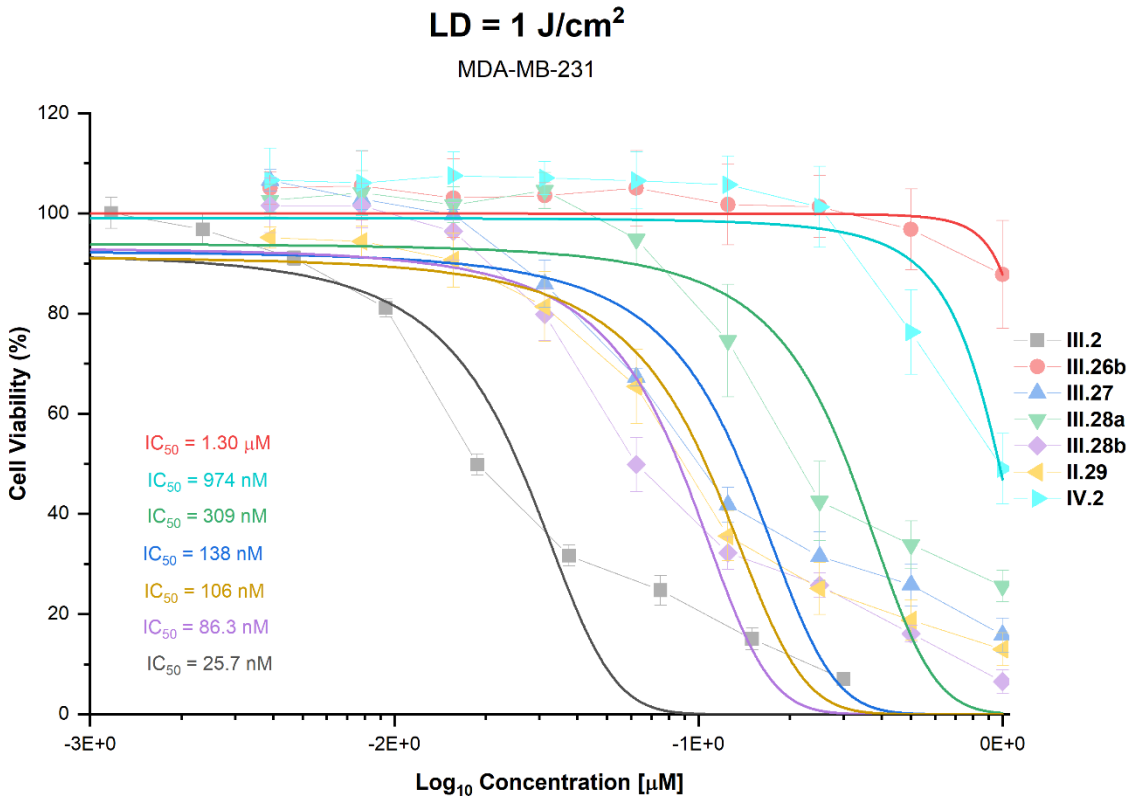

Figure VI–4. Phototoxicity evaluation with a LD of 1 J/cm² in MDA-MB-231 cells. Data is presented as mean ± SEM (N=3), with the respective dose-response fitted curve used for IC_{50} calculation.

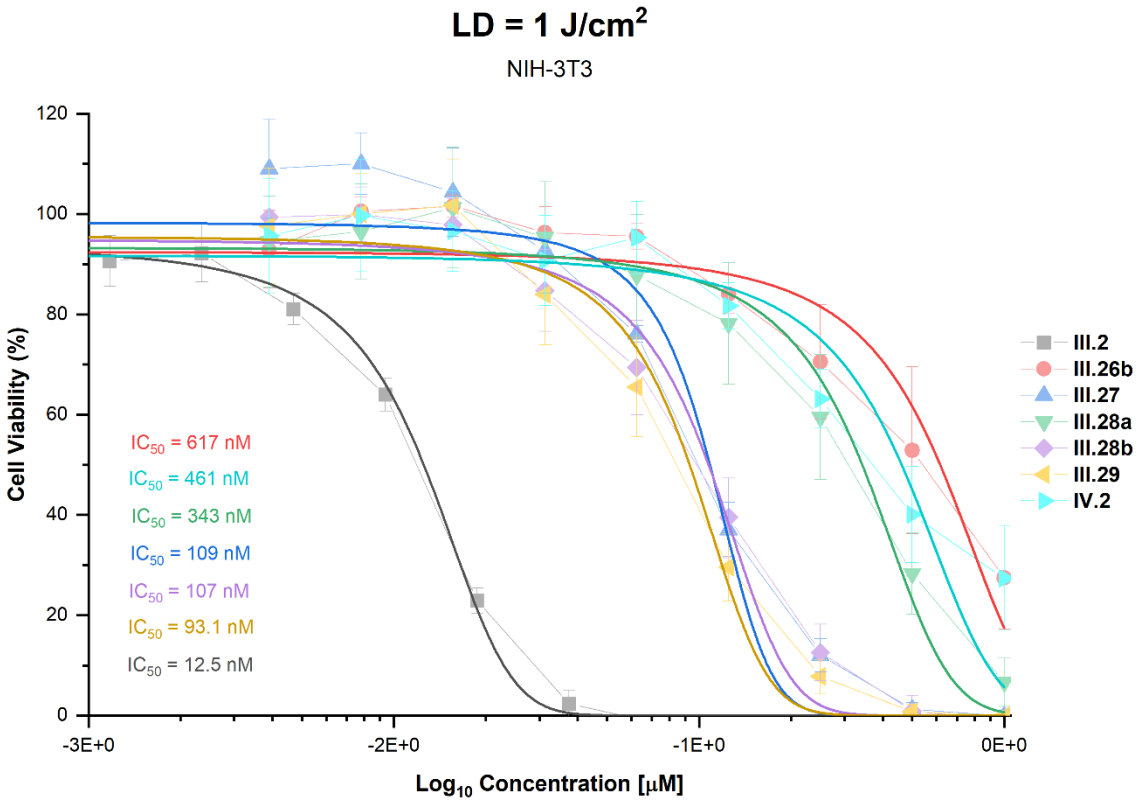

Figure VI–5. Phototoxicity evaluation with a LD of 1 J/cm² in NIH-3T3 cells. data is presented as the mean ± SEM (N=3), with the respective dose-response fitted curve used for IC_{50} calculation.

4. Cellular uptake

The differences observed on the phototoxicity studies are not explained by the chlorins photophysical/photochemical properties, which are relatively similar. We then hypothesized that the different chlorins derivatives might have different cellular internalization levels. Cellular uptake studies were performed by flow cytometry in both MDA-MB-231 and NIH/3T3 cells after an incubation period of 3, 6 or 24 h with 2.5 µM of each chlorin. Our data demonstrated that the uptake of all chlorins increase over time however, relative levels of internalization appear to be different across our family of compounds. The following trend of cell internalization, **III.2** >> **III.27** > **III.28b** > **III.29** > **III.28a** > **IV.2** > **III.26b**, was observed on both cell lines. Of note, the order of cell uptake (Figure VI–6 and Figure VI–7) follows the same trend of the phototoxicity (Figure VI–4 and Figure VI–5).

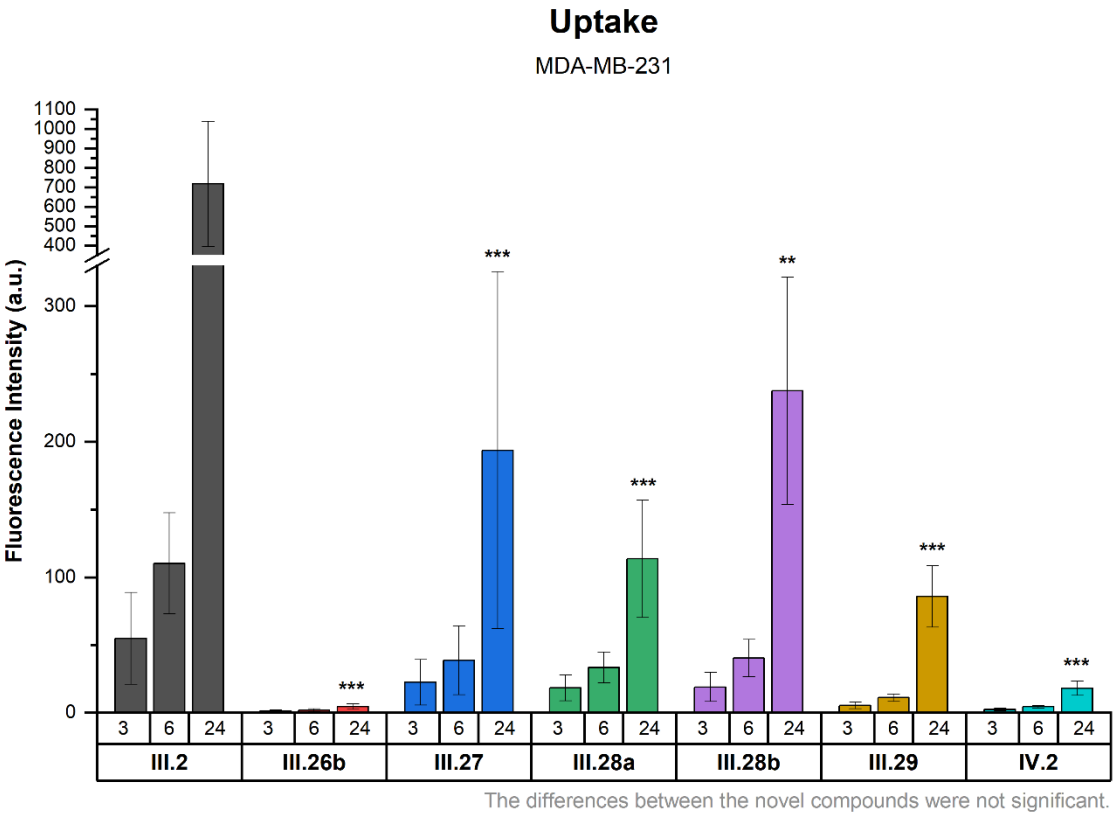

Figure VI–6. Cellular internalization of all chlorins in MDA-MB-231 cells. Data is presented as the mean ± SEM (N = 2). Statistical significance was evaluated using two-way ANOVA in comparison to temoporfin (III.2). *p < 0.05; **p < 0.01; ***p < 0.001.

Temoporfin **III.2** uptake was significantly higher than observed for the other chlorins. which corroborates the phototoxicity results, and what is known about this compound being considered one of the most active commercial PS even with low drug and LD [40,42,44].

As for the synthesised chlorins, compounds **III.28b**, **III.27**, and **III.26b** were chosen amongst the novel 4,5,6,7-tetrahydropyrazolo[1,5-*a*]pyridine-fused chlorins for comparison of different levels of protected hydroxyl groups. Chlorin **III.26b** showed the lower uptake values out of all the chlorins, which can be explained not only by the bulkier geometry of the *meta*-acetoxy groups (see Figure VI–2), but the most plausible reason is the significant increase of the molecule's hydrophobicity. Compounds **III.28b** and **III.27** on the other hand, showed similar uptake values which were higher than the other synthesised PS, with **III.27** having a slightly lower uptake at the 24-hour timepoint, possibly because of having a bulkier exocyclic-ring substituent (Figure VI–2), not to mention the methyl ester of **III.27** is more hydrophobic than the hydroxylmethyl group found on **III.28b**.

Chlorin **III.28a**, having an additional hydroxymethyl group at the exocyclic ring than chlorin **III.28b**, showed lower cellular uptake than PS **III.28b** and **III.27**. This difference was most likely caused by the larger size as well as the lower amphiphilicity of chlorin **III.28a**. The PS that showed the lowest uptake, besides chlorin **III.26b**, was the "clickable" variant **III.29**. As mentioned before, this chlorin was derivatised from **III.28b** through replacement of the hydroxylmethyl group substituent (Figure VI–2) by an azide-containing functional group that could participate in "click" chemistry. This functional group interconversion leads to a molecule having a 1,3-dipolar moiety which might affect the ability of **III.29** to cross the cell membrane.

The observed low uptake of the conjugate **IV.2** explains the decreased phototoxicity going from the azide derivative **III.29** to the triazole derivative **IV.2**, an effect that seems to lessen the impact expected for a targeted molecule in the presence of a cell line that overexpresses the target receptor.

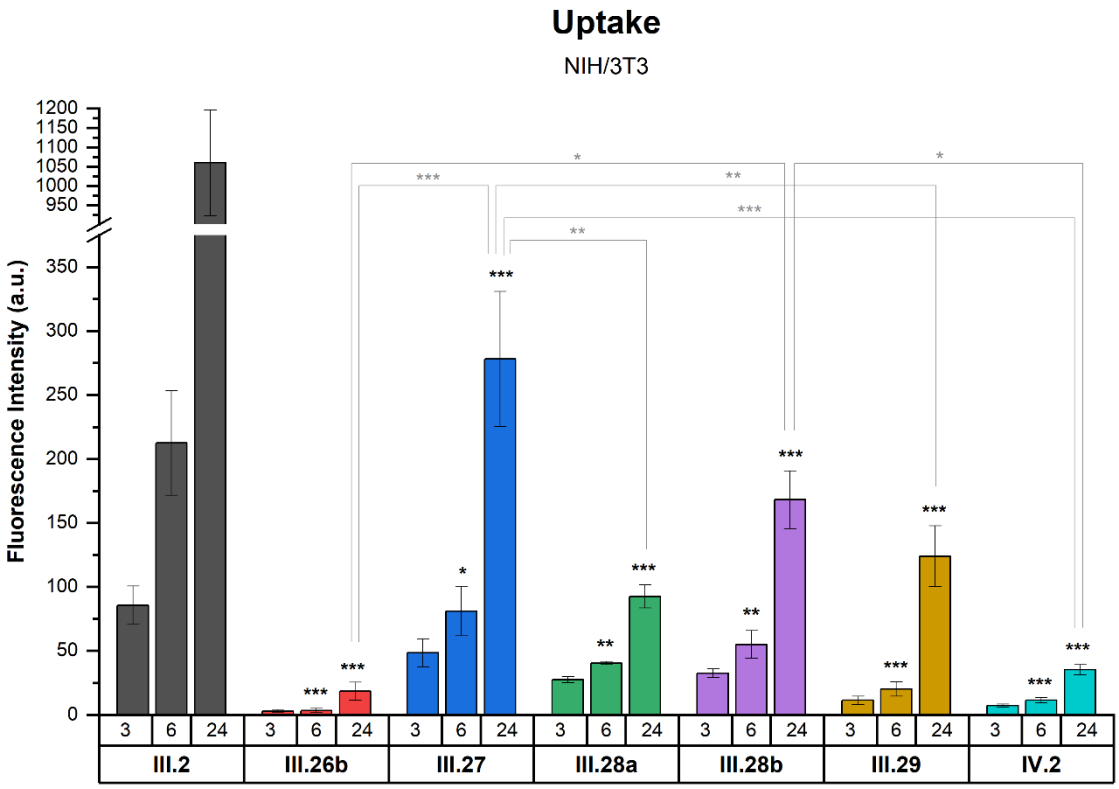

Figure VI–7. Cellular internalization of all chlorins derivatives evaluated in NIH/3T3 cells. Data is presented as mean ± SEM (N=3). Statistical significance was evaluated using two-way ANOVA in comparison to temoporfin (III.2) *p < 0.05; **p < 0.01; ***p < 0.001. The same values of significance apply to the markings in grey above the brackets, representing the statistical difference between PS.

In the NIH/3T3 cell line, the conjugate **IV.2** was also one of the molecules with lowest uptakes, with levels above **III.26b** only. Overall, the PS evaluated showed an increased fluorescence intensity relative to negative controls, compared to MDA-MB-231 cells (Figure VI–6), but comparable to what was expected from the dark toxicity results. The statistical significance of the increased uptake of temoporfin **III.2** was higher than for MDA-MB-231 cells, at the 24-hour and 6-hour timepoints, with the difference at 6-hour timepoint being more pronounced.

The decreasing trend in uptake of the other chlorins was similar to the one observed for the breast adenocarcinoma cells (Figure VI–6), with two differences: chlorin **III.27** was the one showing the highest uptake instead of **III.28b** and **III.29** showed higher uptake than **III.28a**, although these differences may not be statistically significant. Unlike the cancer cell line, in the case of NIH/3T3 cells it was possible to see significant differences between the synthesised chlorins with higher uptake (**III.27** and **III.28b**) and the most protected chlorin **III.26b**, chlorin **III.27** showing also significant higher internalization than chlorins **III.29** and **III.28a**.

Overall, the cellular uptake order correlates with the observed photocytotoxicity, with chlorins with the higher uptake values being the more phototoxicity (Figure VI–4 and Figure VI–5). However, azide-substituted chlorin **III.29** showed dark toxicity and uptake values similar to those presented by chlorine **III.28a**, but when irradiated it was the second most phototoxic molecule among the novel synthesised chlorins (only after **III.28b**).

5. Co-localization studies

Intracellular distribution studies were performed by confocal microscopy with the goal of confirming the data obtained by flow cytometry while studying the organelle tropism of each chlorin derivative. It is known that temoporfin **III.2** accumulates mainly at the endoplasmic reticulum (ER) with some presence in the Golgi apparatus (GA) [25,272]. Therefore, our study focused on determining whether the novel chlorin derivatives presented the same subcellular accumulation feature. Osteosarcoma cells, U-2 OS, stably expressing green fluorescent protein (GFP) attached to *CALR* (ER staining) or *GALT1 (GA staining)*, were incubated with 5 μM of each PS for 24 hours.

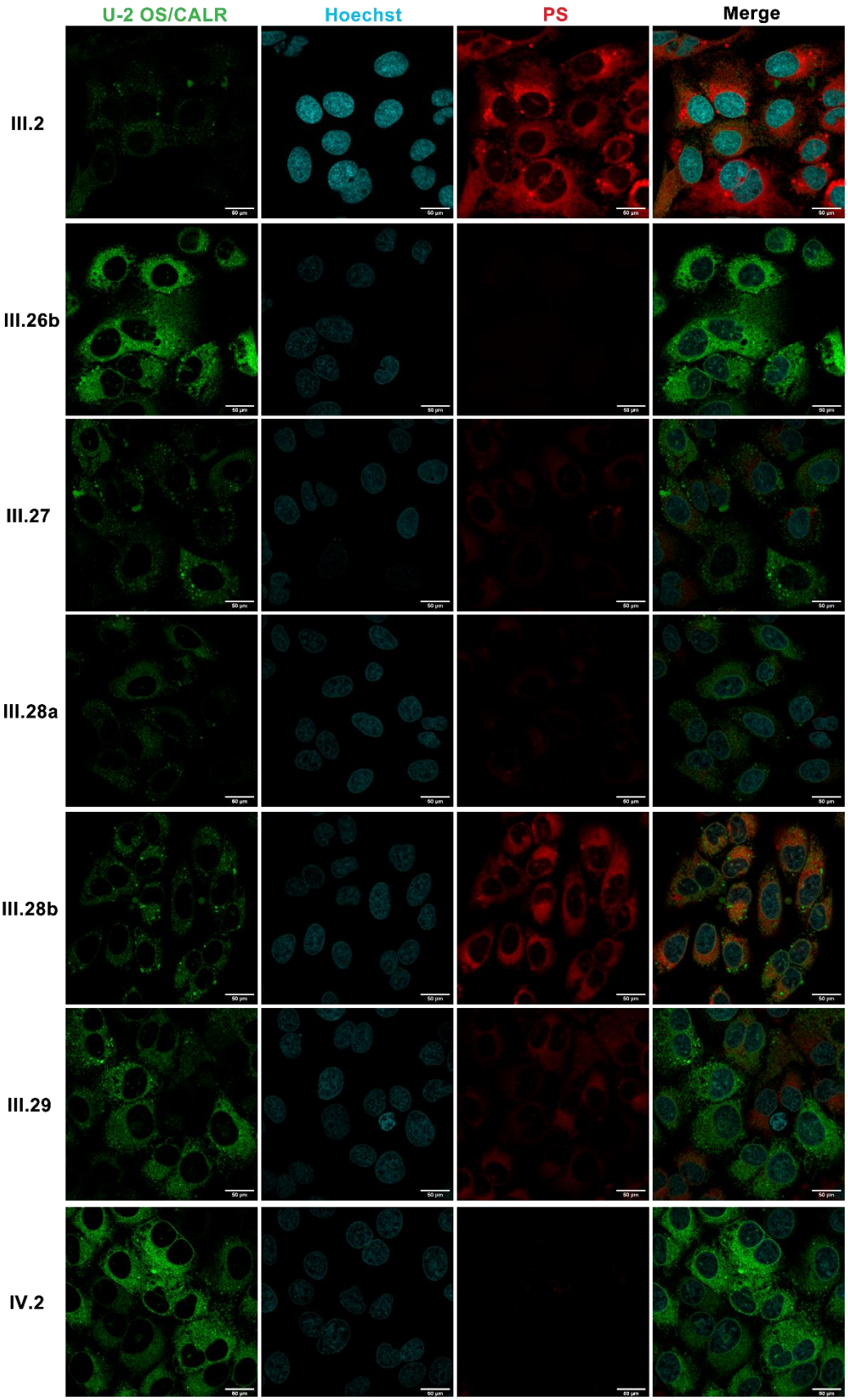

Figure VI–8. Representative images of confocal microscopy of U-2 OS stably expressing CALR-GFP (ER staining, green) incubated with each chlorin (red) and nucleus stained with Hoechst (blue). Scale bar = 10 µm.

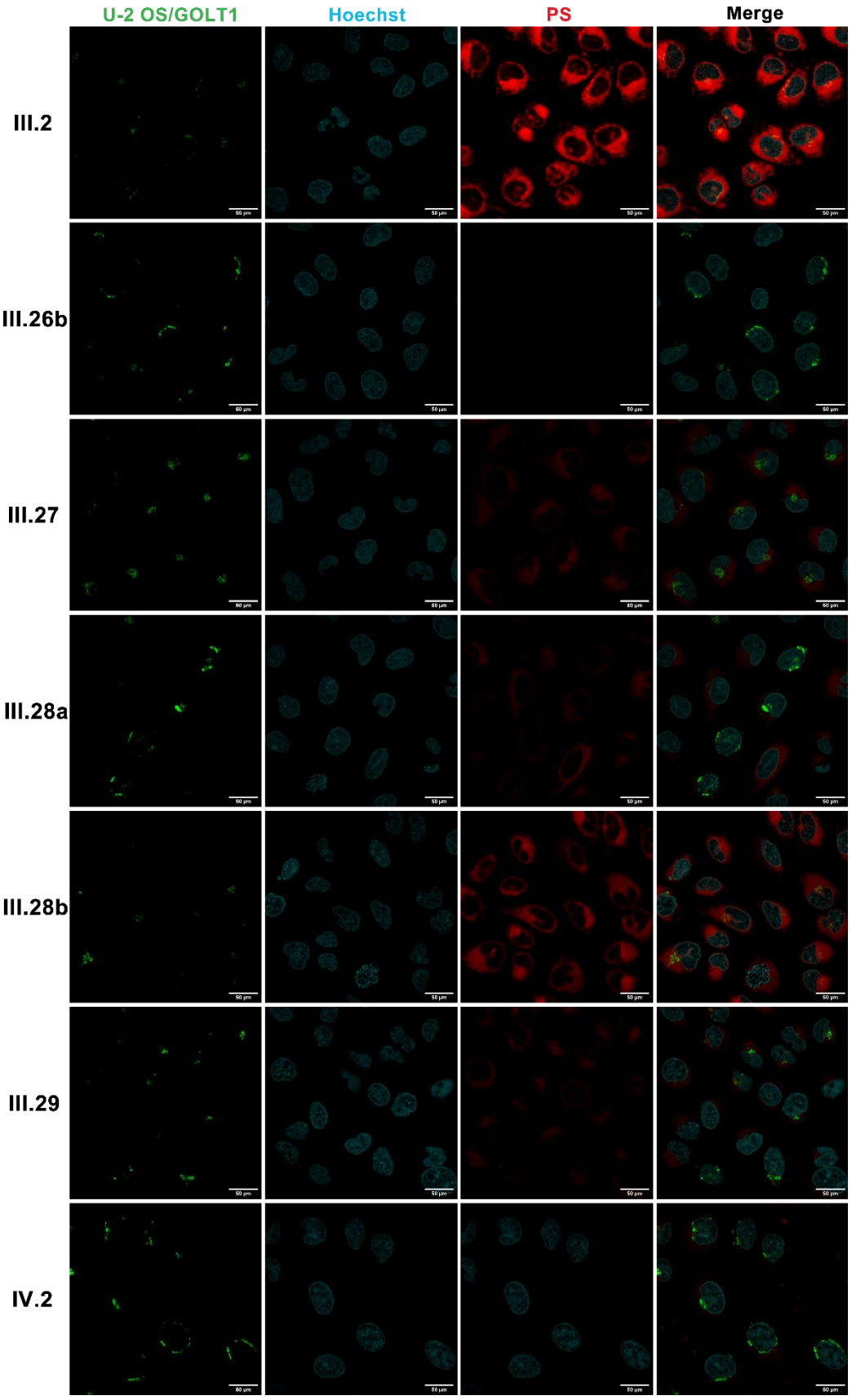

Figure VI–9. Representative images of confocal microscopy of U-2 OS stably expressing GALT1-GFP (GA staining, green) incubated with each chlorin (red) and nucleus stained with Hoechst (blue). Scale bar = 10 µm.

The same acquisition settings were used for all chlorins. The trend of intracellular accumulation, **III.2** > **III.28b** > **III.27** ~ **III.29** ~ **III.28a** > **III.26b** ~ **IV.2**, suggested by the obtained images is in accordance with the data obtained by flow cytometry. For PS with lower uptakes, the pictures taken were edited to increase the signal gain to better understand the location (not shown on Figure VI–8 nor Figure VI–9).

In addition, it was possible to conclude that the organelles in which our novel chlorins were located were the same as for temoporfin, with subcellular accumulation in the ER, along with some evidence of accumulation in the GA.

6. Discussion

The *in vitro* evaluation of temoporfin and of our synthesised chlorins covered cytotoxicity (all IC_{50} values summarised in Table VI-2), uptake, and co-localization studies.

Table VI-2. IC_{50} values from cytotoxic evaluation of temoporfin III.2 and novel chlorins III.28b, III.27, III.26b, III.29, and III.28a, and the conjugate IV.2.

PS	DARK TOXICITY	PHOTOTOXICITY (1 J/CM^2)		PHOTOTHERAPEUTIC INDEX
	MDA-MB-231 $IC_{50,dark}$	**MDA-MB-231** $IC_{50,photo}$	**NIH/3T3** $IC_{50,photo}$	**MDA-MB-231** $IC_{50,dark}$ / $IC_{50,photo}$
III.2	3.31 ± 0.50 µM (R^2 = 0.88)	25.7 ± 4.3 nM (R^2 = 0.88)	12.5 ± 0.5 nM (R^2 = 0.99)	129
III.26b	*1.28 ± 6.41E4 M* > 10 µM (R^2 < 0.50)	† *1.30 ± 0.64 µM* > 1 µM (R^2 < 0.50)	617 ± 68 nM (R^2 = 0.88)	*9.85E+5*
III.27	7.74 ± 0.26 µM (R^2 = 0.99)	138 ± 30 nM (R^2 = 0.79)	109 ± 8 nM (R^2 = 0.97)	56.3
III.28a	11.4 ± 2.4 µM (R^2 = 0.76)	309 ± 61 nM (R^2 = 0.76)	343 ± 26 nM (R^2 = 0.96)	37.0
III.28b	8.06 ± 0.49 µM (R^2 = 0.95)	86.3 ± 15.2 nM (R^2 = 0.87)	107 ± 8 nM (R^2 = 0.98)	93.4
III.29	15.8 ± 1.9 µM (R^2 = 0.92)	106 ± 17 nM (R^2 = 0.88)	93.1 ± 6.3 nM (R^2 = 0.98)	150
IV.2	*4.17 ± 518.87 mM* > 10 µM (R^2 < 0.50)	974 ± 69 nM (R^2 = 0.80)	461± 64 nM (R^2 = 0.84)	*4.28E+3*

The IC_{50} values are taken from the equation that represents the fitted curve: LOGx0± standard error. Values in italics might not be representative of the actual data.

The dark cytotoxicity studies act as an indicator of the safety of the PSs without irradiation, that ideally should be minimal since only photoactivated PSs should be cytotoxic. The results (Table VI-2) showed that temoporfin (**III.2**) had the lowest IC_{50} out of the evaluated compounds, with our

novel chlorins and conjugate being less cytotoxic, with IC_{50} values over two-fold higher than temoporfin's. Chlorins **III.27** and **III.28b** (methyl ester and deprotected mono-hydroxylmethyl at the chlorins' exocyclic-ring, respectively) showed relatively similar cytotoxicity, followed by the slightly higher value for the di-substituted chlorin **III.28a**, and the safer azide derivative **III.29**. With IC_{50} values over 10 μM, chlorin **III.26b** (all hydroxyl groups protected) and the conjugate **IV.2** were the safest compounds.

This trend remained mostly the same when evaluating their phototoxicity in both cancer and normal cell lines (Table VI-2), except for chlorin **III.29** that showed an increased cytotoxicity, on par with chlorin **III.28b** (precursor of **III.29**), which was the most cytotoxic among the synthesised chlorins in the different cytotoxic studies. This was an interesting observation, as **III.29** was one of the chlorins with lowest singlet oxygen quantum yield (while still in the same range as the other chlorins, as seen in Table V-4), superior only to compounds **III.26b** and **IV.2**. For the breast adenocarcinoma cell line, MDA-MB-231, it was possible to calculate a phototherapeutic index [286] of each PS (shown in Table VI-2) evaluated in this study and, apart from chlorin **III.26b** and conjugate **IV.2** because of the lack of accurate values for IC_{50}. Chlorin **III.29** had the highest phototherapeutic index, surpassing the one calculated for temoporfin **III.2**, due to having one of the lowest dark toxicity, but when photoactivated being one of the most phototoxic, attesting to the interest in this compound. On the other hand, the *in vitro* evaluation of the conjugate **IV.2** appear to indicate the lack of purity of the sample, as was suggested in Chapter III.

To better understand these cytotoxicity results, we considered important to analyse the internalisation of the chlorins in cancer and non-cancer cells. The 24-hour timepoint was always the one with the highest uptake. In the MDA-MB-231 cells, the decreasing uptake order found for chlorins **III.28b** (highest uptake of the synthesised PS), **III.27** and **III.26b** was consistent with the expected decreased of hydrophobicity corresponding to molecules with decreasing number of free hydroxyl groups.

The presence of esters instead of hydroxymethyl substituents at the exocyclic-ring of 4,5,6,7-tetrahydropyrazolo[1,5-*a*]pyridine-fused chlorins increase the hydrophobicity and should reduce the uptake, as supported by previous work in our group with similar chlorins in melanoma cell lines [155]. A particularly evident effect of increased hydrophobicity in the uptake of chlorins, was seen in the case of chlorins **III.27** and **III.26b** in MDA-MB-231 cells (Figure VI–6). Chlorin **III.26b** had the lowest uptake of all PS tested with chlorin **III.27** showing significantly higher values, the latter having the important *meta*-hydroxyphenyl substituents at the *meso* positions of the chlorin (known for their contribution to accumulation in tumour tissue and solubility [39–41]) whereas as the former bears *meso*-(*meta*-acetoxyphenyl) substituents, most likely leading to aggregation. From higher to lower uptake of the free chlorins, after **III.28b** and **III.27**, followed

chlorins **III.28a** and **III.29**, respectively. The decrease in uptake found in chlorin **III.28a** might be explained by the increase in size compared to the mono-substituted variant **III.28b**. As for chlorin **III.29**, the reduced uptake might be a consequence not only of the increase in size compared to **III.28b**, but also the possible interactions of the 1,3-dipole moiety, the azide group, with the cell membrane [25].

The low uptake of the conjugate **IV.2** was underwhelming as the FA warhead would be expected to target the FRα overexpressed in MDA-MB-231. These results combined with the ones from NIH/3T3 (the conjugate was the molecule with the second lowest uptake) are proof that there was not a preferential accumulation in cancer cells. Considering the initial hypothesis that there might be impurities – namely, the linker **IV.1** from an incomplete "click" reaction – in this sample, the presence of a smaller molecule with the same FA warhead would compete for binding to the FRα and subsequently would hinder the internalisation of any conjugate present in the sample (that would be removed during the PDT protocol). Herein, we were able to discern that any effect (in both cytotoxicity and uptake) associated with the presence of the conjugate **IV.2** was shadowed by possible competition of linker that did not react and was not purified through precipitation.

The cellular internalization of 4,5,6,7-tetrahydropyrazolo[1,5-*a*]pyridine-fused chlorins in NIH/3T3 cells (Figure VI–7) displayed a similar trend with a few dissonances. Of the novel chlorins, **III.27** surpassed the uptake of the remaining synthesised chlorins, with statistical significance for all except **III.28b**. This latter followed next in higher uptake, with statistical significance found for compounds **IV.2** and **III.26b**. The rest of the chlorins despite the differences found in uptake as **III.29** > **III.28a** > **IV.2** > **III.26b**, they were not statistically significant. However, when analysing the results from the fibroblast cell line, the uptake relative to negative controls showed to be higher than the uptake in the cancer cell line, allowing room to observe a statistically significant higher uptake of both chlorins **III.27** and **III.28b** compared to chlorin **III.26b**, and of chlorin **III.27** compared to chlorins **III.29** and **III.28a**.

This higher uptake observed in NIH/3T3 cells, compared to MDA-MB-231 cells, could indicate that none of the PS studied have preferential tumour accumulation. However, as it was mentioned before, the MDA-MB-231 cell line is from a TNBC [76,287,288] and besides being highly aggressive, these cells are also known to having multidrug-resistance [288,289], so the possibility of observing lower PS uptake on the cancerous cell line was expected due to this chemoresistance (e.g., efflux mechanisms that pump drugs out of the cells). Still, in both MDA-MB-231 and NIH/3T3 cell lines, the positive control **III.2** had statistically significant higher uptake than all novel chlorins which is in agreement with the higher dark toxicity of temoporfin.

Further studies on the subcellular location of the PS after 24 hours showed the co-localization of the GFP from ER (and even GA, on a smaller scale) and the fluorescence of the different chlorins, as expected from the structural similarity to temoporfin **III.2**, and what is known about its primary accumulation sites [25,272]: **III.2** at an incubation (in MCF-7 cells) of 3 hours is found in the ER and GA, but if extending that period up to 24 hours, it extrudes from the GA and consequently increases its presence on the ER. Nonetheless, the fact that the novel chlorins are internalised to this location is of interest, as PS with ER and/or GA tropism are considered potential inducers of immunogenic cell death (ICD). This is relevant because, in 2012, Agostinis *et al*. [290–292] reviewed the concept of ICD and reported the importance of ER stress and ROS in regulating the immunogenicity of dying cells, through an hypericin-based PDT protocol [291] that focused ROS-based ER stress, increasing the production of danger signals that trigger an anti-tumour immune response, which contribute to the long-term control of the disease.

Taking into account that our synthesised chlorins have the potential to induce ICD and relatively similar photochemical and photophysical characteristics, by reviewing the data discussed in this section, we can conclude that the novel 4,5,6,7-tetrahydropyrazolo[1,5-*a*]pyridine-fused 5,10,15,20-tetra(3-hydroxyphenyl)chlorins **III.28b** and **III.29** show the most promising photodynamic activity as free PS (Figure VI–10). Their phototoxic IC_{50} values are found in the 100 nM range, which is 100-fold lower than their values for dark toxicity, making them safe PDT agents as shown by the calculated phototherapeutic indexes (Table VI-2). This opens the possibility of further research on these chlorins, with special interest in the azide derivative **III.29** that can be a precursor to different conjugates through “click” chemistry. In Figure VI–10, the results obtained for the conjugate **IV.2** are also included which, despite the purity issues, still showed significant photodynamic activity upon irradiation and with minimal uptake into the cell. Nevertheless, these results are a good indication that the 4,5,6,7-tetrahydropyrazolo[1,5-*a*]pyridine-fused *meso*-tetra(3-hydroxyphenyl)chlorin conjugate **IV.2** hold the potential to become a promising third-generation PS.

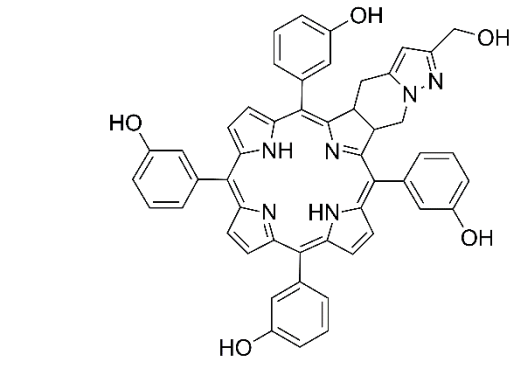

III.28b

$IC_{50,dark}$ (MDA-MB-231) = 8.06 μM
$IC_{50,photo}$ (MDA-MB-231) = 86.32 nM
Φ_{Δ} (EtOH) = 0.50
Φ_{pd} (DMSO) = 52.69 x 10^{-6}

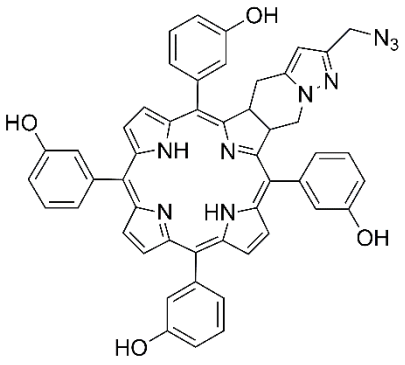

III.29

$IC_{50,dark}$ (MDA-MB-231) = 15.82 μM
$IC_{50,photo}$ (MDA-MB-231) = 105.68 nM
Φ_{Δ} (EtOH) = 0.47
Φ_{pd} (DMSO) = 60.81 x 10^{-6}

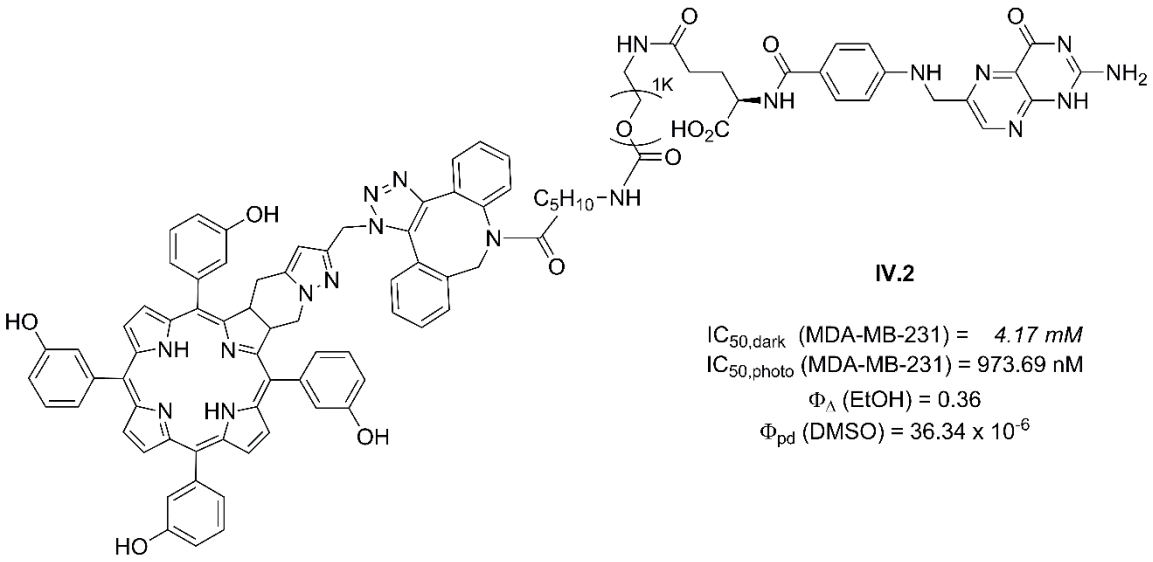

IV.2

$IC_{50,dark}$ (MDA-MB-231) = *4.17 mM*
$IC_{50,photo}$ (MDA-MB-231) = 973.69 nM
Φ_{Δ} (EtOH) = 0.36
Φ_{pd} (DMSO) = 36.34 x 10^{-6}

Figure VI–10. Summary of the characteristics from chlorins III.28b and III.29, as well as from conjugate IV.2.

7. Experimental

7.1. Instrumentation

Procedures dealing with the cell manipulation growth media, PBS solutions, and other reagents and materials were performed in a Thermo Scientific MSC-Advantage laminar flow hood.

Culture flasks, culture test plates, 15/50 mL conical centrifuge tubes, micropipettes, and ComfoPette used were purchased from Orange Scientific. Glass Pasteur pipettes, standard tips, and 1.5/2.0/5.0 mL Eppendorf tubes were purchased from Frilabo. For confocal microscopy, 8-well chambered coverslips were purchased from Ibidi. Unsterilised material used to deal with cells was previously sterilised in the AJC Uniclave 88 autoclave, before entering the hood environment.

The light source used for phototoxicity assays was a LED lamp from HIGROW LED (model GL36A), emission maximum at 660 nm with HWL = 26.4 nm. The fluence of the LED was verified before each irradiation with a Coherent LaserCheck power meter, choosing a wavelength of 660 nm with the filter position.

Fluorescence emission of resorufin (λ_{ex} = 528/20 nm and λ_{em} = 590/35 nm) was measured using a Synergy HT Multi-Mode Microplate Reader (BioTek).

The PS uptake was analysed by flow cytometry in the Flow Cytometer NovoCyte® 3000 + NovoSampler® Pro (ACEA Bioscience).

An Olympus CKX41 inverted microscope equipped with an Olympus U-RFLT50 power supply unit was used to observe cell morphology and dyes to assess cell viability. Confocal fluorescence microscopy was performed with Zeiss LSM 710 Confocal Microscope (at the MICC Imaging facility of the Centre for Neuroscience and Cell Biology (CNC), Coimbra, Portugal), using a HeNe (633 nm) diode (405 nm), an argon (488 nm) excitation lasers for the chlorins, Hoechst, and GFP, respectively, and a 63x oil immersion objective. The images were taken using the Zeiss ZEN software and processed using Image J 1.53k (freely available at https://imagej.nih.gov/ij) and Adobe® Photoshop® Elements 11 (Adobe Systems Incorporated, San Jose, CA, USA).

7.2. Materials

7.2.1. Reagents and solvents

For preparing the culture media, DMEM, 4-(2-hydroxyethyl)piperazine-1-ethanesulfonic acid buffer (HEPES), and sodium bicarbonate were purchased from Sigma-Aldrich, while foetal bovine serum (FBS), penicillin, and streptomycin were purchased from Gibco. Potassium phosphate dibasic, potassium chloride, sodium phosphate dibasic, and sodium chloride were purchased from Sigma-Aldrich and used to prepare the PBS solution. Trypsin-EDTA solution (10x), trypan blue, resazurin sodium salt, and DMSO Hybri-Max™ were purchased from Sigma-Aldrich. Hoechst 33342 stain was purchased from Life Technologies.

7.2.2. Photosensitisers

Chlorins **III.26b**, **III.27**, **III.28a**, **III.28b**, and **III.29** were synthesised as described in Chapter III and the conjugate **IV.2** was synthesised as described in Chapter IV. Temoporfin **III.2** was kindly provided by Senge Group at Trinity College Dublin. All the structures are represented in Figure VI–2. Stock solutions of all PS were prepared in DMSO Hybri-Max™ in the mM range and stored at -20 °C. The PS dilutions used *in vitro* studies were freshly prepared in DMEM culture medium at the desired concentrations. The percentage of DMSO administered to the cells was never superior to 1% ensuring no effect of DMSO on cell viability.

7.2.3. Cell lines

NIH/3T3 cells (ATCC® CRL-1658™), MDA-MB-231 cells (kindly provided by the Center for Neuroscience and Cell Biology (CNC), Coimbra, Portugal), and U-2 OS cells transfected with GFP for specific organelles (kindly provided by the Kroemer Lab at Centre de Recherche des Cordeliers (CRC)/Institut Gustave Roussy (IGR), Paris, France) were cultured in DMEM supplemented with 10% (v/v) heat-inactivated FBS, 10 mM HEPES, 10 mM sodium bicarbonate, 100 U/ml penicillin, and 100 ng/ml streptomycin. Cells were maintained at exponential growth in a humidified incubator with 5% CO_2 at 37°C.

7.3. Methods

7.3.1. Dark cytotoxicity evaluated by the resazurin reduction assay

A density of 14.000 MDA-MB-231 cells/well, were seeded in 96-well plates, with 200 µL/well of growth medium, and left to adhere overnight. Cells were treated with 200 µL/well at of each PS at a concentration range from 0.3125 to 10 µM. After 24 h, cells were washed once with 100 µL/well of PBS to remove the excess of PS that was not internalized by the cells. After an additional incubation of 24 h, cell viability was measured using the resazurin reduction assay. Briefly, DMEM was removed and replaced by 150 µL/well of resazurin stock solution diluted in DMEM (0.01 mg/mL) followed by approximately 2 h of incubation. The fluorescence emission of the metabolic product, resorufin, was measured with a microplate reader (Biotek Synergy HT) using 528/20 nm excitation and 590/35 nm emission filters. Cell viability of each condition was compared to the control group, which level of resazurin metabolization was assumed as 100% of viability.

7.3.2. Phototoxicity evaluated by the resazurin reduction assay

MDA-MB-231 (14,000 cells/well) and NIH/3T3 (3,000 cells/well) were seeded in 96-well plates with 200 µL/well of DMEM and left to adhere overnight. Then, the DMEM was removed and replaced with 200 µL/well of the respective concentration of each PS dissolved in growth medium. For temoporfin, concentration from 0.00117 to 300 nM were used whereas for all the other chlorins, concentration from 0.00391 to 10 µM were used. After an incubation of 24 h, cells were washed once with 100 µL/well of PBS to remove any excess of PS that was not internalized by the cells. Then, 200 µL/well of DMEM was added to the cells, followed by LED irradiation at a LD of 1 J/cm^2 using LED. Light dose was corrected considering the overlap between the LED and chlorins spectra [267].Cell viability was assessed 24 h post-irradiation through the fluorescence emission of resorufin as described above.

7.3.3. Cellular Uptake

MDA-MB-231 and 3T3 cells were seeded in flat-bottom, 24-well plates. The cell densities used were of 80.000cells/well for the MDA-MB-231 cell line and 30.000cells/well for the NIH/3T3 cell line. After 24h, cells were incubated with PS at 2.5 µM and at each timepoint (3, 6, or 24 hours), cells were washed twice with 500 µL of PBS. The cells were then detached with 250 µL of trypsin and centrifuged at 1500 rpm for 10 min at 4 ºC and the supernatant discarded. The obtained pellet was resuspended in 250 µL of 4% paraformaldehyde (PFA) for 30 min at RT. Afterwards, cells were once again centrifuged in the previous conditions and the supernatant discarded. The obtained cellular pellet weas washed with 250 µL of PBS, followed by resuspension of the cellular pellet in 250 µL of PBS. The fluorescence intensity of 10,000 events was measured, inside a gate defined for the live cells, using the RL1 laser filter (ex. 640 nm; em. 675/30 nm) in the flow cytometer.

7.3.4. Confocal microscopy

Co-localization studies were assessed using U2-OS cells stably expressing CALR-GFP (to identify the ER; N=2) or GALT1-GFP (to identify the GA; N=2). For each cell line, a density of 17,000 cells/well was seeded in an µ-Slide 8-well treated plate and left to adhere overnight. A concentration of 5 µM of each PS in DMEM was added to the cells. Cells were incubated for 24 h, after which they were washed with PBS, fixed for 20 minutes with 300 µL of a solution containing 4% PFA in PBS and the nucleus stained with Hoechst. After two wash steps with 300 µL of PBS, cells were analysed on a Carl Zeiss LSM 710 confocal microscope using excitations lasers at 405, 488, and 633 nm for Hoechst, GFP, and chlorins, respectively. For each PS, three images from different places of the well were obtained in equivalent conditions and camera settings, with the occasional increase of gain for PSs that did not show as much fluorescence (to confirm co-localisation).

7.3.5. Statistical analysis

Results shown for dark toxicity and phototoxicity are represented as mean ± SEM, for three individual experiments with triplicate wells for each concentration, as well as the negative control group. Graphical representations and curve adjustments for IC_{50} calculations were created and processed with OriginPro© 2018 (64-bit) software (OriginLab Corporation, Northampton, MA, USA), using a sigmoidal fit (Dose-Response function, Levenberg Marquardt algorithm) through the following Equation VI-2:

$$y = A_1 + \frac{A_2 - A_1}{1 - 10^{(LOGx0 - x)p}} \quad \text{(VI-2)}$$

where A_1 (fixed at 0) and A_2 (fixed at 100) are the bottom and top asymptotes, respectively, LOG*x*0 (lower bound > 0) is the centre, and *p* (upper bound < 0) is the hill slope.

Results shown for PS uptake are represented as mean ± SEM, for three individual experiments with duplicate wells for each timepoint evaluated, relatively to the negative control group. Repeated measures, two-way ANOVA with Bonferroni's post-test was performed to compare the means of each group for the different timepoints. Two-way ANOVA calculations were performed on GraphPad Prism® 5 (version 5.01 for Windows) software (GraphPad Software, San Diego, CA, USA).

Chapter VII:
Final remarks and future perspectives

Science (…) is made up of mistakes, but they are mistakes which it is useful to make, because they lead little by little to the truth.

Jules Vernes

Photodynamic therapy (PDT) is a minimally invasive approach to target cancer cells through light irradiation. Its advantages also include absence of drug resistance, healing with almost no scarring, and activation of anti-tumour immunity which is the main reason for the long-term remission of the disease. However, there are undesirable side effects such as prolonged skin photosensitivity after PDT treatment [1,23,29–31]. To improve PDT efficacy, while reducing the side effects, the conjugation of photosensitisers (PSs) with different ligands specifically recognised and, eventually, internalized by cancer cells, has been one of the most popular approaches. And, although there have been improvements regarding cellular uptake, these ligand-targeting approaches still present limited success *in vivo* [149]. The goal of this project was to develop a new strategy for targeted-PDT, where we proposed as proof-of-concept to synthesise a new "clickable" chlorin that could then be conjugated with a ligand to obtain a targeted-PS.

Using the [8π+2π] cycloaddition method previously developed by Pinho e Melo *et al*. [153–157], we synthesised novel chlorins, related to temoporfin (**III.2**), with different degrees of amphiphilicity (Figure III–9). From the first chlorin obtained through cycloaddition, **III.26b**, subsequent derivatisations lead to molecules with higher number of hydroxyl groups. Then, the terminal alcohol group in the pyrazolo ring of the most hydrophilic chlorin, **III.28b**, that was synthesised in our mono-functionalised series, was further derivatised to obtain an azide group. This allows for an efficient functionalisation through "click" chemistry with a targeting moiety, containing an alkyne group, to obtain third-generation PSs.

As proof-of-concept, we designed a conjugate (**IV.2**) using a commercially available linker and folic acid (FA) as the targeting moiety. The *in silico* evaluation of the designed conjugate corroborated the binding to folate receptor α-isoform (FRα), despite the size of the conjugate. Therefore, we proceeded with the synthesis but, upon characterization of the sample obtained after the "click" reaction, we were able to confirm the presence of **IV.2**, indirectly, but not its purity. Moreover, photophysical characterisation of all the synthesised compounds supported the presence of the chlorin derivatives.

Analysis of cytotoxicity in the dark demonstrated improvement of the novel PSs relative to temoporfin, with the most hydrophobic chlorin (**III.26b**) and conjugate (**IV.2**) being the safest compounds ($IC_{50,dark}$ > 10 μM). These results combined with the phototoxic evaluation (light-dose of 1 J/cm^2) in FRα-positive MDA-MB-231 cancer cells (where temoporfin performed better, followed by the most hydrophilic chlorin in the series, **III.28b** with $IC_{50,photo}$ = 86.32 nM), resulted in higher phototherapeutic indexes for chlorin **III.26b** (*9.85E+5*) and conjugate **IV.2** (*4.28E+3*) – largely due to their safety in the dark – along with the azide derivative **III.29** (149.70), when compared to temoporfin **III.2** (128.84).

The inability to develop an efficacious purification protocol for the conjugate **IV.2** may raise questions concerning the results obtained in the *in vitro* cell assays. The presence of linker **IV.1**, with the same FA warhead, in the **IV.2** sample, resulting from a potential incomplete conjugation reaction, would compete for binding to the FRα and hinder the internalisation of the conjugate present in the sample (later removed during the PDT protocol, before illumination).

Nonetheless, conjugate **IV.2** still showed significant phototoxicity towards the cancer cells, especially considering that there was minimal cellular uptake, which might be a favourable indication of the potential of 4,5,6,7-tetrahydropyrazolo[1,5-*a*]pyridine-fused *meso*-tetra(3-hydroxyphenyl)chlorin conjugates as promising third-generation PSs. Despite the issues found with purification of the FA-targeted conjugate described in this thesis (**IV.2**), it is important to highlight that FA is fairly susceptible to different environmental factors: such as light, solution medium, high temperatures, and presence of oxygen [199,293].

We are currently researching the synthesis and characterisation of new 4,5,6,7-tetrahydropyrazolo[1,5-*a*]pyridine-fused *meso*-tetra(3-hydroxyphenyl)chlorin conjugates obtained through this same protocol chlorin **III.29**, but as a biotin-targeted PS. Biotin (another vitamin) is also a small molecule with high specificity to the sodium-dependent multivitamin transporter, which can be found overexpressed in even higher levels than the FR in different aggressive cancer cell lines (e.g., 4T1 breast cancer cell line) [75]. With a different, smaller, symmetrical spacer, we expect to reduce purification issues found with conjugate **IV.2** (expected mixture of two regioisomers), and thus successfully purify and evaluate the new conjugate's selectivity for cancer cells.

References

1. Gierlich, P.; Mata, A.I.; Donohoe, C.; Brito, R.M.M.; Senge, M.O.; Gomes-da-Silva, L.C. Ligand-Targeted Delivery of Photosensitizers for Cancer Treatment. *Molecules* **2020**, *25*, 5317, doi:10.3390/molecules25225317.

2. American Cancer Society *Global Cancer Facts & Figures - 4th Edition*; 4th Editio.; Atlanta, 2018;

3. Hanahan, D.; Coussens, L.M. Accessories to the Crime: Functions of Cells Recruited to the Tumor Microenvironment. *Cancer Cell* **2012**, *21*, 309–322, doi:10.1016/j.ccr.2012.02.022.

4. Hanahan, D.; Weinberg, R.A. The Hallmarks of Cancer. *Cell* **2000**, *100*, 57–70, doi:10.1016/S0092-8674(00)81683-9.

5. Hanahan, D.; Weinberg, R.A. Hallmarks of Cancer: The Next Generation. *Cell* **2011**, *144*, 646–674, doi:10.1016/j.cell.2011.02.013.

6. Hanahan, D. Hallmarks of Cancer: New Dimensions. *Cancer Discov.* **2022**, *12*, 31–46, doi:10.1158/2159-8290.CD-21-1059.

7. Quail, D.F.; Joyce, J.A. Microenvironmental Regulation of Tumor Progression and Metastasis. *Nat. Med.* **2013**, *19*, 1423–1437, doi:10.1038/nm.3394.

8. Falzone, L.; Salomone, S.; Libra, M. Evolution of Cancer Pharmacological Treatments at the Turn of the Third Millennium. *Front. Pharmacol.* **2018**, *9*, doi:10.3389/fphar.2018.01300.

9. Abbas, Z.; Rehman, S. An Overview of Cancer Treatment Modalities. *Neoplasm* **2018**, doi:10.5772/intechopen.76558.

10. Arruebo, M.; Vilaboa, N.; Sáez-Gutierrez, B.; Lambea, J.; Tres, A.; Valladares, M.; González-Fernández, Á. Assessment of the Evolution of Cancer Treatment Therapies. *Cancers (Basel).* **2011**, *3*, 3279–3330, doi:10.3390/cancers3033279.

11. Dilalla, V.; Chaput, G.; Williams, T.; Sultanem, K. Radiotherapy Side Effects: Integrating a Survivorship Clinical Lens to Better Serve Patients. *Curr. Oncol.* **2020**, *27*, 107–112, doi:10.3747/co.27.6233.

12. Zwicke, G.L.; Ali Mansoori, G.; Jeffery, C.J. Utilizing the Folate Receptor for Active Targeting of Cancer Nanotherapeutics. *Nano Rev.* **2012**, *3*, 18496, doi:10.3402/nano.v3i0.18496.

13. Seebacher, N.A.; Stacy, A.E.; Porter, G.M.; Merlot, A.M. *Clinical Development of Targeted and Immune Based Anti-Cancer Therapies*; Journal of Experimental & Clinical Cancer Research, 2019; Vol. 38; ISBN 1304601910942.

14. Zhao, X.; Li, H.; Lee, R.J. Targeted Drug Delivery via Folate Receptors. *Expert Opin. Drug Deliv.* **2008**, *5*, 309–319, doi:10.1517/17425247.5.3.309.

15. Siamof, C.M.; Goel, S.; Cai, W. Moving Beyond the Pillars of Cancer Treatment: Perspectives From Nanotechnology. *Front. Chem.* **2020**, *8*, 1–14, doi:10.3389/fchem.2020.598100.

16. Masoud, V.; Pagès, G. Targeted Therapies in Breast Cancer: New Challenges to Fight against Resistance. *World J. Clin. Oncol.* **2017**, *8*, 120, doi:10.5306/wjco.v8.i2.120.

17. La-Beck, N.M.; Jean, G.W.; Huynh, C.; Alzghari, S.K.; Lowe, D.B. Immune Checkpoint Inhibitors: New Insights and Current Place in Cancer Therapy. *Pharmacother. J. Hum. Pharmacol. Drug Ther.* **2015**, *35*, 963–976, doi:10.1002/phar.1643.

18. Al-Ramadi, B.K.; Fernandez-Cabezudo, M.J.; El-Hasasna, H.; Al-Salam, S.; Attoub, S.; Xu, D.; Chouaib, S. Attenuated Bacteria as Effectors in Cancer Immunotherapy. *Ann. N. Y. Acad. Sci.* **2008**, *1138*, 351–357, doi:10.1196/annals.1414.036.

19. Pardoll, D.M. The Blockade of Immune Checkpoints in Cancer Immunotherapy. *Nat. Rev. Cancer* **2012**, *12*, 252–264, doi:10.1038/nrc3239.

20. Lobo, C.S.; Gomes-da-Silva, L.C.; Arnaut, L.G. Potentiation of Systemic Anti-Tumor Immunity with Photodynamic Therapy Using Porphyrin Derivatives. In *Handbook of Porphyrin Science*; 2022; pp. 279–344.

21. Zugazagoitia, J.; Guedes, C.; Ponce, S.; Ferrer, I.; Molina-Pinelo, S.; Paz-Ares, L. Current Challenges in Cancer Treatment. *Clin. Ther.* **2016**, *38*, 1551–1566, doi:10.1016/j.clinthera.2016.03.026.

22. Daniell, M.D.; Hill, J.S. A HISTORY OF PHOTODYNAMIC THERAPY. *ANZ J. Surg.* **1991**, *61*, 340–348, doi:10.1111/j.1445-2197.1991.tb00230.x.

23. Dąbrowski, J.M.; Arnaut, L.G. Photodynamic Therapy (PDT) of Cancer: From Local to Systemic Treatment. *Photochem. Photobiol. Sci.* **2015**, *14*, 1765–1780, doi:10.1039/c5pp00132c.

24. Qiang, Y.G.; Zhang, X.P.; Li, J.; Huang, Z. Photodynamic Therapy for Malignant and Non-Malignant Diseases: Clinical Investigation and Application. *Chin. Med. J. (Engl).* **2006**, *119*, 845–857, doi:10.1097/00029330-200605020-00009.

25. Castano, A.P.; Demidova, T.N.; Hamblin, M.R. Mechanisms in Photodynamic Therapy: Part One - Photosensitizers, Photochemistry and Cellular Localization. *Photodiagnosis Photodyn. Ther.* **2004**, *1*, 279–293, doi:10.1016/S1572-1000(05)00007-4.

26. Aroso, R.T.; Schaberle, F.A.; Arnaut, L.G.; Pereira, M.M. *Photodynamic Disinfection and Its Role in Controlling Infectious Diseases*; Springer International Publishing, 2021; Vol. 20; ISBN 0123456789.

27. Dolmans, D.E.J.G.J.; Fukumura, D.; Jain, R.K. Photodynamic Therapy for Cancer. *Nat. Rev. Cancer* **2003**, *3*, 380–387, doi:10.1038/nrc1071.

28. Dougherty, T.J.; Grindey, G.B.; Fiel, R.; Weishaupt, K.R.; Boyle, D.G. Photoradiation Therapy. II. Cure of Animal Tumors with Hematoporphyrin and Light. *J. Natl. Cancer Inst.* **1975**, *55*, 115–121, doi:10.1093/jnci/55.1.115.

29. Kwiatkowski, S.; Knap, B.; Przystupski, D.; Saczko, J.; Kędzierska, E.; Knap-Czop, K.;

Kotlińska, J.; Michel, O.; Kotowski, K.; Kulbacka, J. Photodynamic Therapy – Mechanisms, Photosensitizers and Combinations. *Biomed. Pharmacother.* **2018**, *106*, 1098–1107, doi:10.1016/j.biopha.2018.07.049.

30. Brown, S.B.; Brown, E.A.; Walker, I. The Present and Future Role of Photodynamic Therapy in Cancer Treatment. *Lancet Oncol.* **2004**, *5*, 497–508, doi:10.1016/S1470-2045(04)01529-3.

31. Donohoe, C.; Senge, M.O.; Arnaut, L.G.; Gomes-da-Silva, L.C. Cell Death in Photodynamic Therapy: From Oxidative Stress to Anti-Tumor Immunity. *Biochim. Biophys. Acta - Rev. Cancer* **2019**, *1872*, 188308, doi:10.1016/j.bbcan.2019.07.003.

32. Agostinis, P.; Berg, K.; Cengel, K.A.; Foster, T.H.; Girotti, A.W.; Gollnick, S.O.; Hahn, S.M.; Hamblin, M.R.; Juzeniene, A.; Kessel, D.; et al. Photodynamic Therapy of Cancer: An Update. *CA Cancer J Clin* **2011**, *61*, 250–281, doi:10.3322/caac.20114.

33. Ormond, A.; Freeman, H. Dye Sensitizers for Photodynamic Therapy. *Materials (Basel).* **2013**, *6*, 817–840, doi:10.3390/ma6030817.

34. O'Connor, A.E.; Gallagher, W.M.; Byrne, A.T. Porphyrin and Nonporphyrin Photosensitizers in Oncology: Preclinical and Clinical Advances in Photodynamic Therapy. *Photochem. Photobiol.* **2009**, *85*, 1053–1074, doi:10.1111/j.1751-1097.2009.00585.x.

35. Dougherty, T.J.; Gomer, C.J.; Henderson, B.W.; Jori, G.; Kessel, D.; Korbelik, M.; Moan, J.; Peng, Q. Photodynamic Therapy. *J. Natl. Cancer Inst.* **1998**, *90*, 889–905, doi:10.1093/jnci/90.12.889.

36. Bonnett, R.; White, R.D.; Winfield, U.J.; Berenbaum, M.C. Hydroporphyrins of the Meso-Tetra(Hydroxyphenyl)Porphyrin Series as Tumour Photosensitizers. *Biochem. J.* **1989**, *261*, 277–280, doi:10.1042/bj2610277.

37. Zenkevich, E.; Sagun, E.; Knyukshto, V.; Shulga, A.; Mironov, A.; Efremova, O.; Bonnett, R.; Songca, S.P.; Kassem, M. Photophysical and Photochemical Properties of Potential Porphyrin and Chlorin Photosensitizers for PDT. *J. Photochem. Photobiol. B Biol.* **1996**, *33*, 171–180, doi:10.1016/1011-1344(95)07241-1.

38. Senge, M.O.; Brandt, J.C. Temoporfin (Foscan®, 5,10,15,20-Tetra(m-Hydroxyphenyl)Chlorin) - A Second-Generation Photosensitizer. *Photochem. Photobiol.* **2011**, *87*, 1240–1296, doi:10.1111/j.1751-1097.2011.00986.x.

39. Berenbaum, M.C.; Akande, S.L.; Bonnett, R.; Kaur, H.; Ioannou, S.; White, R.D.; Winfield, U.J. Meso-Tetra(Hydroxyphenyl)Porphyrins, a New Class of Potent Tumour Photosensitisers with Favourable Selectivity. *Br. J. Cancer* **1986**, *54*, 717–725, doi:10.1038/bjc.1986.232.

40. Banfi, S.; Caruso, E.; Buccafurni, L.; Murano, R.; Monti, E.; Gariboldi, M.; Papa, E.; Gramatica, P. Comparison between 5,10,15,20-Tetraaryl- and 5,15-Diarylporphyrins as Photosensitizers: Synthesis, Photodynamic Activity, and Quantitative Structure-Activity Relationship Modeling. *J. Med. Chem.* **2006**, *49*, 3293–3304, doi:10.1021/jm050997m.

41. Songca, S.P. In-Vitro Activity and Tissue Distribution of New Fluorinated Meso - Tetrahydroxyphenylporphyrin Photosensitizers . *J. Pharm. Pharmacol.* **2010**, *53*, 1469–1475, doi:10.1211/0022357011778007.

42. Triesscheijn, M.; Baas, P.; Schellens, J.H.M.; Stewart, F.A. Photodynamic Therapy in Oncology. *Oncologist* **2006**, *11*, 1034–1044, doi:10.1634/theoncologist.11-9-1034.

43. Wagner, A.; Denzer, U.W.; Neureiter, D.; Kiesslich, T.; Puespoeck, A.; Rauws, E.A.J.; Emmanuel, K.; Degenhardt, N.; Frick, U.; Beuers, U.; et al. Temoporfin Improves Efficacy of Photodynamic Therapy in Advanced Biliary Tract Carcinoma: A Multicenter Prospective Phase II Study. *Hepatology* **2015**, *62*, 1456–1465, doi:10.1002/hep.27905.

44. Hudson, R.; Boyle, R.W. Strategies for Selective Delivery of Photodynamic Sensitisers to Biological Targets. *J. Porphyr. Phthalocyanines* **2004**, *8*, 954–975, doi:10.1142/S1088424604000325.

45. Chiaviello, A.; Postiglione, I.; Palumbo, G. Targets and Mechanisms of Photodynamic Therapy in Lung Cancer Cells: A Brief Overview. *Cancers (Basel).* **2011**, *3*, 1014–1041, doi:10.3390/cancers3011014.

46. Kessel, D. Pharmacokinetics of N-Aspartyl Chlorin E6 in Cancer Patients. *J. Photochem. Photobiol. B Biol.* **1997**, *39*, 81–83, doi:10.1016/S1011-1344(96)00009-7.

47. Fine, S.L. Photodynamic Therapy with Verteporfin Is Effective for Selected Patients with Neovascular Age-Related Macular Degeneration. *Arch. Ophthalmol.* **1999**, *117*, 1400–1402, doi:10.1001/archopht.117.10.1400.

48. Abrahamse, H.; Hamblin, M.R. New Photosensitizers for Photodynamic Therapy. *Biochem. J.* **2016**, *473*, 347–364, doi:10.1042/BJ20150942.

49. Laranjo, M.; Aguiar, M.C.; Pereira, N.A.M.; Brites, G.; Nascimento, B.F.O.; Brito, A.F.; Casalta-Lopes, J.; Gonçalves, A.C.; Sarmento-Ribeiro, A.B.; Pineiro, M.; et al. Platinum(II) Ring-Fused Chlorins as Efficient Theranostic Agents: Dyes for Tumor-Imaging and Photodynamic Therapy of Cancer. *Eur. J. Med. Chem.* **2020**, *200*, 112468, doi:10.1016/j.ejmech.2020.112468.

50. Pereira, N.A.M.; Laranjo, M.; Casalta-Lopes, J.; Serra, A.C.; Piñeiro, M.; Pina, J.; Seixas de Melo, J.S.; Senge, M.O.; Botelho, M.F.; Martelo, L.; et al. Platinum(II) Ring-Fused Chlorins as Near-Infrared Emitting Oxygen Sensors and Photodynamic Agents. *ACS Med. Chem. Lett.* **2017**, *8*, 310–315, doi:10.1021/acsmedchemlett.6b00476.

51. Sorrin, A.J.; Kemal Ruhi, M.; Ferlic, N.A.; Karimnia, V.; Polacheck, W.J.; Celli, J.P.; Huang, H.C.; Rizvi, I. Photodynamic Therapy and the Biophysics of the Tumor Microenvironment. *Photochem. Photobiol.* **2020**, *96*, 232–259, doi:10.1111/php.13209.

52. ClinicalTrials.gov; Luzitin, S. Photodynamic Therapy With LUZ11 in Advanced Head and Neck Cancer Available online: https://clinicaltrials.gov/ct2/show/NCT02070432?term=LUZ11&rank=1 (accessed on 16 July 2017).

53. Arnaut, L.G.; Pereira, M.M.; Dąbrowski, J.M.; Silva, E.F.F.; Schaberle, F.A.; Abreu, A.R.; Rocha, L.B.; Barsan, M.M.; Urbańska, K.; Stochel, G.; et al. Photodynamic Therapy Efficacy Enhanced by Dynamics: The Role of Charge Transfer and Photostability in the Selection of Photosensitizers. *Chem. - A Eur. J.* **2014**, *20*, 5346–5357, doi:10.1002/chem.201304202.

54. Rocha, L.B.; Gomes-da-silva, L.C.; Dąbrowski, J.M.; Arnaut, L.G. Elimination of Primary Tumours and Control of Metastasis with Rationally Designed Bacteriochlorin Photodynamic Therapy Regimens. *Eur. J. Cancer* **2015**, doi:10.1016/j.ejca.2015.06.002.

55. Gomes-da-Silva, L.C.; Zhao, L.; Bezu, L.; Zhou, H.; Sauvat, A.; Liu, P.; Durand, S.; Leduc, M.; Souquere, S.; Loos, F.; et al. Photodynamic Therapy with Redaporfin Targets the Endoplasmic Reticulum and Golgi Apparatus. *EMBO J.* **2018**, *37*,

doi:10.15252/embj.201798354.

56. Dilkes, M.G.; Dejode, M.L.; Gardiner, Q.; Kenyon, G.S.; McKelvie, P. Treatment of Head and Neck Cancer with Photodynamic Therapy: Results after One Year. *J. Laryngol. Otol.* **1995**, *109*, 1072–1076, doi:10.1017/S0022215100132050.

57. Dilkes, M.G.; DeJode, M.L.; Rowntree-Taylor, A.; McGilligan, J.A.; Kenyon, G.S.; McKelvie, P. M-THPC Photodynamic Therapy for Head and Neck Cancer. *Lasers Med. Sci.* **1996**, *11*, 23–29, doi:10.1007/BF02161289.

58. Copper, M.P.; Tan, I.B.; Oppelaar, H.; Ruevekamp, M.C.; Stewart, F.A. Meta-Tetra(Hydroxyphenyl)Chlorin Photodynamic Therapy in Early-Stage Squamous Cell Carcinoma of the Head and Neck. *Arch. Otolaryngol. - Head Neck Surg.* **2003**, *129*, 709–711, doi:10.1001/archotol.129.7.709.

59. Hopper, C. Photodynamic Therapy: A Clinical Reality in the Treatment of Cancer. *Lancet Oncol.* **2000**, *1*, 212–219, doi:10.1016/S1470-2045(00)00166-2.

60. Hopper, C.; Kübler, A.; Lewis, H.; Tan, I.B.; Putnam, G.; Patrice, T.; Beauvillain, C.; Evensen, J.; Butow, K.; Smit, B.; et al. MTHPC-Mediated Photodynamic Therapy for Early Oral Squamous Cell Carcinoma. *Int. J. Cancer* **2004**, *111*, 138–146, doi:10.1002/ijc.20209.

61. Yakavets, I.; Millard, M.; Zorin, V.; Lassalle, H.P.; Bezdetnaya, L. Current State of the Nanoscale Delivery Systems for Temoporfin-Based Photodynamic Therapy: Advanced Delivery Strategies. *J. Control. Release* **2019**, *304*, 268–287, doi:10.1016/j.jconrel.2019.05.035.

62. Senge, M.O. MTHPC - A Drug on Its Way from Second to Third Generation Photosensitizer? *Photodiagnosis Photodyn. Ther.* **2012**, *9*, 170–179, doi:10.1016/j.pdpdt.2011.10.001.

63. Reichlin, S. *Handbook of Experimental Pharmacology*; 1969; Vol. 258; ISBN 354022565X.

64. Muro, S. Challenges in Design and Characterization of Ligand-Targeted Drug Delivery Systems. *J. Control. Release* **2012**, *164*, 125–137, doi:10.1016/j.jconrel.2012.05.052.

65. Akhtar, M.J.; Ahamed, M.; Alhadlaq, H.A.; Alrokayan, S.A.; Kumar, S. Targeted Anticancer Therapy: Overexpressed Receptors and Nanotechnology. *Clin. Chim. Acta* **2014**, *436*, 78–92, doi:10.1016/j.cca.2014.05.004.

66. Polo, L.; Valduga, G.; Jori, G.; Reddi, E. Low-Density Lipoprotein Receptors in the Uptake of Tumour Photosensitizers by Human and Rat Transformed Fibroblasts. *Int. J. Biochem. Cell Biol.* **2002**, *34*, 10–23, doi:10.1016/S1357-2725(01)00092-9.

67. Fogal, V.; Zhang, L.; Krajewski, S.; Ruoslahti, E. Mitochondrial/Cell-Surface Protein P32/GC1qR as a Molecular Target in Tumor Cells and Tumor Stroma. *Cancer Res.* **2008**, *68*, 7210, doi:10.1158/0008-5472.CAN-07-6752.

68. Ahmad, I.; Iwata, T.; Leung, H.Y. Mechanisms of FGFR-Mediated Carcinogenesis. *BBA - Mol. Cell Res.* **2012**, *1823*, 850–860, doi:10.1016/j.bbamcr.2012.01.004.

69. Katoh, M. FGFR Inhibitors: Effects on Cancer Cells, Tumor Microenvironment and Whole-Body Homeostasis. *Int. J. Mol. Med.* **2016**, *38*, 3–15, doi:10.3892/ijmm.2016.2620.

70. Xu, M.J.; Johnson, D.E.; Grandis, J.R. EGFR-Targeted Therapies in the Post-Genomic Era. *Cancer Metastasis Rev.* **2017**, *36*, 463–473, doi:10.1007/s10555-017-9687-8.

71. Aboud-pirak, E.; Hurwitz, E.; Pirak, M.E.; Bellot, F.; Schlessinger, J.; Sela, M. Efficacy of Antibodies to Epidermal Growth Factor Receptor Against KB Carcinoma In Vitro and in Nude Mice. *J. Natl. Cancer Inst.* **1988**, *80*, 1605–1611, doi:10.1093/jnci/80.20.1605.

72. Spector, N.L.; Blackwell, K.L. Understanding the Mechanisms Behind Trastuzumab Therapy for Human Epidermal Growth Factor Receptor 2–Positive Breast Cancer. *J. Clin. Oncol.* **2009**, *27*, 5838–5847, doi:10.1200/JCO.2009.22.1507.

73. Denison, T.A.; Bae, Y.H. Tumor Heterogeneity and Its Implication for Drug Delivery. *J. Control. Release* **2012**, *164*, 187–191, doi:10.1016/j.jconrel.2012.04.014.

74. Iqbal, N.; Iqbal, N. Human Epidermal Growth Factor Receptor 2 (HER2) in Cancers: Overexpression and Therapeutic Implications. *Mol. Biol. Int.* **2014**, *2014*, 1–9, doi:10.1155/2014/852748.

75. Kue, C.S.; Kamkaew, A.; Burgess, K.; Kiew, L. V; Chung, L.Y.; Lee, H.B. Small Molecules for Active Targeting in Cancer. *Med. Res. Rev.* **2016**, *36*, 494–575, doi:10.1002/med.21387.

76. Yin, L.; Duan, J.J.; Bian, X.W.; Yu, S.C. Triple-Negative Breast Cancer Molecular Subtyping and Treatment Progress. *Breast Cancer Res.* **2020**, *22*, 61, doi:10.1186/s13058-020-01296-5.

77. Vagia, E.; Mahalingam, D.; Cristofanilli, M. The Landscape of Targeted Therapies in TNBC. *Cancers (Basel).* **2020**, *12*, 916, doi:10.3390/cancers12040916.

78. Gucalp, A.; Tolaney, S.; Isakoff, S.J.; Ingle, J.N.; Liu, M.C.; Carey, L.A.; Blackwell, K.; Rugo, H.; Nabell, L.; Forero, A.; et al. Phase II Trial of Bicalutamide in Patients with Androgen Receptor–Positive, Estrogen Receptor–Negative Metastatic Breast Cancer. *Clin. Cancer Res.* **2013**, *19*, 5505–5512, doi:10.1158/1078-0432.CCR-12-3327.

79. Bonnefoi, H.; Grellety, T.; Tredan, O.; Saghatchian, M.; Dalenc, F.; Mailliez, A.; L'Haridon, T.; Cottu, P.; Abadie-Lacourtoisie, S.; You, B.; et al. A Phase II Trial of Abiraterone Acetate plus Prednisone in Patients with Triple-Negative Androgen Receptor Positive Locally Advanced or Metastatic Breast Cancer (UCBG 12-1). *Ann. Oncol.* **2016**, *27*, 812–818, doi:10.1093/annonc/mdw067.

80. Traina, T.A.; Miller, K.; Yardley, D.A.; Eakle, J.; Schwartzberg, L.S.; O'Shaughnessy, J.; Gradishar, W.; Schmid, P.; Winer, E.; Kelly, C.; et al. Enzalutamide for the Treatment of Androgen Receptor–Expressing Triple-Negative Breast Cancer. *J. Clin. Oncol.* **2018**, *36*, 884–890, doi:10.1200/JCO.2016.71.3495.

81. Hamidi, H.; Pietilä, M.; Ivaska, J. The Complexity of Integrins in Cancer and New Scopes for Therapeutic Targeting. *Br. J. Cancer 2016 1159* **2016**, *115*, 1017–1023, doi:10.1038/bjc.2016.312.

82. Jiang, Y.; Dai, J.; Yao, Z.; Shelley, G.; Keller, E.T. Abituzumab Targeting of Av-Class Integrins Inhibits Prostate Cancer Progression. *Mol. Cancer Res.* **2017**, *15*, 875–883, doi:10.1158/1541-7786.MCR-16-0447/80358/AM/ABITUZUMAB-TARGETING-OF-ALPHAV-CLASS-INTEGRINS.

83. Danhier, F.; Feron, O.; Préat, V. To Exploit the Tumor Microenvironment: Passive and Active Tumor Targeting of Nanocarriers for Anti-Cancer Drug Delivery. *J. Control. Release* **2010**, *148*, 135–146, doi:10.1016/J.JCONREL.2010.08.027.

84. Wagner, S.; Rothweiler, F.; Anhorn, M.G.; Sauer, D.; Riemann, I.; Weiss, E.C.; Katsen-Globa, A.; Michaelis, M.; Cinatl, J.; Schwartz, D.; et al. Enhanced Drug Targeting by

Attachment of an Anti Av Integrin Antibody to Doxorubicin Loaded Human Serum Albumin Nanoparticles. *Biomaterials* **2010**, *31*, 2388–2398, doi:10.1016/J.BIOMATERIALS.2009.11.093.

85. Alexander-Bryant, A.A.; Vanden Berg-Foels, W.S.; Wen, X. Bioengineering Strategies for Designing Targeted Cancer Therapies. In *Adv Cancer Res*; 2013; Vol. 118, pp. 1–59 ISBN 9780124071735.

86. Chen, S.; Zhao, X.; Chen, J.; Chen, J.; Kuznetsova, L.; Wong, S.S.; Ojima, I. Mechanism-Based Tumor-Targeting Drug Delivery System. Validation of Efficient Vitamin Receptor-Mediated Endocytosis and Drug Release. *Bioconjug. Chem.* **2010**, *21*, 979–987, doi:10.1021/bc9005656.

87. Maiti, S.; Park, N.; Han, J.H.; Jeon, H.M.; Lee, J.H.; Bhuniya, S.; Kang, C.; Kim, J.S. Gemcitabine–Coumarin–Biotin Conjugates: A Target Specific Theranostic Anticancer Prodrug. *J. Am. Chem. Soc.* **2013**, *135*, 4567–4572, doi:10.1021/ja401350x.

88. Bhuniya, S.; Maiti, S.; Kim, E.-J.; Lee, H.; Sessler, J.L.; Hong, K.S.; Kim, J.S. An Activatable Theranostic for Targeted Cancer Therapy and Imaging. *Angew. Chemie Int. Ed.* **2014**, *53*, 4469–4474, doi:10.1002/anie.201311133.

89. Chavva, S.R.; Pramanik, A.; Nellore, B.P.V.; Sinha, S.S.; Yust, B.; Kanchanapally, R.; Fan, Z.; Crouch, R.A.; Singh, A.K.; Neyland, B.; et al. Theranostic Graphene Oxide for Prostate Cancer Detection and Treatment. *Part. Part. Syst. Charact.* **2014**, *31*, 1252–1259, doi:10.1002/ppsc.201400143.

90. Vineberg, J.G.; Zuniga, E.S.; Kamath, A.; Chen, Y.-J.; Seitz, J.D.; Ojima, I. Design, Synthesis, and Biological Evaluations of Tumor-Targeting Dual-Warhead Conjugates for a Taxoid–Camptothecin Combination Chemotherapy. *J. Med. Chem.* **2014**, *57*, 5777–5791, doi:10.1021/jm500631u.

91. Golani, L.K.; Wallace-Povirk, A.; Deis, S.M.; Wong, J.; Ke, J.; Gu, X.; Raghavan, S.; Wilson, M.R.; Li, X.; Polin, L.; et al. Tumor Targeting with Novel 6-Substituted Pyrrolo [2,3-d] Pyrimidine Antifolates with Heteroatom Bridge Substitutions via Cellular Uptake by Folate Receptor α and the Proton-Coupled Folate Transporter and Inhibition of de Novo Purine Nucleotide Biosynthesi. *J. Med. Chem.* **2016**, *59*, 7856–7876, doi:10.1021/acs.jmedchem.6b00594.

92. Sudimack, J.; Lee, R.J. Targeted Drug Delivery via the Folate Receptor. *Adv. Drug Deliv. Rev.* **2000**, *41*, 147–162, doi:10.1016/S0169-409X(99)00062-9.

93. Parker, N.; Jo, M.; Westrick, E.; Je, V.; Lewis, D.; Low, P.S.; Leamon, C.P. Folate Receptor Expression in Carcinomas and Normal Tissues Determined by a Quantitative Radioligand Binding Assay. *Anal. Biochem.* **2005**, *338*, 284–293, doi:10.1016/j.ab.2004.12.026.

94. Hou, Z.; Matherly, L.H. Biology of the Major Facilitative Folate Transporters SLC19A1 and SLC46A1. In *Current Topics in Membranes*; 2014; Vol. 73, pp. 175–204 ISBN 9780128002230.

95. O'Connor, C.; Wallace-Povirk, A.; Ning, C.; Frühauf, J.; Tong, N.; Gangjee, A.; Matherly, L.H.; Hou, Z. Folate Transporter Dynamics and Therapy with Classic and Tumor-Targeted Antifolates. *Sci. Rep.* **2021**, *11*, 1–14, doi:10.1038/s41598-021-85818-x.

96. Wallace-Povirk, A.; Tong, N.; O'Connor, C.; Hou, Z.; Gangjee, A.; Matherly, L.; Zhou, X. Abstract 3983: Tumor-Targeting with Novel Dual-Targeted 6-Substituted Thieno[2,3-*d*]Pyrimidine Antifolates via Cellular Uptake by Folate Receptor α, and Inhibition of de

Novo Purine Nucleotide Biosynthesis. *Cancer Res.* **2018**, *78*, 3983–3983, doi:10.1158/1538-7445.AM2018-3983.

97. He, B.; Chai, G.; Duan, Y.; Yan, Z.; Qiu, L.; Zhang, H.; Liu, Z.; He, Q.; Han, K.; Ru, B.; et al. BDB: Biopanning Data Bank. *Nucleic Acids Res.* **2016**, *44*, D1127–D1132, doi:10.1093/nar/gkv1100.

98. Das, M.; Mohanty, C.; Sahoo, S.K. Ligand-Based Targeted Therapy for Cancer Tissue. *Expert Opin. Drug Deliv.* **2009**, *6*, 285–304, doi:10.1517/17425240902780166.

99. Schrama, D.; Reisfeld, R.A.; Becker, J.C. Antibody Targeted Drugs as Cancer Therapeutics. *Nat. Rev. Drug Discov.* **2006**, *5*, 147–159, doi:10.1038/nrd1957.

100. Sandland, J.; Boyle, R.W. Photosensitizer Antibody–Drug Conjugates: Past, Present, and Future. *Bioconjug. Chem.* **2019**, *30*, 975–993, doi:10.1021/acs.bioconjchem.9b00055.

101. Kijanka, M.; Dorresteijn, B.; Oliveira, S.; van Bergen en Henegouwen, P.M.P. Nanobody-Based Cancer Therapy of Solid Tumors. *Nanomedicine* **2015**, *10*, 161–174, doi:10.2217/nnm.14.178.

102. Marques, A.C.; Costa, P.J.; Velho, S.; Amaral, M.H. Functionalizing Nanoparticles with Cancer-Targeting Antibodies: A Comparison of Strategies. *J. Control. Release* **2020**, *320*, 180–200, doi:10.1016/j.jconrel.2020.01.035.

103. Wu, A.M.; Senter, P.D. Arming Antibodies: Prospects and Challenges for Immunoconjugates. *Nat. Biotechnol.* **2005**, *23*, 1137–1146, doi:10.1038/nbt1141.

104. Mitsunaga, M.; Ogawa, M.; Kosaka, N.; Rosenblum, L.T.; Choyke, P.L.; Kobayashi, H. Cancer Cell-Selective in Vivo near Infrared Photoimmunotherapy Targeting Specific Membrane Molecules. *Nat. Med.* **2011**, *17*, 1685–1691, doi:10.1038/nm.2554.

105. Railkar, R.; Krane, L.S.; Li, Q.Q.; Sanford, T.; Siddiqui, M.R.; Haines, D.; Vourganti, S.; Brancato, S.J.; Choyke, P.L.; Kobayashi, H.; et al. Epidermal Growth Factor Receptor (EGFR)-Targeted Photoimmunotherapy (PIT) for the Treatment of EGFR-Expressing Bladder Cancer. *Mol. Cancer Ther.* **2017**, *16*, 2201–2214, doi:10.1158/1535-7163.MCT-16-0924.

106. Siddiqui, M.R.; Railkar, R.; Sanford, T.; Crooks, D.R.; Eckhaus, M.A.; Haines, D.; Choyke, P.L.; Kobayashi, H.; Agarwal, P.K. Targeting Epidermal Growth Factor Receptor (EGFR) and Human Epidermal Growth Factor Receptor 2 (HER2) Expressing Bladder Cancer Using Combination Photoimmunotherapy (PIT). *Sci. Rep.* **2019**, *9*, 2084, doi:10.1038/s41598-019-38575-x.

107. Nagaya, T.; Nakamura, Y.; Okuyama, S.; Ogata, F.; Maruoka, Y.; Choyke, P.L.; Kobayashi, H. Near-Infrared Photoimmunotherapy Targeting Prostate Cancer with Prostate-Specific Membrane Antigen (PSMA) Antibody. *Mol. cancer Res. MCR* **2017**, *15*, 1153–1162, doi:10.1158/1541-7786.MCR-17-0164.

108. Watanabe, R.; Hanaoka, H.; Sato, K.; Nagaya, T.; Harada, T.; Mitsunaga, M.; Kim, I.; Paik, C.H.; Wu, A.M.; Choyke, P.L.; et al. Photoimmunotherapy Targeting Prostate-Specific Membrane Antigen: Are Antibody Fragments as Effective as Antibodies? *J. Nucl. Med. Off. Publ. Soc. Nucl. Med.* **2015**, *56*, 140–144, doi:10.2967/jnumed.114.149526.

109. Nagaya, T.; Nakamura, Y.; Okuyama, S.; Ogata, F.; Maruoka, Y.; Choyke, P.L.; Allen, C.; Kobayashi, H. Syngeneic Mouse Models of Oral Cancer Are Effectively Targeted by Anti-CD44-Based NIR-PIT. *Mol. cancer Res. MCR* **2017**, *15*, 1667–1677, doi:10.1158/1541-

7786.MCR-17-0333.

110. Isobe, Y.; Sato, K.; Nishinaga, Y.; Takahashi, K.; Taki, S.; Yasui, H.; Shimizu, M.; Endo, R.; Koike, C.; Kuramoto, N.; et al. Near Infrared Photoimmunotherapy Targeting DLL3 for Small Cell Lung Cancer. *EBioMedicine* **2020**, *52*, 102632, doi:10.1016/j.ebiom.2020.102632.

111. Jing, H.; Weidensteiner, C.; Reichardt, W.; Gaedicke, S.; Zhu, X.; Grosu, A.-L.; Kobayashi, H.; Niedermann, G. Imaging and Selective Elimination of Glioblastoma Stem Cells with Theranostic Near-Infrared-Labeled CD133-Specific Antibodies. *Theranostics* **2016**, *6*, 862–874, doi:10.7150/thno.12890.

112. Wei, W.; Jiang, D.; Ehlerding, E.B.; Barnhart, T.E.; Yang, Y.; Engle, J.W.; Luo, Q.; Huang, P.; Cai, W. CD146-Targeted Multimodal Image-Guided Photoimmunotherapy of Melanoma. *Adv. Sci.* **2019**, *6*, 1801237, doi:10.1002/advs.201801237.

113. Kobayashi, H.; Choyke, P.L. Near-Infrared Photoimmunotherapy of Cancer. *Acc. Chem. Res.* **2019**, *52*, 2332–2339, doi:10.1021/acs.accounts.9b00273.

114. Gomes-da-Silva, L.C.; Kepp, O.; Kroemer, G. Regulatory Approval of Photoimmunotherapy: Photodynamic Therapy That Induces Immunogenic Cell Death. *Oncoimmunology* **2020**, *9*, doi:10.1080/2162402X.2020.1841393.

115. Sato, K.; Ando, K.; Okuyama, S.; Moriguchi, S.; Ogura, T.; Totoki, S.; Hanaoka, H.; Nagaya, T.; Kokawa, R.; Takakura, H.; et al. Photoinduced Ligand Release from a Silicon Phthalocyanine Dye Conjugated with Monoclonal Antibodies: A Mechanism of Cancer Cell Cytotoxicity after Near-Infrared Photoimmunotherapy. *ACS Cent. Sci.* **2018**, *4*, 1559–1569, doi:10.1021/acscentsci.8b00565.

116. Kobayashi, H. Near Infrared Photoimmunotherapy: A New Type of Immune Theranostic Technology for Cancer. In Proceedings of the Clinical Biophotonics; Elson, D.S., Gioux, S., Pogue, B.W., Elson, D.S., Gioux, S., Pogue, B.W., Eds.; Online Only, France, August 3 2020; p. 26.

117. van Driel, P.B.A.A.; Boonstra, M.C.; Slooter, M.D.; Heukers, R.; Stammes, M.A.; Snoeks, T.J.A.; de Bruijn, H.S.; van Diest, P.J.; Vahrmeijer, A.L.; van Bergen en Henegouwen, P.M.P.; et al. EGFR Targeted Nanobody–Photosensitizer Conjugates for Photodynamic Therapy in a Pre-Clinical Model of Head and Neck Cancer. *J. Control. Release* **2016**, *229*, 93–105, doi:10.1016/j.jconrel.2016.03.014.

118. Heukers, R.; Mashayekhi, V.; Ramirez-Escudero, M.; de Haard, H.; Verrips, T.; van Bergen en Henegouwen, P.; Oliveira, S. VHH-Photosensitizer Conjugates for Targeted Photodynamic Therapy of Met-Overexpressing Tumor Cells. *Antibodies* **2019**, *8*, 26, doi:10.3390/antib8020026.

119. De Groof, T.W.M.; Mashayekhi, V.; Fan, T.S.; Bergkamp, N.D.; Sastre Toraño, J.; van Senten, J.R.; Heukers, R.; Smit, M.J.; Oliveira, S. Nanobody-Targeted Photodynamic Therapy Selectively Kills Viral GPCR-Expressing Glioblastoma Cells. *Mol. Pharm.* **2019**, *16*, 3145–3156, doi:10.1021/acs.molpharmaceut.9b00360.

120. Yamaguchi; Pantarat; Suzuki; Evdokiou Near-Infrared Photoimmunotherapy Using a Small Protein Mimetic for HER2-Overexpressing Breast Cancer. *Int. J. Mol. Sci.* **2019**, *20*, 5835, doi:10.3390/ijms20235835.

121. Li, Z.J.; Cho, C.H. Peptides as Targeting Probes against Tumor Vasculature for Diagnosis and Drug Delivery. *J. Transl. Med.* **2012**, *10 Suppl 1*, S1–S1, doi:10.1186/1479-5876-10-

S1-S1.

122. Brown, K.C. Peptidic Tumor Targeting Agents: The Road from Phage Display Peptide Selections to Clinical Applications. *Curr. Pharm. Des.* **2010**, *16*, 1040–1054, doi:10.2174/138161210790963788.

123. Li, Z.; Zhao, R.; Wu, X.; Sun, Y.; Yao, M.; Li, J.; Xu, Y.; Gu, J. Identification and Characterization of a Novel Peptide Ligand of Epidermal Growth Factor Receptor for Targeted Delivery of Therapeutics. *FASEB J.* **2005**, *19*, 1978–1985, doi:10.1096/fj.05-4058com.

124. Yu, L.; Wang, Q.; Wong, R.C.-H.; Zhao, S.; Ng, D.K.P.; Lo, P.-C. Synthesis and Biological Evaluation of Phthalocyanine-Peptide Conjugate for EGFR-Targeted Photodynamic Therapy and Bioimaging. *Dye. Pigment.* **2019**, *163*, 197–203, doi:10.1016/j.dyepig.2018.11.055.

125. Kim, J.; Chae, J.; Kim, J.S.; Goh, S.-H.; Choi, Y. Photosensitizer-Conjugated Tryptophan-Containing Peptide Ligands as New Dual-Targeted Theranostics for Cancers. *Int. J. Pharm.* **2016**, *513*, 584–590, doi:10.1016/j.ijpharm.2016.09.071.

126. Kim, J.; Won, Y.; Goh, S.H.; Choi, Y. A Redox-Responsive Theranostic Agent for Target-Specific Fluorescence Imaging and Photodynamic Therapy of EGFR-Overexpressing Triple-Negative Breast Cancers. *J. Mater. Chem. B* **2016**, *4*, 6787–6790, doi:10.1039/c6tb01519k.

127. Xu, P.; Jia, Y.; Yang, Y.; Chen, J.; Hu, P.; Chen, Z.; Huang, M. Photodynamic Oncotherapy Mediated by Gonadotropin-Releasing Hormone Receptors. *J. Med. Chem.* **2017**, *60*, 8667–8672, doi:10.1021/acs.jmedchem.7b01216.

128. Zhang, C.; Gao, F.; Wu, W.; Qiu, W.-X.; Zhang, L.; Li, R.; Zhuang, Z.-N.; Yu, W.; Cheng, H.; Zhang, X.-Z. Enzyme-Driven Membrane-Targeted Chimeric Peptide for Enhanced Tumor Photodynamic Immunotherapy. *ACS Nano* **2019**, *13*, 11249–11262, doi:10.1021/acsnano.9b04315.

129. Daniels, T.R.; Bernabeu, E.; Rodríguez, J.A.; Patel, S.; Kozman, M.; Chiappetta, D.A.; Holler, E.; Ljubimova, J.Y.; Helguera, G.; Penichet, M.L. The Transferrin Receptor and the Targeted Delivery of Therapeutic Agents against Cancer. *Biochim. Biophys. Acta* **2012**, *1820*, 291–317, doi:10.1016/j.bbagen.2011.07.016.

130. Bazak, R.; Houri, M.; El Achy, S.; Kamel, S.; Refaat, T. Cancer Active Targeting by Nanoparticles: A Comprehensive Review of Literature. *J. Cancer Res. Clin. Oncol.* **2015**, *141*, 769–784, doi:10.1007/s00432-014-1767-3.

131. Balçik-Erçin, P.; Çetin, M.; Göksel, M.; Durmuş, M. Improved Targeting for Photodynamic Therapy *via* a Biotin–Phthalocyanine Conjugate: Synthesis, Photophysical and Photochemical Measurements, and *in Vitro* Cytotoxicity Assay. *New J. Chem.* **2020**, *44*, 3392–3401, doi:10.1039/C9NJ04991F.

132. Li, J.; Zeng, L.; Xiong, K.; Rees, T.W.; Jin, C.; Wu, W.; Chen, Y.; Ji, L.; Chao, H. A Biotinylated Ruthenium(II) Photosensitizer for Tumor-Targeted Two-Photon Photodynamic Therapy. *Chem. Commun.* **2019**, *55*, 10972–10975, doi:10.1039/C9CC05826E.

133. Li, K.; Dong, W.; Liu, Q.; Lv, G.; Xie, M.; Sun, X.; Qiu, L.; Lin, J. A Biotin Receptor-Targeted Silicon(IV) Phthalocyanine for in Vivo Tumor Imaging and Photodynamic Therapy. *J. Photochem. Photobiol. B Biol.* **2019**, *190*, 1–7,

doi:10.1016/j.jphotobiol.2018.09.001.

134. Zolottsev, V.A.; Ponomarev, G. V; Taratynova, M.O.; Morozevich, G.E.; Novikov, R.A.; Timofeev, V.P.; Solyev, P.N.; Zavialova, M.G.; Zazulina, O. V; Tkachev, Y. V; et al. Conjugates of 17-Substituted Testosterone and Epitestosterone with Pyropheophorbide a Differing in the Length of Linkers. *Steroids* **2018**, *138*, 82–90, doi:10.1016/j.steroids.2018.06.011.

135. Tanaka, M.; Kataoka, H.; Mabuchi, M.; Sakuma, S.; Takahashi, S.; Tujii, R.; Akashi, H.; Ohi, H.; Yano, S.; Morita, A.; et al. Anticancer Effects of Novel Photodynamic Therapy with Glycoconjugated Chlorin for Gastric and Colon Cancer. *Anticancer Res.* **2011**, 7.

136. Hayashi, N.; Kataoka, H.; Yano, S.; Tanaka, M.; Moriwaki, K.; Akashi, H.; Suzuki, S.; Mori, Y.; Kubota, E.; Tanida, S.; et al. A Novel Photodynamic Therapy Targeting Cancer Cells and Tumor-Associated Macrophages. *Mol. Cancer Ther.* **2015**, *14*, 452–460, doi:10.1158/1535-7163.MCT-14-0348.

137. Hamblin, M.R.; Newman, E.L. Photosensitizer Targeting in Photodynamic Therapy I. Conjugates of Haematoporphyrin with Albumin and Transferrin. *J. Photochem. Photobiol. B Biol.* **1994**, *26*, 45–56, doi:10.1016/1011-1344(94)85035-6.

138. Cavanaugh, P.G. Synthesis of Chlorin E6-Transferrin and Demonstration of Its Light-Dependent in Vitro Breast Cancer Cell Killing Ability. *Breast Cancer Res. Treat.* **2002**, *72*, 117–130, doi:10.1023/A:1014811915564.

139. Kaspler, P.; Lazic, S.; Forward, S.; Arenas, Y.; Mandel, A.; Lilge, L. A Ruthenium(II) Based Photosensitizer and Transferrin Complexes Enhance Photo-Physical Properties, Cell Uptake, and Photodynamic Therapy Safety and Efficacy. *Photochem. Photobiol. Sci.* **2016**, *15*, 481–495, doi:10.1039/C5PP00450K.

140. Jadia, R.; Kydd, J.; Rai, P. Remotely Phototriggered, Transferrin-Targeted Polymeric Nanoparticles for the Treatment of Breast Cancer. *Photochem. Photobiol.* **2018**, *94*, 765–774, doi:10.1111/php.12903.

141. Dixit, S.; Novak, T.; Miller, K.; Zhu, Y.; Kenney, M.E.; Broome, A.-M. Transferrin Receptor-Targeted Theranostic Gold Nanoparticles for Photosensitizer Delivery in Brain Tumors. *Nanoscale* **2015**, *7*, 1782–1790, doi:10.1039/C4NR04853A.

142. Zhu, X.; Zhou, H.; Liu, Y.; Wen, Y.; Wei, C.; Yu, Q.; Liu, J. Transferrin/Aptamer Conjugated Mesoporous Ruthenium Nanosystem for Redox-Controlled and Targeted Chemo-Photodynamic Therapy of Glioma. *Acta Biomater.* **2018**, *82*, 143–157, doi:10.1016/j.actbio.2018.10.012.

143. Stallivieri, A.; Colombeau, L.; Jetpisbayeva, G.; Moussaron, A.; Myrzakhmetov, B.; Arnoux, P.; Acherar, S.; Vanderesse, R.; Frochot, C. Folic Acid Conjugates with Photosensitizers for Cancer Targeting in Photodynamic Therapy: Synthesis and Photophysical Properties. *Bioorg. Med. Chem.* **2017**, *25*, 1–10, doi:10.1016/j.bmc.2016.10.004.

144. Suvorov, N. V; Mironov, A.F.; Grin, M.A. Folic Acid and Its Derivatives for Targeted Photodynamic Therapy of Cancer. *Russ. Chem. Bull.* **2017**, *66*, 1982–2008, doi:10.1007/s11172-017-1973-7.

145. Yang, M.; Deng, J.; Guo, D.; Zhang, J.; Yang, L.; Wu, F. A Folate-Conjugated Platinum Porphyrin Complex as a New Cancer-Targeting Photosensitizer for Photodynamic Therapy. *Org. Biomol. Chem.* **2019**, *17*, 5367–5374, doi:10.1039/C9OB00698B.

146. Jenni, S.; Sour, A.; Bolze, F.; Ventura, B.; Heitz, V. Tumour-Targeting Photosensitisers for One- and Two-Photon Activated Photodynamic Therapy. *Org. Biomol. Chem.* **2019**, *17*, 6585–6594, doi:10.1039/C9OB00731H.

147. Liu, Q.; Wang, J.; Li, S.; Li, G.; Chen, Q.; Hong, Z. Folate-Targeted Polyethylene Glycol–Modified Photosensitizers for Photodynamic Therapy. *J. Pharm. Sci.* **2019**, *108*, 2102–2111, doi:10.1016/j.xphs.2019.01.014.

148. Gravier, J.; Schneider, R.; Frochot, C.; Bastogne, T.; Schmitt, F.; Didelon, J.; Guillemin, F.; Barberi-Heyob, M. Improvement of Meta-Tetra(Hydroxyphenyl)Chlorin-like Photosensitizer Selectivity with Folate-Based Targeted Delivery. Synthesis and in Vivo Delivery Studies. *J. Med. Chem.* **2008**, *51*, 3867–3877, doi:10.1021/jm800125a.

149. Bartlett, D.W.; Su, H.; Hildebrandt, I.J.; Weber, W.A.; Davis, M.E. Impact of Tumor-Specific Targeting on the Biodistribution and Efficacy of SiRNA Nanoparticles Measured by Multimodality in Vivo</Em> Imaging. *Proc. Natl. Acad. Sci.* **2007**, *104*, 15549, doi:10.1073/pnas.0707461104.

150. Jain, M.; Venkatraman, G.; Batra, S.K. Optimization of Radioimmunotherapy of Solid Tumors: Biological Impediments and Their Modulation. *Clin. Cancer Res.* **2007**, *13*, 1374–1382, doi:10.1158/1078-0432.CCR-06-2436.

151. Goldenberg, D.M. Advancing Role of Radiolabeled Antibodies in the Therapy of Cancer. *Cancer Immunol. Immunother.* **2003**, *52*, 281–296, doi:10.1007/s00262-002-0348-5.

152. Verhaar-Langereis, M.J.; Zonnenberg, B.A.; De Klerk, J.M.H.; Blijham, G.H. Radioimmunodiagnosis and Therapy. *Cancer Treat. Rev.* **2000**, *26*, 3–10, doi:10.1053/ctrv.1999.0146.

153. Pereira, N.A.M.; Serra, A.C.; Pinho e Melo, T.M.V.D. Novel Approach to Chlorins and Bacteriochlorins: [8π+2π] Cycloaddition of Diazafulvenium Methides with Porphyrins. *European J. Org. Chem.* **2010**, 6539–6543, doi:10.1002/ejoc.201001157.

154. Pereira, N.A.M.; Fonseca, S.M.; Serra, A.C.; Pinho e Melo, T.M.V.D.; Burrows, H.D. [8π+2π] Cycloaddition of Meso-Tetra- and 5,15-Diarylporphyrins: Synthesis and Photophysical Characterization of Stable Chlorins and Bacteriochlorins. *European J. Org. Chem.* **2011**, *2011*, 3970–3979, doi:10.1002/ejoc.201100465.

155. Pereira, N.A.M.; Laranjo, M.; Pineiro, M.; Serra, A.C.; Santos, K.; Teixo, R.; Abrantes, A.M.; Gonçalves, A.C.; Ribeiro, A.B.S.; Casalta-Lopes, J.; et al. Novel 4,5,6,7-Tetrahydropyrazolo[1,5-*a*]Pyridine Fused Chlorins as Very Active Photodynamic Agents for Melanoma Cells. *Eur. J. Med. Chem.* **2015**, *103*, 374–380, doi:10.1016/j.ejmech.2015.08.059.

156. Pereira, N.A.M.; Laranjo, M.; Nascimento, B.F.O.; Simões, J.C.S.; Pina, J.; Costa, B.D.P.; Brites, G.; Braz, J.; Seixas de Melo, J.S.; Pineiro, M.; et al. Novel Fluorinated Ring-Fused Chlorins as Promising PDT Agents against Melanoma and Esophagus Cancer. *RSC Med. Chem.* **2021**, *12*, 615–627, doi:10.1039/d0md00433b.

157. Laranjo, M.; Pereira, N.A.M.; Oliveira, A.S.R.; Campos Aguiar, M.; Brites, G.; Nascimento, B.F.O.; Serambeque, B.; Costa, B.D.P.; Pina, J.; Seixas de Melo, J.S.; et al. Ring-Fused Meso-Tetraarylchlorins as Auspicious PDT Sensitizers: Synthesis, Structural Characterization, Photophysics, and Biological Evaluation. *Front. Chem.* **2022**, *10*, 1–14, doi:10.3389/fchem.2022.873245.

158. Simões, J.C.S.; Sarpaki, S.; Papadimitroulas, P.; Therrien, B.; Loudos, G. Conjugated

Photosensitizers for Imaging and PDT in Cancer Research. *J. Med. Chem.* **2020**, *63*, 14119–14150, doi:10.1021/acs.jmedchem.0c00047.

159. Pereira, M.M.; Monteiro, C.J.P.; Simões, A.V.C.; Pinto, S.M.A.; Abreu, A.R.; Sá, G.F.F.; Silva, E.F.F.; Rocha, L.B.; Dbrowski, J.M.; Formosinho, S.J.; et al. Synthesis and Photophysical Characterization of a Library of Photostable Halogenated Bacteriochlorins: An Access to near Infrared Chemistry. *Tetrahedron* **2010**, *66*, 9545–9551, doi:10.1016/j.tet.2010.09.106.

160. Huang, Y.-Y.; Balasubramanian, T.; Yang, E.; Luo, D.; Diers, J.R.; Bocian, D.F.; Lindsey, J.S.; Holten, D.; Hamblin, M.R. Stable Synthetic Bacteriochlorins for Photodynamic Therapy: Role of Dicyano Peripheral Groups, Central Metal Substitution (2H, Zn, Pd), and Cremophor EL Delivery. *ChemMedChem* **2012**, *7*, 2155–2167, doi:10.1002/cmdc.201200351.

161. Jacobi, P.A.; Lanz, S.; Ghosh, I.; Leung, S.H.; Löwer, F.; Pippin, D. A New Synthesis of Chlorins. *Org. Lett.* **2001**, *3*, 831–834, doi:10.1021/ol006983m.

162. Lindsey, J.S. De Novo Synthesis of Gem-Dialkyl Chlorophyll Analogues for Probing and Emulating Our Green World. *Chem. Rev.* **2015**, *115*, 6534–6620, doi:10.1021/acs.chemrev.5b00065.

163. Montforts, F.-P. Ein Gezielter Aufbau Des Chlorinsystems. *Angew. Chemie* **1981**, *93*, 795–796, doi:10.1002/ange.19810930916.

164. Montforts, F.-P.; Schwartz, U.M. Ein Gezielter Aufbau Des Chlorinsystems. *Liebigs Ann. der Chemie* **1985**, 1228–1253, doi:10.1002/jlac.198519850614.

165. Burns, D.H.; Shi, D.C.; Lash, T.D. Synthesis of the Chlorin Macrocycle by the '3 + 1' Approach. *Chem. Commun.* **2000**, 299–300, doi:10.1039/a908784b.

166. Battersby, A.R.; Dutton, C.J.; Fookes, C.J.R.; Turner, S.P.D. Synthesis of the Chlorin Macrocycle by a Photochemical Approach. *J. Chem. Soc. Chem. Commun.* **1983**, 1235, doi:10.1039/c39830001235.

167. Taniguchi, M.; Lindsey, J.S. Synthetic Chlorins, Possible Surrogates for Chlorophylls, Prepared by Derivatization of Porphyrins. *Chem. Rev.* **2017**, *117*, 344–535, doi:10.1021/acs.chemrev.5b00696.

168. Meunier, I.; Pandey, R.K.; Senge, M.O.; Dougherty, T.J.; Smith, K.M. Benzoporphyrin Derivatives: Synthesis, Structure and Preliminary Biological Activity. *J. Chem. Soc. Perkin Trans. 1* **1994**, 961–969, doi:10.1039/p19940000961.

169. Chan, W.M.; Lim, T.H.; Pece, A.; Silva, R.; Yoshimura, N. Verteporfin PDT for Non-Standard Indications-a Review of Current Literature. *Graefe's Arch. Clin. Exp. Ophthalmol.* **2010**, *248*, 613–626, doi:10.1007/s00417-010-1307-z.

170. Chin, W.W.L.; Heng, P.W.S.; Bhuvaneswari, R.; Lau, W.K.O.; Olivo, M. The Potential Application of Chlorin E6–Polyvinylpyrrolidone Formulation in Photodynamic Therapy. *Photochem. Photobiol. Sci.* **2006**, *5*, 1031–1037, doi:10.1039/b605772a.

171. Usuda, J.; Kato, H.; Okunaka, T.; Furukawa, K.; Tsutsui, H.; Yamada, K.; Suga, Y.; Honda, H.; Nagatsuka, Y.; Ohira, T.; et al. Photodynamic Therapy (PDT) for Lung Cancers. *J. Thorac. Oncol.* **2006**, *1*, 489–93.

172. Biswas, R.; Moon, J.H.; Ahn, J.C. Chlorin E6 Derivative Radachlorin Mainly Accumulates

in Mitochondria, Lysosome and Endoplasmic Reticulum and Shows High Affinity toward Tumors in Nude Mice in Photodynamic Therapy. *Photochem. Photobiol.* **2014**, *90*, 1108–1118, doi:10.1111/php.12273.

173. Whitlock, H.W.; Hanauer, R.; Oester, M.Y.; Bower, B.K. Diimide Reduction of Porphyrins. *J. Am. Chem. Soc.* **1969**, *91*, 7485–7489, doi:10.1021/ja01054a044.

174. Fischer, H.; Eckoldt, H. Überführung von Porphyrinen in Dioxy-Chlorine Durch Einwirkung von Osmiumtetroxyd. *Justus Liebig's Ann. der Chemie* **1940**, *544*, 138–162, doi:10.1002/jlac.19405440109.

175. Brückner, C.; Dolphin, D. 2,3-Vic-Dihydroxy-Meso-Tetraphenylchlorins from the Osmium Tetroxide Oxidation of Meso-Tetraphenylporphyrin. *Tetrahedron Lett.* **1995**, *36*, 3295–3298, doi:10.1016/0040-4039(95)00524-G.

176. Callott, H.J.; Johnson, A.W.; Sweeney, A. Additions to Porphins Involving the Formation of New Carbon–Carbon Bonds. *J. Chem. Soc., Perkin Trans. 1* **1973**, 1424–1427, doi:10.1039/P19730001424.

177. Pangka, V.S.; Morgan, A.R.; Dolphin, D. The Diels-Alder Reactions of Protoporphyrin IX Dimethyl Ester with Electron-Deficient Alkynes. *J. Org. Chem.* **1986**, *51*, 1094–1100, doi:10.1021/jo00357a029.

178. Tomé, A.C.; Lacerda, P.S.S.; Neves, M.G.P.M.S.; Cavaleiro, J.A.S. Meso-Arylporphyrins as Dienophiles in Diels–Alder Reactions: A Novel Approach to the Synthesis of Chlorins, Bacteriochlorins and Naphthoporphyrins. *Chem. Commun.* **1997**, 1199–1200, doi:10.1039/a702504a.

179. Silva, A.M.G.; Tomé, A.C.; Neves, M.G.P.M.S.; Silva, A.M.S.; Cavaleiro, J.A.S. Meso-Tetraarylporphyrins as Dipolarophiles in 1,3-Dipolar Cycloaddition Reactions. *Chem. Commun.* **1999**, 1767–1768, doi:10.1039/a905016g.

180. Silva, A.M.G.; Tomé, A.C.; Neves, M.G.P.M.S.; Silva, A.M.S.; Cavaleiro, J.A.S. 1,3-Dipolar Cycloaddition Reactions of Porphyrins with Azomethine Ylides. *J. Org. Chem.* **2005**, *70*, 2306–2314, doi:10.1021/jo048349i.

181. Adler, A.D.; Longo, F.R.; Shergalis, W. Mechanistic Investigations of Porphyrin Syntheses. I. Preliminary Studies on Ms -Tetraphenylporphin. *J. Am. Chem. Soc.* **1964**, *86*, 3145–3149, doi:10.1021/ja01069a035.

182. Adler, A.D.; Longo, F.R.; Finarelli, J.D.; Goldmacher, J.; Assour, J.; Korsakoff, L. A Simplified Synthesis for Meso-Tetraphenylporphine. *J. Org. Chem.* **1967**, *32*, 476–476, doi:10.1021/jo01288a053.

183. Ormond, A.B.; Freeman, H.S. Effects of Substituents on the Photophysical Properties of Symmetrical Porphyrins. *Dye. Pigment.* **2013**, *96*, 440–448, doi:10.1016/j.dyepig.2012.09.011.

184. Sutcliffe, O.B.; Storr, R.C.; Gilchrist, T.L.; Rafferty, P. Cycloadditions to Pyrrolo[1,2-c]Thiazoles and Pyrazolo[1,5-c]Thiazoles. *Tetrahedron* **2000**, *56*, 10011–10021, doi:10.1016/S0040-4020(00)00956-X.

185. Lopes, S.M.M.; Correia, C.F.O.; Nunes, S.C.C.; Pereira, N.A.M.; Ferreira, A.R.F.; Sousa, E.P.; Gomes, C.S.B.; Salvador, J.A.R.; Pais, A.A.C.C.; Pinho e Melo, T.M.V.D. Synthesis of Chiral Hexacyclic Steroids *via* [8π + 2π] Cycloaddition of Diazafulvenium Methides. *Org. Biomol. Chem.* **2015**, *13*, 9127–9139, doi:10.1039/C5OB01110H.

186. Kolb, H.C.; Finn, M.G.; Sharpless, K.B. Click Chemistry: Diverse Chemical Function from a Few Good Reactions. *Angew. Chemie Int. Ed.* **2001**, *40*, 2004–2021, doi:10.1002/1521-3773(20010601)40:11<2004::AID-ANIE2004>3.0.CO;2-5.

187. Huisgen, R. Proceedings of the Chemical Society. *Proc. Chem. Soc.* **1961**, 357–396, doi:10.1039/ps9610000357.

188. Agard, N.J.; Baskin, J.M.; Prescher, J.A.; Lo, A.; Bertozzi, C.R. A Comparative Study of Bioorthogonal Reactions with Azides. *ACS Chem. Biol.* **2006**, *1*, 644–648, doi:10.1021/cb6003228.

189. Evans, R.A. The Rise of Azide–Alkyne 1,3-Dipolar "Click" Cycloaddition and Its Application to Polymer Science and Surface Modification. *Aust. J. Chem.* **2007**, *60*, 384, doi:10.1071/CH06457.

190. Appel, R. Tertiary Phosphane/Tetrachloromethane, a Versatile Reagent for Chlorination, Dehydration, and P-N Linkage. *Angew. Chemie Int. Ed. English* **1975**, *14*, 801–811, doi:10.1002/anie.197508011.

191. Armarego, W.L.F.; Chai, C.L.L. *Purification of Laboratory Chemicals*; Elsevier, Ed.; 6th ed.; Butterworth-Heinemann: Burlington, 2009; ISBN 978-1-85617-567-8.

192. Gazizov, M.B.; Ivanova, S.Y.; Ibragimov, S.N.; Bagauva, L.R.; Khairullin, R.A.; Medvedeva, K.A. New Method of Synthesis of Functionally Substituted Aromatic Aldehydes. *Russ. J. Gen. Chem.* **2016**, *86*, 2129–2131, doi:10.1134/S1070363216090267.

193. Sutcliffe, O.B.; Storr, R.C.; Gilchrist, T.L.; Rafferty, P. Azafulvenium Methides: New Extended Dipolar Systems. *J. Chem. Soc. Perkin Trans. 1* **2001**, 1795–1806, doi:10.1039/b103250j.

194. Chen, C.; Ke, J.; Zhou, X.E.; Yi, W.; Brunzelle, J.S.; Li, J.; Yong, E.-L.; Xu, H.E.; Melcher, K. Structural Basis for Molecular Recognition of Folic Acid by Folate Receptors. *Nature* **2013**, *500*, 486–489, doi:10.1038/nature12327.

195. Trindade, A.F.; Frade, R.F.M.; Maçôas, E.M.S.; Graça, C.; Rodrigues, C.A.B.; Martinho, J.M.G.; Afonso, C.A.M. "Click and Go": Simple and Fast Folic Acid Conjugation. *Org. Biomol. Chem.* **2014**, *12*, 3181–3190, doi:10.1039/C4OB00150H.

196. Scaglione, F.; Panzavolta, G. Folate, Folic Acid and 5-Methyltetrahydrofolate Are Not the Same Thing. *Xenobiotica* **2014**, *44*, 480–488, doi:10.3109/00498254.2013.845705.

197. Biamonte, A.R.; Schneller, G.H. A Study of Folic Acid Stability in Solutions of the B Complex Vitamins. *J. Am. Pharm. Assoc. (Scientific ed.)* **1951**, *40*, 313–320, doi:10.1002/jps.3030400704.

198. Scheindlin, S.; Lee, A.; Griffith, I. The Action of Riboflavin on Folic Acid. *J. Am. Pharm. Assoc. (Scientific ed.)* **1952**, *41*, 420–427, doi:10.1002/jps.3030410806.

199. Jamil Akhtar, M.; Ataullah Khan, M.; Ahmad, I. Identification of Photoproducts of Folic Acid and Its Degradation Pathways in Aqueous Solution. *J. Pharm. Biomed. Anal.* **2003**, *31*, 579–588, doi:10.1016/S0731-7085(02)00724-0.

200. Dawidczyk, C.M.; Kim, C.; Park, J.H.; Russell, L.M.; Lee, K.H.; Pomper, M.G.; Searson, P.C. State-of-the-Art in Design Rules for Drug Delivery Platforms: Lessons from FDA-Approved Nanomedicines. *J. Control. Release* **2014**, *187*, 133–144, doi:10.1016/j.jconrel.2014.05.036.State-of-the-Art.

201. Ramzy, L.; Nasr, M.; Metwally, A.A.; Awad, G.A.S. Cancer Nanotheranostics: A Review of the Role of Conjugated Ligands for Overexpressed Receptors. *Eur. J. Pharm. Sci.* **2017**, *104*, 273–292, doi:10.1016/j.ejps.2017.04.005.

202. Chen, C.; Ke, J.; Edward Zhou, X.; Yi, W.; Brunzelle, J.S.; Li, J.; Yong, E.L.; Xu, H.E.; Melcher, K. (SI) Structural Basis for Molecular Recognition of Folic Acid by Folate Receptors. *Nature* **2013**, *500*, 486–489, doi:10.1038/nature12327.

203. Hassan Baig, M.; Ahmad, K.; Roy, S.; Mohammad Ashraf, J.; Adil, M.; Haris Siddiqui, M.; Khan, S.; Amjad Kamal, M.; Provazník, I.; Choi, I. Computer Aided Drug Design: Success and Limitations. *Curr. Pharm. Des.* **2016**, *22*, 572–581, doi:10.2174/1381612822666151125000550.

204. Hidayat, A.T.; Yusuf, M.; Bachti, H.H.; Diantini, A.; Zainuddin, A. Computational Model of Doxorubicin Conjugate with Docosahexaenoic Acid and Integrin Avß3 Ligand for Anticancer. *J. Appl. Pharm. Sci.* **2018**, 1–6, doi:10.7324/JAPS.2018.8401.

205. Berman, H.M.; Westbrook, J.; Feng, Z.; Gilliland, G.; Bhat, T.N.; Weissig, H.; Shindyalov, I.N.; Bourne, P.E. The Protein Data Bank. *Nucleic Acids Res.* **2000**, *28*, 235–242, doi:10.1093/nar/28.1.235.

206. RCSB PDB RCSB PDB Available online: https://www.rcsb.org/.

207. Pinzi, L.; Rastelli, G. Molecular Docking: Shifting Paradigms in Drug Discovery. *Int. J. Mol. Sci.* **2019**, *20*, doi:10.3390/ijms20184331.

208. Li, J.; Fu, A.; Zhang, L. An Overview of Scoring Functions Used for Protein–Ligand Interactions in Molecular Docking. *Interdiscip. Sci. – Comput. Life Sci.* **2019**, *11*, 320–328, doi:10.1007/s12539-019-00327-w.

209. Salmaso, V.; Moro, S. Bridging Molecular Docking to Molecular Dynamics in Exploring Ligand-Protein Recognition Process: An Overview. *Front. Pharmacol.* **2018**, *9*, 1–16, doi:10.3389/fphar.2018.00923.

210. Joosten, R.P.; Salzemann, J.; Bloch, V.; Stockinger, H.; Berglund, A.-C.; Blanchet, C.; Bongcam-Rudloff, E.; Combet, C.; Da Costa, A.L.; Deleage, G.; et al. PDB_REDO: Automated Re-Refinement of X-Ray Structure Models in the PDB. *J. Appl. Crystallogr.* **2009**, *42*, 376–384, doi:10.1107/S0021889809008784.

211. The UniProt Consortium UniProt: A Worldwide Hub of Protein Knowledge. *Nucleic Acids Res.* **2019**, *47*, D506–D515, doi:10.1093/nar/gky1049.

212. UniProt Consortium UniProt Available online: https://www.uniprot.org/.

213. Pettersen, E.F.; Goddard, T.D.; Huang, C.C.; Couch, G.S.; Greenblatt, D.M.; Meng, E.C.; Ferrin, T.E. UCSF Chimera - A Visualization System for Exploratory Research and Analysis. *J. Comput. Chem.* **2004**, *25*, 1605–1612, doi:10.1002/jcc.20084.

214. UCSF Resource for Biocomputing Visualization and Informatics; National Institutes of Health UCSF Chimera Available online: https://www.cgl.ucsf.edu/chimera/.

215. Laskowski, R.A.; MacArthur, M.W.; Moss, D.S.; Thornton, J.M. PROCHECK: A Program to Check the Stereochemical Quality of Protein Structures. *J. Appl. Crystallogr.* **1993**, *26*, 283–291, doi:10.1107/S0021889892009944.

216. Ramachandran, G.N.; Ramakrishnan, C.; Sasisekharan, V. Stereochemistry of Polypeptide

Chain Configurations. *J. Mol. Biol.* **1963**, *7*, 95–99, doi:10.1016/S0022-2836(63)80023-6.

217. Morris, A.L.; MacArthur, M.W.; Hutchinson, E.G.; Thornton, J.M. Stereochemical Quality of Protein Structure Coordinates. *Proteins Struct. Funct. Genet.* **1992**, *12*, 345–364, doi:10.1002/prot.340120407.

218. Hekkelman, M.L.; Perrakis, A.; Joosten, R.P. PDB-REDO Available online: https://pdb-redo.eu/.

219. Wibowo, A.S.; Singh, M.; Reeder, K.M.; Carter, J.J.; Kovach, A.R.; Meng, W.; Ratnam, M.; Zhang, F.; Dann, C.E. Structures of Human Folate Receptors Reveal Biological Trafficking States and Diversity in Folate and Antifolate Recognition. *Proc. Natl. Acad. Sci.* **2013**, *110*, 15180–15188, doi:10.1073/pnas.1308827110.

220. Yan, W.; Ratnam, M. Preferred Sites of Glycosylphosphatidylinositol Modification in Folate Receptors and Constraints in the Primary Structure of the Hydrophobic Portion of the Signal. *Biochemistry* **1995**, *34*, 14594–14600, doi:10.1021/bi00044a039.

221. Kitchen, D.B.; Decornez, H.; Furr, J.R.; Bajorath, J. Docking and Scoring in Virtual Screening for Drug Discovery: Methods and Applications. *Nat. Rev. Drug Discov.* **2004**, *3*, 935–949, doi:10.1038/nrd1549.

222. Morris, G.M.; Huey, R.; Lindstrom, W.; Sanner, M.F.; Belew, R.K.; Goodsell, D.S.; Olson, A.J. AutoDock4 and AutoDockTools4: Automated Docking with Selective Receptor Flexibility. *J. Comput. Chem.* **2009**, *30*, 2785–2791, doi:10.1002/jcc.21256.

223. Sanner, M.F. Python: A Programming Language for Software Integration and Development. *J. Mol. Graph. Model.* **1999**, *17*, 57–61.

224. Huey, R.; Morris, G.M.; Forli, S. Using AutoDock 4 and AutoDock Vina with AutoDockTools: A Tutorial. *User Guid.* **2012**, 32.

225. Morris, G.M.; Goodsell, D.S.; Halliday, R.S.; Huey, R.; Hart, W.E.; Belew, R.K.; Olson, A.J. Automated Docking Using a Lamarckian Genetic Algorithm and an Empirical Binding Free Energy Function. *J. Comput. Chem.* **1998**, *19*, 1639–1662, doi:10.1002/(SICI)1096-987X(19981115)19:14<1639::AID-JCC10>3.0.CO;2-B.

226. Goodsell, D.S.; Olson, A.J. Automated Docking of Substrates to Proteins by Simulated Annealing. *Proteins Struct. Funct. Bioinforma.* **1990**, *8*, 195–202, doi:10.1002/prot.340080302.

227. Morris, G.M.; Goodsell, D.S.; Huey, R.; Olson, A.J. Distributed Automated Docking of Flexible Ligands to Proteins: Parallel Applications of AutoDock 2.4. *J. Comput. Aided. Mol. Des.* **1996**, *10*, 293–304, doi:10.1007/BF00124499.

228. Trott, O.; Olson, A.J. AutoDock Vina: Improving the Speed and Accuracy of Docking with a New Scoring Function, Efficient Optimization, and Multithreading. *J. Comput. Chem.* **2009**, *32*, NA-NA, doi:10.1002/jcc.21334.

229. Guedes, I.A.; Pereira, F.S.S.; Dardenne, L.E. Empirical Scoring Functions for Structure-Based Virtual Screening: Applications, Critical Aspects, and Challenges. *Front. Pharmacol.* **2018**, *9*, 1–18, doi:10.3389/fphar.2018.01089.

230. Humphrey, W.; Dalke, A.; Schulten, K. VMD: Visual Molecular Dynamics. *J. Mol. Graph.* **1996**, *14*, 33–38, doi:10.1016/0263-7855(96)00018-5.

231. Feinstein, W.P.; Brylinski, M. Calculating an Optimal Box Size for Ligand Docking and Virtual Screening against Experimental and Predicted Binding Pockets. *J. Cheminform.* **2015**, *7*, 18, doi:10.1186/s13321-015-0067-5.

232. Smyslova, P.; Popa, I.; Lyčka, A.; Tejral, G.; Hlavac, J. Non-Catalyzed Click Reactions of ADIBO Derivatives with 5-Methyluridine Azides and Conformational Study of the Resulting Triazoles. *PLoS One* **2015**, *10*, 1–33, doi:10.1371/journal.pone.0144613.

233. Zayas, J.; Annoual, M.; Das, J.K.; Felty, Q.; Gonzalez, W.G.; Miksovska, J.; Sharifai, N.; Chiba, A.; Wnuk, S.F. Strain Promoted Click Chemistry of 2- or 8-Azidopurine and 5-Azidopyrimidine Nucleosides and 8-Azidoadenosine Triphosphate with Cyclooctynes. Application to Living Cell Fluorescent Imaging. *Bioconjug. Chem.* **2015**, *26*, 1519–1532, doi:10.1021/acs.bioconjchem.5b00300.

234. O'Boyle, N.M.; Banck, M.; James, C.A.; Morley, C.; Vandermeersch, T.; Hutchison, G.R. Open Babel: An Open Chemical Toolbox. *J. Cheminform.* **2011**, *3*, 33, doi:10.1186/1758-2946-3-33.

235. Yoshikawa, N.; Hutchison, G.R. Fast, Efficient Fragment-Based Coordinate Generation for Open Babel. *J. Cheminform.* **2019**, *11*, 49, doi:10.1186/s13321-019-0372-5.

236. Wallace, A.C.; Laskowski, R.A.; Thornton, J.M. LIGPLOT: A Program to Generate Schematic Diagrams of Protein-Ligand Interactions. *Protein Eng.* **1995**, *8*, 127–34, doi:10.1093/protein/8.2.127.

237. Laskowski, R.A.; Swindells, M.B. LigPlot+: Multiple Ligand-Protein Interaction Diagrams for Drug Discovery. *J. Chem. Inf. Model.* **2011**, *51*, 2778–86, doi:10.1021/ci200227u.

238. Brooijmans, N.; Kuntz, I.D. Molecular Recognition and Docking Algorithms. *Annu. Rev. Biophys. Biomol. Struct.* **2003**, *32*, 335–373, doi:10.1146/annurev.biophys.32.110601.142532.

239. Agard, N.J.; Prescher, J.A.; Bertozzi, C.R. A Strain-Promoted [3 + 2] Azide-Alkyne Cycloaddition for Covalent Modification of Biomolecules in Living Systems. *J. Am. Chem. Soc.* **2004**, *126*, 15046–15047, doi:10.1021/ja044996f.

240. Baskin, J.M.; Prescher, J.A.; Laughlin, S.T.; Agard, N.J.; Chang, P. V.; Miller, I.A.; Lo, A.; Codelli, J.A.; Bertozzi, C.R. Copper-Free Click Chemistry for Dynamic in Vivo Imaging. *Proc. Natl. Acad. Sci.* **2007**, *104*, 16793–16797, doi:10.1073/pnas.0707090104.

241. Codelli, J.A.; Baskin, J.M.; Agard, N.J.; Bertozzi, C.R. Second-Generation Difluorinated Cyclooctynes for Copper-Free Click Chemistry. *J. Am. Chem. Soc.* **2008**, *130*, 11486–11493, doi:10.1021/ja803086r.

242. Gordon, C.G.; MacKey, J.L.; Jewett, J.C.; Sletten, E.M.; Houk, K.N.; Bertozzi, C.R. Reactivity of Biarylazacyclooctynones in Copper-Free Click Chemistry. *J. Am. Chem. Soc.* **2012**, *134*, 9199–9208, doi:10.1021/ja3000936.

243. Debets, M.F.; Van Berkel, S.S.; Schoffelen, S.; Rutjes, F.P.J.T.; Van Hest, J.C.M.; Van Delft, F.L. Aza-Dibenzocyclooctynes for Fast and Efficient Enzyme PEGylation via Copper-Free (3+2) Cycloaddition. *Chem. Commun.* **2010**, *46*, 97–99, doi:10.1039/b917797c.

244. Dommerholt, J.; Schmidt, S.; Temming, R.; Hendriks, L.J.A.; Rutjes, F.P.J.T.; Van Hest, J.C.M.; Lefeber, D.J.; Friedl, P.; Van Delft, F.L. Readily Accessible Bicyclononynes for Bioorthogonal Labeling and Three-Dimensional Imaging of Living Cells. *Angew. Chemie* -

Int. Ed. **2010**, *49*, 9422–9425, doi:10.1002/anie.201003761.

245. Brünger, A.T. Free R Value: A Novel Statistical Quantity for Assessing the Accuracy of Crystal Structures. *Nature* **1992**, *355*, 472–475, doi:10.1038/355472a0.

246. Kleywegt, G.J.; Alwyn Jones, T. Model building and refinement practice. In *Macromolecular Crystallography: part B*; 1997; pp. 208–230.

247. EMBL-EBI PROCHECK Available online: https://www.ebi.ac.uk/thornton-srv/software/PROCHECK/.

248. Alessi, M.L.; Norman, A.I.; Knowlton, S.E.; Ho, D.L.; Greer, S.C. Helical and Coil Conformations of Poly(Ethylene Glycol) in Isobutyric Acid and Water. *Macromolecules* **2005**, *38*, 9333–9340, doi:10.1021/ma051339e.

249. Scheidt, W.R.; Lee, Y.J. Recent advances in the stereochemistry of metallotetrapyrroles. In *Metal Complexes with Tetrapyrrole Ligands I*; Springer-Verlag: Berlin/Heidelberg; pp. 1–70.

250. Kingsbury, C.J.; Senge, M.O. The Shape of Porphyrins. *Coord. Chem. Rev.* **2021**, *431*, 213760, doi:10.1016/j.ccr.2020.213760.

251. Gaillard, T. Evaluation of AutoDock and AutoDock Vina on the CASF-2013 Benchmark. *J. Chem. Inf. Model.* **2018**, *58*, 1697–1706, doi:10.1021/acs.jcim.8b00312.

252. Nguyen, N.T.; Nguyen, T.H.; Pham, T.N.H.; Huy, N.T.; Bay, M. Van; Pham, M.Q.; Nam, P.C.; Vu, V. V.; Ngo, S.T. Autodock Vina Adopts More Accurate Binding Poses but Autodock4 Forms Better Binding Affinity. *J. Chem. Inf. Model.* **2020**, *60*, 204–211, doi:10.1021/acs.jcim.9b00778.

253. Dhanik, A.; McMurray, J.S.; Kavraki, L. Auto Dock-Based Incremental Docking Protocol to Improve Docking of Large Ligands. *Proc. - 2012 IEEE Int. Conf. Bioinforma. Biomed. Work. BIBMW 2012* **2012**, 48–55, doi:10.1109/BIBMW.2012.6470370.

254. Devaurs, D.; Antunes, D.A.; Hall-Swan, S.; Mitchell, N.; Moll, M.; Lizée, G.; Kavraki, L.E. Using Parallelized Incremental Meta-Docking Can Solve the Conformational Sampling Issue When Docking Large Ligands to Proteins. *BMC Mol. Cell Biol.* **2019**, *20*, 1–15, doi:10.1186/s12860-019-0218-z.

255. Antunes, D.A.; Moll, M.; Devaurs, D.; Jackson, K.R.; Lizée, G.; Kavraki, L.E. DINC 2.0: A New Protein–Peptide Docking Webserver Using an Incremental Approach. *Cancer Res.* **2017**, *77*, e55–e57, doi:10.1158/0008-5472.CAN-17-0511.

256. Dhanik, A.; McMurray, J.S.; Kavraki, L.E. DINC: A New AutoDock-Based Protocol for Docking Large Ligands. *BMC Struct. Biol.* **2013**, *13*, S11, doi:10.1186/1472-6807-13-S1-S11.

257. Thapa, P.; Li, M.; Karki, R.; Bio, M.; Rajaputra, P.; Nkepang, G.; Woo, S.; You, Y. Folate-PEG Conjugates of a Far-Red Light-Activatable Paclitaxel Prodrug to Improve Selectivity toward Folate Receptor-Positive Cancer Cells - SI. *ACS Omega* **2017**, *2*, 6349–6360, doi:10.1021/acsomega.7b01105.

258. Schrödinger, L. *The PyMOL Molecular Graphics System, Version 2.0*; 2015;

259. PerkinElmer Informatics; CambridgeSoft ChemDraw Ultra 2010.

260. Adobe Inc. Adobe Photoshop Elements 2012.

261. Chang, L.; Li, Y.; Chu, J.; Qi, J.; Li, X. Preparation of Core-Shell Molecularly Imprinted Polymer via the Combination of Reversible Addition-Fragmentation Chain Transfer Polymerization and Click Reaction. *Anal. Chim. Acta* **2010**, *680*, 65–71, doi:10.1016/j.aca.2010.09.017.

262. Xu, Z.; Kuang, D.; Zhang, F.; Tang, S.; Deng, P.; Li, J. Fluorogenic Molecularly Imprinted Polymers with Double Recognition Abilities Synthesized via Click Chemistry. *J. Mater. Chem. B* **2013**, *1*, 1852, doi:10.1039/c3tb00584d.

263. Gao, M.; Ren, J.; Tian, K.; Jia, L. Characterization of Non-Specific Protein Adsorption Induced by Triazole Groups on the Chromatography Media Using Cu (I)-Catalyzed Alkyne-Azide Cycloaddition Reaction for Ligand Immobilization. *J. Chromatogr. A* **2016**, *1476*, 63–68, doi:10.1016/j.chroma.2016.11.017.

264. Gouterman, M. Spectra of Porphyrins. *J. Mol. Spectrosc.* **1961**, *6*, 138–163, doi:10.1016/0022-2852(61)90236-3.

265. Gouterman, M.; Wagnière, G.H.; Snyder, L.C. Spectra of Porphyrins. Part II. Four Orbital Model. *J. Mol. Spectrosc.* **1963**, *11*, 108–127, doi:10.1016/0022-2852(63)90011-0.

266. Parusel, A.B.J.; Grimme, S. DFT / MRCI Calculations on the Excited States of Porphyrin , Hydroporphyrins , Tetrazaporphyrins and Metalloporphyrins. **2001**, 225–232.

267. Schaberle, F.A. Assessment of the Actual Light Dose in Photodynamic Therapy. *Photodiagnosis Photodyn. Ther.* **2018**, *23*, 75–77, doi:10.1016/j.pdpdt.2018.06.009.

268. Braslavsky, S.E. Glossary of Terms Used in Photochemistry 3rd Edition: (IUPAC Recommendations 2006). *Pure Appl. Chem.* **2007**, *79*, 293–465, doi:10.1351/pac200779030293.

269. Parker, C.A.; Rees, W.T. Correction of Fluorescence Spectra and Measurement of Fluorescence Quantum Efficiency. *Analyst* **1960**, *85*, 587, doi:10.1039/an9608500587.

270. Rurack, K.; Spieles, M. Fluorescence Quantum Yields of a Series of Red and Near-Infrared Dyes Emitting at 600-1000 Nm. *Anal. Chem.* **2011**, *83*, 1232–1242, doi:10.1021/ac101329h.

271. Dąbrowski, J.M.; Krzykawska, M.; Arnaut, L.G.; Pereira, M.M.; Monteiro, C.J.P.; Simões, S.; Urbańska, K.; Stochel, G. Tissue Uptake Study and Photodynamic Therapy of Melanoma-Bearing Mice with a Nontoxic, Effective Chlorin. *ChemMedChem* **2011**, *6*, 1715–1726, doi:10.1002/cmdc.201100186.

272. Sasnouski, S.; Pic, E.; Dumas, D.; Zorin, V.; D'Hallewin, M.A.; Guillemin, F.; Bezdetnaya, L. Influence of Incubation Time and Sensitizer Localization on Meta-Tetra(Hydroxyphenyl)Chlorin (MTHPC)-Lnduced Photoinactivation of Cells. *Radiat. Res.* **2007**, *168*, 209–217, doi:10.1667/0033-7587(2007)168[209:IOITAS]2.0.CO;2.

273. Silva, E.F.F.; Schaberle, F.A.; Monteiro, C.J.P.; Dąbrowski, J.M.; Arnaut, L.G. The Challenging Combination of Intense Fluorescence and High Singlet Oxygen Quantum Yield in Photostable Chlorins - a Contribution to Theranostics. *Photochem. Photobiol. Sci.* **2013**, *12*, 1187–1192, doi:10.1039/c3pp25419d.

274. Wilkinson, F.; Helman, W.P.; Ross, A.B. Quantum Yields for the Photosensitized Formation of the Lowest Electronically Excited Singlet State of Molecular Oxygen in

Solution. *J. Phys. Chem. Ref. Data* **1993**, *22*, 113–262, doi:10.1063/1.555934.

275. Krasnovsky, A.A. Singlet Molecular Oxygen in Photobiochemical Systems: IR Phosphorescence Studies. *Membr. Cell Biol.* **1998**, *12*, 665–90.

276. Chen, K.; Wacker, M.; Hackbarth, S.; Ludwig, C.; Langer, K.; Röder, B. Photophysical Evaluation of MTHPC-Loaded HSA Nanoparticles as Novel PDT Delivery Systems. *J. Photochem. Photobiol. B Biol.* **2010**, *101*, 340–347, doi:10.1016/j.jphotobiol.2010.08.006.

277. Kim, H.; Lindsey, J.S. De Novo Synthesis of Stable Tetrahydroporphyrinic Macrocycles: Bacteriochlorins and a Tetradehydrocorrin. *J. Org. Chem.* **2005**, *70*, 5475–5486, doi:10.1021/jo050467y.

278. Galezowski, M.; Gryko, D. Recent Advances in the Synthesis of Hydroporphyrins. *Curr. Org. Chem.* **2007**, *11*, 1310–1338, doi:10.2174/138527207782023157.

279. Dąbrowski, J.M.; Arnaut, L.G.; Pereira, M.M.; Urbańska, K.; Simões, S.; Stochel, G.; Cortes, L. Combined Effects of Singlet Oxygen and Hydroxyl Radical in Photodynamic Therapy with Photostable Bacteriochlorins: Evidence from Intracellular Fluorescence and Increased Photodynamic Efficacy in Vitro. *Free Radic. Biol. Med.* **2012**, *52*, 1188–1200, doi:10.1016/j.freeradbiomed.2011.12.027.

280. International Agency for Research on Cancer; World Health Organization Global Cancer Observatory Available online: https://gco.iarc.fr/.

281. Bray, F.; Ferlay, J.; Soerjomataram, I.; Siegel, R.L.; Torre, L.A.; Jemal, A. Global Cancer Statistics 2018: GLOBOCAN Estimates of Incidence and Mortality Worldwide for 36 Cancers in 185 Countries. *CA. Cancer J. Clin.* **2018**, *68*, 394–424, doi:10.3322/caac.21492.

282. Goldhirsch, A.; Winer, E.P.; Coates, A.S.; Gelber, R.D.; Piccart-Gebhart, M.; Thürlimann, B.; Senn, H.-J.; Albain, K.S.; André, F.; Bergh, J.; et al. Personalizing the Treatment of Women with Early Breast Cancer: Highlights of the St Gallen International Expert Consensus on the Primary Therapy of Early Breast Cancer 2013. *Ann. Oncol.* **2013**, *24*, 2206–2223, doi:10.1093/annonc/mdt303.

283. El-Akra, N.; Noirot, A.; Faye, J.C.; Souchard, J.P. Synthesis of Estradiol–Pheophorbide a Conjugates: Evidence of Nuclear Targeting, DNA Damage and Improved Photodynamic Activity in Human Breast Cancer and Vascular Endothelial Cells. *Photochem. Photobiol. Sci.* **2006**, *5*, 996–999, doi:10.1039/b606117f.

284. Hu, Z.; Rao, B.; Chen, S.; Duanmu, J. Targeting Tissue Factor on Tumour Cells and Angiogenic Vascular Endothelial Cells by Factor VII-Targeted Verteporfin Photodynamic Therapy for Breast Cancer in Vitro and in Vivoin Mice. *BMC Cancer* **2010**, *10*, 235, doi:10.1186/1471-2407-10-235.

285. Hu, D.; Sheng, Z.; Fang, S.; Wang, Y.; Gao, D.; Zhang, P.; Gong, P.; Ma, Y.; Cai, L. Folate Receptor-Targeting Gold Nanoclusters as Fluorescence Enzyme Mimetic Nanoprobes for Tumor Molecular Colocalization Diagnosis. *Theranostics* **2014**, *4*, 142–153, doi:10.7150/thno.7266.

286. Berlanda, J.; Kiesslich, T.; Engelhardt, V.; Krammer, B.; Plaetzer, K. Comparative in Vitro Study on the Characteristics of Different Photosensitizers Employed in PDT. *J. Photochem. Photobiol. B Biol.* **2010**, *100*, 173–180, doi:10.1016/j.jphotobiol.2010.06.004.

287. European Collection of Authenticated Cell Cultures (ECACC); UK Health Security Agency (UKHSA) European Collection of Authenticated Cell Cultures (ECACC) Cell Line Profiles

Available online: https://www.phe-culturecollections.org.uk/collections/ecacc-cell-line-profiles.aspx.

288. Bello, E.; Taraboletti, G.; Colella, G.; Zucchetti, M.; Forestieri, D.; Licandro, S.A.; Berndt, A.; Richter, P.; D'Incalci, M.; Cavalletti, E.; et al. The Tyrosine Kinase Inhibitor E-3810 Combined with Paclitaxel Inhibits the Growth of Advanced-Stage Triple-Negative Breast Cancer Xenografts. *Mol. Cancer Ther.* **2013**, *12*, 131–140, doi:10.1158/1535-7163.MCT-12-0275-T.

289. Chen, J.; Lu, L.; feng, Y.; Wang, H.; Dai, L.; li, Y.; Zhang, P. PKD2 Mediates Multi-Drug Resistance in Breast Cancer Cells through Modulation of P-Glycoprotein Expression. *Cancer Lett.* **2011**, *300*, 48–56, doi:10.1016/j.canlet.2010.09.005.

290. Krysko, D. V; Garg, A.D.; Kaczmarek, A.; Krysko, O.; Agostinis, P.; Vandenabeele, P. Immunogenic Cell Death and DAMPs in Cancer Therapy. *Nat. Rev. Cancer* **2012**, *12*, 860–75, doi:10.1038/nrc3380.

291. Garg, A.D.; Krysko, D. V.; Vandenabeele, P.; Agostinis, P. Hypericin-Based Photodynamic Therapy Induces Surface Exposure of Damage-Associated Molecular Patterns like HSP70 and Calreticulin. *Cancer Immunol. Immunother.* **2012**, *61*, 215–221, doi:10.1007/s00262-011-1184-2.

292. Garg, A.D.; Vandenberk, L.; Koks, C.; Verschuere, T.; Boon, L.; Van Gool, S.W.; Agostinis, P. Dendritic Cell Vaccines Based on Immunogenic Cell Death Elicit Danger Signals and T Cell–Driven Rejection of High-Grade Glioma. *Sci. Transl. Med.* **2016**, *8*, 1–16, doi:10.1126/scitranslmed.aae0105.

293. Gazzali, A.M.; Lobry, M.; Colombeau, L.; Acherar, S.; Azaïs, H.; Mordon, S.; Arnoux, P.; Baros, F.; Vanderesse, R.; Frochot, C. Stability of Folic Acid under Several Parameters. *Eur. J. Pharm. Sci.* **2016**, *93*, 419–430, doi:10.1016/j.ejps.2016.08.045.